Georgii Krikun

# Impact of thermal transport parameters on the operating temperature of OLEDs

**DISSERTATION**

zur Erlangung des akademischen Grades
Doctor der Technischen Wissenshaften

eingereicht an der
**Graz University of Technology**

Betreuer
Univ.-Prof. Dipl-Ing. Dr.techn. Egbert Zojer

Mitbetreuer
Ass. Prof. Dr. rer. nat. Karin Zojer

Institute of Solid State Physics

Graz, December 2020

# Affidavit

I declare that I have authored this thesis independently, that I have not used other than the declared sources/resources, and that I have explicitly indicated all material which has been quoted either literally or by content from the sources used. The text document uploaded to TUGRAZonline is identical to the present doctoral thesis.

| | |
|---|---|
| Date | Signature |

**Abstract**

Today, organic electronics comprise a rapidly growing market with a total capitalization measured in billions and, if the predictions are correct, this market will continue to steadily grow in the nearest future. Despite that, some potential applications of organic semiconductors (OSCs) are still facing substantial technical difficulties. In this dissertation we will take a close look on one of such applications - organic light emitting diodes (OLEDs) for lighting.

Lighting requires substantial output power. Operating OLEDs to emit such power increases the operating temperature. This increase must be particularly carefully monitored, because the charge transport in organic semiconductors is thermally activated. That means that higher temperature may cause higher currents and, possibly, thermal runaway. In this dissertation, we combine the established techniques of drift-diffusion-based modeling of charge transport and the heat equation to simultaneously capture both electrical and thermal properties of OLED. To capture the electrothermal behavior of the organic semiconductor, we use an established mobility model for hopping transport, which depends on the electric field, charge carrier densities, and operating temperature.

In the first part of the dissertation we will show how thermal transport parameters of the layers the OLED consists of influence the operating device temperature and the current voltage characteristics. The thermal transport parameters considered were the thermal conductivity of each layer and the effective heat transfer coefficient between the electrically active organic layers and ambient environment. We found that the heat transfer coefficient affects the operating temperature most. This indicates that efficient heat dissipation is of prime importance. Contrary to that, thermal conductivity of the electrically active layers does not contribute to elevated operating temperatures, because the layers are thin enough. This implies that the temperature distribution within the electrically active layer is almost constant, and both charge transport and light propagation can be optimized without compromising the thermal transport and vice versa.

In the second part we make an effort to find the possible limitations of the model in predicting the current-voltage-temperature charactistics. For that, modeling results are compared to experimental data. We found that particularly the width of the density of states (DOS) in the OSC has a pronounced effect on both current-voltage and current-temperature characteristics of the device. With the correct choice of this width the current-temperature dependence of the considered OLED is reproduced most closely in voltage regions relevant for elevated operating temperatures. We also found, that the modeled current-voltage characteristics strongly deviate from the experimental data in the low-voltage region. Our results suggest that the formulation of charge injection in our model is not well suited for low voltage operation.

# Contents

# Acknowledgments

I want to thank my supervisors Karin Zojer and Egbert Zojer for giving me the opportunity to work in TU Graz on the ThermOLED project. Starting with a new job in a foreign county for a first time turned out to be difficult for me, and their advices and guidance helped me navigate through my PhD with ease. Karin was always there to answer my questions and encouraging at difficult times, providing me with useful information and keeping up-to-date with modern advances in the field, which otherwise could be overlooked by me. Under her supervision, I had almost complete freedom in my research activities, which resulted in my personal and professional growth. Her guidance is a number one reason for this thesis to even exist.

Egbert has influenced my work a lot by numerous reasonable thought-trough questions and suggestions, both during the project and thesis writing phases. As the reader might notice, I sometimes struggle to express my thoughts in a precise scientific writing and the first version of the thesis had immensely improved by his comments about certain inconsistencies as well as sometimes plainly wrong statements.

I would also like to thank the funding organizations, specifically FFG and FWF, which funded the project and allowed me to work here in the first place.

I am also very grateful to the personnel of Johanneum research, who worked on the project, in particular Florian Kolb, who spent a lot of time explaining me the experimental setup and the implications of its realization, Dr. Manuel Auer-Berger, who actually constructed this experimental setup.

Natalia Bedoya-Martinez for scientific discussions and help with implementation of parallel computing in the simulation.

Jimmy Mangalam, for being a great company and a great friend during my stay in Austria. Jimmy, who finished his PhD in Chemistry department of TU Graz, also helped me broaden my knowledge in the material science and in chemistry during our beer sessions.

Elisabeth Stern, who guided me through all paperwork, required to stay employed. I am particularly bad with modern bureaucracy and without her help, I would definitely not last long here.

Olivia Kettner, for being great company and being my tandem partner improving my German skills.

Markus Krammer, for a scientific discussions and improving my programming skills.

Markus Burgstaller and Michael Schoefmann for hiring me after the project ended, effectively allowing me to stay in Austria and finish this thesis properly.

# 1 Introduction

## 1.1 Scope of this thesis

This thesis is dedicated to the theoretical exploration of temperature-related characteristics of Organic Light Emitting Diodes (OLEDs), concentrating on lighting applications. Lighting is a very specific application for any light source, as it requires a large power output, which inevitably results in a noticeable heating of the light emitter. The heating is often considered as an undesired byproduct of useful work performed by electrical devices. Combining the raw amount of power required to light up the average living room and the fact that no commercially available lighting device surpasses 50 % power efficiency, one can understand why lighting always goes hand in hand with heating.

The work presented here was performed as a part of the ThermOLED project and, as the name suggests, it was aimed to investigate the influence of heating on OLEDs. The large surface area of OLEDs, which is required to use it as a lighting device, is a first very distinct feature, that separates them into a different class of devices, compared to traditional zero-dimensional (LEDs) or one-dimensional (incandescent bulbs or fluorescent bulbs) sources, and makes it worth to investigate. Large surface lighting area, compared to traditional point-like sources, imposes a new requirement on the device, i.e. a uniform surface. It turns out that such a uniformity is hard to achieve.

The problems related to establishing uniformity partially stem from the fact that the conductivity of organic materials may change by orders of magnitude depending on the operating conditions, which include the material temperature. An increased conductivity may in turn improve the device efficiency due to a decreased energy dissipation. On the other hand, large electric currents may also drive a device into a vicious cycle, in which an increase in temperature causes a higher electrical current, which in turn increases heat generation and, consequently, the temperature. In experiments, such a behavior is frequently observed not on the whole surface of the device but localized spatially, manifesting itself in local, bright hot spots, which quickly degrade into black spots.

This means, that the very same effect can either beneficially or detrimentally affect the device performance. In this thesis, we will combine the established approaches to theoretically model electric devices with the recent, parametrized models for the electrical conductivity of organic semiconductors to capture the complex device behavior within a single simulation tool. With that tool, we will explore the aforementioned features of OLEDs in detail. In particular, we will demonstrate that our simulations suggest plausible origins of hot spot formation, show the role of the vicious cycle, and point out ways to further improve the simulations.

In the introduction chapter, I will give a brief overview of existing devices that are also used (or could be used) for lighting to convince the reader, that OLEDs are promising candidates for that purpose. In this section, I will also give a brief overview of OLED properties, their working principles and characteristics.

In the methodology chapter, I will provide the complete description of our approach to model the device. Every detail of the simulations, which was established during the course of my PhD will be presented there. Note that not every method we used is a conventional method to model a device, hence, the methodology section might not only serve as a guide on how to repeat the results obtained in this thesis, but can be interesting on its own.

In the third section the reader can find a full set of the results obtained from the simulations, which were prepared using the described methodology. Most of them are relevant from a purely scientific point of view, i.e. expand our knowledge of the thermal behavior of OLEDs. They clearly show, which tuning handles are suited to improve the performance in terms of electrical and thermal material properties. Some will be dedicated to the comparison of experiment and modeling. This part is important, as it proves the merit of the overall simulation approach and supports the original, purely theoretically obtained results. We think that the developed simulation tool is powerful and can be used for a variety of different tasks for which it is crucial to assess the impact of device heating. This will be demonstrated with selected showcases.

## 1.2 OLEDs in the context of lighting devices - a brief history

During the last two centuries of human history people witnessed a dramatic progress of science in general. Different scientific branches like mathematics, physics, chemistry and others finally got a chance to meet and merge into something, which today forms our understanding of the world. For example, the discovery of quantum mechanics by physicists lead to a leap in our understanding of molecules and their interactions, which beforehand was a purely chemistry prerogative. This development in turn would have been impossible without a solidly developed apparatus of linear algebra, differential equations, and complex analysis in mathematics.

The rapid progress which took off back then has not lowered in pace yet and this brought a lot of fancy high tec devices into our everyday life, such as smartphones, computers, cars, etc. However, in this thesis, we will talk about a topic that did not develop over the last decade or even century, because humanity knew lighting devices for most of its recorded history and they were always a cornerstone of its survival. For most parts of history, lighting was tightly associated with fire.

### 1.2.1 A Brief history of lighting devices

The revolutionizing invention of incandescent light bulbs in the second half of the 19th century along with the invention of electricity substantially changed our daily life, providing us with an easy access to light. Since then, by continuous improvements, light bulb efficiency has been drastically improved and today it reaches 5.1 % of idealized 100% light source efficacy. Given that the efficacy is related to the power efficiency, 5.1% may seem very small. Yet, it still outperforms by orders of magnitude light sources previously known to humanity [1]. Nevertheless, the process which allows to extract light from electrical current is thermal radiation, which is not efficient due to its broad radiation spectrum. Therefore, people started to investigate whether it is possible to build a light source, for which one can better control the radiation

spectrum and does not waste a substantial part of it due to electromagnetic radiation invisible to the human eye. The general world-wide trend since the beginning of 2000th is to phase out incandescent light bulbs, replacing them with more efficient light sources.

The next important step was made with fluorescent lamps. They work as follows: Electric current in a gas (generally, mercury) produces UV light, which then causes a phosphor inside the bulb to glow. There are several reasons, why this process is inefficient, even though fluorescent lamps are more efficient than incandescent light bulbs. First of all, there is some heating related to the electric current. Secondly, not all UV photons excite visible light photons. Last and most important, visible light photons have less energy than UV photons which excited them. They are generally more costly in manufacturing, although their price can be compensated by their efficiency around 15 % and they have also 10 to 20 times higher lifetime. However, there is also a number of disadvantages, not related to the efficacy. First of all, they have a complicated starting process, which leads to fast degradation if one switches them on and off too often. They might trigger health problems in general, either when mercury contained inside spills out or for particular individuals, who are sensitive to their high speed flickering.

With the continuous development of physics, people discovered electroluminescence phenomena [2], which after 20 years led to the first light emitting diode [3]. Nevertheless practical difficulties delayed the creation of first visible spectrum LEDs, that were not demonstrated until the 1960th [4], followed by yellow LEDs [5], and high-brightness blue LEDs [6], initiating commercialization of these devices for lighting purposes. Nowadays, we have commercialized solid state lighting devices, which are suitable for usage in everyday life with the efficacy going up to 25%, while their theoretical limit is 44%.

The development of organic LEDs (OLEDs) started much later. The first discovery of electroluminescence of organic material dates back to 1950th [7–10]. After that it was quite rapidly discovered that organic materials, which were generally considered to be insulators, can conduct electric currents. The problem with them does not relate to the charge carrier mobilities, but to the contacts which are required to have suitable workfunction to inject charge carriers [11–13]. This discovery created a new field, namely organic electronics. In 1987 eventually, the first practical OLED was created [14].

Such discovery revolutionized our understanding of LEDs, as it brings an enormous amount of new organic materials into the field of lighting devices. Since then, investigations of OLEDs has continued and in 2007 AMOLED matrices, which consist of OLEDs, entered the market and became widely used in mobile phones, cameras and TVs [15–18]. However, OLEDs are still not developed enough to become a general purpose lighting device. Some market solutions already exist, but they are priced substantially higher than any of the previously mentioned devices. To get enough lighting output from an OLED to, e.g, light up a room, its surface area should be from a hundred squared centimeters to a couple of square meters and the lighting should be homogeneous across the whole surface. Such requirements cannot be easily satisfied for the reasons we will explain later in this thesis. This still poses a huge problem.

## 1.3 Structure and working principle of OLEDs

In this section, we will talk about the general structure and the operating principle of OLEDs. Before moving forward, we want to emphasize that in this thesis we are talking particularly about so-called small molecule OLEDs. There exists another large class of organic light-emitting devices, polymer organic light emitting diodes [19], often abbreviated as P-OLED or PLED. There are only few similarities between OLEDs, POLEDs and inorganic LEDs, thus, for the purpose of this thesis, it makes sense to start directly with the small molecule OLEDs. Sometimes, however, the comparison between PLEDs, OLEDs, and inorganic LEDs can be useful to understand a broader context, as all devices serve the same purpose.

### 1.3.1 Basic OLED structure

The basic OLED structure is depicted on fig. 1.1 [20]. The organic layer of the device, called the emitting layer in this figure, is sandwiched between the two electrodes, cathode and anode. The electrodes provide the emitting layer with two types of oppositely charged charge carriers. When a voltage is applied, negatively charged *electrons* are injected into the emitting layer from the cathode, and positively charged *holes* are injected from the opposite side, where the anode is located.

When injected, the charge carriers start to move towards each other due to the applied electric field. When they meet, they *recombine*, forming *excitons*. Excitons, are an electrically neutral bound pair of electrons and holes. The motion of excitons is not affected by the electric field applied between the contacts. They can diffuse through the device until they finally. The decay can involve the emission of a *photon* (radiative recombination). Only small fraction of the produced light can escape the device through the transparent contact, which is often made from indium tin oxide (see fig. 1.1). Such setup is more common and is often referred to as bottom-emitting OLED, although it is also possible to manufacture top-emitting structures [21, 22]. Ultimately, the difference between top and bottom emitting structures comes from the location of transparent contact relative to the substrate.

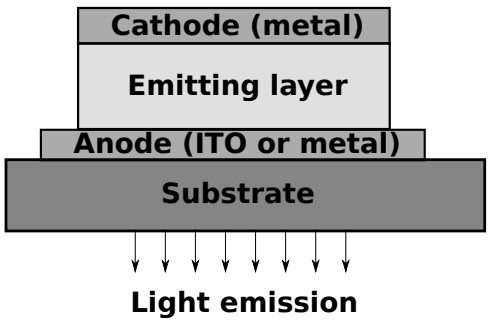


Figure 1.1: Basic OLED setup, adopted from [20]

Processes such as injection, charge transport and recombination are heavily influenced by the energetic landscape for the charge carriers in the material. In the sec. 1.3.5, we will thoroughly describe the constituents of the energy level diagram and possible effects, which manifest at interfaces and may result in energy level rearrangements. In sec. 2.4.2, we will show how the combined influence of all the constituent layers influences the charge carrier injection. To introduce basic material properties, we will

first take a look at the extremely simplified energy diagram of an OLED in fig. 1.2, adopted from [23].

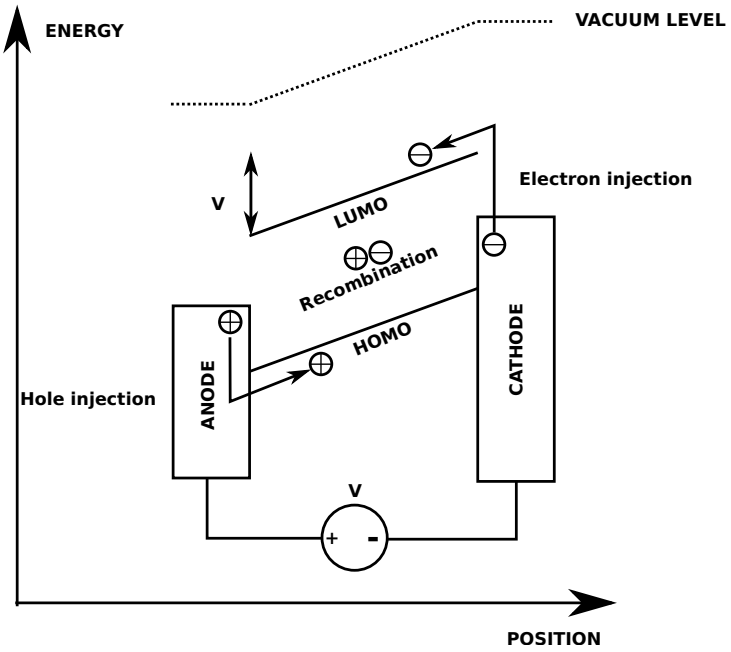


Figure 1.2: Simplified energy diagram of OLED with one organic later under applied bias $V$. Adopted from [23]

Applying an external voltage between cathode and anode generates a electrostatic potentials difference, $V$, between the contacts, which gradually changes from one contact to another, introducing a spatially dependent shift in energy levels of LUMO (for electrons) and HOMO (for holes). LUMO stands for the Lowest Unoccupied Molecular Orbital, which is most often defines the energy level of an electron in the material. HOMO in turn is the Highest Occupied Molecular Orbital, which determines the energy of a hole. Energy level diagrams are normally drawn for electrons. Therefore, electrons "want" to move downwards in these diagrams, while positively charged holes move upwards. Hence, hole and electron injection from the contacts into the organic layer is hindered by the possible energy offsets to the Fermi levels in the contacts due to which injection barriers form. Fermi level in the metallic contact describes the average energy of the charge carrier. After injection, charge carriers start to drift towards each other. If hole and electron are spatially close they can either form an exciton which may lead to radiative recombination of the two, or have non-radiative recombination via, e.g., gap states [24].

However, this simplistic picture does not reflect the complex structure of OLEDs manufactured today. The efficiency of charge carrier injection, transport, and recombination can be further improved by properly arranging several different organic layers between the electrodes, see for example [25]. This improvement can be achieved in a multilayer setup, where separate layers improve the efficiency of different processes, fig. 1.3. Following the path from the electrodes inside the device, one first encounters the electron (EIL) and the hole (HIL) injection layers. They are optionally placed between the contact and the transport layers to enhance charge carrier injection by leveraging the injection barrier at the contact [26]. We will elaborate further in the thesis what are the main constituents of the injection barrier in sec. 1.3.5. For now, it is sufficient to know that a lower injection barrier allows more charge carriers to get

into the device and to potentially recombine. Next, we see the hole transport layer and the electron transport layer [26], whose function is to supply charge carriers for the emissive region. These transport layers possess a high mobility for the desired charge carrier type and may be optionally doped to enhance the transport layer charge carrier densities [27]. Transport layers are succeeded by the Hole and the Electron Blocking Layers (HBL and EBL). Their purpose is to prevent the charge carriers from reaching the opposite electrode [28]. Finally, an emission layer (EML) defines the emission properties of the device. For example if it consists of or doped by chromophores with specific energies of triplet and singlet states [29], one can manually change the emission profile. There can be multiple emission layers, whose individual emission spectra are superimposed for example to blend several emission wavelength profiles, to give perfect white emission [30, 31].

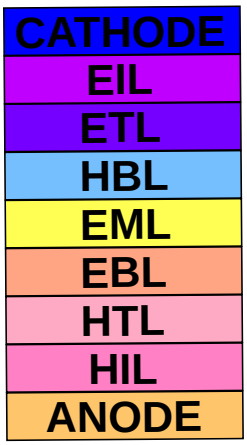


Figure 1.3: Device setup with a number of additional layers, which can further improve device efficiency compared to fig. 1.1 and are often used in practice. HIL and EIL are the hole and electron injection layers, HTL and ETL stand for the hole and electron transport layers. HBL and EBL are in turn hole and electron blocking layers. EML is the emission layer, which is responsible for the wavelength profile of light, emitted by OLED.

### 1.3.2 OLED efficiency

Considering the elaborate design of the OLED layer stack given in fig. 1.3, it is useful to immediately introduce quantities, which describe the efficiency of an OLED. These quantities allow to quickly assess the device performance and to compare different device setups in terms of their efficiency. The OLED can be characterized by its quantum efficiency, luminous efficacy $\eta_P$ measured in $lm\ W^{-1}$ or current efficiency $cd\ A^{-1}$ [20]. One should further distinguish between $\eta_{ext}$, the external quantum efficiency, and $\eta_{int}$, the internal quantum efficiency. These two are related to each other as eq. 1.1 [32]:

$$\eta_{ext} = \eta_{int}\eta_{out} \tag{1.1}$$

The external quantum efficiency $\eta_{ext}$ denotes the inverse ratio between the number of electrically injected carriers and the number of externally observed photons. It can be easily measured experimentally [33]. $\eta_{out}$ is an outcoupling efficiency and denotes the inverse ratio between the number of photons generated and the number of photons registered outside the device. It depends on a chosen device geometry,

material absorption coefficients, and refractive indices, which are chosen in such a way that the chance of the photon being reabsorbed or trapped due to total internal reflection is minimal. A number of techniques can also be employed to improve this ratio, such as chip shaping [34], the use of patterned substrates [35], photonic crystals [36], or surface roughening [37]. Finally, the internal quantum efficiency $\eta_{int}$ is defined as the ratio between the number of electrically injected carriers and the emitted (but not necessarily registered outside) photons. It is determined by a number of device parameters such as the quality of the active layer, the doping profile, the defect density, and the uniformity of the layer [33]. Often, $\eta_{int}$ can be further divided into separate constituents, which affect the total IQE multiplicatively [38].

Finally, there is one more constituent for evaluating the performance of OLEDs when used for lighting purposes, the luminous efficacy. Not all photons, that leave a light source are within the narrow wavelength range, which can be perceived by human eye, located between 380 and 740 $nm$. In fact, even within this range, different light wavelengths are perceived differently, with the maximum visible intensity located at the famous peak of green light at 555 $nm$. The ration of the luminous flux (perceived power of light) to the total power of the light source, is called luminous efficacy [1].

### 1.3.3 Charge carrier mobilities

The hole and electron transport layers in fig. 1.3 are extremely important constituents of OLEDs. The key performance parameter of these layers with respect to their function is athe charge carrier mobility. By definition (see sec. 2.2.1) the charge carrier mobility is the proportionality coefficient between the average carrier drift velocity and the applied electric field. The unit for the mobility in SI is $m^2/(V\ s)$, however, it is also often measured in $cm^2/(V\ s) = 10^{-4}m^2/(V\ s)$ [39]. A high mobility allows a fast device operation, as needed for large area electronics with performance meeting market demands [40–43]. In the particular case of OLEDs, large mobilities can reduce charge carrier accumulation in the transport layers and allow unobstructed access of the injected charge carriers into the emissive layer.

#### Transport regimes

The mobility value is highly influenced by the material structure, which in turn is determined by the molecular structure and the forces between the molecules. Different growth conditions also influence formation of different phases [44]. In this thesis we will not try to cover all possible materials, stuctures and phases as they are described elsewhere [45]. In organic materials, the intermolecular forces that hold molecules together, such as hydrogen bonds, van der Waals forces, or forces in the charge transfer complexes are relatively weak, compared to intramolecular forces or the forces which are present in inorganic semiconductors [46]. Depending on the strength and type of these interactions different structures may thus form. Regarding the charge transport in organic semiconductors there are three relevant structure types: (i) crystalline layers, or structure with periodic molecule arrangements (ii) polymer, which are one-dimensional chains of small monomers, tied together with strong covalent bonds [47], and (iii) amorphous structures. Multiple different material structures can still be present at distinct phases [48] with distinct properties. Note that high charge carrier mobilities $\mu$ still do not necessarily correspond to a high conductivity $\sigma$ of

the material. Following the textbook definition of condictivity $\sigma = en\mu$, where $e$ is elementary charge and $n$ is the carrier concentration [39], one can see that low carrier concentration may result in a low conductivity despite high values of the mobility.

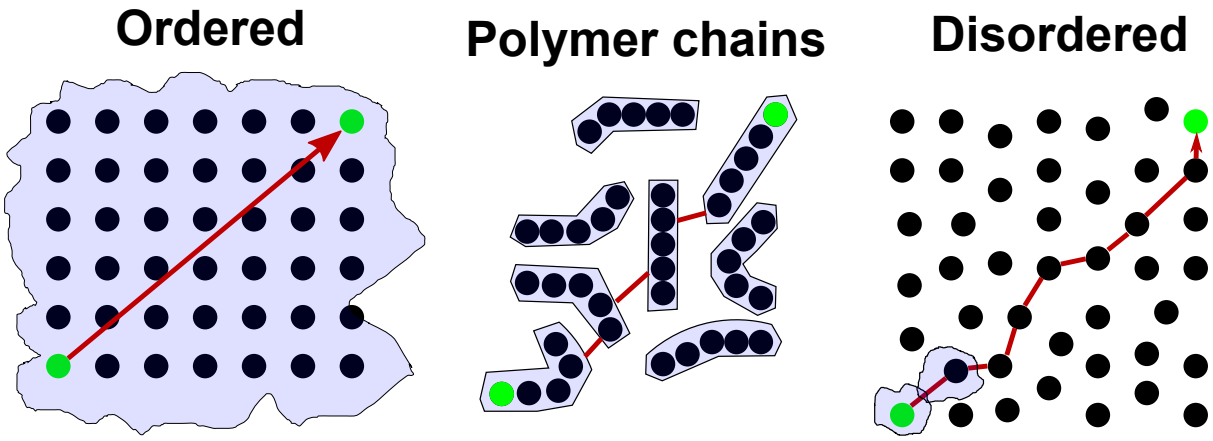


Figure 1.4: Difference between localized and delocalized charge transport. In ordered crystals the electron is delocalized in an electron cloud (pictured in light blue), which is essentially the probability density $\psi^*(x)\psi(x)$ to find an electron in the position $x$. It can easily move from one site to another, in fact, it does not even move between the sites and is spatially *delocalized*. In case of disordered charge transport, the wave function is localized around some site, therefore it is possible for the charge carrier to jump only to another center nearby, where there is some coupling between wave functions. Thus, to move from one site to another, it is necessary to make several distinct jumps. In other words, most of the time electron is *localized* and can be found on site.

Ordered structures will normally display the highest mobility values. Periodicity is inherently advantageous for mobility and can lead to band transport; the wavefunction of a charge carrier in ordered materials, due to the Bloch theorem [49], is periodic with a periodicity matching that of a crystal lattice and, therefore, is spatially delocalized, as can be see in fig. 1.4. There are still exceptions from this statement, for instance Mott insulators [50], where interactions between the charge carriers lead to their localization. Amorphous materials do not have this property and the electron wavefunction is localized close to the molecule with only a small overlap between the wavefunctions of neighboring molecules. Such transport mechanism is called hopping transport [51, 52]. Finally, electrons in polymers may demonstrate a combination of both types of the charge trasport; efficient movement along the chains and only hopping type between separate chains.

Hopping and band transport are fundamentally different not only in the resulting mobility values, but also in the dependence of the mobility on other parameters. Most notably for hopping transport higher temperature are beneficial for the mobility, whereas for band transport they are slightly detrimental, see sec. 2.7. This is particularly important for organic crystals as charge transport in organic crystals often displays hopping-like properties. Normally, low mobility crystals are described better by the hopping type transport, while large mobilities are associated with the band transport [53]. However, one should really be careful and not directly associate the transport in organics either with the hopping or the band transport. The debates about actual transport regime in organics are still present in the literature [54].

In this thesis, both transport layers in the device stack will be in the amorphous state,

where hopping transport is dominant [55]. Despite lower mobility values, amorphous materials are often chosen for OLEDs, as deposition of thin crystalline layers often results in inhomogeneous growth [27]. This might create dangerous shortcuts for the carrier flow, which become even more frequent in the case of large device surfaces. Moreover, amorphous organic semiconductors in combination with a flexible substrate can make the whole device flexible [56, 57].

### Hopping transport

As described, hopping transport is a type of transport regimes, in which a charge carrier is localized on the site and its macroscopic movement consists only from the discrete jumps from one site to another. Note that site itself does not have to be a one molecule, in fact the site can be only a part of a large molecule or even collection of molecules. There are several different reasons why charge carrier localization occurs; however, they are not that important for us, because the disorder in amorphous materials is present just due to the static disorder [58]. For a more thorough description one can refer to either [54] review article, which is very recent or [59] which is already relatively old, but is still incredibly useful.

In essence, the quantities which form the basis of any model, which aims at the description of macroscopic quantities based on site formalism, are:

- $p_i(t)$ is the probability that the site $i$, located at the point $x_i$ is occupied at time $t$
- $W_{i,j}(t)$ is the transition rate between sites $i$ and $j$

The transition rate $W_{i,j}(t)$ is the most crucial component of hopping transport. If we would be able to describe the whole system as a collection of sites, assigning each site a distinct index $i$, provide transition rates between each pair of sites, and set up initial condition $p_i(t = t_0)$, we could follow the evolution of such system. Of course, such general description cannot provide anything useful in practice. To make the problem feasible, one needs to (i) parametrize the transition rates and (ii) parametrize the material structure. Afterwards, one needs to find a way to extract from the resulting jump rates some useful quantities, such as mobility or diffusion coefficients, because bare site occupation probabilities $p_i$ are not interesting for the macroscopic description. We will start with the transition rates.

Often, two parametrizations of the transition rates $W_{i,j}$ between two sites are considered. Both are using $r_{i,j}$, the distance between the sites, and $\epsilon_i$, the energy of a charge carrier residing on this site, as a parameters. These equations are: eq. 1.2, Miller-Abrahams model, and eq. 1.3, Markus jump rate equations [60]. In these equations, $a$ stands for the localization radius of the charge carrier and $\nu_0$ is attempt-to-escape frequency. Markus equation is a simiplified version of Miller-Abrahams transfer rate and can be used when the energetic disorder in the system is much smaller that polaronic activation energy [60].

$$W_{i,j} = \nu_0 exp\left[-2\frac{r_{i,j}}{a} - \frac{\left|\epsilon_j - \epsilon_i\right| + \left(\epsilon_j - \epsilon_i\right)}{2k_BT}\right] \tag{1.2}$$

$$W_{i,j} = \nu_0 exp\left[-2\frac{r_{i,j}}{a} - \frac{\epsilon_j - \epsilon_i}{2k_BT}\right] \tag{1.3}$$

These rates already simplify the problem by a lot. What is left however, is the parametrization of the system itself, which will in essence describe the distances $r_{i,j}$ and the site energy $\epsilon_i$. The parametrization of the spacial disorder, if present, should result in random distribution of the site spatial positions $x_i$. It depends a lot on the morphology of the layer and is normally done to specifically adjust for the material of interest. The parametrization of energetic landscape, following the pioneering work of Bässler [61], is often chosen as a Gaussian disorder model, i.e.

$$\epsilon_i(x) \propto exp\left[-\frac{1}{2}\left(\frac{E_{mean}-x}{\sigma}\right)^2\right] \tag{1.4}$$

Having these parametrizations in hand, one can now proceed solving resulting equations to extract quantities such as mobility, diffusion coefficient and their dependence on different factors. There are variety of methods to extract quantities of interest, such as direct solution of Master equation, effective medium model, Kinetic Monte Carlo equations [62]. On top of that, some percolation approaches exist [63]. Regardless of the method, used to solve these equations, the mobility appears to be dependent of three key macroscopic quantities: the temperature, the carrier concentration and the electric field.

#### Doping of transport layers

To improve the conductivity of the amorphous layers, doping is often necessary. Doping is the introduction of impurities (dopants) into an intrinsic semiconductor. The transport level of the properly selected dopant must be very close to the transport level of the doped semiconductor, which allows additional charge carriers from the dopant material to participate in charge transport. The doping of organic materials is substantially different than the doping of inorganic materials. First of all, the fraction of dopants in the doped material in organic materials is substantially higher and may approach several percent molar ratio [27], while such heavy doping normally turns inorganic semiconductors into metals (degenerate doping). Secondly, in organics not only a substantial increase of free charge carriers is observed, but also the mobility of charge carriers rises. This phenomenon manifests itself as a non-linear dependence of the conductivity on the molecular doping ratio [64]. However, the materials which will appear later in this chapter and serve us as the source of model parametrization, were intrinsic, not doped, materials. Despite that doping is often incredibly important for manufacturing microelectronic devices, it is not that important for the purpose of this thesis.

### 1.3.4 Recombination process

As we outlined in sec. 1.3.1, by recombination we understand two different processes. The first process is when opposite charge carriers meet and form an exciton, a neutral quasiparticle. After formation, the exciton migrates in the device and finally potentially generates a photon. It was demonstrated that the exciton movement can be extremely well described by a diffusion mechanism [65]. Excitons in organic semiconductors generally have a large binding energy $0.1 - 1\ eV$ [66–68] and it can be associated with a molecule in an excited state. This excited state typically corresponds to an electron that has been promoted from the HOMO into the LUMO. Excited molecules induce

reorganisation of intermolecular distances and polarization of their surroundings [69]. Contrary to that, excitons in inorganic semiconductors normally have a lower binding energy [70]. The high binding energy leads to substantially different recombination properties.

Generally speaking, any light emitting process should be related to the change of energy and momentum of a charged particle. Any such process will involve several particles and the total (i) energy, (ii) momentum and (iii) angular momentum must be conserved. These conservation laws would normally forbid the emission of a photon from a single electron without interaction with its surrounding. In semiconductors, the most probable event which causes light emission is the recombination of a conduction electron and a hole [39]. In inorganic semiconductors the energy/momentum conservation laws are more important, due to presence of custom energy-momentum relations for electrons and holes. This is not the case however in amorphous organic materials, which have low mobility and, therefore, low macroscopic momentum values. On top of that, the absence of a band structure in these materials makes the definition of the macroscopic momentum of a charge carrier and its conservation harder. Hence, in such materials, conservation of angular momentum becomes most crucial for light-emission events.

In amorphous semiconductors, electrons and holes are most of the time localized in coordinate space due to the nature of hopping transport, sec. 1.3.3. When electron and hole come together so that the energy of their interaction become substantially higher than thermal energy $kT$, they form an exciton. As the exciton consists of two spin $1/2$ particles, it can be in either the singlet state, i.e, a state with total spin equal 0 and, therefore the $z$-component equal 0, or in the triplet state, with a total spin equal to one and the $z$-component being either 1, 0 or $-1$. Both states have different energies due to the exchange interaction and spin-orbit coupling [71]. A radiative decay from a excited singlet state back to the singlet ground state is more likely because it does not require any further spin transition. The internal quantum efficiency $\eta_{int}$ defined in sec. 1.3.2 denotes the effectiveness of such a process and dictates how many radiative recombination events are there relative to the total amount of recombination events.

Charge carriers do not have any preferred single-particle spin direction when they come close enough to each other to form an exciton. This means that the singlet state is formed only with a probability of $1/4 = 25\%$. Hence, quantum efficiency of the most likely $S_1$ to $S_0$ transition, the fluorescence, fig. 1.5-a cannot exceed 25%. Of course, this circumstance substantially reduces device efficiency. During the last 30 years a variety of methods has been proposed to improve this efficiency [72]:

- Under certain conditions two formed triplets may form one singlet exciton, fig. 1.5-b. This is the so-called process of triplet fusion (TF) [73, 74] and it may improve the theoretical quantum efficiency up to 62.5%, because two triplets will contribute to one radiative event.
- If one enhances the rate of the triplet-to-singlet transition, e.g., by improving intersystem crossing (ISC) due to heavy atoms[1], it is possible to create phosphorescent devices, fig. 1.5-c, which can theoretically achieve 100% quantum efficiency. The drawback is that such triplet states are sufficiently long-lived to decay non-radiatively by the other triplet [75, 76].

[1]Heavy atoms improve spin-orbit coupling and thus ease the transition from triplet to singlet state)

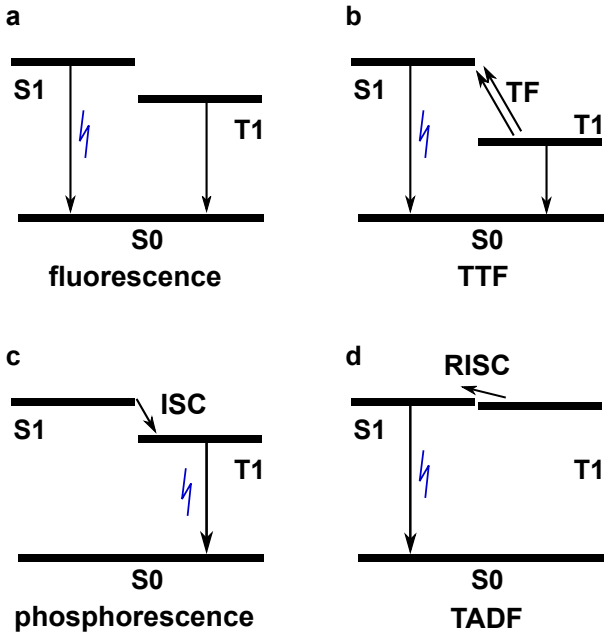


Figure 1.5: Light emission mechanisms in organic semiconductors, involving the lowest singlet S1, triplet T1 and the singlet ground state S0. Depending on the energy level composition and the amount of particles, different ways to achieve exciton decay are present. TF corresponds to the triplet fusion, TADF stands for Thermally Activated Delayed Fluorescence and ISC is inter-system crossing. See main text for a detailed explanation.

- The recently emerged idea of Thermally Activated Delayed Fluorescence (TADF) technology is very promising, due to its theoretical ability to turn all exciton decays into light emission events. The idea behind this process is to minimize the energy gap between S1 and T1 states by minimizing their exchange energy. Then, if this energy is less than 0.1 eV, TADF may happen, when the triplet state becomes a fluorescent singlet state by borrowing thermal energy from the ambient [77]. This approach also theoretically allows to reach 100 % quantum efficiency.

### 1.3.5 Charge carrier injection

Mobile charge carriers in the transport layers must be initially injected from the electrodes. No matter how well the charge carriers are transported within the transport layers or how efficient their recombination in the emissive layer is, poor injection will reduce the device performance. Before methods emerged, which allowed efficient injection of charge carriers from metals into organic materials, most of them were considered to be insulators [11, 13]. To this day, surface science directs a lot of effort towards investigation of metal-organic interfaces. The interfaces, formed between the electrically active layers may possess properties drastically differ from the materials, which make up the interface [78, 79].

Interfaces are also proven to substantially impact the electric properties of the resulting device, especially in the case of OLEDs [80–82]. Additional localized energy levels may form there and trap charge carriers. The charge carriers in two different materials also have distinct energies for a given momentum, i.e. energy has to be dissipated or obtained by the charge carrier while it passes through the interface.

It is worth mentioning, that the consequences of an energy misalignment could be devastating for the device and cannot be easily circumvented [83–92]. There are a few materials, which have a high enough electric conductivity to transport electric current over large, macroscopic distances, which is required to, e.g., transport electric energy from the power plant to the power socket. These materials have often misaligned energy levels with materials of interest, such as Alq3 or $\alpha$-NPB, as we will see in sec. 1.4.2.

To illustrate how much an interface can influence the injection, we can make a very rough estimate of the energy level differences in the microelectronics and their consequences. The elongation of the interface can be anywhere from $10^{-10}m$ to $10^{-8}m$. Effective forces, acting on the electron with its elementary charge $e$ and an energy of 1 $eV$ (normally, injection barriers are lower than that value, so it serves as an upper limit here) as placeholder value can be located anywhere between $10^8 V/m$ and $10^{10} V/m$. These values should be compared to the actual electric fields, which can be applied in the device. Normally, microelectronic devices operate in the range $0 - 100V$, while their thickness is often larger than $100nm$. Taking an extremely large voltage of $100V$ and a thickness of $100nm$, the largest estimated field in the device will be then $10^9 V/m$. Comparing this field to the effective one, we see that they are at least in the same order of magnitude. Hence, poor interface can easily become a bottleneck for a charge transport in the whole device.

From the energy point of view, the quantity which will hinder (or enhance) the charge transport across the interface is the misalignment of energy levels or an associated *potential or injection barrier*. This quantity, however, is in turn composed of multitude different physical phenomena, which occur at the interface. To start the description of interface, one must first introduce the concept of energy levels. The energy level alignment is one of the most important concepts in the field of microelectronics [93]. During growth, interfaces often influence the structure of the material, the growth mode, the size of grown crystallites, and even sometimes induce surface phases (phases, which could not be observed in the bulk material) [94, 95]. We will start with the least complicated constituent to the energy level diagram, the metal contact.

To remove an electron from the metal, it needs to have a kinetic energy above a certain threshold. This threshold was initially discovered with the photoelectric effect [96] and named workfunction $\psi$, fig. 1.6-a. In this section we will use a widely accepted convention, which states that the zero-energy level for the electrical charge is infinitely far away from any other electro-magnetic sources should be 0. This means, in turn, that an electron must possess only positive kinetic energy in a vacuum without any external potentials and its energy within the material should be negative. The energy level located infinitely far away from the material is called *Vacuum level* $E_V$. Vacuum levels for different materials should be the same, as they are located infinitely far to feel any influence of the material's internal structures. The electron workfunction then is just the difference between the vacuum level and the Fermi level $\psi = E_V - E_F$. The Fermi level denotes the energy, at which every site in the material will have 50% chance of being occupied in thermodynamic equilibrium. When measured close to the surface however, the electron workfunction appears to be different, see for example [83]. The reason for that is that the electron wavefunction "spills" out from the metal surface [97]. This can be seen as a dipole layer, where positive charge comes from the absence of electrons in the material (which otherwise is electrically neutral)

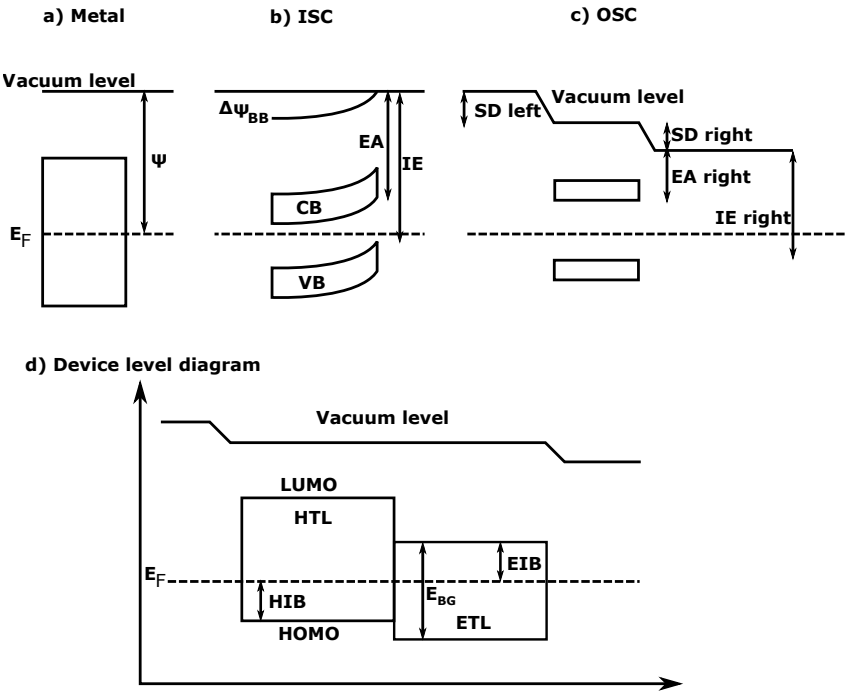


Figure 1.6: a) Metal Band Diagram. Ψ represents the substrate workfunction. b) Band diagram of an inorganic semiconductor (ISC) in contact with the substrate. EA stands for electron affinity, IE - Ionization energy, $\Delta\Phi_{BB}$ is a total change of workfunction due to band bending c) Level diagram of an organic semiconductor in contact with the substrate. SD is the surface dipole. Note that, in this picture, surface dipoles at the left and right side of the organic semiconducting layer are oriented in the same direction, resulting in vacuum levels shift in the same direction. Different vacuum levels on one and another surface give rise to surface dependent IEs and EAs. d) Level diagram of 2 organic layers, sandwiched between two metal contacts. HIB and EIB stand for hole and electron injection barrier. $E_{BG}$ is the energy of the bandgap (fundamental gap).

and the negative part comes from the electrons outside.

Such dipole layers will appear several more times in this section, as they can appear due to a variety of different phenomena, in particular at interfaces. Therefore it is important to understand their influence on the energy level alignment within the device. An infinite sheet of dipole moment per area, with a sheet density of $\bar{d}$, will not produce any long reaching electric fields, but will create a sharp step in the electrostatic energy [98] of a size $-q\bar{d}/\epsilon_0$. However, (i) in reality the material surface is not infinitely extended and (ii) a dipole is just the first order approximation to the distribution of charges in the electrically neutral system. The first observation is not critical, as the lateral elongation of the injected charge carrier will normally be much smaller than the electrode surface. The second issue signals that what is seen as a point dipole from a distance, may turn into complex charge density arrangement, especially close to it. This may cause some non-trivial injection behavior [93].

In the case of semiconductors, in addition to the Fermi level, two more quantities play a role, the *electron affinity* and the *ionization energy* of the material, i.e. energy gain/loss when an electron is added/removed from the semiconductor, fig. 1.6-b. In one particle picture, these can be well approximated by the positions of conduction band minimum and valence band maximum. As the material should be electrically neutral, the Fermi level is located in such a way, that the total amount of positively and negatively charged particles in conduction and in valence bands is equal. For an undoped semiconductor that means that it is located approximately in the middle of the gap. However, most inorganic semiconductors for microelectronics are doped, shifting Fermi level away from the center of the band gap. As in the case of metals, surface dipoles may appear and change energy level diagrams, for instance, due to surface reconstructions or terminations, see for example [99]. Moreover, dangling bonds on the surface or surface reconstructions may trigger charge carrier rearrangements at the interface [100]. In an energy diagram these rearrangements are captured as a bending of the valence/conduction bands close to the surface. While bend bending is crucial for the device work and cannot be dismissed [101], it is also caused by accumulation or depletion of mobile charge carriers. The resulting band bending might, therefore, change when the device is not in thermodynamic equilibrium.

In organic semiconductors, the situation becomes even more complicated, fig. 1.6-c. First of all, the actual position of the energy levels may change with geometry relaxation [83]. Here, the average time required for geometry relaxations $T_R$ and its relation to the average time scale $T_P$ of the process of interest determines whether that process may change the positions of the energy levels or not. For instance, the timescale of a photoionization processes is much smaller than $T_R$ and no geometric relaxation will happen. Ionization energy and electron affinity in that example are called *vertical*. On the other hand, charge transport is a slow process with timescale higher than $T_R$ and will, therefore, behave as if positions of the levels were different. These positions are called *adiabatic*. This is important for us, as the first process may be used to experimentally determine vertical levels, while in our work we have to use the adiabatic ones, due to the process of interest.

There are also a variety of different effects, which could further shift the levels in OSCs. For instance, dielectric screening within monolayers or the formation of finite-width bands due to the interaction of the molecules. Another crucial aspect is the formation of dipole layers. Due to the complex structures of organic molecules, they can easily possess polar constituents, which contribute to an inherent molecular

dipole. Even the most common C-H bonds bonds are polar. Once these dipoles arrange regularly into layers, e.g. at interfaces, they may decisively affect transport. Then they either lead to unsurmountable barriers [102] in case, where dipoles shifts energy levels even further apart increasing the length of inhection barriers. Alternatively, dipole layers may shift energy levels at interface closer together to form perfect, barrier-free contact. In that case, dipole layers counteract the inherent injection barrier.

The deposition of an organic material on the metal surface leads to further effects. Screening effects are increased due to the presence of the metal surface, chemical interactions between organic molecules and substrate turn on, and molecules can change their geometry due to interactions with the surface [93]. All these effects combined will change the ionization energy and electron affinity at the interface. Furthermore, there will always be interfacial charge rearrangements, leading to the formation of so-called bond dipoles fig. 1.6-d.

Surface science strives to successfully describe interfaces and to determine injection barriers. This task is however not a primary focus of that thesis. To determine injection barriers we will only refer to experimentally obtained values, that combine all the complicated physical interactions that lead to the particular value of the barrier. The shape of the barrier will come from studies, which were able to successfully describe injection into OSCs, however, in the chosen methodology they will never appear explicitly.

## 1.4 Reference OLED setup

In the previous section, we were looking at the general structures and working principles of OLED devices without referring to any particular device structures. However, in the present work, we limited ourselves only to one particular device structure, which was realized experimentally as a part of our project by our collaboration partners. The experimental side of ThermOLED project (848905) which was funded by the Österreichische Forschungsförderungsgesellschaft mbH (FFG), was performed by the Materials Institute of Joanneum Research ForschungsGesmbH. The experimental setup was manufactured by Dr. Manuel Auer-Berger. Consequently, the experimental part was supported by MSc. Florian Kolb and Dr. Roman Trattnig. The manufactured experimental setup served as a reference to compare theoretical and experimental results. In this section, we will describe the device setup and quantify some important device parameters which emerged already in previous sections.

### 1.4.1 Device Setup

For the simulations in this work, we used a specific device setup, which is shown in fig. 1.7. The setup has been inspired by the similar work on the heat dissipation in OLEDs [103]. Light in this setup is emitted from the top surface. Compared to the general device setup, shown in fig. 1.3, it possesses two additional injection layers. Hole/electron blocking layers are absent. The central Alq3 layer (full chemical structure is depicted in fig. 1.8-(b)) serves both as electron transport layer and as emission layer, i.e., light-emitting events primarily are located here. This results in the emission of green light (which is perceived best by the human eye). $\alpha$-NPB in fig. 1.8-a represents the hole transport layer. Silver layers serve as contacts on both sides. The top silver

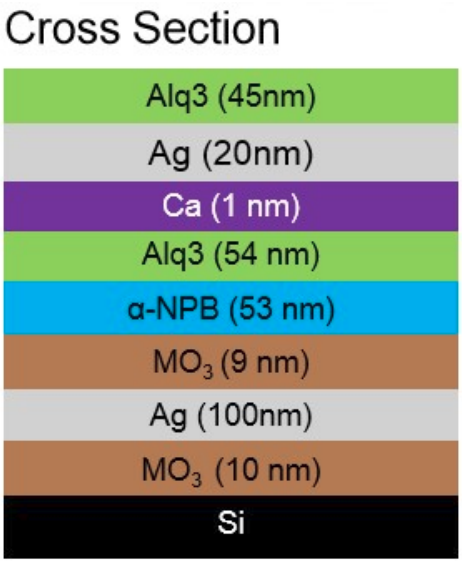


Figure 1.7: Schematic depiction of a device, which was experimentally manufactured within the project. This device was the basis for the comparison between experiment and modeling. For a description of particular layers see the main text. Most of values, which were used in the modeling will be equal to or justified by the correspoding layers or interfaces, emerging in this experimental setup.

layer is thin enough for light to pass through, which is a requirement for the light emission.

A thin Alq3 layer on top of the device serves to improve the outcoupling of light. It does not affect the electric properties of the device as it is located on the "other" side of injecting contact. The thin 1 nm calcium layer serves as a cathode, with electrons provided by the silver layer above. A direct injection of holes from silver to $\alpha$-NPB is highly inefficient as the energetic barrier for this process is approximately $1.2eV$. Therefore, it is required to add some transition layer in between. Molybdenum oxide is a very prominent material to reduce this barrier and to improve hole injection injection [104]. The reason why, despite having bad injection properties, silver is still used as bottom contact is its high reflectivity. In a top-emitting device setup it is required that light, which is emitted from the emitting layer in all directions, does not propagate back into the substrate, e.g., a silicon wafer, but is reflected. A silver layer with its high reflectance is very well suited for that purpose.

### 1.4.2 Level alignment in the reference device

Some of the quantities in fig. 1.6-d can be easily obtained from the literature:

**Alq3**. $E_{HOMO} = -5.7eV$, $E_{LUMO} = -3.0eV$

**$\alpha$-NPB**. $E_{HOMO} = -5.5eV$, $E_{LUMO} = -2.5eV$ [105].

**Ag**. Silver workfunction, according to [106] is equal to 4.5 $eV$.

However, following the discussion in sec. 1.3.5, it is obvious that these values are not sufficient to estimate the actual injection barriers. Moreover, from fig. 1.7 one can spot two thin layers between the contacts and the corresponding transport layers, namely, a 1 $nm$ Ca layer at the top contact and molybdenum oxide at the bottom.

A first educated guess to estimate values of the barriers can be made, following the investigations presented in [107]. In this article, Fermi levels were measured for

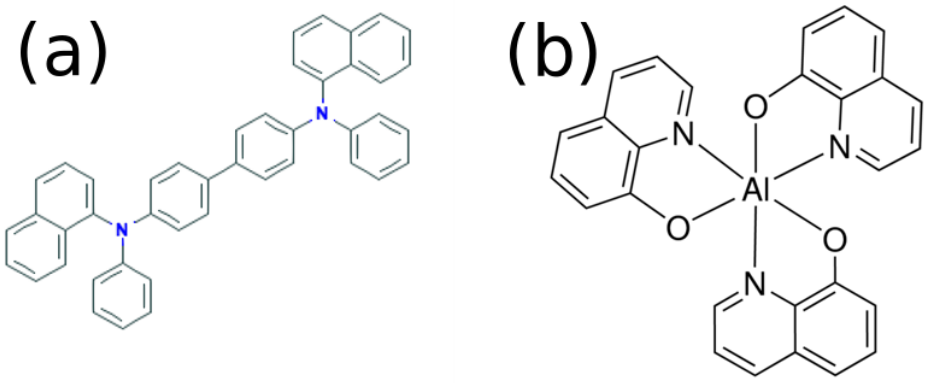


Figure 1.8: Organic molecules, which are used in the OLEDs studied in this thesis. (a) - N,N'-Di(1-naphthyl)-N,N'-diphenyl-(1,1'-biphenyl)-4,4'-diamine, or in short $\alpha$-NPB, (b) - Tris(8-hydroxyquinoline)aluminum(III), or Alq3 in short.)

different metal contacts and different organic materials with Ultraviolet Photoelectron Spectroscopy; the authors present the position of the Fermi level relative to the HOMO level of the corresponding organic semiconductor. In the case of silver and Alq3, this relative position equals to 2.2 $eV$. Simple calculation using the value of fundamental gap then results in a value of the injection barrier for electrons: $E_e = -3.0 - (-5.7 + 2.2) = 0.5eV$. In the case of HOMO levels of $\alpha$-NPB, the article gives a value for the injection barrier for holes of $E_h = 1.7\ eV$ . The value is enormous and will not allow any hole injection from the Ag contact to the device.

This simplistic calculation is still far away from the real values of injection barrier due to presence of additional layers between contacts and organic layers. In fact, the thin Ca layer in this OLED setup could be considered as the cathode, while the relatively thick molybdenum oxide layer on top of the silver layer is placed there to assist the injection. [20].

For hole injection, two different methods to circumvent the large injection barrier are often considered. The first option is to perform injection through the indium-tin oxide (ITO), with a workfunction of $4.9 - 5.2eV$ and with a corresponding injection barrier $0.3 - 0.6\ eV$. Also, ITO is transparent and, therefore, can serve as emitting surface of the OLED. There are no problems with ITO, however, silver is a much better conductor and could potentially reduce the hot spot formations, by keepeing the electrostatic potential more homogeneous across the device surface. If one wants to have silver as the anode, the important constituent for injection is the molybdenum oxide, fig. 1.7. This material has bee n shown to drastically increase injection from silver to an $\alpha$-NPB layer [104, 108–110]. Moreover, the injection efficiency for this material changes substantially with the thickness of the layer. From [104] one can deduce that the resulting injection barrier should be in the region $0.4 - 0.6eV$. Throughout this thesis we will set it equal to the 0.5 $eV$.

The electron injection however is harder to assess. Current consensus on the nature of the substantial injection improvement with the ultrathin Ca layer is the formation of a large number of additional interface states, which cause a pinning of Fermi level [111, 112]. The formation of such states can be clearly observed with UPS. Fermi level pinning is demonstrated clearly in works, in which different metals with significantly different work functions were chosen to serve as contacts (2.0 $eV$

difference across all samples) which in the presence of the Ca layer resulted in a very small difference ($< 0.1\ eV$) in the values of the injection barriers [113]. Similar effects have been observed in the case of electron injection from an Al cathode into the Alq3 layer, when a LiF interlayer is introduced to enhance electron injection [114–116]. Rather than LiF, also other Cs or Li containing compounds can be utilized [117].

This inevitably leads us to the problem, that we cannot provide here a solidly determined value for the electron injection barrier, which could also be backed up by some experimental results. We will describe and explain in sec. 2.8, that it is therefore convenient to assume equal injection barriers for the electrons and holes for the purpose of this thesis.

## 1.5 Active layer degradation

A crucial problem for most of organic devices and for OLEDs in particular is the degradation of their performance over time. For OLEDs, two main sources of degradation were found. The first is cathode degradation due to moisture [118–120]. The second is thermal degradation of organic layers [121–127]. Moisture degradation can be treated in a variety of ways, from proper encapsulation of the device from ambient to nanoscale patterns on the OLEDs surface, which retract moisture [128]. Thermal degradation is more crucial for the device performance. There are several reasons why OLEDs suffer so much from it, even though LEDs have similar problems. The most important stand-alone issue of OLEDs relates to the fact that the charge carrier mobility in organic semiconductors increases with temperature [61]. In inorganic devices actually the opposite happens [39]. Therefore, the thermal properties of layers and interfaces become extremely important [129–140].

To emphasize the importance of thermal degradation, we refer the reader to article [125]. In this work, ITO / CuPc / NPB / Alq3 OLEDs were fabricated and heated up under either nitrogen, $N_2$, or oxygen, $O_2$, atmosphere. Afterwards, the influence of temperature on the device was assessed using atomic force microscopy, which is able to detect even slightest changes in the surface morphology. Authors observed substantial morphological changes in the Alq3 layer for temperatures higher than $70^\circ C$. In the case of $\alpha$-NPB even temperatures of $60^\circ C$ were enough to sufficiently damage the transport layer. Notably, that such profound changes in the device morphology happened after a less than an hour and without the flow of electrical currents. This hints us to the possibility, that a real OLED must be either always cooled or operated under low voltage conditions.

Using OLEDs for lighting immediately poses another challenge: the larger the device surface the harder it becomes to maintain lighting homogeneity across the whole area. Real devices turn out to be extremely susceptible to such local temperature variations [131], which occur mainly for two reasons. The first reason is that transparent electrodes will normally have higher sheet resistances, which in turn lowers the locally available bias from the contact towards the surface. This can be counteracted with a highly conductive mesh, see for example [141]. In our case we are using the silver as an anode, so the local variations might be not so pronounced. The second reason is the dependence of the mobility on temperature, as outlined previously. Numerous techniques were employed to theoretically describe this phenomenon, most notably the ones described in [131,142–145]. We will discuss the dependence of the mobility on

temperature insec. 2.7. However, we are not familiar with any modern drift-diffusion analysis of the problem, where full electrothermal properties of the OLED device would be taken into account. Low efficiencies and high prices of currently available OLED panels are a direct consequence of degradation and efficiency problems.

These issues, related to OLED degradation are the primary motivation for the present work. To properly address these problems, one requires to model the device behavior including such important phenomena as its electric and thermal behavior including their strong interplay in organic layers.

# 2 Methodology

Note that some sections of the methodology were part of my publication [146] and its preprint version available on arxiv.org [147] These publications were a joint effort of me and my co-supervisor Dr. Karin Zojer. In these papers I developed the topic, provided all the calculations shown and designed the figures. The papers were co-written by Karin Zojer and me. As these papers contain a number of usefully formulated explanations, I am using these formulations in section 2.8. These verbatim passages are marked accordingly with quotes.

This chapter collects and motivates all model equations used to simulate the transport of charge, heat and the time evolution of the electrostatic potential in OLEDs. Then, we will describe our approach to numerically solve the selected model equations.

The numerical simulation, written in the Fortran which uses the methodology described in this chapter will be available on GitHub. One can use the following URL to clone it: https://github.com/GeorgiiKrikun/ThermOLED.

The heat transport equation and drift-diffusion equations for charge transport attain the form of a continuity equation. This is highly convenient because different equations can be described using the same language and can be solved using similar numerical approaches. We will briefly describe them and associated notations here.

A continuity equation, in its general form in three dimensions reads as follows:

$$\frac{\partial \rho(\mathbf{x})}{\partial t} + \nabla \mathbf{J}(\mathbf{x}) = S(\mathbf{x}) \tag{2.1}$$

where $\mathbf{x}$ is a three-dimensional position vector, $\rho(\mathbf{x})$ is the density, $t$ is the time, $\mathbf{J}(\mathbf{x})$ stands for the flux and $S(\mathbf{x})$ for the source. Note that we intentionally do not specify density, flux or source of *what quantity* is described.

When integrated over volume and with the help of the divergence theorem, one can deduce that the continuity equation is the differential form of a conservation law [148]. That implies, that conserved physical quantities, such as charge, energy and particles [1] should satisfy a continuity equation. This is the reason, why time and position dependence of any conserved quantity could potentially be cast in a continuity equation, with an appropriate choice of density, flux and the source terms.

The density term $\rho(\mathbf{x})$ can stand for the density of any quantity which should be conserved without the source term. The flux $\mathbf{J}(\mathbf{x})$ is then associated with the flux of the chosen density. Finally, a source term $S(\mathbf{x})$ is the way to add or remove the quantity from the system. We will clarify previous definitions of continuity equations provided in literature with examples of how they will be used in this work. Charge carrier densities and thermal energy will correspond to a density terms. Charge carrier fluxes and the thermal flux act as a flux terms. The source term in the case of charge carriers will describe generation and recombination phenomena, while the source term in the heat equation will describe device heating due to the electric current. Finally, a process

[1] In fact, it holds even for quantum mechanical fields, for instance, electron wavefunctions

where charge carriers are injected from the outside is covered by the border condition to a continuity equation.

Continuity equations in their common form originate from the Boltzmann transport equation (BTE). To adopt its potential to describe a material one is required to define (i) (quasi-)particles, whose propagation results in transport of some macroscopic quantity and (ii) the particle momenta and coordinates. For instance, in conventional semiconductor materials, which bear a periodic structure, propagation of electrons in the conduction band and holes in the valence band will be responsible for charge transport. Phonon propagation will result in heat transport. However these definitions are difficult for amorphous semiconductors.

Due to Heisenberg's uncertainty principle, particles do not simultaneously possess both sharply defined momenta and coordinates. This implies that the BTE, when used to deal with quantum mechanical systems, holds an innate problem that cannot be solved in this formalism. Nevertheless, it can still be justified for periodic systems in which the Bloch theorem holds. It states, that in a periodic medium a particle wave-function $\psi(\mathbf{x})$ can be separated into a periodic part $u(\mathbf{x})$, with the periodicity of the crystal structure, and a plane wave $e^{-i\mathbf{kx}}$, where $\mathbf{k}$ stands for particle quasimomentum. This definition of particle momentum allows to still employ the BTE, though some additional actions might be necessary [39].

In our case, the medium does not possess any periodicity, so it is hard to justify a BTE-based description of charge and heat transport. Therefore, derivations presented in this section will either be non-conventional ones or ones which thoroughly avoid the assumptions employed in BTE, due to the amorphous nature of materials of interest.

## 2.1 Maxwell equations and continuity equations

In this section we are going to derive the continuity equation for moving charges from the Maxwell equation. As in OLEDs we are going to deal with moving charged particles, we should account for their electromagnetic interaction. If we want to continue thinking in the terminology of continuity equations, the density in the continuity equation is naturally associated with the *charge density*. The flux in this case corresponds to an electric current. We can assume that the charged particles in the material are independent and that they interact only via the electric field. Under this assumption, the motion of charges can be described classically by the Maxwell equations.

To this aim, we should start from the Maxwell equations in dielectric media, eqs. 2.2 - 2.5.

$$\nabla \cdot \mathbf{D} = \rho \tag{2.2}$$

$$\nabla \cdot \mathbf{B} = 0 \tag{2.3}$$

$$\nabla \times \mathbf{E} = -\frac{\partial \mathbf{B}}{\partial t} \tag{2.4}$$

$$\nabla \times \mathbf{H} = \mathbf{J} + \frac{\partial \mathbf{D}}{\partial t}. \tag{2.5}$$

This is a macroscopic version of the Maxwell equations, which already accounts for the possible electric and magnetic polarization in the medium with functions $\mathbf{D}$ being the displacement field and $\mathbf{H}$ the magnetizing field. These two vector fields

are composed as a linear superposition of the outer fields and polarization fields. Polarization can be further decomposed into a spontaneous polarization that is present without an external electric field and a field which reflects the reaction of the material to the applied external field.

We will not proceed with a full derivation here, but rather provide it in the appendix sec. 6. The important parts of this derivation for us will be (i) assumptions, made to derive the following equations and (ii) the actual equations. We will start with the assumptions.

- The system at hand is required to be small and we are looking for effects on a large time scale, i.e., for stable and time-independent solutions.
- The velocities of the charged particles are substantially lower than the speed of light. [2]
- Charged particles do not interact magnetically.

These assumptions yield several equations, out of which two equations will be important for us, eq. 2.6 and eq. 2.7.

$$\mathrm{div}\mathbf{E} = \frac{\rho}{\epsilon} \tag{2.6}$$

The eq. 2.6 is the so-called Poisson equation and inherently links together the electric field $\mathbf{E}$, charge density $\rho$ and the dielectric constant $\epsilon$[3]. Essentially it means that if one knows the charge carrier density and has a way to solve eq. 2.6, then one knows the electric field distribution in the material. It is also important to note that it is also very similar to a continuity eq. 2.1, that lacks the time-dependent density term. This reminiscence will allow to apply the same solution methods as to all other continuity equations.

The second eq. 2.7

$$\mathrm{div}\mathbf{J} + \frac{\partial \rho}{\partial t} = 0 \tag{2.7}$$

is the continuity equation for the charge density. It states that charge is always conserved in the entire system, as no source term exists.

## 2.2 Drift-Diffusion equations

A solution of eq. 2.7 requires a connection between the electric current $\mathbf{J}$ and the charge density $\rho$. In semiconductors, the total charge density normally consists of several contributions, such as holes, electrons, dopants e.t.c. Hence it is useful to formulate a dedicated continuity equation for each kind of mobile charge.

In this section, we will provide the Drift-Diffusion equations, which are commonly used to connect electron $n(\mathbf{x})$ and hole densities $p(\mathbf{x})$ to their respective fluxes $\mathbf{J}_e(\mathbf{x})$ and $\mathbf{J}_h(\mathbf{x})$. Note that the commonly used form of the drift-diffusion equations is based

[2] Both requirements are for the same purpose, namely that the characteristic timescale, on which system may change is considerably smaller than the size of the system divided by the speed of light. In essence, if this requirement is fulfilled we can put the speed of light $c$ being equal to infinity

[3] which describes the relation of the electric field to the displacement field

on the BTE, whose underlying assumptions are in conflict with the nature of hopping transport.

In sec. 2.2.1, we will provide a general argumentation of why drift-diffusion equations should hold no matter what is underlying charge transport mechanism. Afterward, we will provide a full mathematical derivation of them from the basic equations of hopping transport.

### 2.2.1 Physical justification of the approach

This section aims at explaining, why Drift-Diffusion equations on the macroscopic level logically connect carrier flux to the carrier density. On microscopic level, different approaches can be chosen with very promising results [149]. However, they cannot be applied on the scale of a macroscopic device due to the required large computational resources.

In the following Gedankenexperiment, we look at some infinitely extended material, in which charge carriers are localized (as in amorphous organic semiconductors) and only one type of mobile charge carriers exists. For the experiment, we will consider only positive charge carriers for simplicity, i.e. holes. When a constant electric field is applied to this system, charge carriers accelerate in the direction of the electric field. This acceleration however cannot last forever, otherwise, we could observe devices under constant bias with ever-increasing current, whereas in reality steady current is observed. Therefore, there should exist some mechanism that counteracts acceleration, so that only one possible current is realized for every applied voltage. The variable, which connects the electric field $\mathbf{E}$ to the average charge carrier velocity $< \mathbf{v} >$ is called charge carrier mobility $\mu$, eq. 2.8

$$< \mathbf{v} >= \mu \mathbf{E} \tag{2.8}$$

This relation, multiplied by the charge carrier density, yields the charge carrier flux $\mathbf{J}_{drift}$, eq. 2.9.

$$\mathbf{J}_{drift}(x) = \mu \rho(x) \mathbf{E}(x) \tag{2.9}$$

What would happen if the material is not infinite, i.e. charge carriers cannot move forever and have to stop at some point due to the presence of boundaries? The only conceivable mechanism which may counteract drift motion due to the electric field in thermostatic equilibrium is the diffusion of charge carriers. Every charge carrier possesses certain thermal energy and moves randomly in all possible directions with an average velocity being called the thermal velocity. Any spatial gradient of a charge carrier density will create a flux associated with this thermal motion because the randomness of this process should eventually distribute charge carriers equally in the material:

$$\mathbf{J}_{diff}(x) = -f \left( \frac{\partial \rho}{\partial x} \right) \tag{2.10}$$

Therefore, we can cast these terms $\mathbf{J}_{drift}(x) + \mathbf{J}_{diff}(x)$ that counteract each other, into eq. 2.11 for charge carrier density $\rho$:

$$\mu \rho E + f \left( \frac{d\rho}{dx} \right) = 0 \tag{2.11}$$

where $f$ is the function which determines the diffusion flux as a function of a charge gradient. The shape of this function $f$ can be deduced from statistical physics. According to Boltzmanns law, the distribution of particles under a applied potential energy $U(x)$ should be proportional to $\exp(-U(x)/(kT))$. Therefore, the solution of eq. 2.11 adapts the form $\rho_0 \cdot \exp(Ex)$. Then eq. 2.11 turns into eq. 2.12.

$$\mu\rho_0 E\exp\left(\frac{Ex}{kT}\right) + f\left(\rho_0\frac{E}{kT}\exp\left(\frac{Ex}{kT}\right)\right) = 0 \tag{2.12}$$

This equation implies that the function $f$ should be a purely linear function of its argument, $f(t) = Dt = -\mu tkT$. Here we introduced a diffusion constant $D$ which acts as the proportionality coefficient between the diffusion current and the gradient of carriers. Therefore, on top of eq. 2.9, we can state here two more equations. eqs. 2.13 - 2.14:

$$\mathbf{J}_{diffusion}(x) = -D\nabla\rho(x) \tag{2.13}$$

$$D = \mu kT \tag{2.14}$$

The eq. 2.9 shows the dependence of the charge carrier flux on the electric field. One important remark here is that the mobility, in general, should not be constant, but can be a function of different system properties.

The eq. 2.13 shows the dependence of charge carrier flux on their density. This equation will remain the same for negative charges, because diffusion naturally always goes in the direction where there are fewer charge carriers.

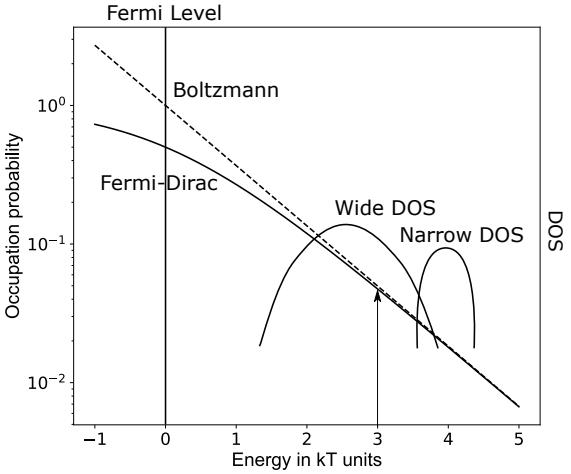


Figure 2.1: Fermi-Dirac and Boltzmann distributions in the energetic region of several $kT$'s around chemical potential. Note that the difference between the two is pronounced for a low values of energy, however, when a particle energy increases to $3kT$, this difference disappears. In these circumstances, the wide density of states, contrary to the narrow one, may have non-vanishing concentration of states in the region, where distributions show substantial difference. This is one of the main reasons for Einstein relation to fail even in a case of thermodynamic equilibrium.

Finally, eq. 2.14 connects mobility and diffusion constant and is named after Einstein. Note it relies on two substantial assumptions. First of all, the charge carriers are

assumed to obey the Boltzmann distribution. Even though charge carriers with half spin should obey the Fermi-Dirac distribution, the Boltzmann distribution is acceptable when bands are located sufficiently away from Fermi energy, $> 3kT$, fig. 2.1. However, as amorphous organic semiconductors do not possess exact band energy but rather energy levels that are spread across the energetic landscape, this approximation may fail in case of a wide density of states. As $1kT$ corresponds roughly to $25meV$ at room temperature, the difference between HOMO and LUMO levels is of the order of $1eV$, therefore, the Boltzmann distribution should very well approximate Fermi-Dirac. However, if both HOMO and LUMO correspond to a wide density of states, this assumption may fail.

Einstein's equation was derived in the case of thermodynamic equilibrium and is not strictly true in case there is an electric current in the system. Realistically, Einstein relation fails when charge carrier densities are extremely high, $> 10^{26}m^{-3}$ which we never observed during simulations. The width of the DOS for the materials of interest is in the range $0.01eV$ - $0.15eV$. Finally, under large applied voltages most contribution to the current comes from the drift, eq. 2.9, making errors in determining diffusion currents insignificant.

Due to that, we will use the Einstein relation bearing in mind that we have low diffusion currents and low charge carrier densities.

### 2.2.2 Drift-diffusion equations in the hopping transport scenario

One can find various ways to obtain drift-diffusion equations starting from the Boltzmann transport equation. However, when we talk about hopping transport, we cannot use the BTE at all, because the momentum of the electron is not well defined. Rather, the electron is assumed to hop swiftly between sites and to dwell most of the time on a site without any macroscopic momentum. Therefore, we need to derive these equations for hopping transport. This will serve two purposes, (i) we can be sure that the drift-diffusion approach can be applied to the problem at hand and (ii) we will have an idea of how various microscopic parameters are connected to the macroscopic picture.

Fortunately, one derivation was already suggested by A. Liemant [150], but unfortunately, this article did not get attention we think it deserves, which might be related to quite elaborate mathematics he uses in his article. We will explain it here to relate the derivation to the physical context of the problem and to give the essential physical motivation for the steps performed. Hence, we will cover only the most important steps. For the full derivation, refer to [150].

Note that drift-diffusion equations in the conventional form were already successfully used to study device transport in organic semiconductors [151–153], so the form of drift-diffusion equations which we will arrive at in this section for hopping transport are not expected to be notably different.

#### Derivation of drift-diffusion equations for hopping transport

The crucial starting point is to introduce two time and coordinate scales. The first scale would be a microscopic $t'$ time and microscopic $x'$ coordinates. Macroscopic coordinates are related to the microscopic ones with a scaling ansatz eq. 2.15, where $\epsilon$ is some small number.

$$t = \epsilon^2 t', \ \mathbf{x} = \epsilon \mathbf{x}' \tag{2.15}$$

The microscopic coordinate $\mathbf{x}'$ represents locations, the distance between which is around 1 unit of length. It ensures that mathematical operations performed on $\mathbf{x}'$ will not change $\mathbf{x}'$ by several orders of magnitude. In turn, $\mathbf{x}$ is a macroscopic scale in which the distance between sites appears to be very small, i.e. in the order of the value of $\epsilon$. For instance, in organic semiconductors, the convenient microscopic scale would be 1 $nm$, which is close to the average distance between molecules. A suitable macroscopic scale in could be meter as a length unit.

The relation for the timescale $t$ is distinctively different because the scaling parameter $\epsilon$ enters squared in the relation. In a random walk process (both hopping transport and diffusion fall under this category), the average squared distance from a starting point $< R^2 >$ is proportional to the time $T$, needed to cover distance $R$; the proportionality constant between them is the diffusion constant $D$: $< R^2 >= DT$. Therefore, if we want our scaling procedure to be consistent among several scales, we need to introduce it differently for the time and spatial coordinates.

Then, we can introduce a hopping rate $w$ which generally depends on the distance between two sites and the energy of these sites. A hopping rate is an inverse probability of hopping and represents the number of hops performed per unit of time. A fairly general starting point would be to factorize the hopping rate from the point $\mathbf{x}$ with energy $E$ to the point $\mathbf{y}$ with energy $Q$ into a purely distance-dependent part (accounting for tunneling, whose rate rapidly decreases with distance) and an energy-dependent part (thermally activated jumps):

$$w(\mathbf{x}, E, \mathbf{y}, Q) = r(|\mathbf{x}' - \mathbf{y}'|) \cdot s(\mathbf{x}, E, \mathbf{y}, Q) \tag{2.16}$$

This equation is defined on the microscopic timescale and gives the number of hops per time $t'$. Basically, $r$ is a microscopic diffusion term while $s$ is a macroscopic term, which accounts for any applied external potential.

These two terms are subjects to different constraints. The function $r$ should give identity when integrated over the whole landscape:

$$S_0 = \int_{R^3} r(|\mathbf{x}'|) d^3 x' = 1 \tag{2.17}$$

As the diffusion current should be finite, a second requirement is imposed:

$$S_2 = \int_{R^3} |\mathbf{x}'|^2 |r(|\mathbf{x}'|) d^3 x' < \infty \tag{2.18}$$

Finally, to be able to find a steady operation state for a given macroscopic rate $s$, we ought to be able to establish the steady state condition with a smooth, large scale electrostatic potential, which does NOT depend on the local energetic/spatial disorder, eq. 2.19.

$$\exp\left(-\frac{E + e\phi(\mathbf{x})}{kT}\right) s(\mathbf{x}, E, \mathbf{y}, Q) = \exp\left(-\frac{Q + e\phi(\mathbf{y})}{kT}\right) s(\mathbf{y}, Q, \mathbf{x}, E) \tag{2.19}$$

This equation is closely related to detailed balance for the Boltzmann Transport equation, hence, we refer to it as a detailed balance.

Before proceeding it is also convenient to define two other quantities which will play an important role: (i) a local density of states (DOS) $g(\mathbf{x}, E)$ which should be normalized, eq. 2.20, (ii) a concentration of sites $N'(\mathbf{x})$, which can be both micro- and macroscopic, see eq. 2.21 and (iii) an occupation function $f_t(\mathbf{x}, E)$ , which describes the local site occupation.

$$g(\mathbf{x}, E), \text{ where } \int_{-\infty}^{\infty} g(\mathbf{x}, E)\, dE = 1 \tag{2.20}$$

$$N'(\mathbf{x}) = \epsilon^3 N(\mathbf{x}) \tag{2.21}$$

With all these parameters, one can define a relative to the amount of available states carrier density $h_t(\mathbf{x})$ and a charge density $\rho_t(\mathbf{x})$:

$$h_t(\mathbf{x}) = \int f_t(\mathbf{x}, E) g(\mathbf{x}, E) dE \tag{2.22}$$

$$\rho_t(\mathbf{x}) = eN'(\mathbf{x}) h_t(\mathbf{x}) \tag{2.23}$$

Using the quantities defined above we can write down the hopping rate equation

$$\begin{aligned} \frac{\partial f_{t'}(\mathbf{x}, E)}{\partial t'} = \\ \int_{R^3} \int \Big[ - f_{t'}(\mathbf{x}, E)(1 - f_{t'}(\mathbf{y}, Q)) \Big] \Big[ s(\mathbf{x}, E, \mathbf{y}, Q) r(|\mathbf{x}' - \mathbf{y}'|) \Big] \Big[ g(\mathbf{y}, Q) N(\mathbf{y}) \Big] dQ d^3y + \\ \int_{R^3} \int \Big[ (1 - f_{t'}(\mathbf{x}, E)) f_{t'}(\mathbf{y}, Q) \Big] \Big[ s(\mathbf{y}, Q, \mathbf{x}, E) r(|\mathbf{x}' - \mathbf{y}'|) \Big] \Big[ g(\mathbf{y}, Q) N(\mathbf{y}) \Big] dQ d^3y \end{aligned} \tag{2.24}$$

The integrand in the equation corresponds to fluxes between $\mathbf{x}$ and $\mathbf{y}$. Fluxes are composed of (on the example of $\mathbf{x} \to \mathbf{y}$ flux). Hopping rates $s(\mathbf{x}, E, \mathbf{y}, Q) r(|\mathbf{x}' - \mathbf{y}'|)$, which are weighted by the local density of sites $g(\mathbf{y}, Q) N(\mathbf{y})$ and multiplied by the probability that both the site "from" is occupied and the site "to" $f_{t'}(\mathbf{x}, E)(1 - f_{t'}(\mathbf{y}, Q)$ is unoccupied. The occupation function is obtained from the second condition, which implies that the density in thermal equilibrium should be equal to the Fermi-Dirac distribution.

Now, one can Taylor expand the integrands in eq. 2.24, in powers of $|y - x|$:

$$\int r(|\mathbf{y}' - \mathbf{x}'|) u(\mathbf{y}) d^3y = \epsilon^3 u(\mathbf{x}) + \epsilon^5 \frac{S_2}{6} \Delta u(\mathbf{x}) \tag{2.25}$$

The function $u(\mathbf{x})$ contains the remaining $\mathbf{y}$-dependent terms in the integrand. Note that after expansion, microscopic timescales are gone, which causes an additional $\epsilon$ terms to appear.

In a next step eq. 2.24 is multiplied by $eN(\mathbf{x}) g(\mathbf{x}, E)$ and integrated over the energy $E$ to obtain a relation between the charge density and the flux, i.e., to obtain a continuity equation:

$$\frac{\partial \rho_t(\mathbf{x}, E)}{\partial t} = \frac{eV[f_t](\mathbf{x}, \mathbf{x})}{\epsilon^2} + \frac{1}{6} S_2 e \Delta_{\mathbf{y}} V[f_t](\mathbf{x}, \mathbf{y}) \Big|_{y=x} \tag{2.26}$$

Function $V[f](\mathbf{x}, \mathbf{x})$ integrates over all possible hops for every possible energy from point $\mathbf{x}$ to point $\mathbf{y}$:

$$V[f](\mathbf{x},\mathbf{y}) = \int\int N'(\mathbf{x})N'(\mathbf{y})\Big[ -f(\mathbf{x},E)(1-f(\mathbf{y},Q))s(\mathbf{x},E,\mathbf{y},Q) \\ +f(\mathbf{y},Q)(1-f(\mathbf{x},E))s(\mathbf{y},Q,\mathbf{x},E)\Big]\, g(\mathbf{x},E)g(\mathbf{y},Q)\, dQdE \tag{2.27}$$

Because the constant $\epsilon$ is small, eq. 2.26 is essentially a two-scale equation. The first term is large while the second one should be only taken into account if the first term is absent. It can be shown that it is the case if one invokes here the detailed balance eq. 2.19 and sets the occupation function $f(\mathbf{x},E)$ to the Fermi-Dirac distribution. This will also require a proper choice of the chemical potential $\mu(\mathbf{x})$ in the Fermi-Dirac distribution.

Invoking detailed balance results in an elongated expression for $V[f](\mathbf{x},\mathbf{y})$, which is symmetrical with respect to the interchange of $\mathbf{x}$ and $\mathbf{y}$. We denote the double integral in eq. 2.27 as $I(\mathbf{x},\mathbf{y})$. Every energy-independent factor, which can be pulled out of the double integral is denoted as $b(\mathbf{y})-b(\mathbf{x})$, precisely:

$$b(\mathbf{x}) = \exp\left[\frac{\mu(\mathbf{x},h(\mathbf{x}))+e\phi(\mathbf{x})}{kT}\right] \tag{2.28}$$

This factor $b(\mathbf{x})$ contains the local chemical potential $\mu(\mathbf{x})$ and the local relative charge carrier density. Combining that with the relation:

$$\nabla_{\mathbf{y}} I(\mathbf{x},\mathbf{y})\Big|_{\mathbf{y}=\mathbf{x}} = 0.5\nabla_{\mathbf{x}} I(\mathbf{x},\mathbf{x}) \tag{2.29}$$

one can explicitly express the remaining term of the right hand side of the eq. 2.26:

$$\Delta_{\mathbf{y}} V[f](\mathbf{x},\mathbf{y})\Big|_{\mathbf{y}=\mathbf{x}} = \nabla_{\mathbf{x}}\left[I(\mathbf{x},\mathbf{x})\nabla_{\mathbf{x}} b(\mathbf{x})\right] = \nabla_{\mathbf{x}}\left[b(\mathbf{x})I(\mathbf{x},\mathbf{x})\nabla_{\mathbf{x}}\log(b(\mathbf{x}))\right] \tag{2.30}$$

Combining these equations and introducing some definitions, we can finally arrive at the drift-diffusion equation for hopping transport, eq. 2.31.

$$\frac{\partial\rho}{\partial t} = \nabla\mathbf{J} \tag{2.31}$$

and eq. 2.32

$$\mathbf{J} = D\nabla\rho - \mu^N\rho\nabla N' - \mu^\Theta\rho\nabla\Theta + \mu^\psi\rho\nabla e\psi \tag{2.32}$$

The current density equations contain four terms: a diffusion term $D\nabla\rho$, drift term $\mu^\psi\rho\nabla e\psi$, a term $\mu^N\rho\nabla N'$ accounting for possible inhomogeneities in the local concentration of sites, and a term $\mu^\Theta\rho\nabla\Theta$ that accounts for the change in the local DOS. The new potential $\Theta$ comes from the parametrization of the local density of states $g(\mathbf{x},E)$ into $g_{\Theta(\mathbf{x})}(E)$ [4].

The constants $D$, $\mu^N$,$\mu^\Theta$,$\mu^\psi$, introduced in eq. 2.32 are related to each other as follows:

$$D : \mu^N : \mu^\Theta : \mu^\psi = \rho : \frac{\partial\rho}{\partial N} : \frac{\partial\rho}{\partial\Theta} : \frac{\partial\rho}{\partial\psi} \tag{2.33}$$

[4]This parametrization is not always possible, but for the task in hand it is more than enough.

And $D$ can be formally calculated from the following expression:

$$D(\mathbf{x},h) = \frac{S_2' N'(\mathbf{x})}{6} \iint \frac{\exp[(\mu(\mathbf{x},h)-E)/kT] s(\mathbf{x},E,\mathbf{x},Q) g_{\Theta(\mathbf{x})}(E) g_{\Theta(\mathbf{x})}(Q)}{(1+\exp[(\mu(\mathbf{x},h)-E)/kT])(1+\exp[(\mu(\mathbf{x},h)-Q)/kT])} dE dQ \Big/ \int \frac{\exp[(\mu(\mathbf{x},h)-E)/kT] g_{\Theta(\mathbf{x})}(E)}{(1+\exp[(\mu(\mathbf{x},h)-E)/kT])^2} dE \tag{2.34}$$

$$\tag{2.35}$$

In which $D$ is the diffusion constant, the parameter $\mu^{\psi}$ is the familiar drift mobility. Two other mobilities $\mu^N$, $\mu^{\Theta}$ are related to new driving potentials $N$ and $\Theta$.

The presented equations represent a complete description of the hopping transport on the macroscopic level provided that all quantities entering them are known. Unfortunately, in reality most of these parameters are either unknown or can be only roughly estimated. A possible choice of these parameters will be shown in the next section.

#### Drift-diffusion equations in the particular case of amorphous organic semiconductors

Equation 2.32 contains four different driving potentials, two of which are not present in the conventional drift-diffusion equations. The $\nabla N'$ term is related to spatial inhomogeneities in the site distribution. Although spatial inhomogeneity is common for organic semiconductors, one is required to provide the exact probability distribution of that inhomogeneity to obtain a numeric result. The actual extent of this term may be revealed from averaging the outcome of several simulations, each of which is initiated with the random distribution of site densities $N_i'$, i.e. a task that is far beyond the scope of this thesis. We decided to discard this potential term, because it is expected to play a subordinate role in the total current and it is difficult to account for. Starting from now, we consider that $N'(\mathbf{x}) = const$ and therefore $\nabla N'(\mathbf{x}) = 0$.

The term related to $\Theta$ is more complicated and cannot be readily discarded. Basically, it stems from the assumed spatial dependence of density of states: $g(\mathbf{x},E) = g_{\Theta(\mathbf{x})}(E)$. This assumption is justified in organic amorphous materials, in which the DOS is considered to be either Gaussian or exponential, i.e. $DOS(E) \propto exp(-\frac{E-E_0}{\sigma^2})$ or $DOS(E) \propto exp(-\alpha E)$. For organic materials it is regularly assumed that the density of states is normally distributed with a fixed width. Therefore, the whole term proportional to $\nabla\Theta$ is irrelevant for bulk transport.

However, it is still important for the interfaces where two layers come in contact. Then, the DOS may experience a "jump" in width from one material to another. We will take a closer look at the interfaces afterward, because they should be implemented differently from the bulk simulation. If we focus on bulk transport, we are left with only two terms - the drift and diffusion current densities.

Furthermore, the parameters $\mu^{\psi}$ and $D$ cannot be directly obtained from eqs. 2.34 - 2.33. Their determination requires us to account for effects, that were not considered in this derivation. For example, if a charge carrier gets trapped in a deep energy level,

it can be easily pushed out due to the electric field exerted by another charge carrier. These microscopic interactions are not considered in the macroscopic picture, but rather must be obtained in experiments, Monte-Carlo modeling [154] or analytical approaches [155–158]. Such studies can give a more precise picture of how mobility depends on all external and material parameters. We are using a very particular model for the mobility as a function of temperature, charge carrier density, and applied electric field [159], which has been proposed based on the solution of a master equation for hopping transport. This model can be straightforwardly implemented in the device simulation, where it is necessary to quickly and precisely calculate mobilities as a function of all the parameters.

Note that apart from Monte-Carlo and master equation there are also some percolation theory approaches to determine the mobility for hopping transport [63, 160].

The only parameter we need to provide is the diffusion constant. From eq. 2.33, one can derive a generalized Einstein relation [161], which connects the mobility and with the diffusion constant:

$$\frac{\mu^{\phi}(\rho)}{D(\rho)} = \frac{\partial \log \rho}{\partial \mu} \tag{2.36}$$

This equation reproduces the previously derived Einstein relation eq. 2.14 in the particular case of small concentrations of charge carriers with $n << N$, where $n$ is the concentration of charge carriers and $N$ is the concentration of sites. In the course of the performed simulations, we never exceed charge densities larger than $n = 10^{25}\ m^{-3}$, while the site concentration is $N = 10^{27}\ m^{-3}$. Therefore, we can safely use the regular Einstein relation for the simulations.

If one also takes into the account the existence of two charge carriers (electrons and holes), eqs. 2.31 - 2.32 become eqs. 2.37 - 2.38, where $n$, $p$ are concentrations of electrons and holes respectively, and $\mu_e$ and $\mu_h$ are the corresponding mobilities.

$$\mathbf{J_h} = \mu_h \left( -p \nabla \phi - \frac{\nabla p}{kT} \right) \tag{2.37}$$

$$\mathbf{J_e} = \mu_e \left( n \nabla \phi - \frac{\nabla n}{kT} \right) \tag{2.38}$$

Finally, we account for the generation and recombination of electrons and holes. We will expand on this term later in sec. 2.5 together with the source terms for other equations. However, we already have the means to introduce this term in its general form. According to already shown eq. 6.8, the charge should be conserved. As electrons and holes possess opposite charges, generation and recombination should enter the drift-diffusion for electrons and holes equations in a similar manner.

The generation rate $G$ should increase the number of charge carriers when no charge flux is present precisely by the amount of generated particles. Conversely, recombination $R$ should decrease the number of particles. That means that in the case of absent particle flux $\mathbf{J} = 0$ we get:

$$\frac{\partial \rho}{\partial t} = G - R$$

Where $\rho$ stands either for electron $n$ or hole $p$ density. Comparing this equation with eq. 2.31, we can finally write down the drift-diffusion equations:

$$\frac{\partial p}{\partial t} + \nabla \left[ \mu_h \left( -p \nabla \phi - \frac{\nabla p}{kT} \right) \right] = G - R \tag{2.39}$$

$$\frac{\partial n}{\partial t} + \nabla \left[ \mu_e \left( n \nabla \phi - \frac{\nabla n}{kT} \right) \right] = G - R \tag{2.40}$$

## 2.3 Heat equation

### 2.3.1 Fourier law

The heat equation is the last equation required for the modeling and it also has the form of a continuity equation. The quantity which is conserved in the scenario of heat propagation is the heat energy. Heat energy is the energy of disordered motion and vibrations of molecules. When one part of the material is heated more than another, molecular interactions will tend to average thermal energy and, eventually, equilibrate the temperature throughout the material. Macroscopically, this process can be seen as a flux of heat energy from more heated to less heated regions. The relation between the gradient of the driving potential (temperature) and the flux (thermal energy flux) might be complex, but can be as well linearized by truncating a Taylor expansion at the linear term: $\mathbf{q}(\nabla T) = \mathbf{q}_0 - \kappa \nabla T + O((\nabla T)^2)$, where $\mathbf{q}$ is the heat flux in Joules per unit area per unit time, $T$ is the temperature and $\kappa$ is the tensor that connects one vector (gradient of temperature) with another (thermal flux).

There are constraints for both quantities $q$ and thermal conductivity $\kappa$. When the gradient of temperature is absent, there should be no heat flux in the absence of other driving potentials. Moreover, coordinate inversion symmetry requires that there should be no distinct flow direction, i.e. $\mathbf{q}_0 = 0$. Furthermore, the thermal conductivity is required to be a scalar, otherwise any rotations will change the tensor while the physical system would be the same. As the last requirement, heat should always propagate from hot regions to the cold ones, i.e. we need a negative sign in front of the linear term. Summarizing everything, we arrive at the equation $\mathbf{q}(\nabla T) = -\kappa \nabla T + O((\nabla T)^2)$. Without the quadratic term, this equation is called the Fourier law:

$$\mathbf{q}(\nabla T) = -\kappa \nabla T \tag{2.41}$$

### 2.3.2 Fourier law in OSC

Even though there are no physical reasons to a priory neglect non-linear in temperature terms, several reasons supporting it. First of all, the temperature region of interest for the thesis is room temperature +/- 40 degrees, which realistically corresponds to the conditions of the devices. Secondly, the thermal conductivity $\kappa$ of amorphous organic semiconductors is barely investigated, especially its temperature dependence. Moreover, $\kappa$ may change depending on the manufacturing process.

For any ordered material, the transport can be described as being carried by different quasi-particles. For example, if one is talking about an electrically active material, such as metal for example, it will have a large number of very mobile charge carriers, which can carry a lot of energy (conduction electrons). These types of materials are the best

heat conductors with a thermal conductivity ranges from 50 to 1000 $Wm^{-1}K^{-1}$. Then, if the material is not inherently conductive, there are only a few charge carriers that can transport the heat. Then, phonon transport takes over. Phonon is the quasi-particle, which can be obtained by diagonalizing the Hamiltonian of inter- and intra- molecular interactions in the harmonic approximation. Phonon thermal transport is rarely as effective as electron thermal transport and it resides in the range of 0.1 - 100 $Wm^{-1}K^{-1}$.

Amorphous semiconductors and materials described above differ due to the absence of macroscopic order. They generally possess much fewer electrons which in turn are less mobile. Phonons, which can exist, have a very small wavelength and are localized in single molecules rather than being spread over the material. Phonons at molecules can only excite phonons on nearby molecules. This type of heat transport is very slow. Generally all materials with this type of heat transport do not exceed thermal conductivity values of glass 1 $Wm^{-1}K^{-1}$. Therefore, only diffusive thermal transport is possible in such materials and it is well described by thermal conductivity.

### 2.3.3 Heat equation

The explicit formulation of the heat equation is based on the continuity equation, because eq. 2.41 established the connection between flux and temperature. To utilize this connection in a continuity equation, we first identify what the driving potential and the flux are.

As a thermal flux, $\kappa\nabla T$ corresponds to the amount of energy transferred per unit surface per time, the driving potential should have the units of an energy density, i.e., that potential should have a unit of energy per unit volume, and should be connected to temperature. There exist two physical constants which connect both. The first constant is the heat capacity $c_p$ which describes the amount of heat energy which is contained in 1 kg of a given material. Then, we convert mass units to volume units utilizing the mass density of the material $\rho$. Multiplying these two constants by the temperature yields the heat energy density for a given temperature, $E_{heat} = \rho c_p T$. This quantity has a correct dimensionality and can be inserted into the heat equation as a source.

Unlike the drift-diffusion equations, where a current is injected into the system via boundary conditions, the most important source of heating is located in the device rather than in the ambient environment. Electric current heats the device and establishes a heat power concentration $Q(\mathbf{x})$, which will in turn depend on the electrical properties of the device in the position $\mathbf{x}$.

The resulting equation is eq. 2.42. We will discuss the additional terms which contribute to the $Q$ term later.

$$\rho c_p \frac{\partial T}{\partial t} - \nabla(\kappa\nabla T) = Q \tag{2.42}$$

## 2.4 Boundary conditions

Each of the transport equations stated in the previous sections requires boundary conditions to obtain a numerical solution. One requires one condition for each order of the equation and for every variable.

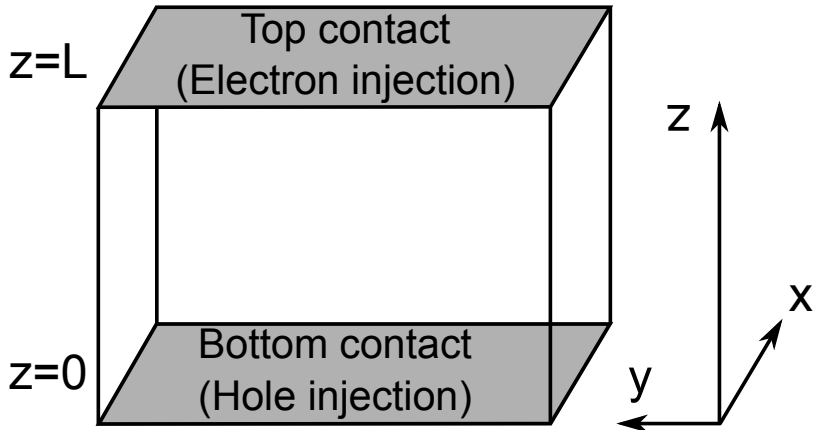


Figure 2.2: Coordinate system we use throughout this thesis. The exact direction of $x$ and $y$ axis is not important, as all the equations are identical under point inversion symmetry, as the equations of interest do not contain pseudo-scalars or axial vectors. The direction of the $z$-axis is important, because the two contacts will have different boundary conditions applied. The $z$-axis points from the bottom contact to the top.

The boundary conditions are introduced on the fixed boundaries, and we should first introduce the coordinate system, fig. 2.2 to relate to particular boundaries.

In this section, we will be mainly interested in the boundary conditions on the $z$ axis, because this is the direction of current flow in our setup. This leads to a situation, in which the derivatives of all quantities with respect to $x$ and $y$ axes are considerably lower than the corresponding derivatives of quantities along the $z$ axis. Therefore, unless stated specifically, we will apply periodic boundary conditions along the $x$ and $y$ axis.

### 2.4.1 Boundary conditions for Poisson Equations

The bias applied externally to the device in an experiment can be seamlessly introduced into the Poisson equation by fixing the potentials on both sides of the device $z = 0$ and $z = L$. As only relative values of the electrostatic potential are important we choose the electrostatic potential at the top contact $z = L$ to be zero. If we fix one of the boundaries, the second boundary condition accounts for the externally applied bias. Therefore we impose boundary conditions eq. 2.43 and eq. 2.44 on the Poisson equation.

$$\phi(\mathbf{r})\Big|_{(z=0)} = V \tag{2.43}$$

$$\phi(\mathbf{r})\Big|_{(z=L)} = 0 \tag{2.44}$$

Note that the boundary conditions at contacts do not necessarily need to be constant, but can retain a dependence on the position within the $xy$ plane. Then, the right hand side of eq. 2.43 should be a function of $x$ and $y$. A possible example of such a situation is large surface area devices, to which the bias is applied via a small wire. In that case we cannot call $xy$ plane a contact, but the same boundary condition can be applied. The sheet resistance of the contact layer then might be sufficiently large to cause a non-negligible voltage variation.

### 2.4.2 Drift-diffusion equation boundary conditions

In sec. 1.3.5, we described the injection barrier in thermodynamic equilibrium, which will inevitably form between the contact and the organic material. Here, we would like to describe what happens to the potential barrier in the presence of external electric field.

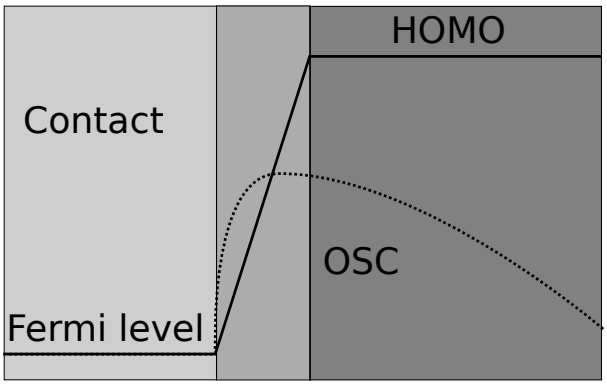


Figure 2.3: Effective electrostatic potential acting on holes (dashed line), when an external bias is applied. The light gray area corresponds to the immediate vicinity the contact, the dark shaded to the OSC. The area in between corresponds to the interface. The solid line shows the level alignment in a bias-free situation.

In fig. 2.3 we show schematic depiction of the combined potential barrier 1.3.5, which is imposed on the charge carrier when it is injected. In case of a metal contact, the offset refers to the difference between the energy of the electron (LUMO) or hole (HOMO) transport level (dark-gray shaded) and the Fermi level of the metal (shaded light gray). We assume here that without superimposed external field, the energy of the charge carrier effectively changes in a step-like manner and the interface does not extent beyond a few intermolecular distances. Treating such an offset in energy with the help of a generalized potential within the drift-diffusion equations, as suggested by Sutherland and Hauser [162], fails as the energy barrier are typically too large (cf. Section 1.3.2.) Therefore, this interface region should be treated with adequately chosen boundary conditions, that also account for the case that no current can be injected.

A common way to treat such a boundary is to set the electric current across the interface for a given shape of the injection barrier, as this current connects the drift-diffusion equations that describe the layers on each side of the interface. Such a current consists of several components [163–167]:

- Charge carriers can overcome the barrier due to thermal excitations. Charge carriers in the metal are not sitting exactly at the Fermi level, but are smeared out across a certain energy region due to the temperature. Hence, part of them may have enough energy to overcome the existing potential barrier. We will call this current *thermal injection current*.
- The thermal injection current will not vanish for a vanishing applied bias. To counterbalance the thermal injection current in equilibrium, another contribution is required, which is called the *interface recombination current*.
- In quantum mechanics, charge carriers may tunnel through a potential barrier. This effect manifests itself the stronger the thinner the potential barrier is. We

will call the current, associated with tunneling from the contact to the OSC as *tunneling current*. Contrary to the thermal current, it does not require any counterbalancing part. Without any bias, barrier bending does not happen and the width of the potential barrier becomes infinite, making tunneling impossible.
- When a reverse bias is applied, charge carriers do not experience any potential barrier on their way and can freely move from the OSC to the contact. In this scenario, the reverse current flow will be limited by the bulk conduction and will be called *backdrift current*. The contributions of a backdrift current are only relevant for reverse bias, i.e. for temporarily high charge-carriers accumulations near the barrier.

In [164] an expression, which jointly accounts for thermal current and interface recombination was derived. It is worth noting, that there are different approaches, for instance, in [163] every contribution mentioned above was implemented separately. These two approaches are not strictly equivalent, but converge to the same injection currents, especially for low driving fields, because first approach is only directed to improve thermal current.

Using these expressions, we implemented all the described constituents for the injection currents. The net thermal injection current density (the interface recombination contribution is taken into account self-consistently in that approach) reads as eq. 2.45 [164],

$$J_{Thermal} = 4\psi^2 N_0 e\mu E \exp(-\phi_B/k_B T)\exp(f^{0.5}) \tag{2.45}$$

where $f$ is the reduced electric field, eq. 2.46

$$f = \frac{eEr_c}{k_B T} \tag{2.46}$$

and $\psi$ is a function of this reduced field $f$ and is derived according to eq. 2.47,

$$\psi(f) = f^{-1} + f^{-0.5} - \frac{\sqrt{1+2\sqrt{f}}}{f} \tag{2.47}$$

$r_c$ is a Coulomb radius, which represents the distance between two opposite charges, at which the attraction energy becomes higher than thermal fluctuations (in other words, charges which get closer than this radius will bind together due to the electrostatic force). $r_c$ is given by eq. 2.48

$$r_c = \frac{e^2}{4\pi\epsilon\epsilon_0 k_B T} \tag{2.48}$$

$N_0$ is the density of charge carriers at the contact, and $\phi_b$ is the energy barrier between contact and transport layer.

The tunneling current density can be obtained with the Wentzel–Kramers–Brillouin

approximation applied to the Schrödinger equation, eqs. 2.49 - 2.51 [163]

$$J_{tunneling} = J_t \left( \frac{E(L)}{E_t t(y)} \right)^2 \exp\left( -\frac{E_t v(y)}{E(L)} \right) \tag{2.49}$$

$$J_t = \frac{e\phi_B^2}{9(\pi a_0)^2 \hbar R} \tag{2.50}$$

$$E_t = \frac{4\phi_B^{3/2}}{3ea_0\sqrt{R}} \tag{2.51}$$

In these equations $a_0$ is the Bohr radius and $R$ is the Rydberg constant. The functions $t(y)$ and $v(y)$ can be determined according to eqs. 2.52 - 2.53.

$$v(y) = (1+y)^{1/2} \left[ E\left( \sqrt{\frac{1-y}{1+y}} \right) - yK\left( \sqrt{\frac{1-y}{1+y}} \right) \right] \tag{2.52}$$

$$t(y) = (1+y)^{-1/2} \left[ (1+y)E\left( \sqrt{\frac{1-y}{1+y}} \right) - yK\left( \sqrt{\frac{1-y}{1+y}} \right) \right] \tag{2.53}$$

$E$ and $K$ in eqs. 2.52 - 2.53 are elliptic integrals.

The numerical integration to obtain $E$ and $K$ is extremely slow and inefficient and it can potentially slow down the calculations. However, it is not necessary, however, to calculate them directly, because there exists extremely fast converging iterative equations to do so [168]. Their exact implementation is presented in the appendix at p. 138.

In these equations, parameters like the mobility $\mu$ and the dielectric permittivity $\epsilon$ are material parameters. They are set to the same values as used for bulk transport. Other parameters, such as the electric field $\mathbf{E}$ and the temperature $T$ are obtained on the fly from the bulk transport simulations. However, there are several parameters that are injection-specific. These parameters and their default values are described in the table below. If not stated otherwise, we use these default values from the table for the parameters. Charge carrier density value was set to be equal to be charge carrier density in silver, according to [169]. For the values of injection barrier we picked the values, determined in 1.3.5.

Note that the table also considers the barrier at the organic-organic interface. In our simulations, the barrier is described by thermal injection eq. 2.45. Initially, we were treating organic/organic interface as a part of a bulk simulation, but this approach seemed to provide unsatisfactory results, because in this case the effective electric field at the organic interface depends on the discretization. The electric field, determined from the simulation, is proportional to the potential difference $\delta\phi_{sim}$, which is modified by the potential barrier at the interface $\phi_{int}$ and is always larger than 0.2 eV in the case for a forward bias. It is also inversely proportional to the discretization $\delta z$. If one casts this observation into the following equation

$$\mathbf{E}_{effective} = \frac{\delta\phi_{sim}}{\delta z} + \frac{\delta\phi_{int}}{\delta z} \tag{2.54}$$

one can deduce that while the simulated potential difference $\delta\phi_{sim}$ will decrease with discretization, the interface potential difference $\delta\phi_{int}$ will remain the same. Therefore, the electric field at the interface suddenly becomes dependent on the discretization.

Therefore, we described the currents across the interface as thermal injection currents, which do not depend on discretization and, thus, provide steady results. The derivation of thermal injection neither requires the disordered nature of the material to inject to, nor an ordered nature of the material to inject from. The situation is different for the tunneling current because the W.K.B. approximation requires wave functions to be expanded in a delocalized fashion. This can be justified in case of metal/organic equation, because at least one side can be considered as semi-infinite, however, it is hard to justify it when there can be no delocalized wavefunctions from both sides. Because of that, we decided to disregard the tunneling current across the organic-organic interface.

### 2.4.3 Problems with the tunneling injection

The injection currents described above possess one very serious issue. We discovered this problem only after investing substantial amount of time into the modeling and comparing them to experimental ones. The issue is in essence a combination of inadvertence of the author combined with a inaccurate description of the injection current in the source article.

If one takes a look on the [163], the tunneling injection is described using a Gaussian Unit system [170]. In the thesis on the other hand, due to the presence of coupling between multiple phenomena which are often described in different units, International unit system [171] is employed. Often, when one is dealing with electrodynamics problem, it is useful to adopt Gaussian unit system, as it changes units of charge in the way, that electrostatic attraction force between two charges does not have a dimensional proportionality coefficient:

$$F_{Coulomb} = \frac{q_1 q_2}{r^2} \tag{2.55}$$

Where $q_1$ and $q_2$ are the charges of the particle and $r$ is the distance between two charges.

Normally, conversion between the two units is trivial. One can use general rules for the conversion described e.g. in [170]. However, if one performs this conversion for the tunneling injection eq. 2.53, the resulted formula still is incorrect. The problem is not obvious, as the resulting current value will not be absurdly different from ones expectation and probably stems from some omitted dimensional constant which is equal to 1 in the Gaussian unit system. For example, actual tunneling current value at 2.5 $V$ for the set of parameters used here for modeling is around 0.1 $A/m^2$, while incorrect formula gives a value of 5 $A/m^2$. Moreover, as we will see in the sec. 4.4, the contribution to the total injection current from the thermal injection under large bias will be actually larger than the (both correct and incorrect) tunneling current. For somebody, who is not too familiar with actual experimental values of the current in the low-voltage regime (and I had in fact no prior knowledge in OLEDs at start of my work in the project), the fact that the tunneling current is too large is quite subtle.

The issue does not makes the equation useless. What one still can do is to calculate the tunneling injection current in the following way:

1. Convert the model quantities into the Gaussian system
2. Calculate the injection current using eq. 2.49

3. Convert the resulting current values back into SI units

As calculating elliptic integrals is much more expensive task from the computation time perspective than these unit conversions, it does not noticeably impact a performance. This is the way the tunneling injection was eventually implemented into the simulation and it drastically improved the correspondence of the modeling results to the experimental ones.

The problem was noticed only in the last year of my work on the project, when I finally got my hand on the experimental results obtained for this device. Unfortunately, this meant that all results had to be recalculated with the new injection implementation, and this alone took me several months to do. Some of the calculations, presented in the thesis, were not adjusted for this issue and we will explicitly mention when it happens.

Furthermore, in the sec. 4.4 we will describe another set of problems related to the injection currents, that surfaced only after the mistake in the injection current was discovered and were never not accounted for. This means, that any results in the thesis will be affected by incorrect injection model in some way and one should always keep that in mind. On the bright side however, we will show in ch. 4 that these problems often do not negate general conclusions and only the results, related to low voltage regions, must be adjusted. High voltages are in fact described quite precisely by our model, as well as the current dependence on temperature. Elevated temperatures will only appear under sufficiently high currents, which in turn exist only under large applied biases. Therefore, most of the results should be adjusted for the phenomenon but not completely discarded.

### 2.4.4 Boundary conditions for the heat transport equation

This section is dedicated to a physically sensible way to implement boundary conditions for the heat transport equation, eq. 2.42. We will start with two major assumptions:

- There exists some fixed ambient temperature $T_0$ which cannot change irregardless of the actual amount of heat produced by the device.
- The boundary conditions should only depend on the difference between the temperature at the boundary of the device $T_D$ and the ambient temperature $T_0$.

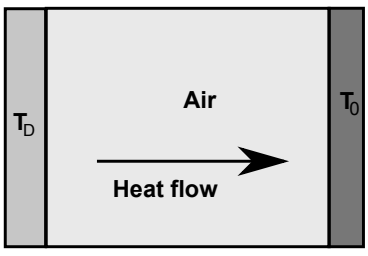


Figure 2.4: Difference between the actual device temperature $T_D$ and the ambient temperature $T_0$. In operating conditions, the device will be in contact with air, which can also store and transport heat. A thick air layer between ambient and the device guarantees a pronounced linear proportionality between $T_D - T_0$ and the value of heat flow from the device to the ambient environment.

From these two assumptions and the fact, that heat should always flow from the warmer to the cooler region and no flow should be observed when these temperatures are equal, we imply that the dependence of heat outflow $q$ from the edge of the device to the environment can be assumed in the form $q = f(T_D - T_0)$; where $\text{sign}(f(T_D - T_0)) = \text{sign}(T_D - T_0)$. However there are two problems with these equations, as indicated in fig. 2.4. First, if the device produces a lot of heat, enough to noticeably increase its temperature, the generated heat will raise the temperature close to the device surface. Therefore, the region, in which $T_0$ is attained, should be located far away from the device surface.

That means, that the function $f$ should depend not only on the properties of the device itself, but also on a number amount of supplementary parameters which are dictated by the ambient environment. Examples of such parameters would be air humidity, the thickness of the air layer, whether there is some convection or wind, which takes away the hot air near the device, etc. Moreover, it will depend on the properties of the device-air interface, for example, on the surface area of the device (which will change for example if it is rough). There are some works in the direction to take into account all these properties, most notably [172–174]. Such large number of free parameters make it impossible to treat everything numerically within reasonable amount of time, therefore, we are required to make some reasonable approximation for the border conditions.

To get this approximation, we expanded our candidate function $f$ into a Taylor expansion with respect to $T_D - T_0$. Due to the second assumption, $f(0)$ should be zero, i.e., the expansion starts from the linear term. The leading linear term may also vanish in case of ballistic transport regime, which was already observed in a variety of different materials [175–179]. The reason for ballistic transport is the absence of almost any interactions between particles which carry heat so that practically free particles can carry energy infinitely far without a noticeable energy cost. Nevertheless, diffusive transport dominates in materials relevant for OLEDs. Then the particles, which carry the heat, are scattered very often. Technically, that means that the scattering-free length for particles is much lower than the characteristic length of the macroscopic region where we expect the temperature to change. Correspondingly, in that regime, the linear term in a Taylor expansion will assume the governing role.

We further consider that the actual ambient environment will be located at some distance from the device, i.e. the thermal conductivity of air is going to play a crucial role. Air transports heat in a very pronounced linear behavior with fixed low thermal conductivity of $0.02 W/mK$. In the Results chapter we will derive eq. 3.12, which states, that in this scenario the thermal conductivity of air will play the most important role. Thus, its linear thermal transport behavior with respect to $T_D - T_0$ will be dominating contribution to the function $f$.

Thus, we arrive to the following form of boundary conditions for the heat equation:

$$q(L) = h(T_D - T_0) \tag{2.56}$$

$$q(0) = h(T_0 - T_D) \tag{2.57}$$

Note the sign change in eq. eq. 2.57. It is necessary to account for the fact that thermal flow is a vector quantity and at the left boundary its direction will be opposite from the right one. We will call $h$ the heat transfer coefficient or, shortly, h-coefficient. These boundary conditions are also known as Newton boundary conditions and they appear

in problems of mathematical physics, in which a linear approximation for the actual evolution across the boundary region is sufficient.

Note here that organic/organic interfaces, in general, may exhibit heat conducting properties that are distinctively different from that of the materials [180] due to different phonon/electron dispersion relations in both materials. However, the heat transfer between two amorphous organic materials will not be hampered to the same degree by disparate phonon dispersions due to the localized nature of wavefunction. Moreover, we did not found any studies which would accurately measure heat transfer between $\alpha$-NPB and Alq3. Even if we could, question would arise whether they are applicable or not, as deposition procedure may as well influence the resulting value of heat transfer coefficient. Finally, in the results chapter we will show that most heat will be generated on the interface, fig. 3.4. This implies that most of the heat generated on the interface will be not go through the organic/organic interface, but rather propagate towards contacts to be dissipated. Therefore, we decided to treat any interface between two amorphous organic materials according to the average of their bulk thermal conductivities.

## 2.5 Source terms in continuity equations

#### Generation and recombination terms

To capture electron/hole recombination, we use Langevin [181] recombination rates, eq. 2.58.

$$R(\mathbf{r}) = \frac{e\left(\mu_e(\mathbf{r}) + \mu_h(\mathbf{r})\right)}{\epsilon_0 \epsilon_r(\mathbf{r})} n(\mathbf{r}) p(\mathbf{r}) \tag{2.58}$$

The recombination is proportional to the sum of the mobilities. The sum of the two mobilities determines the relative speed of two oppositely charged particles towards each other due to their mutually attractive electric field. This electric field is modified by the dielectric permittivity $\epsilon$ of the material, which appears in the denominator. If one of the charge carriers is much more mobile than the other, the nominator will be dominated by the large mobility. The more charge carriers are available, the larger the recombination becomes.

Langevin recombination rates tend to overestimate recombination because they neglect many other processes which may occur [182]. Nevertheless, it approximates the recombination reasonably well and permits a straightforward interpretation due to its simple form.

As we are not interested in any effects, which could provide a substantial generation rate (as for instance in solar cells), we keep a very low generation rate of $10^{10}$ $particles/s/m^3$ in the simulations to aid convergence under low biases.

### 2.5.1 Joule and recombination heating

The source term in the heat equation is crucial for the whole simulation because it introduces heat generation due to the electric current and recombination, and it increases the operating temperature. We consider two main heat sourcesJoule heating and non-radiative recombination heating. Though thermoelectric effects may also be present and contribute to heat generation, we found these contributions to be

negligible after preliminary testing, because thermoelectric constants in the organics are in a order of $0.5mV/K$ [183], which is a very small number, compared to the driving voltages and temperatures in the device.

### Joule heating

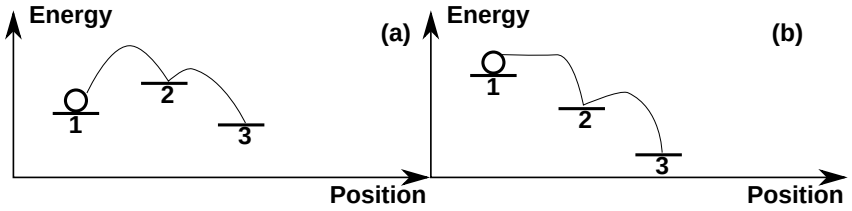


Figure 2.5: Schematic illustration of hopping transport mechanism. Charge carrier performs a hops between energy sites, the probability of which is determined mostly by the sites energy difference. (a) and (b) correspond to the situation without and with electric field applied respectively.

Joule heating is the most impactful mechanism of heating. Usually, it is described as the amount of energy that charge carriers transfer to the material due to inelastic scattering while moving through the media. However, scattering is an inappropriate description for charges in OSC, because they are most of the time localized on a site and rarely (compared to the time spent on one site) hop to other sites.

The mechanism of dispersing energy is, therefore, different. If we look at fig. 2.5, we see that an electron, while moving through the disordered energy landscape, loses and obtains energy with each hop. When the electron performs a hop upwards in energy, it has to borrow thermal energy from the material and when it descends, it has to give this energy back to the material. If there is no external potential applied, fig. 2.5-a, the energy landscape is on average flat and the electron returns the same amount of energy that it borrowed from the system.

However, an externally applied field shifts the energy levels of the sites, fig. 2.5-b. Therefore, an electron, moving from site 1 to site 3 will pass an energy corresponding to the difference between the site energies to the system. The shift of energy levels corresponds to the electric field $\mathbf{E}$ at the point and the total energy dissipated by all charge carriers $Q$ is also proportional to the current $\mathbf{J}$, as it describes total amount of charge carriers,

Hence, although the mechanism is different from the case of ordered materials, Joule heating should maintain its conventional form, eq. 2.59.

$$Q = \mathbf{J} \cdot \mathbf{E} \tag{2.59}$$

The current density is fed into this equation from the drift-diffusion equations and the electric field from the Poisson equation, creating a direct coupling between the modeling equations for charge and heat transport.

### Recombination heating

Accounting for recombination heating is also straightforward in a macroscopic picture. The actual processes, which drive this recombination, should be described quantum mechanically. Generally they are quite complicated to describe, particularly because

of the bare fact that this kinetic process should involve a lot of particles. However, in macroscopic equations recombination heating is a manifestation of energy conservation. To conserve the energy when two charge carriers are removed from the charge densities considered in the drift-diffusion equation, the energy they possess should be transfered into heat equation (otherwise, the total system energy changes). What energy do electron and hole posses? First of all, as they are moving through the media, they have kinetic energy. Secondly, due to the fact that recombination of an electron and a hole involves an electron being removed from the LUMO and a hole being removed from the HOMO (or, in other terms, electron just falls down from the LUMO level to the HOMO level), there should be some energy released in the process, which is equal to the difference between HOMO and LUMO. Due to complicated electrostatic interaction between electrons and holes, and local changes to the energetic landscape they induce, the recombination energy always differs from the $E_{HOMO} - E_{LUMO}$ energies. This process is known as the formation of exciton and is very important for instance in the solar cells, in which the ability of such particles to move around in the device before recombination happens allows extraction of the exciton energy. We will refer to energy of an exciton as *recombination energy*, $E_R$.

Basically, the recombination term in the drift-diffusion equation tells us, how many charge carriers are recombining in the given volume per second. If one multiplies it by the recombination energy, one obtains the amount of energy released due to recombination. Finally, if one multiplies it also by $(1 - \eta)$, with $\eta$ being the internal quantum efficiency, one obtains the amount of heat energy dissipated due to recombination in the element volume per unit time:

$$Q_R = (1 - \eta) E_R R \tag{2.60}$$

## 2.6 Discretization methods

The equations derived so far can be solved analytically only for a narrow subset of specific cases. For instance, we will show an analytic solution to the heat equation in sec. 3.1.3, but this will require us to make several serious assumptions. Numerical methods to solve differential equations, on the other hand, require us to discretize the spatial region of interest. To do so, one can divide this region into small volumes $V_i$ and assume that any quantity of interest $F(x)$ is constant within this region, $F(x \subseteq V_i) = F_i$. In this work, we use the Finite Difference Method, where the shapes of the volumes are restricted to rectangule, as schematically shown in fig. 2.6.

We will demonstrate the discretization procedure on the example of the two dimensional case, however, equations presented in the previous chapter have to be discretized for 3+1 spatial and time dimensions. We use the two dimensional example for two reasons: it is easy to plot explanatory two-dimensional figures, and, contrary to one dimension, it can already describe discretization of partial derivative equation. As illustrated in fig. 2.6, every axis is divided into subsections. The region of interest is divided into $N$ subsections $(x_0; x_1), (x_1; x_2), ..., (x_i; x_{i+1}), ..., (x_{N-1}; x_N)$, where $x_N = L_x$. This is done for every the other axes. Then, every quantity $F(x)$ in the simulation assumes a constant value $F_{i,j} = F(x_i, y_i)$ at every subvolume, depicted as gray rectangle. The discretization rectangle for the point $x_i$, $y_j$ is chosen in such a way, that the point $(x_i, y_j)$ is located in the center of the rectangle. This is done with regards to the points, located on the boundary; for example, $F_{0,0}$ should be located

exactly in the bottom left corner. Therefore the actual distribution of $F(x)$ becomes approximated by a set of values on the mesh. The discretization of the volume requires also the discretization of spatial derivatives.

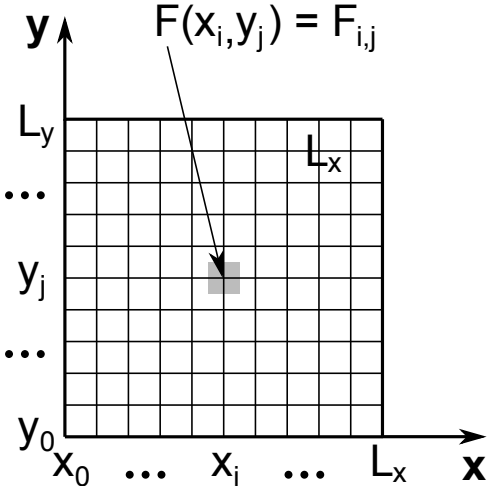


Figure 2.6: Schematic illustration of the discretization of a two dimentional rectangular region.

Besides space, also the time variable $t$ requires discretization. We are generally interested in the steady state of the system, which is reached by the system with no quantities change in time. The timescale to reach a steady state is between seconds and minutes of real-time. When one turns on an OLED, its operating state evolves with time. At first, charge carriers are injected and form a steady state charge carrier distribution after a short time. However, the electric current heats the device. While the device heats up slowly, the increase in temperature, changes carrier distributions and electric fields inside the device. Finally, when the heat outflow balances the heat generation, the device reaches a steady state. In our model, we assume that this steady state can be reached. Note that, in reality, the time required for the device to reach a steady state is long enough to permit slow device degradation, which means that steady state might actually never be observed.

Whatever quantity $F(\mathbf{x}, t)$ is described by the equations, steady state implies that it does not change overtime and, hence, $\frac{dF(\mathbf{x},t)}{dt} = 0$. There are two main methods to solve equations for a steady state. The first method is to explicitly set $F'_t(\mathbf{x}, t) = 0$ and solve the remaining discretized system of equations. This method works when the remaining system of equations can be solved easier and in a shorter time than the full system, for instance, when the remaining equations are linear. We cannot use this method due to the exponential dependence of the mobility terms and the injection on temperature.

The second method is to keep the time derivatives in the equations and let the system evolve in time until it reaches a steady state. The discretized equations provide the connection between the value of quantity $F$ in the current timeframe $t$ and a timeframe a little later $t + \Delta t$.

As to the best of our knowledge, no strict proof of the uniqueness and existence of solutions to the system of equations 2.6, 2.40, 2.39 and 2.42 exists. We checked for each simulation that different initial conditions lead to the same steady state solutions within numerical accuracy.

### 2.6.1 Discretization of the continuity equations in its general form

The continuity equation in its general form with all derivatives explicitly outlined reads as eq. 2.61.

$$\frac{\partial \rho}{\partial t} + \sum_{c=x,y,z} \frac{\partial J_c}{\partial c} = S \tag{2.61}$$

The derivative in terms of discretized variables utilizes the definition of a derivative as $\frac{\partial F}{\partial x} = \lim_{dx \to 0} \frac{f(x+dx)-f(x)}{dx}$.

To discretize derivatives with respect to time, we, therefore, replace the time derivative with the finite difference expression, eq. 2.62.

$$\frac{\partial F}{\partial t} \xrightarrow{discretization} \frac{F(t+\Delta t) - F(t)}{\Delta t} \tag{2.62}$$

We need a discretization of second derivatives because the fluxes in the continuity equations are often constructed from the derivatives of other quantities. The second derivative in one dimension requires three points for discretization. Therefore, it can be calculated based on the given mesh point and its two neighbors. To obtain the necessary equations, one needs to consider the second derivative as the discretization of first derivative at points $x_i - (x_i - x_{i-1})/2$ and $x_i + (x_{i+1} - x_i)/2$. The resulting equations for the second derivative then look like eq. 2.63.

$$F''_{ii} \xrightarrow{discretization} 2\frac{\frac{F(x_{i+1})-F(x_i)}{x_{i+1}-x_i} - \frac{F(x_i)-F(x_{i-1})}{x_i-x_{i-1}}}{x_{i+1} - x_{i-1}} \tag{2.63}$$

One straightforward example to demonstrate the discretization in a device is the heat equation 2.42. At this point, we need to abandon our example of two-dimensional discretization scheme, because following equations will be used in the actual modeling. This means, that every derivative is now exapned into either eq. 2.62 for one-dimensional derivative or eq. 2.63 for the second order of derivative. We can again explicitly expand heat transport equation into partial derivatives:

$$\rho c_p \frac{\partial T}{\partial t} - \sum_{c=x,y,z} \left( \frac{\partial \kappa}{\partial c}\frac{\partial T}{\partial c} + \kappa \frac{\partial^2 T}{\partial c^2} \right) = Q \tag{2.64}$$

The first term in the brackets becomes important only when the mesh point of interest is located on a heterojunction where the thermal conductivity changes. We equip three coordinates $x$,$y$,$z$ with the corresponding discretization indexes $i$,$j$,$k$ and denote $\kappa^t_{i,j,k}$, $T^t_{i,j,k}$, $Q^t_{i,j,k}$, $\rho^t_{i,j,k}$, ${c_p}^t_{i,j,k}$, as discretized qunatities corresponding to terms, that are contributing to the heat transport equation at the moment of time $t$. We then can arrive at the following iterative formula for the time propagation of heat equation, in which the second and third term in square brackets correspond to an expansion of the derivatives in terms of the first coordinate $x$ in eq. 2.64. The four other terms which correspond to two remaining coordinates are collapsed into three dots after the expression. The full equation can be found in the appendix.

$$T_{i,j,k}^{t+\Delta t} = T_{i,j,k}^{t} + \frac{\Delta t}{\rho_{i,j,k} c_{p_{i,j,k}}} \left[ Q_{i,j,k}^{t} + \frac{\kappa_{i+1,j,k} - \kappa_{i-1,j,k}}{x_{i+1} - x_{i-1}} \frac{T_{i+1,j,k}^{t} - T_{i-1,j,k}^{t}}{x_{i+1} - x_{i-1}} + \right. \\ \left. + 2\kappa_{i,j,k} \frac{\frac{T_{i+1,j,k}^{t} - T_{i,j,k}^{t}}{x_{i+1} - x_{i}} - \frac{T_{i,j,k}^{t} - T_{i-1,j,k}^{t}}{x_{i} - x_{i-1}}}{x_{i+1} - x_{i-1}} + \dots \right] \tag{2.65}$$

The equation presented allows one to advance the temperature forward at every discretized point in time. Note that all quantities on the right hand side of that equation are given for this moment of time $t$. Our iteration method is called Euler forward method. It is known, that the forward Euler method suffers from stability issues, i.e., there exists a certain critical timestep $\Delta t_C$, above which such an iterative scheme will not converge but will rather oscillate and diverge [184]. However, we cannot use the more robust Euler backward method, because it yields and intractable system of equations.

### 2.6.2 Specific aspects related to discretizing Poisson equation

The Poisson equation cannot be cast straightforwardly into a discretized form like the iteration scheme Eq. (2.64) for the discretized heat trannsfer equation. One of the reasons is that the Poisson equation lacks a time derivative. Conventionally, an iteration scheme is employed that is customized for the Poisson equation. Applying steps related to eqs. 2.63 - 2.64 for the finite difference discretization, straight-forwardly yields an iterative scheme that relates the electrostatic potential at a position (i,j,k), $\phi_{i,j,k}$ to the nearby potentials $I(\phi_{i+1,j,k}, \phi_{i-1,j,k}, \dots)$ [185]. When applied to every point, the scheme will result in a full iteration for all mesh points. After several full iterations, the scheme will be converged. This discretization scheme is very stable.

However, when combined with the solvers for the other continuity equations, this scheme adversly affects the convergence speed upon changing the discretization. Denominators (as in 2.65) in discretization equations are now totally dependent on discretization volume and can change a lot, depending on the discretization scheme. For the Poisson equation alone, the scheme self-controls its convergence. However, this - as such - appealing property slows down the overall convergence, when the scheme is used together with other schemes that have a fixed convergence speed. Therefore, we sought for another type of discretization scheme, that allows us to control the convergence speed in the same way as for the continuity equations even if we sacrify numerical stability.

A very straightforward way to do so is to add the time derivative of the potential in the Poisson equation so that it will resemble the heat equation 2.66.

$$\frac{\partial \phi}{\partial t} - \nabla \epsilon_r \nabla \phi = \frac{e(p-n)}{\epsilon_0} \tag{2.66}$$

We can do so, because we are interested only in the steady state solution, where time derivative vanishes and the equation left is the Poisson equation. We then use the same discretization scheme for the Poisson equation as we applied to the heat equation. Introduction of the timestep does not influence the steady state, but gives us an invaluable handle for us to control Poisson equation convergence. Utilizing this

handle, we can put convergence of Poisson equation on par with other equations. The exact discretized equations can be found in the appendix.

### 2.6.3 Specific aspects related to drift-diffusion equation

The drift-diffusion equations eq. 2.40 & eq. 2.39 correspond to regular continuity equations (alike the heat transport equation). In practice, however, the discretization scheme akin to the one we used previously for heat transport equation yields unsatisfactory results for the drift-diffusion equations, because the charge carrier densities may change in the device by orders of magnitude. Such large changes can be readily illustrated with the following notion: The charge carrier density, i.e., the occupation of the available electronic states in trap-free semiconductor in thermal equilibrium is well-described with a Boltzmann distribution. If charges are spatially redistributed, e.g., due to an electrostatic potential, the local occupation will change exponentially. The stronger the electric field, the more pronounced is the diffence in occupation between close-by locations. Consequently, strongly inhomogenous charge density profiles may form across the device. Furthermore, also barriers located at interfaces or contacts contribute to inhomogeneous charge carrier distributions, as they cause local charge accumulations.

To account for large differences between adjacent mesh points, one can use a specific discretization scheme, namely the Scharfetter-Gummel method [186–189]. The idea behind this method is simple, yet extremely efficient. In this section we will demonstrate how it works for one spatial dimension and for electrons; the three-dimensional equations are shown in the Appendix.

Let us start with the drift-diffusion expression for the x-component of the electric current density (eq. 2.40) multiplied by the elementary charge $-e$, where every quantity apart from the elementary charge is time and spatially dependent.

$$J_x = en\mu E + De\frac{\partial n}{\partial x} \tag{2.67}$$

We will discretize every quantity in this equation apart from the charge carrier density, which will remain as spatially changing quantity, on the interval $[x_i; x_i + 1]$; the density will be located in the middle between these two points $x_{i+0.5} = x_i + 0.5(x_{i+1} - x_i)$

$$J^t_{x\,i+0.5,j,k} = -en\mu^t_{i+0.5,j,k}E^t_{i+0.5,j,k} + D^t_{i+0.5,j,k}e\frac{\partial n}{\partial x} \tag{2.68}$$

Any discretized quantities are constants in the discretized cells. Therefore, we can treat them as constants in the differential equation above. Consequently, eq. 2.68 corresponds to a simple first order linear differential equation $an' + bn = c$ in $n$, which can be easily treated analytically. To arrive at the analytical solution, the current density is considered as a known constant. There will be one more free parameter after integrating the differential equation. Hence, we are left with two unknowns, i.e., the integration constant and the current density. Eq. 2.68 allows us to extract the electric current from two electron densities $n$ at $x_i$ and $x_{i+1}$. In turn, the current entering as flux permits to solve the continuity equation. We will not show the whole solution procedure here, because this simple linear equation as such is easy to solve and the

process of determining all constants is quite tedious [190]. Finally, the discretized current density reads as follows:

$$J_{x}{}^{t}_{i+0.5,j,k} = \frac{eD^{t}_{i+0.5,j,k}}{x_{i+1} - x_i}\left[ n^{t}_{i+1,j,k} B\left( \frac{e(\phi^{t}_{i+1,j,k} - \phi^{t}_{i,j,k})}{k_B T} \right) - n^{t}_{i,j,k} B\left( - \frac{e(\phi^{t}_{i+1,j,k} - \phi^{t}_{i,j,k})}{k_B T} \right) \right] \tag{2.69}$$

where

$$B(x) = \frac{-x}{1 - \mathrm{e}^{x}} \tag{2.70}$$

One assumption which was used to derive this equation is the validity of Einstein relation eq. 2.14, which we assume to be valid throughout this work. This is the reason why the Scharfetter-Gummel discretization scheme does not explicitly contain the mobility, as it is assumed to be related to the diffusion coefficient. It is possible, however, to keep it explicitly in the discretization scheme, e.g., when the Einstein relation fails or when the mobility displays an involved dependence on the field- and a charge carrier densities.

Now we have the current between two points, therefore, we have the charge carriers density in two neighboring points. We now can finally write down the full discretization scheme for the drift-diffusion equations. As previously, we will write the scheme only for electrons and performed on the $x$ coordinate. Terms, corresponding to other coordinates, and equations, corresponding to the holes, can be found in the Appendix. First, we write down the drift-diffusion equation for electrons eq. 2.71, which is eq. 2.40, in which the electric current is explicitly placed instead of the drift-diffusion term to prepare it for the Scharfetter-Gummel discretization. The charge carrier flux can be obtained from the electric current by dividing it by the elementary charge, which in case of electrons is $-e$, which results in the minus sign before the divergence term.

$$\frac{\partial n}{\partial t} - \nabla\left(\frac{\mathbf{J}}{e}\right) = G - R \tag{2.71}$$

Discretizing this equation at points $x_i, y_j, z_k$, we can obtain the following iterative scheme, where three dots correspond to the discretization of the two other axes.

$$n^{t+\Delta t}_{i,j,k} = n^{t}_{i,j,k} + \Delta t\left[ G^{t}_{i,j,k} - R^{t}_{i,j,k} + \frac{J^{t}_{i+0.5,j,k} - J^{t}_{i-0.5,j,k}}{0.5e(x_{i+1} - x_{i-1})} + \dots \right] \tag{2.72}$$

This way of writing down the discretized continuity equations, keeping the electric current instead of drift-diffusion term, has a very specific advantage: it is easy to insert boundary conditions. As we described in sec. 2.4.2, the conditions on device boundaries are described by the current inflow from the contacts. Therefore, to account for the boundary conditions we just have to insert the correct injection current in eq. 2.72 for any mesh point on the boundary.

## 2.7 Mobility in drift-diffusion equation

For simulations of organic semiconductors we require the charge carrier mobility, which depends on the electric field strength, on the temperature and on the charge carrier density. Assuming the validity of the Einstein relation, these dependencies are also transferred to the diffusion constant. The dependencies are governed by the properties of the material. We used the unified mobility model presented in [159]. In this model the total mobility can be expanded into the product of several functions:

$$\mu(T,p,E) = \mu(T) f_p(T,p) f_E(T,E) \tag{2.73}$$

$$\mu(T) = \mu_0 c_1 \exp\left[-c_2 \hat{\sigma}^2\right] \tag{2.74}$$

$$\mu_0 = \frac{a^2 \nu_0 e}{\sigma} \tag{2.75}$$

$$f_p(T,p) = \exp\left[0.5\left(\hat{\sigma}^2 - \hat{\sigma}\right)\left(2pa^3\right)^{\delta}\right] \tag{2.76}$$

$$\delta = 2\frac{\ln\left(\hat{\sigma}^2 - \hat{\sigma}\right) - \ln(\ln 4)}{\hat{\sigma}^2} \tag{2.77}$$

$$f_E(T,E) = \exp\left[0.44\left(\hat{\sigma}^{3/2} - 2.2\right)\left(\sqrt{1 + 0.8\left(\frac{Eea}{\sigma}\right)^2} - 1\right)\right] \tag{2.78}$$

$$c_1 = 1.8 \cdot 10^{-9} \tag{2.79}$$

$$c_2 = 0.42 \tag{2.80}$$

Note that this thesis will not attempt to perform simulations with mobility values that exactly match the experimentally reported ones. Rather, either a representative mobility value or an illustrative range of mobilities will be considered. The main reason is that mobility values extracted from experiments depend on the acquisition method and sample preparation, even for nominally identical devices. This is particularly well exemplified with an interlaboratory study [191, 192] that has been dedicated to a reliable determination of mobilities from space-charge-limited currents. In this study, preparation, measurement, and mobility extraction was done by different groups for the same target materials. The resulting mobility values are scattered within two orders of magnitude. This scatter in mobility values can be reduced, and the authors present a measurement protocol which aims at reducing it, but not necessarily entirely prevented.

## 2.8 Device symmetrization

Considering the large number of different parameters required by the modeling, our initial step aims at reducing the number of free parameters. This was done by a device symmetrization procedure.

Actual devices contain two main layers, namely the electron (ETL) and hole (HTL) transport layers. In the experimental OLED setup, fig. 1.7, the thicknesses of both layers are almost equal. They possess different electric and thermal parameters, which leads to the fact that certain layers might be more or less important for device performance

than others. To have a more general starting point, we decided to eliminate this inequality and set the device to be symmetric from every point of view. In essence, "we seek a model device for our simulations, that serves three purposes: (i) The device layout should support the setup of a toy model with which the role of the heat transfer coefficients $h$ towards the environment and the heat conductivities $\kappa$ of the organic layers can be conveniently distinguished. (ii) The toy model should operate with a strongly reduced amount of parameters so that the impact of charge and heat transport can be disentangled best. (iii) It must be possible to straight-forwardly extent our toy model to accommodate more involved device structures with our modeling methodology." [146]

We propose that devices that are symmetrized as will be shown below serve this purpose. In terms of electric properties we demand a balanced current. "This condition of balanced current halves the amount of necessary electrical parameters. If realistic parameters are imposed for one layer, only parameters of the second layer require an adjustment to balance the current. In practice, the adjusted parameters are either the electron or the hole mobility in their respective transport layer or the offset between either the electron or the hole transport levels. " [147]

"In the next step, we construct the device to be symmetric from a thermal point of view." [147] "As there is no differentiation between the top (encapsulation) and bottom (substrate) anymore, we can use a common effective heat transfer coefficient $h$ rather than distinguishing between $h_L$ and $h_R$. To guarantee the desired symmetric distribution of the heat density, two conditions must be fulfilled. Firstly, the layers from both sides of the device center must have equal thermal conductivities $\kappa$. With having reduced our thermal parameters to $\kappa$ and $h$, we can more clearly track their impact on the device temperature and performance. Secondly, also the electric current density responsible for heat generation must be equal in the layers left and right of the device center." [146] "We propose that such symmetric devices are ideal starting points to monitor the impact of subtle changes in the coupling between charge and heat transport." [146]

It is important to note that the current in the device, independent of the actual parameters in corresponding layers, should still be constant across the layers due to charge conservation. Nevertheless, we still have to impose symmetric charge transport parameters, to obtain a symmetric heating profile. This is because heating, as described by eq. 2.59 and eq. 2.60 depends on the variety of electric parameters as well.

Note that in the OLED structure we aim to model, the ETL has a lower charge carrier mobility than the HTL. Therefore, holes from the anode penetrate the HTL and recombine with electrons on the other side. That means that the heating profile and heat transport will be shifted towards the region of the ETL and, inherently, the thermal conductivity of the ETL will be of higher importance compared to the one of the HTL. This property of an actual device [5] is not captured in the symmetrized model, as it corresponds to asymmetric heat generation and temperature profiles.

In summary, the parameters which we set equal in both layers are:

- Thickness of hole and electron transport layers.
- Mobilities of holes in the HTL and electrons in the ETL.
- Mobilities of electrons in the HTL and holes in the ETL.

[5] For example, due to the fact that the emission spectra origins from Alq3, which performs the function of ETL, the spectra of light is much closer to the one of Alq3 than HTL

- Injection barriers for both charge carriers from opposite sides, i.e. hole injection barrier at the anode and electron injection barrier at the cathode.
- Injection barriers associated to the heterogeneous organic/organic interface. The HOMO and the LUMO levels of both ETL and HTL are adjusted in the way, that the barrier for holes and electrons at the interface are equal for holes and electrons.
- Thermal conductivity $\kappa$ and heat transport coefficient $h$.

## 2.9 Default simulation parameters

At the thesis, the reader will see a multitude of different simulation results. Most of these simulations were performed under the same set of parameters and in this section we will specify the default set of parameters to make this investigation reproducible and to not bother the reader with the same parameters over and over. Sources or, in cases where could not provide reliable source, justifications for most values are provided in the respective sections of the thesis, where these parameters are first introduced. However, some of them are not covered and we will discuss them briefly after showing the resulting table 2.1.

| Parameter | Description | Default value |
|---|---|---|
| $N_0$ | Density of charge carriers at contact | $10^{28} m^{-3}$ |
| $\phi_B$ | Injection barrier | 0.5 eV |
| $\phi_B$ | Injection barrier for minority carriers | 2.2 eV |
| $\phi_B$ | Organic/organic interface barrier | 0.2 eV |
| $\mu$ | Mobility of majority carriers | $10^{-9}$ m$^2$/(Vs) |
| $\mu$ | Mobility of minority carriers | $10^{-10}$ m$^2$/(Vs) |
| $\mu$ | Thermal conductivity of organic | $1\ W/(mK)$ |
| $a$ | Intermolecular distance | $1\ nm$ |
| $\sigma$ | Disorder parameter | $55\ meV$ |
| $\rho$ | Material density | $2490\ kg/m^3$ |
| $c_p$ | Specific heat capacity | $800\ J/(kgK)$ |
| $\epsilon_r$ | Relative dielectric permittivity of organic materials | 3.5 |

Table 2.1: Default parameters, which were used in the simulation, if not stated otherwise

Mobility of minority carriers are normally hard to find, as every experimental study is overly concentrated on extracting only the mobilities of majority carriers. We just set it by one order of magnitude lower than the mobility of the majority carriers to ensure that even when minority charge carrier penetrate the organic/organic barrier, it is still hard for them to reach the opposite contact. Disorder parameter was set to that specific value after the investigation, which was performed in ch. 4. Specific heat capacity was taken from [193]. However, material density $\rho$ and specific heat capacity $c_p$ do not actually influence our results, despite being a parameter in the heat transport equation 2.42. The reason for this is that they come as the prefactor to the time derivative of temperature which is equal to 0 in the steady state, which we are interested in. As such, changing the material density and specific heat capacity is akin to changing the timestep in the heat transport equation, which in turn has no influence on the steady state until it converges.

# 3 Simulation results

Most of the results which were obtained and described in this chapter were published in the Journal of Applied Physics in 2019, with the preprint available at arxiv.org [146, 147] which were a joint effort of me and my co-supervisor Dr. Karin Zojer. In these papers I developed the topic, provided all the calculations shown and designed the figures. These papers were co-written by Karin Zojer and me. As these papers contain a number of usefully formulated explanations, I am using these formulations in section 3.1.3. These verbatim passages are marked accordingly with quotes.

In this chapter we will demonstrate the results obtained from the simulations. We will show how our modeling approach, established following all the steps outlined in the methodology section, can offer a description of physical phenomena that cannot be achieved with other modeling techniques and provides valuable insight into what is actually happening inside the OLED. In this chapter, the electrothermal coupling will always be present to demonstrate its strong influence on the device behavior. Later we will dedicate a separate chapter 4 to the comparison between experiment and modeling, where the electrothermal coupling will be off, however, temperature dependence still will be present. First, we describe findings in the theoretical part of our work and then, using the limited experimental data we got our hands on, we will look at the validity of the results presented here. It is worth to immediately note that most of the results, which were obtained in this chapter, qualitatively will not be changed by the conclusions of ch. 4. However, some of them can definitely be improved quantitatively and in ch. 4 we will describe exactly how.

## 3.1 Influence of thermal transport parameters on device temperature

One of the most important parameters which determine the device usability is the operating temperature. Generally speaking, there is a variety of different ways to assess device properties, for instance, via the external quantum efficiency, i.e., the relative amount of charge carriers which actually recombine radiatively, or via the number of available charge carriers for a given applied voltage, etc. As in OLEDs there exists a tight coupling between every phenomenon, it is impossible to find the "root" quantity that every other depends on. Under these circumstances, it is sensible to focus on familiar, experimentally measurable quantities, such as the device operating temperature. In this section, we will deliberately focus only on temperature and leave other parameters aside.

For that purpose, we will need to assume in this chapter that some of the device parameters, which could be influenced by temperature are fixed. We will take a very specific device structure which will be the same $\alpha - NPB$ / $Alq3$ layer composition that is shown in fig. 1.7. The layer thickness as well as the injection barriers at the contacts will not change throughout this investigation.

For the purpose of this section, our device is considered as 1-dimensional. When turning to a one-dimensional description, we can derive some analytic equations which can precisely describe the results.

### 3.1.1 Device parameters responsible for the temperature increase

First and foremost, we need to state which device parameters are responsible for heat dissipation. As in this section the device structure is fixed, we have only a few handles to change the device temperature.

- Applied bias: The larger is the applied bias, the higher is the electric current, which in turn is directly resposible for the heating of the device.
- Thermal conductivity $\kappa$ of the organic layers: It determines, how fast excess heating propagates to the device boundaries. Technically, $\kappa$ may be different for different organic layers. We set it equal in both layers, to comply with the device symmetrization, 2.8.
- Heat transfer coefficient $h$: It determines how fast excess heat can dissipate from the edge of the device to the ambient environment.

Without further altering the device structure, these are the only parameters that can play a role in the modeling of heat dissipation. We want to benchmark, which of the parameters are important and which are not. The voltage is a very distinct parameter. Compared to the other two, it can be readily altered over a very large range without any special treatment. However, in reality one wants to work with a *fixed* optimal bias, at which the device efficiency is maximized. Thus, we will look at fixed voltages and device temperature as a function of the two other parameters.

### 3.1.2 Maximum temperature as a function of thermal transport parameters

As we outlined above, we now investigate what happens with the device for a given voltage. To obtain simulation results the default parameters described in sec. 2.9 were used in this section. The only default parameter we will change for our purposes will be the thermal conductivity of the organic layers $\kappa$. To determine, which parameter values produce an elevated temperature, we performed the following preliminary analysis. We discretized the parameter space of $h$ and $\kappa$ with a coarse discretization grid such that parameters varied by two orders of magnitude. This was done under the applied bias value of 12 $V$, which was the highest experimental value of applied bias (the experimental part will come later in ch. 4). Heat transfer coefficient was discretized between $10^{-10}$ to $10^{10}$ $W/(m^2K)$, with thermal conductivity ranging between $10^{-5}$ to $10^5 W/mK$. With this approach, we obtained for most simulations a temperature increase that was either being negligible or the simulation diverged to $T = \infty$. In the first case, the heat outflow is just too efficient and there are no possible scenarios of how the given device heating can increase the temperature. Diverging temperatures occur due to the exponential dependence of the mobility on temperature. Too much generated heat, i.e. more heat is generated than the device can dissipate, causes overheating. Overall, we found that different combinations of the h-coefficient from $10^2 W/(m^2K)$ to $10^5 W/(m^2K)$ and the thermal conductivity ranging from $10^{-4} W/mK$

to $1 W/mK$ can result in noticeable, but not extreme temperature increase. Based on that, we discretized the corresponding parameters even finer, performed the simulations again in that region and from them extracted the maximum temperature value. Results for the $V = 14\ V$ can be seen in the right panel fig. 3.1.

This figure shows, how the maximum temperature depends on the thermal conductivity $\kappa$ and heat transfer coefficient $h$. As we expected, higher h-coefficient lowers the temperature in the device. When the value of heat transfer coefficient becomes smaller the temperature quickly increases, until the simulation does not converge anymore. What is more intriguing, the x-axis of the plot is in logarithmic scale to better capture the whole discretization region, therefore low values of h-coefficient correspond to smaller distance between the ticks. That means that the temperature actually ramps up in the low h-coefficient region even faster than one perceives from this plot. If the device temperature is already higher than the room temperature, a small change in the heat transfer coefficient (i.e., small changes in the ambient environment or the contact to the heat-absorbing surface) may quickly destroy the OLED.

We also see that different thermal conductivities have an overall impact on temperature, however, unless $\kappa$ reaches very low values of around $10^{-4} W/mK$, these changes are barely noticeable. High thermal conductivities definitely support the heat dissipation by decreasing the operating temperature, but they do not seem to be that important after the value of $10^{-3} W/mK$. This is best seen with the blue and black curves, which correspond to the values of $10^{-2}$ and $1 W/mK$ respectively, and which are exactly on top of each other. This is important, because realistic values of the thermal conductivity for organic layers are in the range of 0.1 - 10 $W/mK$ [193–195], hence never approaching the small value of $10^{-4} W/mK$. In essence, for a particular chosen device setup, there are absolutely no reason to differentiate between materials using the thermal conductivity, because any material will do the job. We will generalize this statement to other possible device setups later in the sec. 3.1.3, where we will derive an analytic approximation to the problem of the heat dissipation.

It is also useful to understand what is exactly different in organic semiconductors and why the mobility dependence on temperature plays such a huge role. To demonstrate that, we also performed some simulations without a temperature-dependent mobility, to emphasize the peculiar consequences for OLEDs it brings. The comparison between the two can be seen in the left panel of the fig. 3.1.

This plot gives us a clear idea of why temperature control became such a huge topic in organic semiconductors. When the mobility is temperature-dependent, the temperature ramps up more steeply and assumes systematically higher values for a given h-coefficient. We call this effect a vicious cycle: a higher temperature lead to a higher mobility, which in turn leads to a higher electric current, which will heat up device even more and further raise the temperature. If this cycle can be counterbalanced by the efficient heat outflow, the OLED can be stable, otherwise the thermal degradation will quickly destroy the device. It was suggested, that the elevated temperature could be beneficial for the device [131] as it increases the mobility of transport layers. However, with the data presented here we doubt that it is possible. Apparently, an elevated temperature in the device may stem only from the insufficient heat outflow; in such circumstances, the temperature becomes really unstable and a small changes of the h-coefficient may result in a burnout.

The behavior presented is preserved across a large voltage range. To begin, one can take a look at the fig. 3.2, which was obtained for 13 $V$ applied bias, which

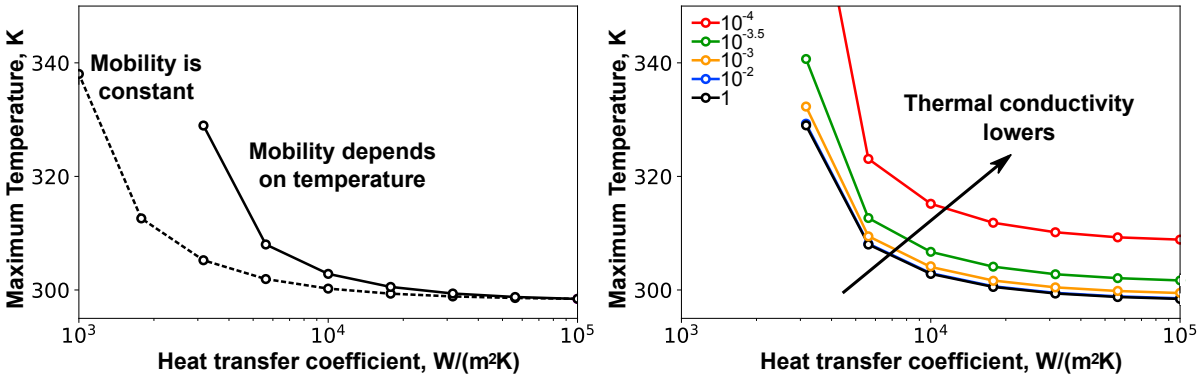


Figure 3.1: Maximum temperature as a function of heat transport coefficient for an applied bias of 14 $V$. (a) Solid line corresponds to different maximal device temperatures obtained for a temperature dependent mobility. The dotted line corresponds to a constant mobility. There are no more points for the solid line below $h = 3.16\ 10^3\ W/(m^2K)$ because maximum temperature in this region diverges when further decreasing the heat transfer coefficient. (b) Mobility dependent curves, where different colors correspond to the different thermal conductivities, value is given on the legend in $W/mK$. One can see previously described temperature skyrocketing if looks on the red line corresponding to thermal conductivity.

unsurprisingly shows the same behavior, as the voltage is nearly the same. However, this plot illustrates nicely the incredibly sharp temperature rise for a small change of the heat transfer coefficient $h$, approaching the value of 380 $K$ right after 320 $K$.

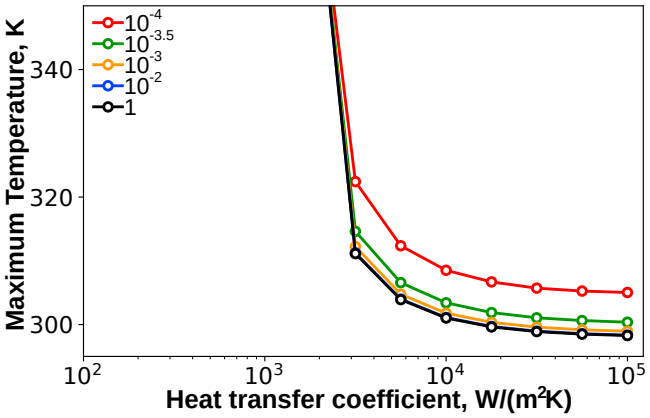


Figure 3.2: Maximal device temperatures as a function of heat transfer coefficient for an applied bias of 13$V$. Different colors correspond to the different thermal conductivities, value is given on the legend in $W/mK$.

Interestingly, the abrupt behavior of temperature vs h-coefficient is still in place when the values of applied bias are smaller. We found the range of voltages from six to nine Volts particularly intriguing, fig. 3.3. As we picked up the discretization range of the h-coefficient and the thermal conductivity to give substantial temperature elevations under applied bias of 12 $V$, there is no question why the curves corresponding to 6 $V$ are almost flat. We are certain, that lower values of the $h$-coefficient could still provoke the increase of the temperature. We are not doing that deliberately, as this figure serves as a nice starting point. At seven Volts we see already that the temperature rises at the value of h-coefficient $10^{2.5}W/m^2K$ and for the previous value of $10^2W/m^2K$ the

simulation already does not converge. At eight Volts nothing changes substantially and we just see an overall temperature increase. But with the final plot obtained for the value of $V = 9V$ we see again the enormous jump of the operating temperature at the value of heat transfer coefficient $h = 10^{2.5} W/m^2K$. We were lucky enough to get some very high temperature simulations, which were able to converge. The black curve, corresponding to the value of thermal conductivity $\kappa = 1 W/mK$ converged to $373K$.

This abrupt temperature increase is prompting us to think, that all non-converged points in this simulations are just belonging to the high temperature, and this is indeed the case. It is fairly easy to distinguish between the simulation which did not converge due to numerical instability and the one which did not converge due to high temperature. First one normally shows oscillating behavior before it diverges, while other simulations behave as it will converge until around 360 $K$ and then, without any oscillations it displays large temperature increase. The first type of divergence can be normally counterbalanced by a lower timestep, while the second one cannot. Later in this section, we will show the simulation behavior over time on a particularly intriguing simulation. It should convince the reader that we are indeed having the problems not with a numerical integration method, but rather with the fundamental device property.

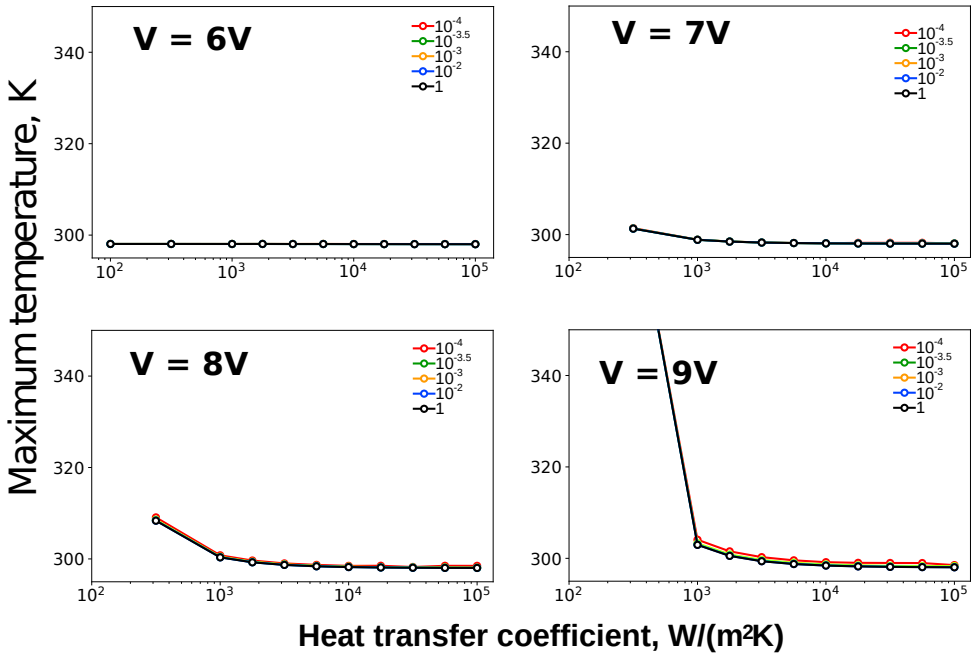


Figure 3.3: Maximal device temperatures as a function of heat transfer coefficient for an applied biases of $6 - 9V$. Different colors correspond to the varied thermal conductivities, value is given on the legend in $W/mK$.

We show the corresponding plots for the whole range of 1 $V$ to 15 $V$ in appendix sec. 6.

In fig. 3.4 we inspect what happens inside the device when the thermal conductivity changes and how the thermal conductivity influences the electric quantities and heat generation. We are particularly interested in thermal conductivity for two reasons. First, because low values of the thermal conductivity have a pronounced influence on how temperature is spatially distributed within the device. Second, it is possible to obtain distributions of several different quantities under the same driving voltage which is

much harder for the $h$-coefficient, whose influence is more substantial. Without having these distributions obtained for the same voltages, it is hard to decouple influences of different parameters.

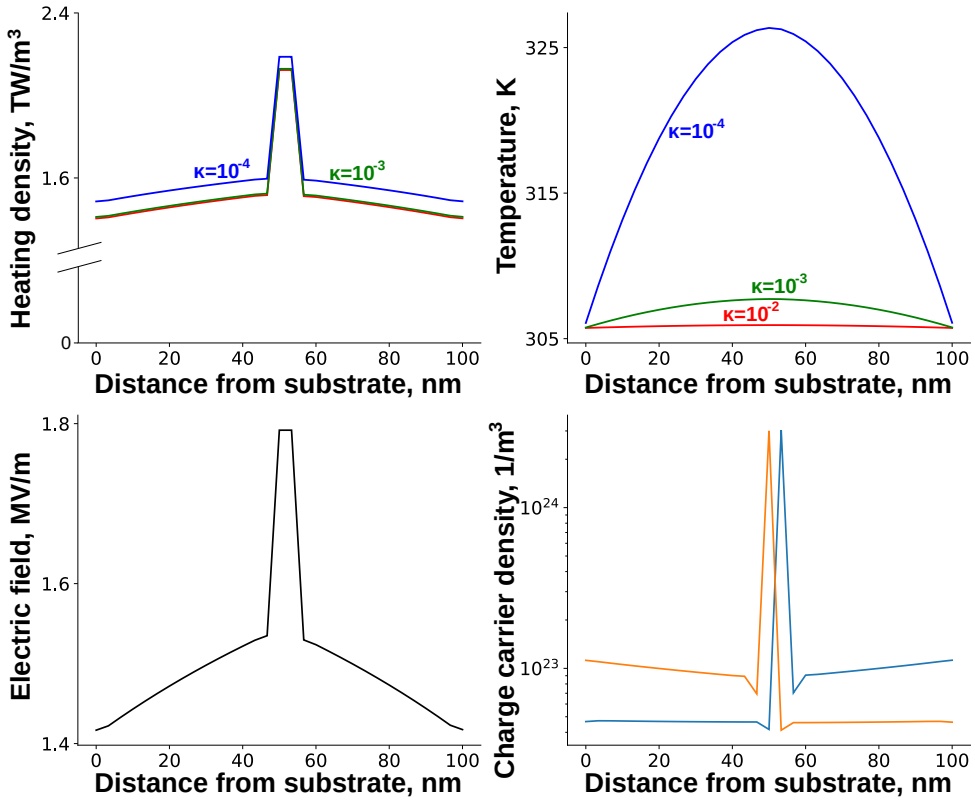


Figure 3.4: Distributions of heating density, temperature, electric field and charge carrier densities inside the device and their dependence on the thermal conductivity. Electric field and charge carrier densities do not change noticeably when thermal conductivity changes, so we show only one distribution for each. Plots were obtained under 13V applied bias. Thermal conductivities are given in the units of W/mK.

The first effect it has is the increase of the maximum temperature. It is caused by the increase of the temperature in the middle of the device, while the temperatures on the both edges are nearly the same (upper right panel). This in turn happens for two distinct reasons. The first and obvious one is that thermal conductivity directly influences the temperature distribution. However, the second reason is more interesting and, as one can see in the top-left panel, with changes of thermal conductivity there are overall changes in the heating profile. This changes are not very pronounced but still are present. This in turn happens due to (i) the electric field distribution and (ii) due to charge carriers distribution in the device. The electric field is lowest near the contacts and is elevated at the organic/organic interface (lower left panel). Due to charge carrier accumulation at the contact, the electric field there is lower than in the device. The large electric field at the interface is explained by the large charge carrier accumulation, present at the interface (lower right panel). As the Joule heating is proportional to the total current, which is constant across 1-dimensional device, and to the electric field, Joule heating density profile will change due to the local changes in the electric field. However, neither charge carrier distribution nor the electric field distribution in the device are not changing noticeably due to different thermal conductivities, that is why one cant see different thermal conductivity plots

for these distributions. The change in the heating density profile comes therefore from the recombination heating, which explicitly depends on the mobility value and the increase of current density.

As we mentioned previously, it is relatively complicated to find a voltage, under which a substantial temperature elevation occurs and, at the same time, $h$-coefficient can be varied. We found one voltage point $V = 10V$, which allows us to capture in the same plot five different heat transfer coefficient values from $10^3$ to $10^5 W/m^2K$ for the thermal conductivity value of $1W/mK$. However, this decision has its drawback, because temperature variations are not that large as in fig. 3.4 and, therefore, thermal effects are less pronounced. The thermal conductivity value of $1W/mK$ leads to constant temperature distribution within the device. However, the electric field and the carrier densities will change now, compared to fig. 3.4. To account for these changes, we separated carrier densities into two different plots and removed the temperature plot. The results one can see in fig. 3.5.

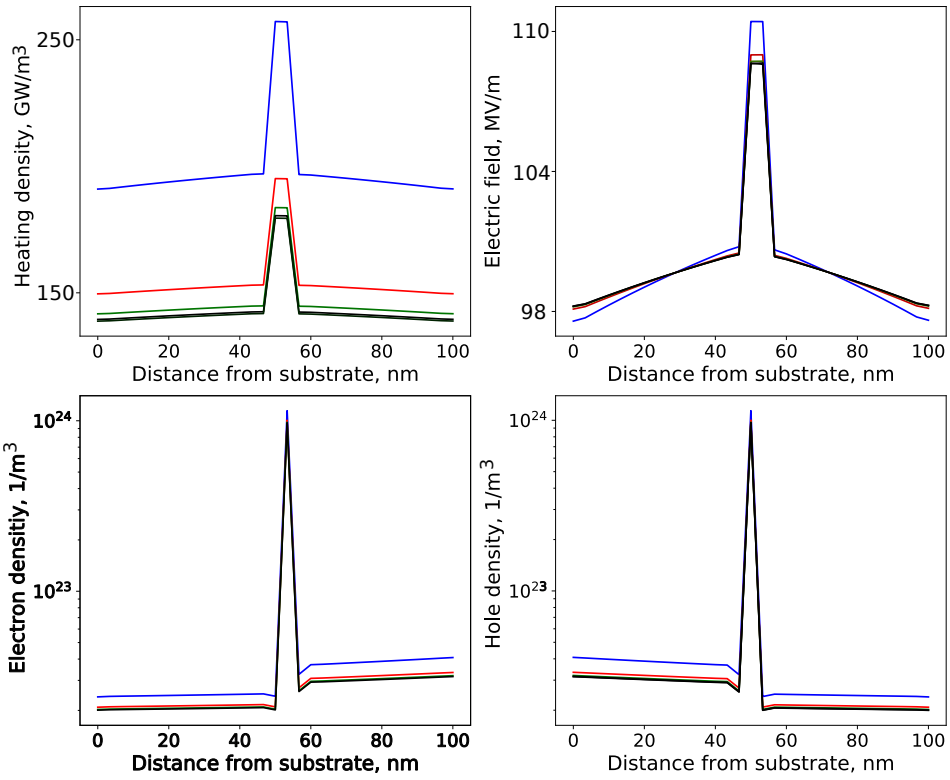


Figure 3.5: Distributions of heating density, electric field and charge carrier densities inside the device and their dependence on the $h$-coefficient. Plots were obtained under 10V applied bias. The two highest $h$-coefficient values, $10^{4.5}$ and $10^5 W/m^2K$ do not change the distributions noticeably and are on top of each other. Hence, they are both colored black. However, values from $10^4$ (green), $10^{3.5}$ (red) and $10^3$ $W/m^2K$ (blue) are actually introducing some changes in at least one of the plots, so they are color coded.

In the figure, $h$-coefficient value correspond to uniform temperature distribution across the device. Temperature values for heat transfer coefficient from low to high are equal: 308 $K$ (blue), 301 $K$ (red), 299 $K$ (green), 298 $K$ (black), 298 $K$ (black). We expect that the value of $h$-coefficient cannot directly influence the distributions and can only influence them via temperature increase. This explains why the two highest values of $h = 10^{4.5} W/m^2K$ and $h = 10^5 W/m^2K$, depicted black in the plots, are directly on

top of each other for every distribution. Nevertheless, we see that 10 $K$ temperature difference between lowest and highest values of heat transfer coefficient result in pronounced changes in heating. As in the case of thermal conductivity, this change must be directly related to the mobility increase, which would in turn result in the larger current and more recombination events. Hence, this is the clear manifestation of the vicious cycle, because the increase in the temperature results in the increase of heating density within the device (which will, of course, produce even larger temperature). The electric field distribution cannot display such pronounced change, because the electrostatic potential is fixed on the boundaries. Nevertheless, it deforms when the temperature increases, which is best seen for a small value of $h = 10^3 W/m^2K$. This deformation is in turn a result of the change in the carrier densities. We see that the elevated temperature results in the overall increase of carrier densities within the device. This happens due to the larger injection, which is in turned amplified by a larger mobility values, which prevent carrier accumulation on the interface.

#### Influence of the heat transfer coefficient on the current-voltage characteristics

To show how the operation changes with applied bias, we turn to inspect the current, as (i) current-voltage characteristics are easily accessible in the experiment and (ii) the current should be severely influenced by the device temperature. To minimize the influence of other quantities, we set the thermal conductivity to $1W/mK$, so that the temperature inside the device is constant. We control device cooling with the heat transfer coefficient $h$, fig. 3.6.

A small applied bias does not change the temperature at all (top panel). However, when the bias increases, the temperature starts rising and it ramps up very steeply close to some critical point. For higher voltages we were unable to obtain any current, as the simulations were diverging. The bottom panel demonstrates, how the current-voltage characteristics depend on the value of the heat transfer coefficient $h$. The higher $h$ is, the more efficient is the cooling. The flat temperature region from the top plot, therefore, corresponds to the part of the plot, where all the curves coincide. Afterward, the temperature starts its rapid elevation, which begins the later the better the cooling is. Thermal parameters can therefore straightforwardly influence the device performance and current-voltage characteristics, which are often considered determined only by electric properties.

#### Simulation convergence under large voltages

In this section we have mentioned several times the convergence issues. To illustrate them better, we picked one particular simulation with heat transfer coefficient $h = 10^{2.5} W/mK^2$, which perfectly serves this purpose. The simulation does not converge and its convergence ends when the temperature reaches the value $T = 380$ $K$, fig. 3.7.

On every panel of the figure, $x$-axis contains numbers of iterations and is presented on logarithmic scale. This is done to be able to capture the effects we are interested in over the large scale. Panel (A) shows the temperature evolution in the simulation as a function of the iteration number (the timestep of the simulation is constant, so it is equally fair to relate time and the iteration number). As we can see, the temperature steadily increases over the course of simulation until it reaches 380 $K$. The curve is smooth almost everywhere and experiences the abrupt changes in the

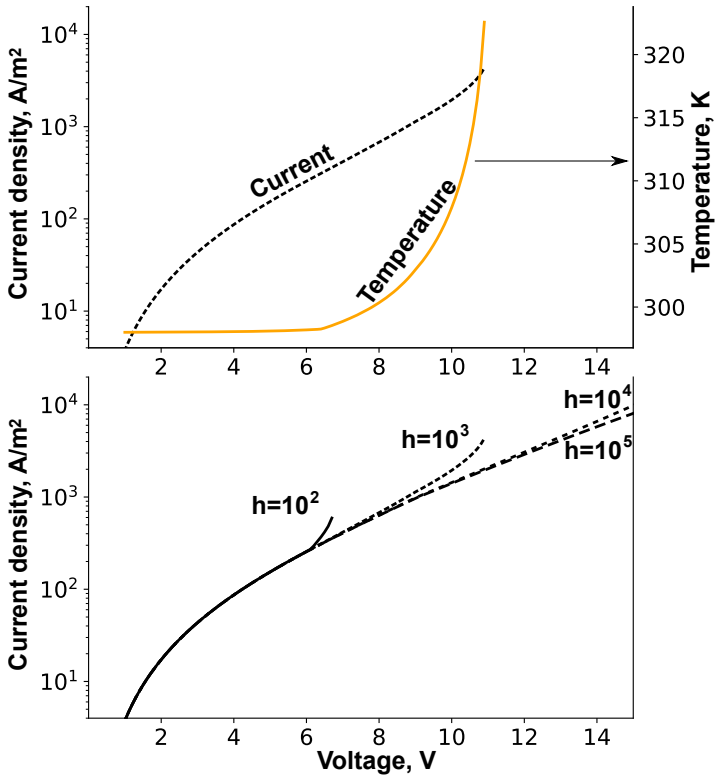


Figure 3.6: Current-voltage characteristics for different heat transfer coefficients. The top plot correspond to the current-voltage (black) and temperature-voltage (orange) characteristics for heat transfer coefficient equal $1000W/m^2K$. The bottom plot contains current-voltage curves for different heat trasfer coefficients.

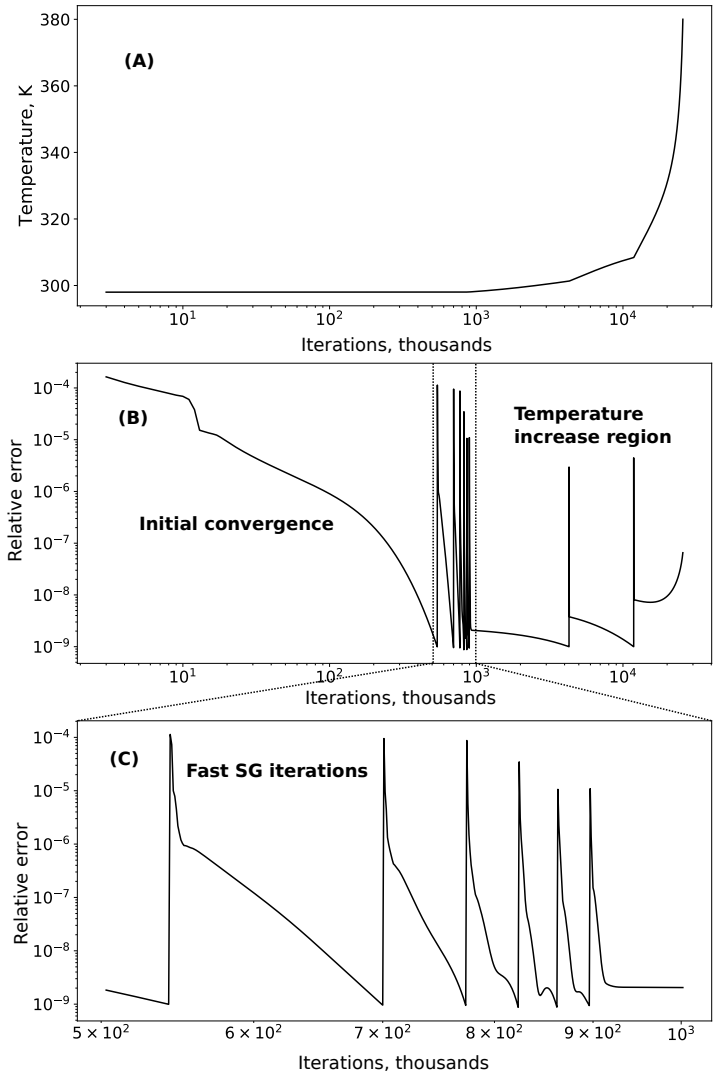


Figure 3.7: The behavior of the simulation which does not converge due to the high temperature value. On panel (A) we show the temperature evolution, on panel (B) the relative precision of the simulation (refer to the text for the explanation) and panel (C) expands the almost invisible but important region on panel (B).

derivative at several points. These points are located the voltage increment of the simulation, therefore, the heating at these points is abruptly increased. Panel (B) shows us the maximum relative error of the Scharfetter-Gummel iterations (for charge carrier densities). By relative we mean that we calculated the difference between the carrier densities at current and previous iteration at each point and took the maximum value of the resulting set. We see here clearly, that the plot can be divided in three separate regions. The first region of the initial convergence displays the continuous improvement of the precision. When it reaches the precision, which is required for simulation convergence ($10^{-9}$), the error bounces and rises again due to the voltage increment. Then, the error starts to oscillate very quickly. This happens because in this region the temperature is almost constant and the simulation is already preconverged. The size of this region is more or less the same, as the precovergence one. This results in the fast calculations for every next voltage value. To capture better this region, we also prepared the panel (C), where this region takes the whole plot scale and one can distinguish between the individual features better.

For anyone, familiar with the drift-diffusion simulations, these both regions must be familiar. However, in our case, these regions combined are actually a fairly small part of simulation. When the temperature changes noticeably, we see that the error of the simulation barely changes across many iterations. With every timestep, due to the increase of temperature, mobility changes and thus the parametrization of drift-diffusion equations 2.39 changes. In other words, we are trying to solve the equation with the iterative scheme, but the equation itself changes every iteration. Nevertheless, two more times the simulation is able to converge, albeit it requires 10 times more time to do so than for the whole preconvergence or oscillating regions. However, after the last change of voltage, this is not the case anymore and the temperature starts to grow steadily together with the relative error. It is hard to determine that the simulation had actually entered in this region, because the relative error may still drop for a lot of time until it rises.

Described here is actually the biggest problem we faced while working with this model. We were not able to find any parameter which could quickly determine whether simulation will or will not eventually converge. In the end, most of the computational time was wasted on simulations which would never converge.

### 3.1.3 Derivation of an analytic solution to the heat transport equation

We saw in fig. 3.2 that the thermal conductivity is practically irrelevant for the device temperature. In fact, "the thermal conductivity of the organic materials would contribute non-negligibly to the maximum temperature if the organic films were at least a factor of ten thicker." [147] However, to prove this for all possible values of thermal conductivity, heat transfer coefficients, and thicknesses, we will have to conduct a lot of simulations, covering all possible scenarios. This process will be extremely inefficient, particularly due to the large computation time of a single simulation for a given voltage point.

Therefore, to demonstrate the impact of the layer thicknesses, we derived several analytical equations, which approximate the simulations well and contain all the key quantities such as the charge transport parameters, the temperature, the layer thickness, the heat transfer coefficient $h$ and the thermal conductivity $\kappa$. It turns out

that our analytical solution also allows us to directly connect our methodology to experimentally measurable quantities.

To obtain an analytic relation, the task should be first formulated in a precise mathematical language. As we already know, the heat generation, due to the electric current distribution, is not constant in the device and varies from layer to layer and within the layers. In general, the generated heat density has a profile, which can be described across layer stacks by a function $Q(z)$, fig. 3.8. Note that we do not require the assumption of symmetric layer sequence here.

If we know the thermal conductivities of each layer, the heat equation can be straightforwardly solved using the Greens function $G(z, z_0)$ technique. Note that this is not quantum mechanical Green function, which corresponds to probability amplitude for particle to propagate from point $z_0$ to the point $z$. The Green function approach in the case of partial differential equations describes the reaction of PDE to the point-like source (heating in case of heat transport equation) and can be used to derive PDE reaction to any source distribution. The heat equation 2.42 considers

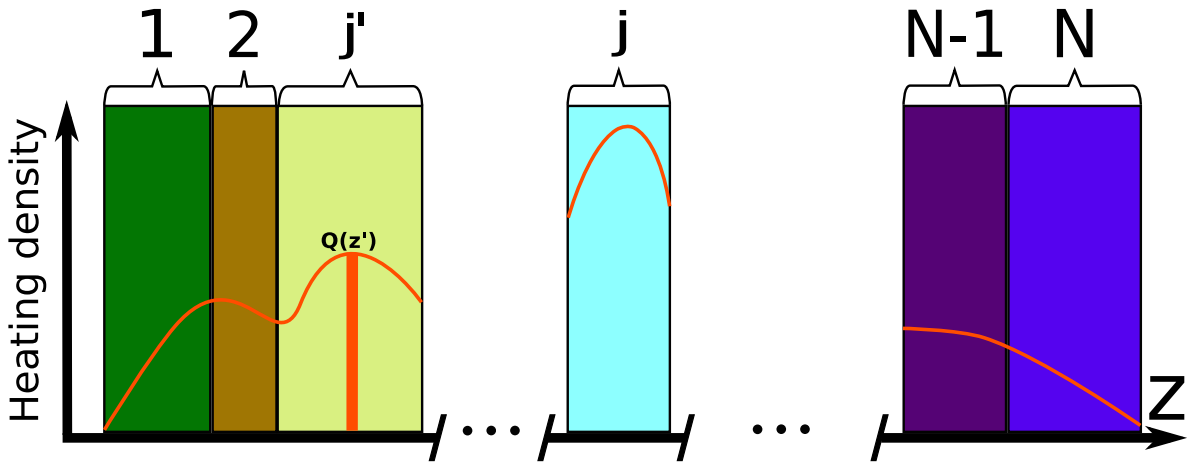


Figure 3.8: Layer description and profile of generated heat as used in the analytic solution. j correspond to the layer whose temperature we are interested in. j' corresponds to the layer, whose thermal contribution we would like to calculate. In the end we are interested in summing the contributions from each layer, i.e., final result should not depend on the "primed" layers.

a profile $Q(z)$ of generated heat and the profile of thermal conductivity within the device, $\kappa(z)$, i.e., each of the layers possesses its own thermal conductivity. Therefore, we can safely assume that $\kappa(z)$ must be piecewise constant, attaining the value of the thermal conductivity $\kappa(z) = \kappa_j$, when point $z$ belongs to the layer $j$. The general solution of the differential eq. 2.42 with these inputs is given by a Greens function $G(z, z_0)$ that fulfills eq. 3.1. The Green function in this particular scenario describes the contribution of the point $z_0$ to the temperature at point $z$.

$$-\frac{d}{dz}\left(\kappa(z)\frac{d}{dz}G_z(z, z_0)\right) = \delta(z - z_0) \tag{3.1}$$

If one multiplies eq. 3.1 by $Q(z_0)$ and integrates it with respect to $z_0$, one obtains the following equation:

$$-\frac{d}{dz}\left(\kappa(z)\frac{d}{dz}\left(\int_0^L dz_0 G(z, z_0)Q(z_0)\right)\right) = Q(z). \tag{3.2}$$

The term in the inner bracket of eq. 3.2 must be equal to $T(z)$ in the presence of the heat density distributed as $Q(z)$, because eq. 3.2 corresponds to the heat transfer equation. Of course, this also means that this term should satisfy the boundary conditions for the heat equation.

The integration of the piecewise constant function $\kappa(z)$ can be cast into the summation over the individual layers. After doing so and imposing the condition of heat flux preservation across the interfaces, one arrives at the following equation:

$$T(z) = \sum_{j'=1}^{N} \int_{z_{j'-1}}^{z_{j'}} Q(z_0) G(z, z_0) dz_0. \tag{3.3}$$

in which $z_{j'}$ is defined as $z_{j'} = \sum_{i=1}^{j'} L_i$ and $L_i$ refers to the thickness of the individual layers. The Greens function $G(z, z_0)$ can then be conveniently written using functions $W^L(z)$ and $W^R(z)$ for each layer $b$ :

$$W_b^L(z) = \frac{1}{h_L} + \sum_{i=1}^{b-1} \frac{L_i}{\kappa_i} + \frac{-\left(\sum_{i=1}^{b-1} L_i\right) + z}{\kappa_b} \tag{3.4a}$$

$$W_b^R(z) = \frac{1}{h_R} + \sum_{i=b+1}^{N} \frac{L_i}{\kappa_i} + \frac{\left(\sum_{i=1}^{b} L_i\right) - z}{\kappa_b}. \tag{3.4b}$$

With the help of $W_b^L(z)$ and $W_b^R(z)$ the Greens functions $G^L(z, z_0)$ for $z < z_0$ and $G^R(z, z_0)$ for $z > z_0$ read:

$$G_{j,j'}^L = \frac{1}{\sum_{i=1}^{N} \frac{L_i}{\kappa_i}} W_j^L(z) W_{j'}^R(z_0), \quad \text{for } z < z_0 \tag{3.5a}$$

$$G_{j,j'}^R = \frac{1}{\sum_{i=1}^{N} \frac{L_i}{\kappa_i}} W_j^R(z) W_{j'}^L(z_0), \quad \text{for } z > z_0. \tag{3.5b}$$

The index "$j$ and $z$ are the coordinates of the layer" [147] at which "the temperature is calculated, $j'$ and $z_0$ correspond to the layer from which one wants to calculate the contribution to the temperature, fig. 3.8. To obtain the temperature distribution in a certain layer $j$ at point $z$ for a given heat distribution $Q(z_0)$ according to eq. 3.3, one (i) integrates $Q(z_0)$ weighted with the corresponding Greens function $G_{j,j'}(z, z_0)$ with respect to $z_0$ and (ii) sums the contributions from all layers $j'$" [147].

Thus far, we were able to obtain the full analytic solution of $T(z)$ for a given $Q(z)$. However, to use these equations one should first have $Q(z)$, which in turn should be obtained from electrical simulations because $Q(z)$ can neither be measured or be approximated analytically in a straightforward manner. Yet a lot of information about how heat in the device is distributed is known from the numerical calculations, performed previously. Even though we do not know exactly, how the charge fluxes and recombination profiles are distributed, but we know their integrated values over the device from the conservation laws. If one assumes that every charge carrier which gets into the device recombines and if one can measure the current for a given voltage,

one can get the total Joule heating from eq. 2.59 and the recombination heating from eq. 2.60.

Then, the distribution of heat, i.e. the heat density $Q(z)$, can be roughly estimated. We know that the recombination happens mostly near the interface between the organic layers. We assume that all recombination happens there and consequently the heat density equals then $Q_{rec}(z) = Q_{rec}^{total} * \delta(z - z_{interface})$, i.e. a heat density profile of a rectangular shape with an extremely small width. In contrast, we assume that Joule heating is equally distributed across the device and equals constant $Q_{Joule}(z) = Q_{Joule}$ as indicated in fig. 3.9.

For the rectangular shapes of $Q(z)$ the analytic equations 3.5 obtain a simple form, because integration over constant values turns into a trivial multiplication of height and size of the corresponding rectangles, resulting in the total heat. Moreover, the analytic solution for $T(z)$ predicts the location of the maximum temperature at the organic/organic interface and the lowest temperatures are assumed on the outer layers of the device, such as substrate or encapsulation.

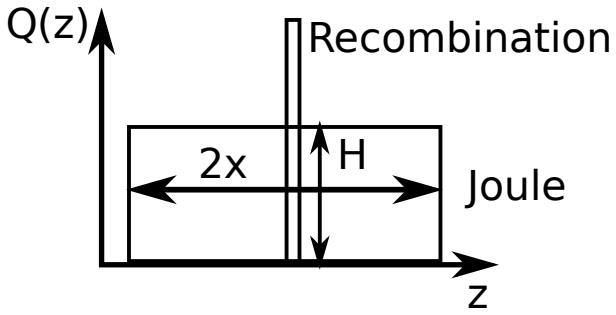


Figure 3.9: Assumed distributions of recombination and Joule heating.

After integrating both of the rectangular shapes, we arrive to eqs. 3.6a - 3.6b, where $H_{uni}$ stands for the height of the rectangle and $x$ is the half-width of the Joule heating profile.

$$T_{min} = xH_{\text{uni}} \frac{1}{h}, \tag{3.6a}$$

$$T_{max} = xH_{\text{uni}} \left( \frac{1}{h} + \frac{L - x}{2\kappa} \right). \tag{3.6b}$$

"Both temperatures are proportional to the total heat generated in the device, $2xH_{uni}$. The surface temperature $T_{min}$ is inversely proportional to $h$, but does not contain any dependence on the thermal conductivities of the electrically active layers. The temperature $T_{max}$ is determined by two terms, one being inversely proportional to $h$ and one being inversely proportional to the thermal conductivity $\kappa$. This second term conveys two important insights: First, the thermal conductivity influences $T_{max}$ less when the" [147] "generated heat density profile is more concentrated, i.e., the smaller the difference $L - x$ between the thickness $L$ of the layers and the halved extension $x$ of the heat density profile is. Second, even in a best-case estimation, in which we insert realistic values $L$ = 150 nm and $\kappa$ = 0.1 $W/mK$, $(L - x)/\kappa$ remains with $\leq$ 1.5 $W/mK$" [146] "at least an order of magnitude smaller than the $1/h$ contribution." [147]

"At this point, the irrelevance of the thermal conductivity $\kappa$ for thermal transport in realistically thin organic films has two important consequences. First, the actual bottleneck for heat dissipation is the combined thermal transfer between the contacts and the exterior, i.e., the thermal conductivities of layers being not electrically active and the associated heat transfer coefficients. Consequently, the layers that are responsible for electric transport are not relevantly involved in heat dissipation. This implies that the thermal and electrical properties can be optimized *independent* of each other in complementary regions of the device to reach the desired performance. Secondly, the temperature within the organic layers is uniform, i.e., $T(z) = T = \text{const.}$" [146] This stems from the fact that the thermal conductivity is responsible for the gradient of temperature and to say that thermal conductivity is too large for given heat flux is equivalent to the "gradient of temperature will be negligibly small". This finding is in line with e.g. [196], where authors found only a tiny drop in temperature across several organic layers.

Summing up our findings, we can safely put all terms containing thermal conductivity of electrically active layers to zero. Then, eq. 3.6a provides both the maximum and the minimum temperature. This, in turn, allows us to take a look on a more complicated nonsymmetrical case, when $h_L$ is not equal to $h_R$. This is a crucial generalization because real devices normally will be mounted on a substrate from one side while the other side (which emits light) will be in contact with air.

For that purpose, one can either repeat the previous derivations or derive the related equations in a more elegant way. A constant temperature $T$ can be related to the total amount of generated heat per unit area, $Q_{tot}$, via the heat balance equation $h_L T + h_R T = Q_{tot}$:

$$T = \frac{Q_{tot}}{h_L + h_R}. \tag{3.7}$$

Knowing the current voltage characteristics, $I(V)$, the Joule heat per unit area $S$, $Q_{Joule}$, is readily given by

$$Q_J = \frac{IV}{S}. \tag{3.8}$$

The recombination heat per unit area $S$, $Q_{\text{rec}}$, equals

$$Q_{\text{rec}} = \frac{(1-\eta_{\text{i}})IE_R(eV)}{S}. \tag{3.9}$$

Inserting eqs. 3.8,3.9 into eq. 3.7 for the maximum temperature, we arrive at:

$$h_L + h_R = \frac{V + (1-\eta_i)E_R\,(eV)}{T_{\text{max}}}\frac{I}{S}. \tag{3.10}$$

The right-hand side of equation eq. 3.10 does not contain any simulation-specific quantities and consists of "quantities which can be assessed by experiment. In contrast the left-hand side contains quantities that cannot be measured directly, but are crucial to describe the thermal behavior of the device.

We subjected this relation to a consistency check to reveal, whether we can safely exclude possible feedback from the heat transported through the encapsulation and substrate layers on the temperature inside the electrically active layers. To this aim, we compared the value $T_{\text{max}}$ extracted from the full simulation with the value obtained from eq. 3.10, in which we inserted only the current densities obtained from the

simulations. For a realistic thermal conductivity of 0.5 $W/mK$ with" [146] "a voltage of 14 V applied, we calculated $T_{\max}$ from eq. 3.10. eq. 3.10 reproduces the exact temperature values for a large range of heat transfer coefficients $h$; for $h_L + h_R \geq 10^4\ W/m^2K$ " [147] "the absolute error in predicted temperatures remains below 1 K. Moreover, the deviation in predicted temperature does not exceed 2.5 K even for the regions in which elevated temperatures close to overheating are encountered." [146]

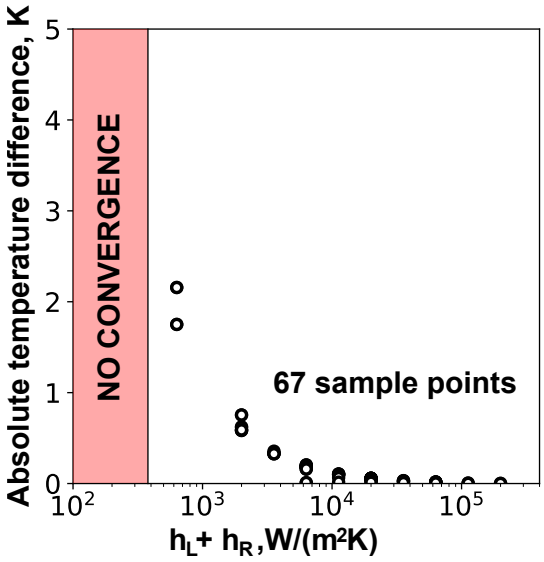


Figure 3.10: Comparison of temperatures predicted analytically by eq. 3.10 and the ones, obtained with simulations. For this comparison we used 67 different simulations with random heat transfer coefficients $h_L$ and $h_R$. Shown is the absolute difference between the fully simulated temperature and the temperature predicted by eq. 3.10 from the simulated current.

"As the results of our simulations are very close to the ones given by eq. 3.10, we think that the analytical expression can be used as a bridge between the experiment and complex multi-parameter drift-diffusion modeling." [146] The analytic equation (even considering all rough estimates we made) closely reproduces the simulation results. Moreover, all quantities on the right-hand side of eq. 3.10 are accessible through experiment and therefore, $h_L + h_R$ can be estimated for a particular experimental setup.

### 3.1.4 Relation between electrically non-active layers and heat transfer coefficient

There is another benefit of the equations presented above. The equations, presented in this section, can be obtained also from the general Green functions. We can take a look at the stack of electrically inactive layers located between organics and the ambient, in fig. 3.11 the left stack of layers. In the absence of heat generation, the value of the energy flux cannot change. Besides, in case of a one-dimensional energy transfer the heat flux is constant across the electrically inactive layers. These two assumptions lead to eq. 3.11.

$$(T_{i+1,i} - T_{i,i-1}) = \frac{L_i}{\kappa_i} \tag{3.11}$$

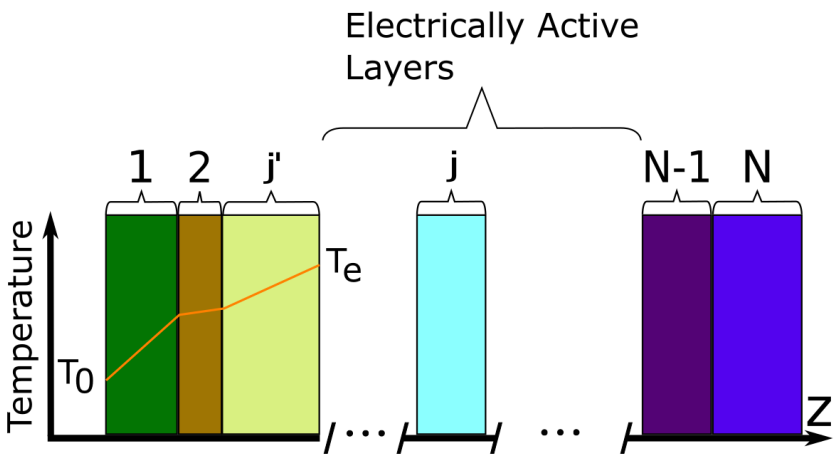


Figure 3.11: Temperature distribution between the border of electrically active layers and ambient environment.

According to this equation, the difference between the temperatures at the left and right interface of a layer is proportional to the layer thickness divided by the thermal conductivity, which is a straightforward result. Using the definitions from fig. 3.11, $T_0$ is the temperature on the interface between the ambient environment and the device and $T_e$ is the temperature on the interface between electrically active and non-active layers. The total temperature change $T_e - T_0$ across the stack of layers is the sum of all temperature differences in the individual layers. $T_0$ assumes the role of ambient temperature $T_{ambient}$ in the simulations. Therefore, to convert the heat transfer coefficient $h$, used in simulations to an $h_{eff}$, which assumes the electrically inactive layers as the environment we need to take their contributions into the account. Let $h_{real}$ be the heat transfer coefficient between the outermost layer and the ambient. By definition, $T_{ambient} - T_e = h_{real}\mathbf{j_{heat}}$ we can finally arrive to the eq. 3.12.

$$\frac{1}{h_{eff}} = \frac{1}{h_{real}} + \sum_{all\ layers} \frac{L_i}{\kappa_i} \tag{3.12}$$

This equation is very important for modeling for several reasons:

- The thermal impact of electrically inactive layers will manifest itself only in the change of the heat transfer coefficient from $h_{real}$ to $h_{eff}$.
- The effective heat transfer coefficient $h_{eff}$ can be easily calculated using known parameters, i.e. thermal conductivities of layers and their thicknesses, which are either fixed in experimental conditions or can be measured. In a worst case, their value can be approximated.
- The effective $h_{eff}$ enters our transport simulations and the analytical estimates eq. 3.6b. We can now straightforwardly relate it to the real heat transfer coefficient $h_{real}$.

Also note that from eq. 3.12 one can deduce which layers will influence this coefficient $h_{eff}$ most. Namely, metals, which have a large thermal conductivity [197], will have a tiny contribution to the corresponding heat transfer coefficient. Finally, this equation can be easily expanded to additionally include the heat trasfer coefficient between the individual layers if they are known:

$$\frac{1}{h_{eff}} = \frac{1}{h_{real}} + \sum_{all\ layers} \frac{L_i}{\kappa_i} + \sum_{all\ interfaces} \frac{1}{h_{interface}} \tag{3.13}$$

**Summary**

This section provides us with insights on the interplay between operating temperature and heat transport. First of all, we found that the thermal conductivity of the organic layers in OLEDs does not play a role in the device self-heating. Existing problems with self-heating must originate from the insufficient heat dissipation from the device to the environment. It also means that the temperature is almost constant across the electrically active organic layers in OLEDs, even when the heating is driving the device into burn-out. The absence of a temperature gradient is a major assumption in microscopic modeling approaches, such as Monte-Carlo. We think that this assumption is well justified. In ch. 4 we will assume a constant temperature in the active organic layers from the beginning.

Secondly, the thermal behavior of OLEDs can be predicted with analytical calculations without drift-diffusion modeling. Rather, drift-diffusion modeling takes fully into account the interplay between mobility, current and temperature. We did not test our analytical equations against the experiment due to the lack of suitable experimental data. However, we did our best to populate these equations only with quantities, which should be easily accessible under lab conditions. As these equations satisfy also modeling results, we hope that they can build a bridge between experiment and modeling for the thermal behavior of OLEDs.

## 3.2 Capabilities of the model: hot spot formation

Before the reader takes a look on this section, we want to warn him that simulations performed in this section did not account for the injection problems we mentioned in sec. 2.4.3 and for the organic/organic injection. This is because these simulations were done in the very beginning of the project and we never found a time to properly recalculate these slow-converging simulations, which would account to all the findings of ch. 3 and ch. 4. Initially, simulations in this section were obtained for the injection current values which were too high and this problem leads to the quantitatively wrong results. Large injection currents coupled with too small injection barrier between organic layers lead to e.g. an absence of charge carrier accumulation on organic/organic interface.

### 3.2.1 Results of three dimensional simulations with inhomogeneous potential distribution

We will inspect a 3D simulation of the two-layered device, which is symmetrized with the procedure presented in sec. 2.8, to highlight spatial effects related to hot spot formation. As will be shown below, our modeling approach allows us to readily incorporate plausible reasons for the hot spot formation and to predict and interpret the location of the spot. The parameters for simulations were picked according to sec. 2.9, except for thermal conductivity. As we have seen in the previous section, a

realistic thermal conductivity value would make the temperature distribution within the device almost constant. This is of course an obstacle if we want to actually see some temperature distribution within the device, hence, thermal conductivity value was picked equal to $10^{-3}W/mK$.

To provoke a hot spot, we assumed that there is a constant change in the voltage applied to the anode across the lateral dimensions $x$ and $y$, while the potential at the cathode remained constant and equal to $0V$, fig. 3.12. By that we tried to mimic the sheet resistance of the anode material. The sheet resistance of a good conductor, like silver, will not be noticeable on the scale of hundred nanometers. This means that the modeling in hands would be insufficient to capture hot spot formation. To circumvent that, the voltage drop we introduced was relatively large and unrealistic for the real OLED, $200mV$ over $50nm$.

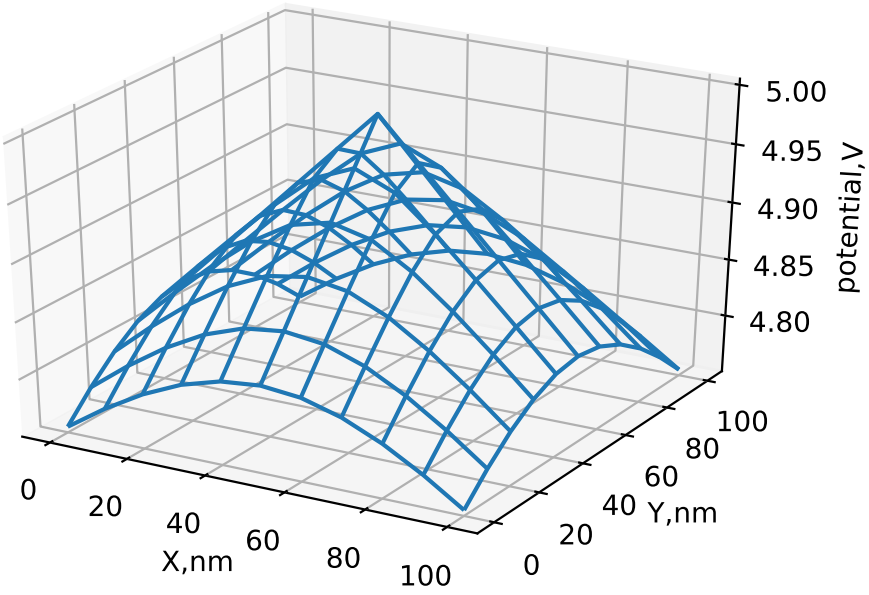


Figure 3.12: Spatial distribution of the potential applied to the anode of the device to mimic a hot spot.

Such an applied potential imposes an inhomogeneous driving field on the device because the opposite contact has a potential fixed to $0\ V$. This inhomogeneous field enhances the injection in the center of the anode and lowers it towards the edges of anode. Note that the voltage variance is relatively low (4%), however, as will be shown below, it results in a pronounced hot spot.

Before we inspect the consequences in the lateral direction, it is useful to consider the behavior in the perpendicular, $z$-direction. Even though we are particularly interested in effects that happen in lateral ($x$ and $y$) directions, these effects appear "on top" of what is happening in the perpendicular direction, because both are closely interrelated. In other words, current density across $z$ axis is the most prominent, while lateral changes of current are definitely lower in magnitude.

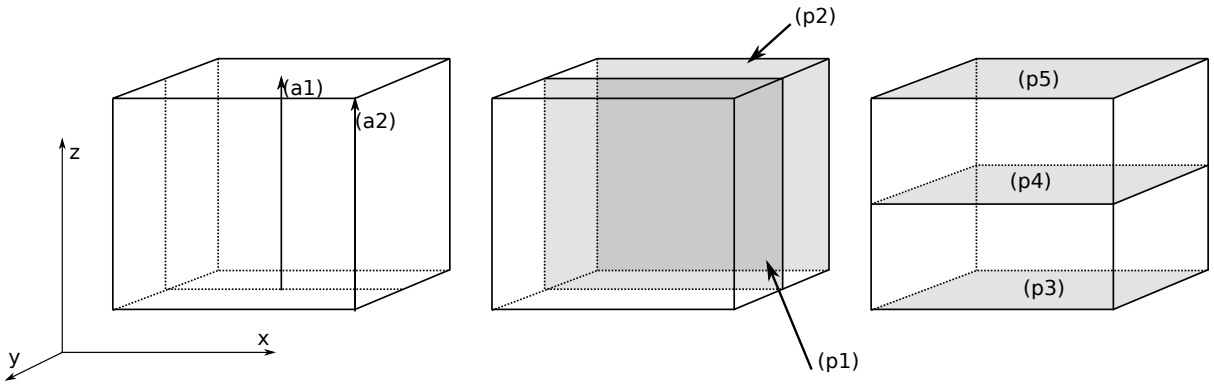


Figure 3.13: Schematic indication of selected axes, along which the most data in fig. 3.14 was plotted. The anode is located at the bottom, cathode at the top. (a1) and (a2) - the device axes, along which data in fig. 3.14 plotted. (p1) - (p5) correspond to the planes, which were used to prepare fig. 3.15 and fig. 3.16

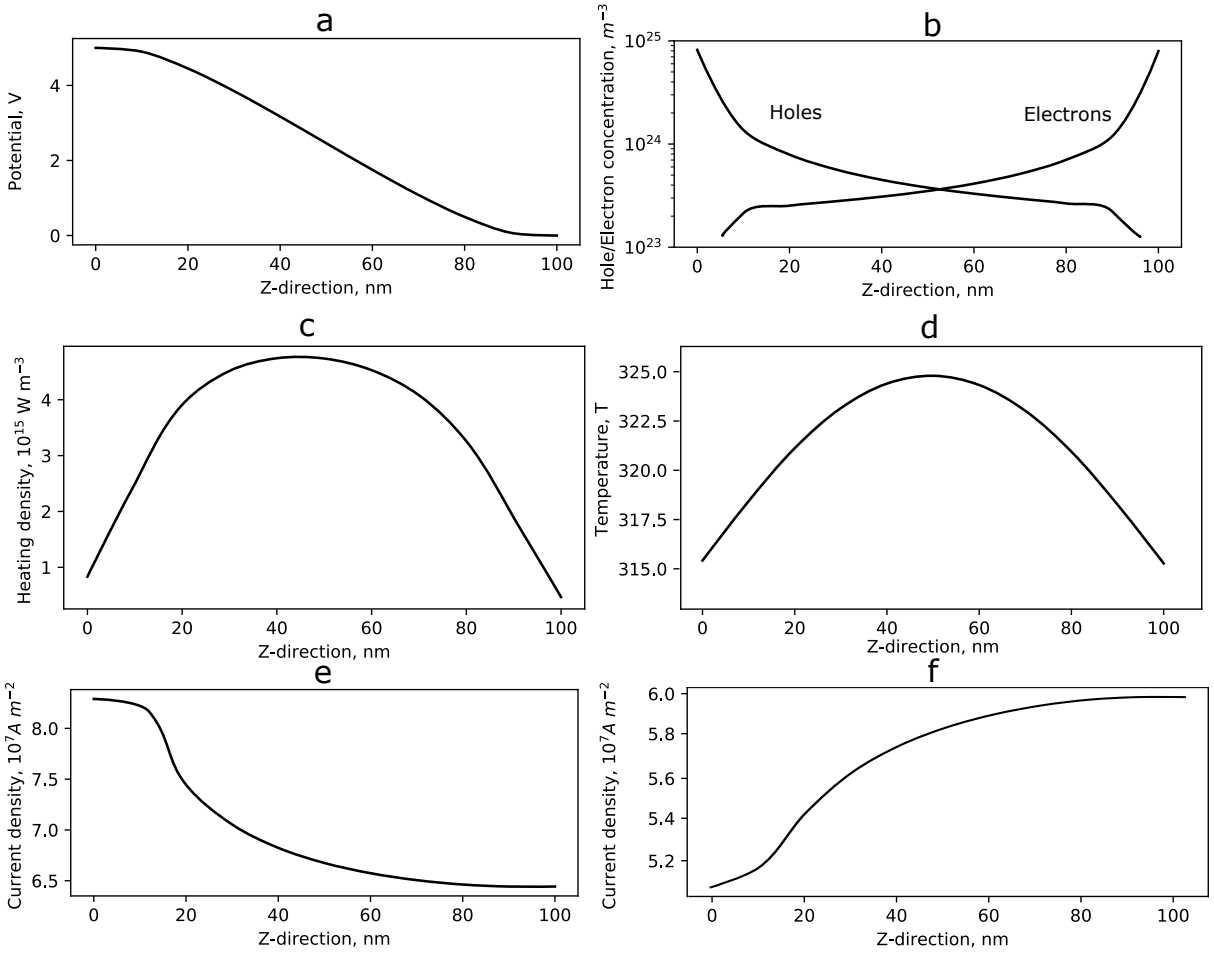


Figure 3.14: Distributions of several different quantities within the device along the z axis. (a) - distribution of the electrostatic potential (a1), (b) hole and electron concentrations (a1), (c) - distribution of heating within the device (a1) and (d) temperature distribution (a1). (e,f) current density in the direction of z-axis in the (e) middle of the device (a1) and (f) in the corner of the grid (a2), where its absolute value is minimal. $z$-axis is chosen according to the fig. 3.13.

On the panels (a) and (b) in fig. 3.14, the electrostatic potential and electron/hole concentrations are given along the central perpendicular axis (1) in fig. 3.13. The potential (a) flattens towards the contacts, where charge carrier accumulation, according to (b) occurs. This charge accumulation implies, that we have a bulk limited current flow inside the device. Also, upon taking a closer look, one can notice a slight asymmetry in the potential, despite the symmetrization procedure. This asymmetry stems from the non-uniformly applied voltage on one of the contacts.

On the panel (d) one can see the temperature distribution inside the device. The center of the device is substantially warmer than its borders. This can be related to two distinct reasons. First, the heating profile also reaches its maximum in the center, panel (c). The Joule heating is largest there due to the strongest electric field. The recombination heating is higher where more recombination events occur and naturally assumes its maximum at the HTL/ETL interface.

Secondly, the heat energy which is created by the electric current propagates towards the device edges to be dissipated into the ambient environment. The heat generated in the center travels the largest distance and establishes the largest temperature difference with respect to the Fourier law [1] (eq. 2.41).

The current density in the device center, in which the applied bias is largest, shown in the fig. 3.14-c, obtains its maximum at the anode ($z = 0$) and declines to the cathode. This lack of homogeneity in the current density implies that there are non-zero lateral components, fig. 3.16. Thus the current flow somewhere away from the center will have an opposite behavior, i.e. growing towards the cathode as seen in e.g. fig. 3.14-d, which depicts current along the axis (2).

To better capture the lateral patters emerging from the inhomogeneous voltage, we would like to take a look on the changes in temperature in the lateral dimensions also. However, we found a static 3-dimensional plots for both temperature and currents too hard to understand, hence we will restrict ourselves to the 2-dimensional temperature heatmaps, fig. 3.15, using the planes defined in fig. 3.13. Figure 3.15-a shows the temperature distribution within the $xz$ plane, located in the middle of the device, p1. It corresponds to the 3.14-d across $z$-axis and we see no lateral changes across $x$ axis. However, we know that there are some lateral changes which are hidden behind huge temperature variations across $z$-axis.

To circumvent this issue and have better view at the lateral temperature distribution we performed following trick; from each point ($x$,$y$,$z$) we substracted an average of the whole plane perpendicular to $z$-axis, which contains point (0,0,$z$). This way, large variations in $z$ directions are canceled by its average and one can see much better the lateral temperature distribution. The result of that one can see in fig. 3.15-b, which shows the same region as fig. 3.15-a, but now it is averaged instead of absolute. We can now clearly see that there are lateral variations of temperature of around $0.3K$. The hot spot visually is closer now to the anode, but this is just an artifact introduced by averaging. This hot spot just depicts where in the device the maximum lateral variations are located. Interestingly, the inhomogeneity of temperature distribution is lower close to the contact than in the center, because excess heat generated there can be dissipated from the anode side.

Figure 3.15-c shows the same distribution in the $xz$ plane, but located on one of the

[1] This is due to the fact that the Fourier law states, that the gradient of temperature is proportional to the heat flux. To get the temperature difference from the temperature gradient, one has to multiply it by distance, hence the result.

device surfaces, p2. We see that on the device surface, corresponding to the $y = 0\ nm$, lateral temperature inhomogeneity is substantially different from the center of OLED. First of all, the sign of temperature variation is different, which means that this device surface is colder than in the center. This is consistent with fig. 3.15-b, where device surfaces are located at $x = 0\ nm$ and $x = 100\ nm$ and are also colder than the device center, located at 50 $nm$. The same effect of smoothing the distribution is happening at the anode and the cathode due to the present heat outflow surface.

Finally, in the figures 3.15-d,e,f we plotted the temperature variations in the $xy$ plane for different $z$ values, where $z = 0\ nm$ in figure (d), $z = 50\ nm$ in figure (e) and $z = 100\ nm$ in figure (f), or p4-p6 respectively. The figures look similar, with the center of the device being the hottest and it becomes cooler closer towards the surfaces. However, there are substantial differences between them in the scale; the largest variations are located in the center, probably this is happening due to the highest value of absolute temperature there. The anode surface is more inhomogenios, due to the fact, that the voltage applied is varied on this surface. Finally, the cathode side seems to be the most homogenious, because it is located on the opposite side of anode and also correspond to the lowest absolute value of temperatures.

Finally, it is interesting to see what happens under these conditions with the electric current. Clearly, $z$-component of the electric current should be higher in the middle of the device, where the highest bias is applied. From the 3.14 we already know that injection in twice as low near the anode at the corner of the device compared to the center. This already implies, that there should also be non-zero lateral components of the electric current and, due to symmetry of the problem, they should also be symmetrical around a1, the same as the temperature distribution in the fig. 3.15. We are not therefore interested anymore in only lateral components, but also in the $z$-component. To demostrate it, we prepared the fig. 3.16.

In this figure, one can see the direction of the electric current in the p1 plane. Correspondingly, $x$ and $z$ components were used to prepare this quiver plot, so the directions of the main axes correspond to the direction of respective components. On the left hand side, one sees the plot, which was constructed with original scale of $x$ and $z$ axes. One can see, that there are almost no lateral distributions on electric current. This is caused by several problems; first of all, as in the case of temperature distributions, $z$-axis provides the highest variations of current, hence, it is hard to see anything in the lateral dimensions on these plots. Secondly, the simulation is 3-dimensional and the change in $z$-component must be accompanied by simultaneous changes of current components across 2 other axes. As simulation is set up simmetrically, the change of the $z$-component is equally distributed between the $x$ and $y$ components, further decreasing variations in the $x$-direction.

Luckily, quiver plot provides us with separate scale for $x$ and $z$ components, which again allow us to see the changes in $x$-component, the right hand side plot in fig. 3.16. We know that these small changes, when accumulated, provide us with a substantial difference in the current value as we have seen from fig. 3.14, so we are not hesitant to change a scale to see them. Intuitively, the plot makes complete sence as the large injected current in the middle of the device gets distributed to towards the borders. This large current in the middle is the source of the lateral distributions of temperatures we have seen in fig. 3.15. Current at the borders is still aligned vertically though - this is an artifact, as it happens because of periodic boundary conditions, imposed across the lateral dimensions.

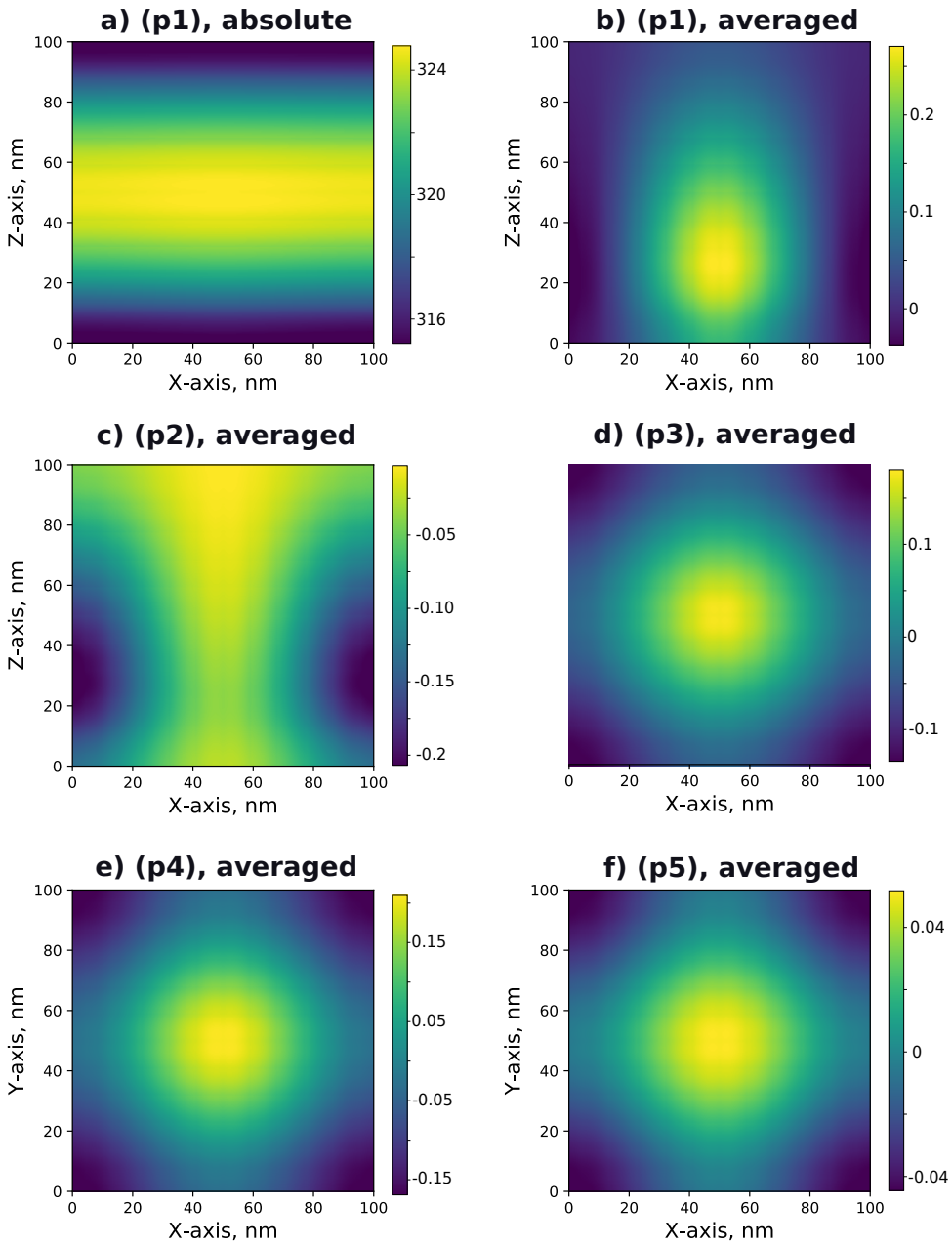


Figure 3.15: Temperature distributions across different planes in the device. Absolute means absolute temperature, averaged means that for each value $z$ the mean value of temperature across $xy$-axis was substracted to have a better look into lateral distributions. For descriptions, refer to the text.

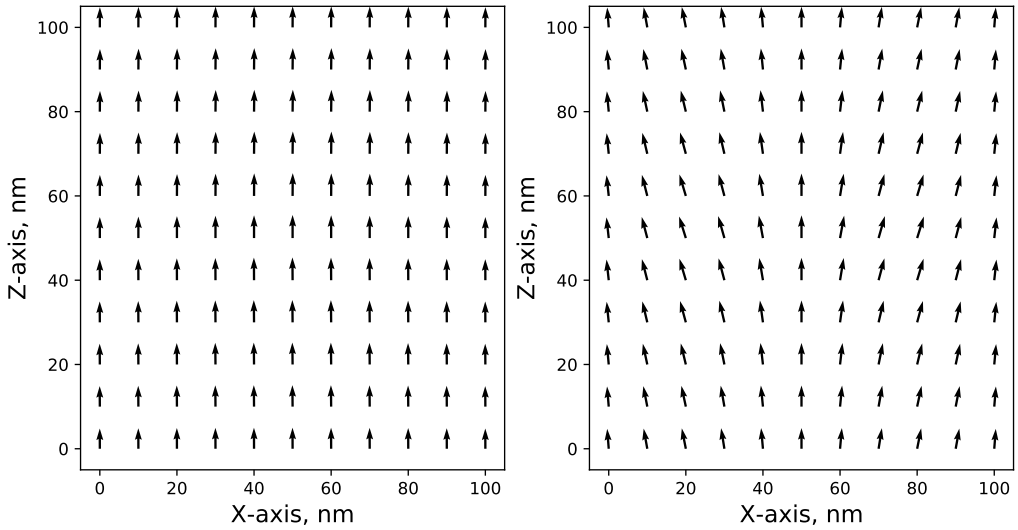


Figure 3.16: The direction of current flow, based on $x$ and $z$ components of the electric current in the p1-plane. Left plot depicts the direction of current with common component scale for $z$ and $x$ axes, the right plot has different scale, selected in such a way that $x$-component becomes more visible.

However, we did not yet discuss what can be the reasons for such an inhomogeneity in the lateral dimensions. For instance, when there is some deformation of the layer structure, which leads to a local decrease of the resistance. A larger electric current in the vicinity of the deformed structure will lead to an enhanced injection, and eventually, to the local bright spot. The elevated temperature in the hot spot according to the eq. 2.80 will locally enhance the mobility, which will even further improve the injection. 0.3 $K$ temperature elevation in that example happens on the scale of 100 nm, while real device lateral dimensions can be in the order of centimeters. If this trend would keep over the macroscopic device, the temperature difference on the scale of 1 $cm$ would then be equal to $0.3\ 10^{-2}/10^{-7} = 30000K$. Of course, it is not possible to reach this value, but this simple linearly extrapolated example shows the actual enormous magnitude of the effect.

### Summary

Summarizing this section, we can point out several important conclusions. First, we can see that a drift-diffusion approach is a capable candidate to theoretically describe hot spot formations. Even though we do not have a direct comparison to the experiment, we can see the utility of the method and how easy it is to get insight into what happens inside the transport layers. Again, we have to remind the reader, that the results presented here were not adjusted for the injections issues, which were found much later. They can only serve as a good starting point and an illustrative example how one can tackle the problem of hot spot formation within the drift-diffusion formalism. Quantitatively, these results are most probably wrong.

Secondly, one can see that rigid description of the hot spot would require a very precise understanding of (i) the injection current, as it will play a huge role at the hot

spot formation and (ii) the mobility of organic layers. When a hot spot is formed, the injection current in the middle of the device can take over injection current in the rest of the device, due to a substantial increase in the temperature, electric field and, hence, the mobility near the hot spot. It will be even more pronounced when the mobility is larger, as it will allow an easier redistribution of charges in lateral dimensions after injection. Despite the fact, that the model shows great results in simulating the hot spot formation, mobility and injection must be described rigorously to move from qualitatively to quantitatively correct results.

# 4 Comparison to the experimental results

In this chapter, we will switch from a purely theoretical description of the device to the comparison of modeling results with the experiments. We will see that the device can operate in several distinctively different operating regimes. Some of them can be described well with the modeling tools and these are located in the high voltage region. Contrary to that, we will see that simulations fail in the low voltage regime and, in particular, at the transition between the two. We were not able to provide a satisfying solution to these issues. We were able however to pinpoint their source.

## 4.1 Experimental results and drift-diffusion modeling

In this section, we will take a look at the device behavior when the temperature stays constant across the device. From the mathematical point of view this means that the heat transport equation does not evolve with time. Multiple parameters, such as injection currents eq. 2.45, eq. 2.49, mobility in eq. 2.80 still contain temperature as a parameter.

From the experiment, we had access to the current-voltage characteristics of a model OLED device. As current in the organic semiconductors depends also on temperature, it is useful to clearly distinguish between two types of OLED current-voltage characteristics. (i) When the device self-heating is present and elevates the total operating temperature and (ii) when self-heating is absent. The first case was realized in ch. 3. When the temperature is self-consistently coupled with the electric current, the current-voltage characteristics are influenced by temperature and vice-versa. That is, the current is uniquely determined by the applied bias $I(V)$. The second case can be realized either when the device is artificially cooled to maintain a certain temperature (its operating temperature is determined by that of cooling element), or when the device self-heating is negligible. Then its operating temperature is determined by the ambient. In this case, the current depends not only on the applied bias but also on temperature $I(V, T)$. This will be the case for the discussion in this chapter due to the presence of the Peltier element in the experimental setup. Peltier element was installed below the device layer stack fig. 1.3, so that the bottom silicon substrate was in contact with it. From the previous ch. 3 we know that with realistic thermal conductivities of organic layers, there will be no substantial temperature difference between the bulk of organic layers and the substrate, which has the temperature of the Peltier element. Therefore, when we are mentioning current-voltage characteristics in this section, keep in mind that we mean $I(V, T_0)$ characteristics under a fixed temperature of $T_0$.

Finally, before the reader takes a look at the results, we want to address in advance one of the problems which will appear in this chapter. In the figures, depicting a comparison between experimental and modeling results, one will notice striking

differences between the two. We felt the need to explain in advance what such inconsistencies mean, why they appear in this work, and why existing theoretical descriptions, for instance [63, 130, 140, 149, 151–153, 159, 163, 167, 198, 199], seem to perform a better job than we do. The reason behind is that our methodology was aimed at setting up a simulation, which depends on as few fitting parameters as possible. Due to the nature of fitting experimental data to some theoretical model, such parameters are often unreliable in case any of the underlying assumptions are not valid anymore.

The articles cited above manage to get a better correspondence mostly for one of three reasons: (i) They employ microscopic modeling techniques, such as Monte-Carlo studies, which are designed to perform better for hopping transport, but fail to describe large systems; (ii) they extensively use fitting of experimental curves to some non-fundamental physical values, that change from one setup to another and as such have dubious usability if one tries to draw general conclusions; (iii) they utilize equivalent electric circuits to describe the device behavior. Such models tend to change quickly, when the device structure changes. One can quickly identify inappropriate fitting parameters: Often, they can be extracted only from existing experimental data (current-voltage characteristics for our purpose) and there exists no robust way to get them from another experiment. In contrast, most of the parameters used in this thesis can be obtained via other techniques [1]. In essence, this decision allowed us to set up the simulation using a multitude of different device parameters, which do not need to come from the same study. The latter would be especially hard, because our simulations take into the account the effect of both thermal and electric phenomena. This decision restricted the freedom to tweak these parameters to achieve better correspondence between the model and the experiment.

### 4.1.1 Experimental results

Here, we present the experimental results obtained for an actually manufactured OLED with a surface area of 2.5mm x 2.5mm. The results that are published here were obtained by Florian Kolb and Dr. Roman Tratting from the Institute for Surface Technologies and Photonics of Johanneum Research in Weiz, Austria. The actual device and measurement setup was designed and manufactured by Dr. Manuel Auer-Berger. The OLED was manufactured with a layer setup as depicted in fig. 1.3-b, and was mounted on a Peltier element to control the device temperature during the experiment. That means that device temperature always corresponds to that of the Peltier element [2]

#### Experimental current-voltage characteristics

In the fig. 4.1, we present the experimental I-V characteristics for the manufactured OLED for different temperatures of the Peltier element. It is useful to immediately divide the presented current-voltage characteristics into three regions, which display

[1] For example, ultraviolet (UPS) and x-ray (XPS) photon spectroscopies give an access to energy level diagrams and density of states of different materials. From these in turn one can calculate or at least estimate the disorder parameter eq. 2.8 and the injection barrier eq. 2.49.

[2] Due to the investigation in chapter 3, we know that realistic thermal conductivities will never be a bottleneck for thermal transport.

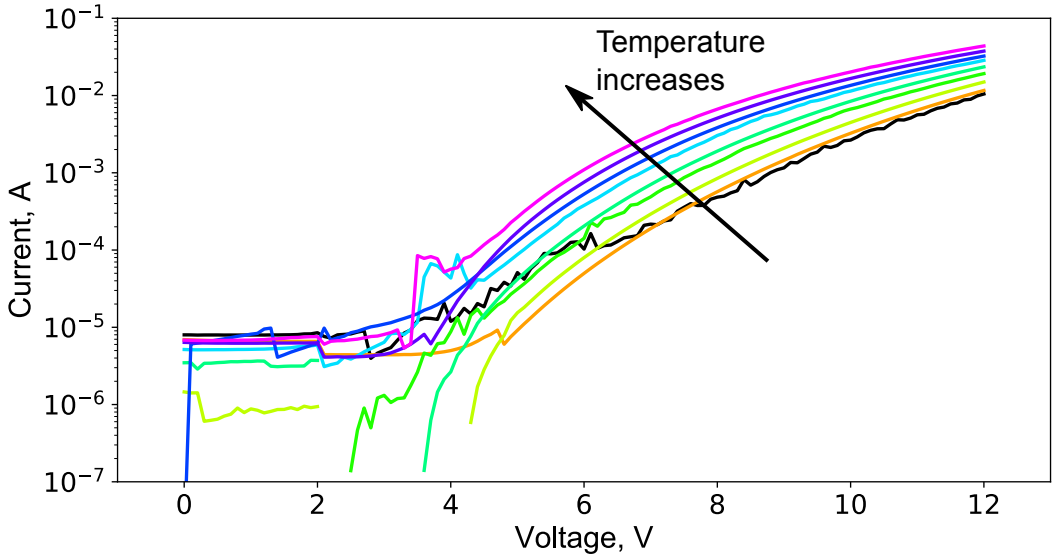


Figure 4.1: Experimentally obtained device I-V characteristics. Different colors correspond to different temperatures. Temperature ranges from 5°C to 85°C, with a step of 10°C, resulting in 9 different plots.

substantial differences in the device behavior. To illistrate that, we have chosen an experimental curve, corresponding to $T = 338\ K$, fig. 4.2.

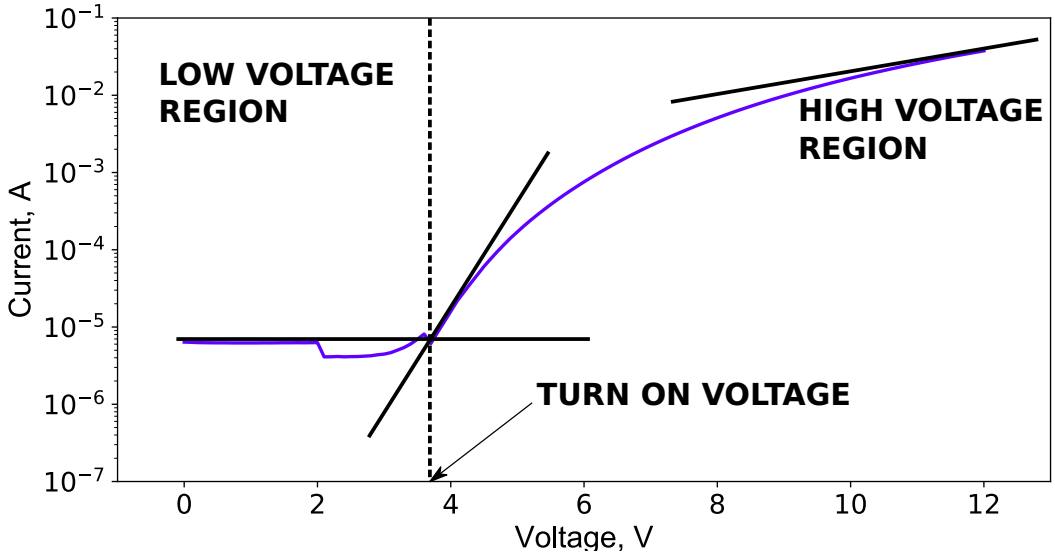


Figure 4.2: Three regions in experimental current-voltage characteristics: low voltage regime (lower than 4V), which is best described as a noisy constant current, and high voltage regime (larger than 8V), where current shows smooth subexponential behavior for every experimental curve. We will refer to the transition region between the two as a turn on region, which we call after turn on voltage, where the constant, low-voltage current abruptly starts to display exponential behavior.

We will give no strict definition where one region ends and another starts, and use

them mostly to aid the narration. However, it is important to note that similar behavior was observed also in variety of other different studies. For example, low voltage behavior is not specific to that experiment, and was observed also elsewhere [200]. The turn-on voltage and the high voltage behavior is also well known for such devices [201–207]. Turn on voltages are often found in the region in which the flat band condition is fulfilled, i.e. when the externally applied bias is sufficient to align the Fermi levels of the cathode and the anode to the same level [199]. In literature, one may also encounter different definitions of turn on voltage, such as when the device brightness becomes visible, or the point where the current becomes non-zero on the linear scale, as in fig. 4.3. As one can see, turn on voltage defined on linear scale is also located somewhere around 4 $V$, however it of course may change in the different plot scales. We think that its initial definition is the most unambiguous and we will stick to it. The apparently constant currents in the low voltage region are not an experimental artifact, as the source measuring unit provides reliable current measurements down to $10^{-9}A$. An elevated current even at zero bias is a clear indication of leakage currents in the system. Therefore, we should be careful not to associate the noisy constant current with our model predictions.

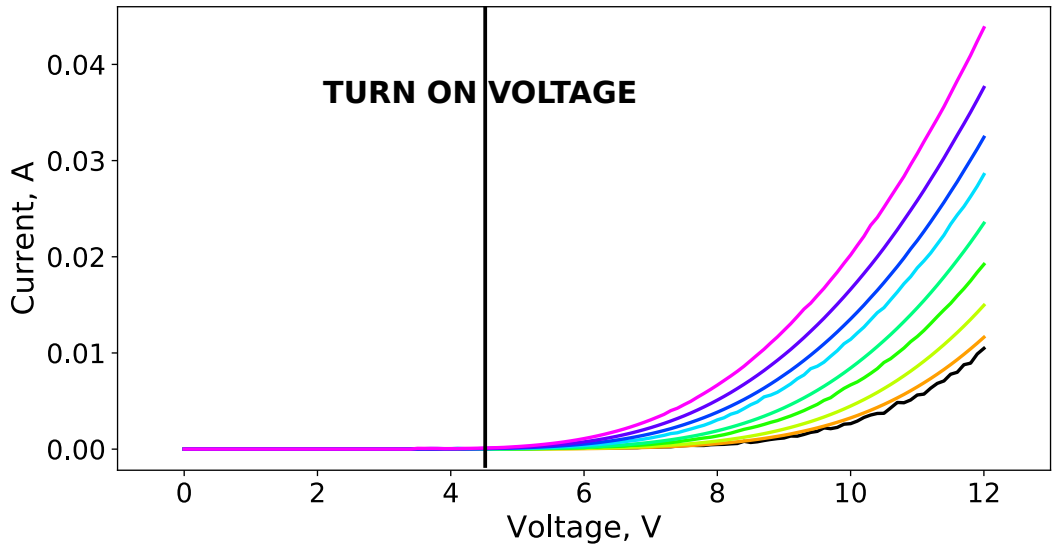


Figure 4.3: Experimentally obtained device I-V characteristics. Different colors correspond to different temperatures. Temperature range and color code is the same as in fig. 4.1

Considering the device thermal behavior, one can also see interesting trends. First of all, the lowest temperature curve (depicted in black), which corresponds to 5°C, has a behavior distinctively different from the other curves, in particular in the turn-on region. This will be useful, when we will try to exclude outliers from the data. The temperature behavior of curves in both fig. 4.1 and fig. 4.3 is very different between high and low voltage regimes. In high voltage regime, in particular at 12 $V$, one can clearly see the current increase due to temperature elevation. However, moving towards the low voltage, the curves start to intersect each other. The point obtained for the higher temperature does not necessarily appear above the lower temperature point. This is very important, because under no circumstances our model, in which current is always larger for elevated temperature, would be able to capture such a behavior

To see this behavior even better, we prepared a plot to observe the dependence of current as the function of temperature for different voltages, fig. 4.4. The curves are obtained from the same experimental data as in fig. 4.1. The curve associated with the low voltage regime (4V) shows an oscillating dependence on temperature. These oscillations stem from the noise, present at that voltage. For voltages larger than 6V we observe a relatively smooth exponential increase in current with temperature. It also seems that the difference between high and low temperatures are smaller for larger voltages on the logarithmic scale.

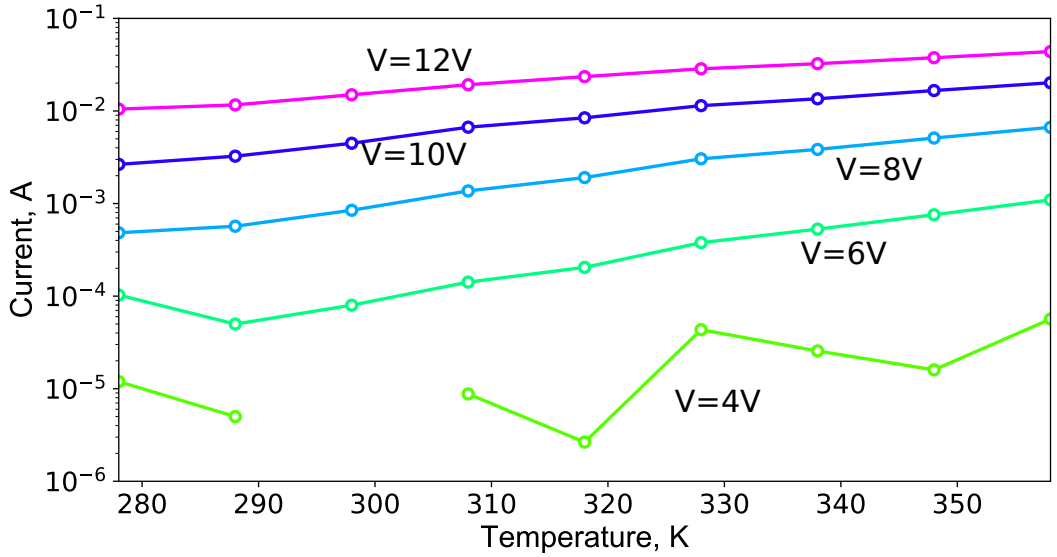


Figure 4.4: Experimentally obtained I-T characteristics. The data in this plot is the same as for the 4.1, but it was rearranged to demonstrate better the device temperature behavior. Different colors correspond to different voltages.

In our device model, multiple parameters depend on temperature. The impact of their temperature dependence is strongly related to the applied voltage. We expect a small current at low voltages and only small concentrations of charge carriers accumulated in the device. Contrary to that, the overall temperature dependence at high voltage should be the result of a complicated interplay between bulk and injection conductivities. Due to the complexity of the interplay and the quality of the measured data, the high voltage data is a particularly intriguing starting point for analyzing the impact of specific model parameters.

#### Influence of different constants on I-V characteristics

To explain the measured current-voltage and current-temperature relations, simulations with varying model parameters are performed. These simulations do not only indicate which parameters describe the behavior best, they also provide clues about how selected device parameters will affect the shape of I-V and I-T curves.

To design the necessary simulations, it is useful to first determine the parameters whose values can be safely tuned. A first parameter is the injection barrier $\phi_B$ from eq. 2.49 and eq. 2.45, related to metal/organic and organic/organic interfaces. A second parameter is the charge carrier density $N_0$ at the metal contact, which in our case

corresponds to the number of free charge carriers in silver in our case and has a well defined value [169]. However, due to the presence of the additional layers between the contacts and the transport layers, this parameter is can be safely tuned.

The equation for the mobility (eq. 2.80) yields further degrees of freedom. There are three parameters to note here: the distances between hopping sites in the OSC, $a$, the mobility prefactor, $\mu_0$, and the disorder parameter, $\sigma$. The distance $a$ cannot profoundly change, as the material density does not markedly change among organic semiconductors for. The mobility [3] cannot be directly measured in experiment and has to be extracted from the comparison of some device model to the experimental I-V curves [4]. The inconsistencies of mobility measurements mentioned in sec. 2.7 give us some freedom to change parametrization without contradicting experimental values.

Therefore, we have four different parameters to tune the electronic properties of the device. Discretization of the whole 4-parameter space to find the parameters which best fit the experimental data is not practically possible, due to the sheer amount of computation time required. Rather, we prioritized the parameters and focused on particular features of experimental curves which should be captured best. Out of all parameters, the disorder parameter has the highest priority, as it profoundly influences both the thermal and electrical behavior of the device. It will govern the changes between curves that correspond to different temperatures.

The most interesting feature of experimental curves to capture with the model is the high voltage behavior. In ch. 3 we applied very high bias (up to 15 $V$) in the model. Self consistent models should, hence, very well capture the behavior in the high voltage regime. We will see in this chapter that the disorder parameter indeed has a profound influence on the high voltage regime, especially when the temperature dependence is considered. The next feature to look at would be the turn on voltage. As mentioned before, it is common among different OLED setups and is easily quantifiable by the actual value of applied bias where the turn on occurs. The disorder parameter might be also relevant here, as it is responsible for the rate of exponential increase in mobility with an applied electric field (which happens only after certain offset $E_{critical}$). Only if the first two experimental features can be successfully addressed in simulations, it will be worthwhile to investigate the low-voltage behavior.

Based on these considerations, we first address the disorder parameter. In sec. 4.3, we will then discuss how the mobility prefactor $\mu_0$, the injection barrier $\phi_B$ and the charge carrier density in the metal contact, $N_0$, influence the I-V characteristics.

## 4.2 Influence of the disorder parameter on the device behavior

The disorder parameter within our model can vary between $50 - 125meV$. Disorder parameters of less than $50meV$ cannot be captured within our mobility model [159] so

[3] In our, model mobility depends both on temperature, carrier density and electric field. However, for the room temperature, low electric field, and low carrier density, mobility is completely determined by the mobility prefactor $mu_0$, and it corresponds to the experimentally measured mobility $\mu$. To avoid references to the mobility prefactor $\mu_0$, which does not have any physical meaning, we will only talk about the experimental value $\mu$, from which one can uniquely determine $\mu_0$

[4] this is not strictly true for instance in case of time-of-flight experiments, however, it does not account for charge carrier densities

that we are not able to investigate this region. Large disorder parameters $> 125\ meV$ make mobility extremely susceptible to the electric field and charge carrier densities and simulations experience a hard time to converge. We discretize $\sigma$ in this range with the steps as low as 5 $meV$ in the region from 50 to $75meV$ with a coarser discretization $7.5meV$ between 75 and $125meV$. Temperatures are set to the experimental values, i.e. they range from 278K to 378K with a step of 10K, resulting in 9 different temperatures. The voltage range extends from 0V to 12V in the experiment and from 0V to 14V in modeling (to capture also the voltage range from ch. 3). The total current is obtained by a multiplication of the current density with the total device area of $2.25\ cm\ x\ 2.25\ cm$.

One can intuitively understand that a high disorder should decrease the mobility value, and this is indeed the case for the mobility eq. 2.8. To keep the low field, low density, room temperature mobility the same across all modeling curves for different disorder parameters, it was therefore necessary to tune the mobility prefactor $\mu_0$.

As a reference we first present the simulated current-voltage curves obtained with the lowest possible disorder parameter $\sigma = 50meV$ in fig 4.5 and compare them qualitatively with the experiment. Note that all the figures we present in this section are plotted on the same scales for both axes, independent of temperature. First, we see that the simulations tend to drastically overestimate the current values in the low-voltage region $V < 4\ V$ by an one order of magnitude. Interestingly, the experimental low-voltage characteristics seem to be independent of temperature, while the simulated curves shift to the higher current values, when the temperature increases. In the high voltage region, where the applied bias is higher than $10\ V$, the simulations tend to converge to the experimental results, especially for moderate temperatures, $298\ K - 328\ K$. The problems in fitting the low voltage regime appear almost in any study, which is not explicitly aimed at this region [198]. However, we expect the simulated values in the high voltage region to be reasonably close to the experimental ones. This is considered to be a good sign. We think that they are closest for moderate temperature values, because most model parameters were measured at room temperature and might actually possess a temperature dependence which is not accounted for in the model.

On top of that, one observes a turn on region between the high and low voltages, where the experimental results quickly catch up in value with the modeling. The modeling curves however do not show any sign of current drop at these voltages and are rather very smooth. The first point of the modeling curves, which is located at $V = 1\ V$, already has a current that is substantially larger than the experimental one. From this point, the slope of the simulated curves only becomes more and more gradual, prompting us to think that the turn on voltage in the modeling results is located around $0\ V$. This could also explain the difference in temperature behavior in the low voltage region. The experimental curves do not show a pronounced temperature dependence in the low voltage region, but display it towards higher voltages. If the simulated curves are all located in the high voltage region, they will display temperature dependence at any operating point. Finally, note that the drift-diffusion simulations are a bad candidate to capture a sharp transition in the turn on region, unless there is a profound rapid change in a model parameter (such as injection or mobility parameters).

Despite the abscense of turn on voltage on the presented plots, we want to remind the reader that different definition of turn on voltage may lead to different results. To be concise, we want to show here also the same plots on the linear scale fig. 4.6.

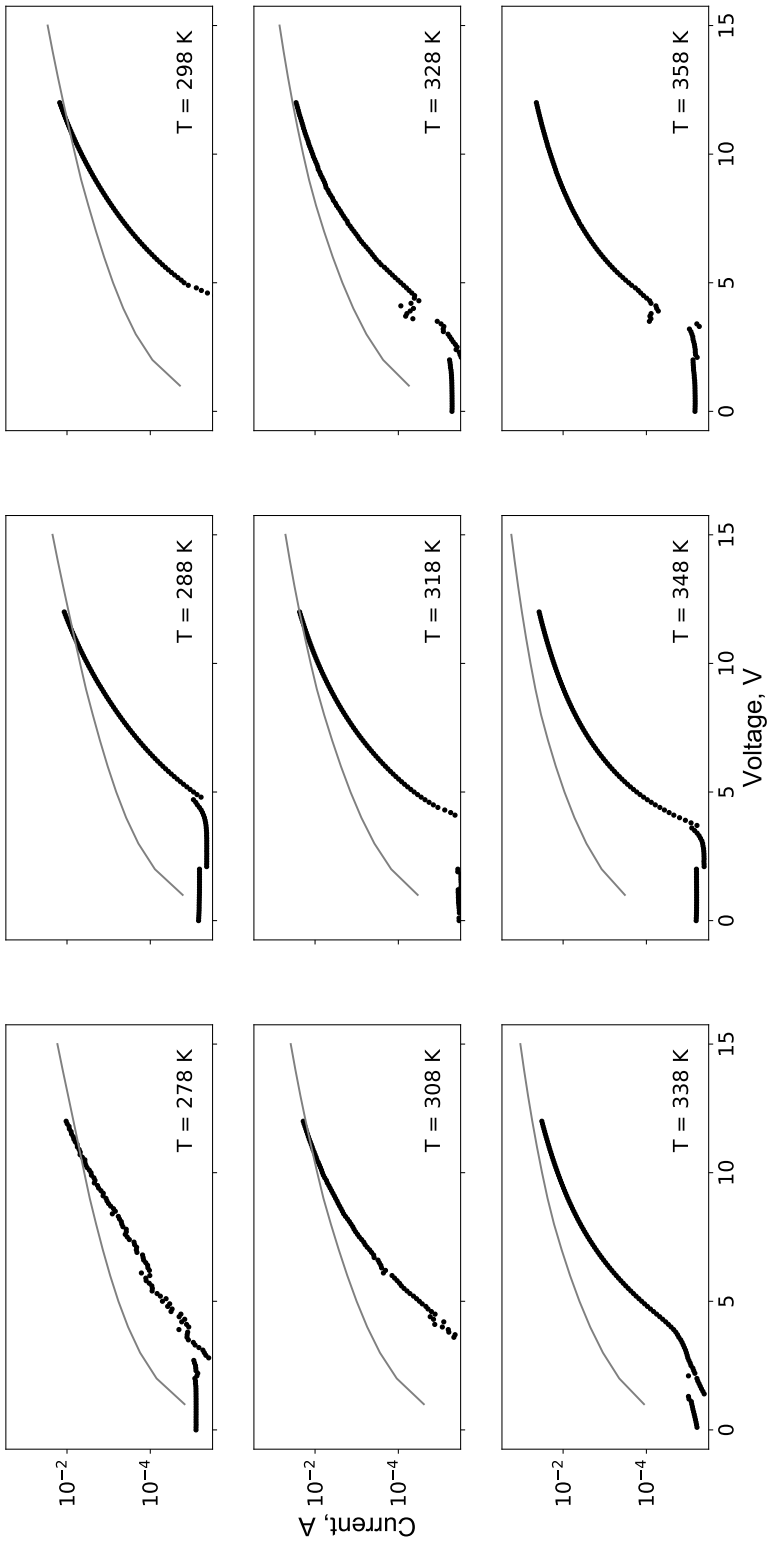


Figure 4.5: Current-voltage characteristics for manufactured OLEDs at different temperatures. Solid lines correspond to the modeling results for the value of the disorder parameter equal $50meV$ and dots correspond to experimental results. The last plot does not contain modeling results, because for this temperature and the chosen small disorder parameter, the mobility model fails. The mobility model does not fail for the disorder parameters higher than $50meV$ and temperature less than $358\ K$.

Linear plots, while hiding the bad behavior of the current-voltage characteristics in the low voltage region due to exponential growth, also show that there are substantial differences between the modeled and experimental curves, especially under high temperatures. However, it seems that this difference stems from the fact, that the experimental curves experience more abrupt change in the turn on region, i.e. the same problem which was already described for the logarithmic scale.

To develop more intuitive understanding of the effect of the disorder parameter on the current, in fig. 4.7 we present another set of superimposed experimental and modeling data, this time for the highest disorder parameter in this investigation, $\sigma = 125\ meV$.

The bottom scale of the y-axis in these plots has remained unchanged, as the values of experimental currents are the lowest, however the maximum is higher due to overall range of values covered by the modeling curves. This increase of the scale might bring data closer visually, but every single modeling curve is now actually more distant from the experimental values as will be demonstrated in the next section. We see that for the lowest temperature $T = 278\ K$ the modeling curve in on the same level as the experimental one in the high voltage region, as opposed to fig 4.5, where the experimental results were higher. However, for any temperature value above that, the modeled current values are substantially larger than experimental ones also in the highest voltages applied in the experiments. One can clearly see that this disorder parameter is just too high to be able to describe the experimental data. Also, note that despite the unfortunate absence of the modeled curve under $T = 358\ K$ both in fig. 4.5 and fig. 4.7, simulation actually does not have a problem converging there for any other value of the disorder parameter (cf. collection in the appendix). One can also see the same behavior on the linear scale plot 4.8.

Finally, to strengthen the understanding of the influence of the disorder parameter on the current-voltage characteristics, we present a plot, which contains all the modeled curves obtained under the different disorder parameter values, fig. 4.9.

The curves in this plot were taken for the temperature value of 308 $K$, very close to the room temperature at which most model parameters were obtained. Note that there are no convergence problem for any value of the disorder parameter and the whole discretization region is covered. Also, the discretization step changes at 75 $meV$ and this explains different distances between the bottom and top curves.

First of all, this figure clearly shows that the disorder parameter influence is higher for the larger voltages. This was expected, as its influence on the mobility grows for higher electric fields and charge carrier densities [159]. Secondly, we see that distances between the curves on logarithmic scale are almost equal, the only discrepancy happens where the discretization step changes. That means that the disorder parameter inroduces an easily predictable and controllable changes of the device current-voltage characteristics. The disorder parameter also changes the slope of the curves, which is steeper for higher voltages. This is also useful, as in fig. 4.5 we see that the slope of the modeled curves differs from the experimental one, especially at low temperatures. A proper choice of the disorder parameter might help us to remove this inconsistency.

A coarse screening of all other $\sigma$ values (c.f. collection in the appendix) reveals that changes in the disorder parameter affect the behavior of the curves, but it is not being able to fit either low-voltage behavior or capture turn on behavior. To quantitatively assess model results in the high voltage regions, we first need the methodology to compare model and experiment.

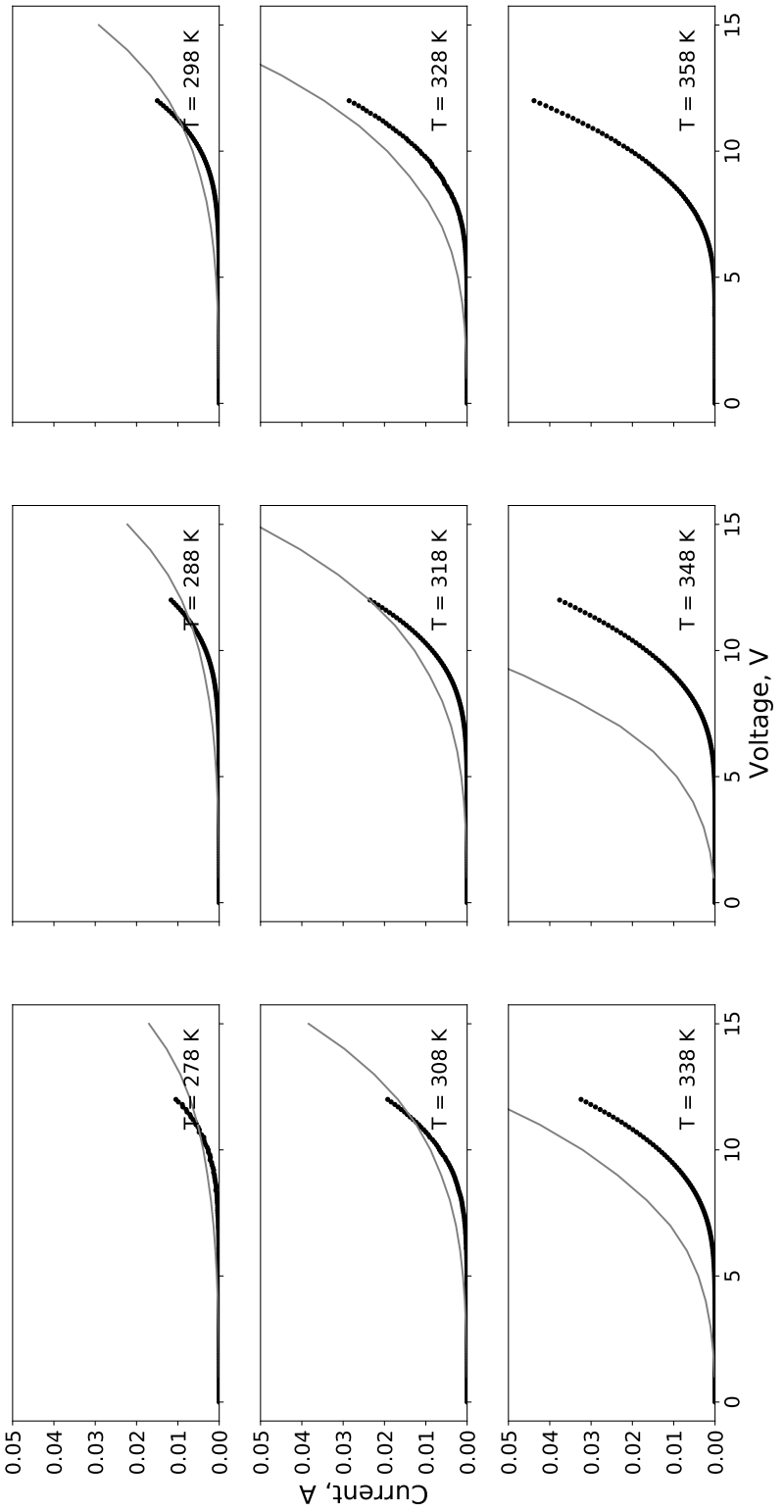


Figure 4.6: Current-voltage characteristics for manufactured OLEDs at different temperatures. Solid lines correspond to the modeling results for the value of the disorder parameter equal $50meV$ and dots correspond to experimental results. The last plot does not contain modeling results, because for this temperature and the chosen small disorder parameter, the mobility model fails. The mobility model does not fail for the disorder parameters higher than $50meV$ and temperature less than $358\ K$.

Figure 4.7: Current-voltage characteristics for different temperatures for the value of the disorder parameter equal $125meV$. Solid lines correspond to the modeling results and dots correspond to experimental results. Drift-diffusion simulation cannot converge at 358 $K$ due to extremely high mobility dependence on the electric field and carrier density.

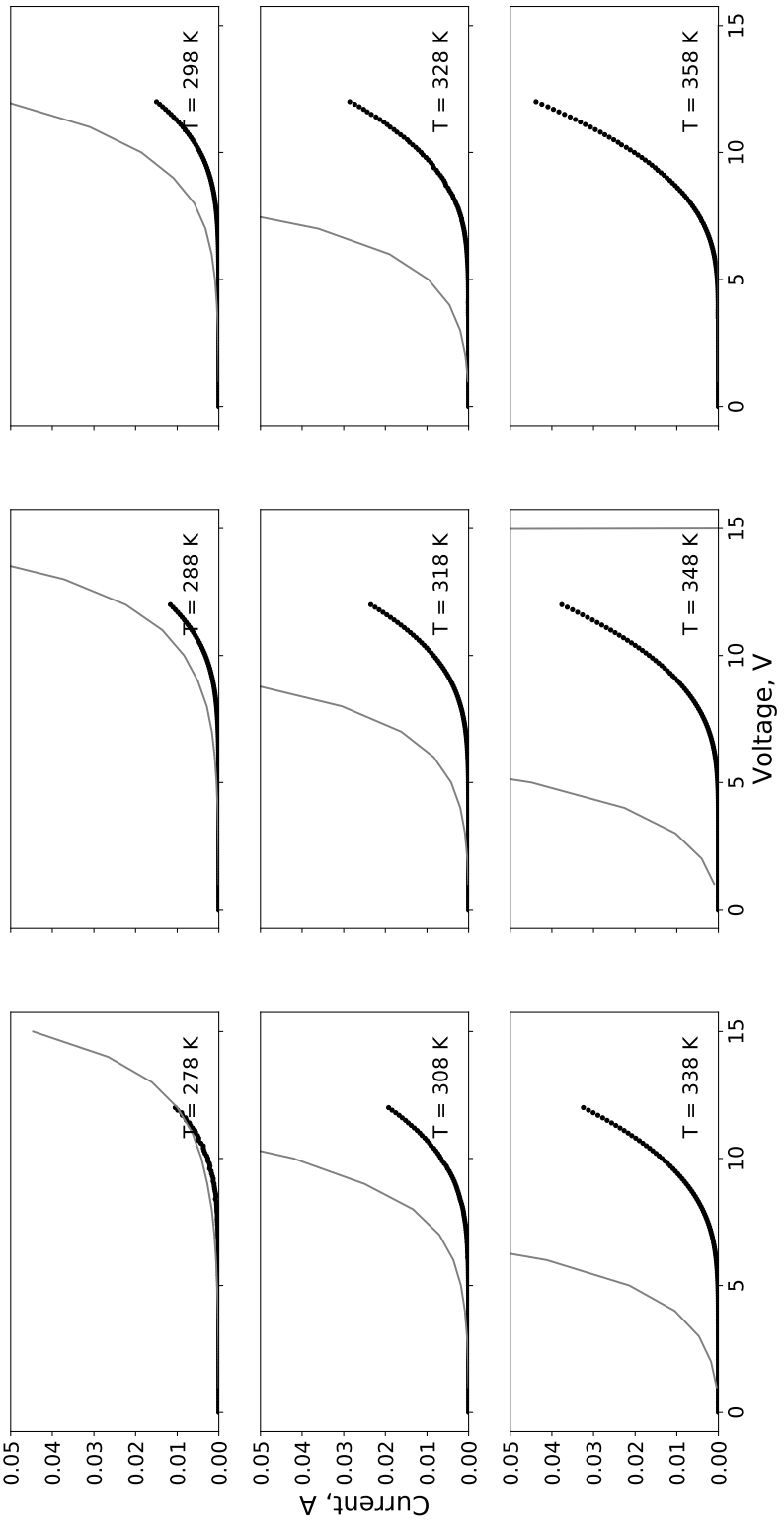


Figure 4.8: Current-voltage characteristics for different temperatures for the value of the disorder parameter equal $125meV$. Solid lines correspond to the modeling results and dots correspond to experimental results. Drift-diffusion simulation cannot converge at 358 $K$ due to extremely high mobility dependence on the electric field and carrier density.

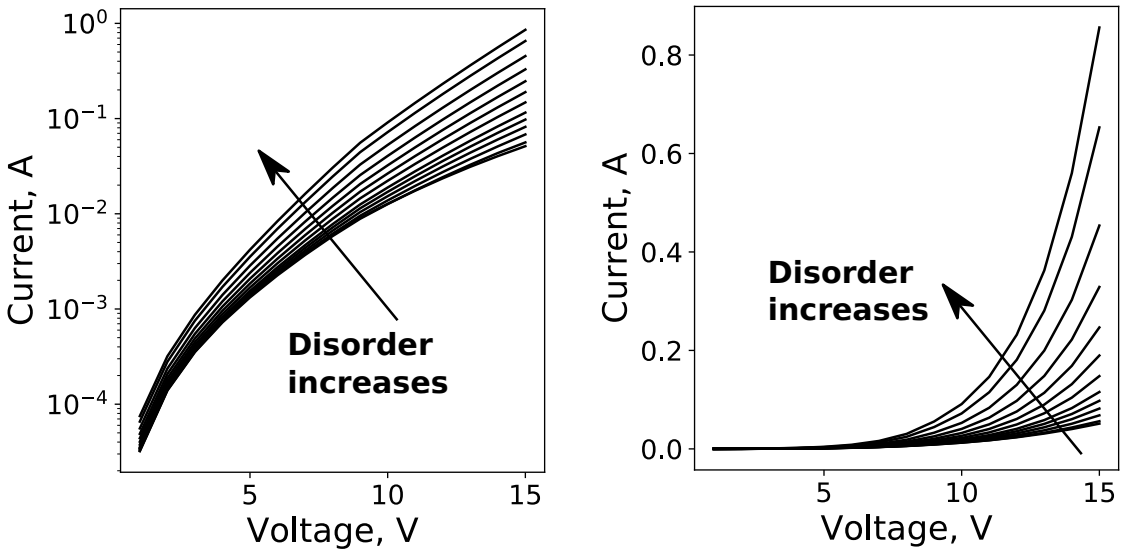


Figure 4.9: Disorder parameter influence on the modeled current-voltage characteristics, both on logarithmic (left) and linear scale (right). Values of disorder parameter are from 50 *meV* to 125 *meV*. For a complete set of values, see description in this section.

### 4.2.1 Quantitative comparison between theory and experiment

To compare simulations with experiment, we require first a method, to quantitatively determine which parameter best describes the experimental curves. To this aim, we utilize Bayesian inference. Let us denote $P(\sigma_j|I_e(V_i,T_k))$ as the probability that the disorder parameter $\sigma_j$ best describes the results the best, that is, the modeling current $I_m^{\sigma_j}(V_i,T_k))$ for the given $\sigma_j$ is closest to the experimental one $I_e(V_i,T_k))$. This probability cannot be directly calculated, however, it can be refactored with a help of the Bayes' theorem into something which can be calculated:

$$P(\sigma_j|I_e(V_i,T_k)) = \frac{P(I_e(V_i,T_k)|\sigma_j)P(\sigma_j)}{P(I_e(V_i,T_k))} \tag{4.1}$$

The term $P(I_e(V_i,T_k)|\sigma_j)$ is called likelihood and it denotes the probability to obtain the experimental results with a given $\sigma_j$. It requires further assumptions to be calculated. $P(\sigma_j)$ is a prior probability, i.e. the probability that a given $\sigma$ is the correct one without any relation to experiment. As we do not favor any value of disorder parameter over any other, this distribution will be set to uniform, i.e. $P(\sigma_j)$ will be just a constant multiplier. The term in denominator can then be seen as an overall normalization. Therefore, it will always cancel the constant multiplier of the prior distribution. With that, eq. 4.1 can be simplified into:

$$P(\sigma_j|I_e(V_i,T_k)) = \frac{1}{Z}P(I_e(V_i,T_k)|\sigma_j) \tag{4.2}$$

where $Z$ is a normalization constant. To calculate $P(I_e(V_i,T_k)|\sigma_j)$ one needs first to introduce the random distribution $f$, which accounts for the difference between the

modeling and the experimental results [5], i.e. :

$$I_m^{\sigma_j}(V_i, T_k)) - I_e(V_i, T_k)) = f \tag{4.3}$$

where $f$ is a random number distributed with some probability distribution $f(t)$. In principle, it can depend on both $V$ and $T$, but must not depend on the value of $\sigma$. Otherwise, it could be possible that with some particular choice of this dependence we would be able to "prefer" one value of $\sigma$ over another. That is, the general form of $f$ can be factored as follows:

$$f = f_{V,T}(t) = f_{i,k}(t) \tag{4.4}$$

Which distribution of $f_{i,k}(t)$ may fit to our problem? As we are sure that modeling results are correct and we know only a little about the error distribution of the measurement device, we proceed with a guess. For this guess, we have chosen two distributions:

1. Normal distribution $f_{i,k}(t, v) = \frac{1}{\sqrt{2\pi v^2}} \exp\left(\frac{-t^2}{2v^2}\right)$, parametrized by an arbitrary value of $v$
2. Log-normal distribution $f_{i,k}(t, v) = \frac{1}{\sqrt{2\pi v^2 t^2}} \exp\left(\frac{-\ln(t)^2}{2v^2}\right)$

The distributions were chosen according to the following criteria. Normal distributions are often used due to the Central Limit Theorem. This theorem states, that measurements of the quantity, whose distribution possesses an average and a finite variance, will inevitably converge to a normal distribution of the measured values, regardless how the actual distribution of the measured quantity looks like.

The log-normal distribution is the derivative of the normal distribution: if the random value $X$ is distributed normally, then the random value $Y = ln(X)$ has a log-normal distribution. This distribution was used primarily as a consistency check. A log-normal distribution captures our expectation that large current values have, in absolute value, higher measurement errors than low current values, which is exactly the case for log-normal distribution. Moreover, as most plots presented in this section are given on a logarithmic scale, the analysis within log-normal distribution yield the curve which fits the best *on logarithmic scale*. Thus, results here should also be consistent with what human perceives from the logarithmic plot.

Note that both distributions do not explicitly contain the values of $T$ and $V$, that is, the resulting distribution is single-variable function without parametrization $f_{i,k}(t) = f(t)$. What we actually need from the analysis in the end is to find which values of $\sigma_j$ results in the largest posterior probability $P(\sigma_j | I_e(V_i, T_k))$. If we consider every measurement being independent from another, the total probability is just the product of individual probabilities for every point $T$ and $V$. Denoting the difference between experimental and modeling curves as $\delta_{i,k,j} = \left(I_m^{\sigma_j}(V_i, T_k) - I_e(V_i, T_k)\right)$:

$$P(I_e | \sigma_j) = \prod_{i,k} f(\delta_{i,k,j}) \tag{4.5}$$

In case of a normal distribution this equation leads to:

[5] In other words, in this approach, we describe the difference between experimental data and modeling as random noise.

$$P(I_e|\sigma_j) = \prod_{i,k} \frac{1}{\sqrt{2\pi v^2}} \exp\left(\frac{-\delta^2_{i,k,j}}{2v^2}\right) \tag{4.6}$$

This equation can be further refactored. We denote $N = \sum_{i,k}^{j} 1$, that is, the amount of points which are contributing to the total probability. With this, we can further simplify eq. 4.6:

$$P(I_e|\sigma_j) = \left(\frac{1}{\sqrt{2\pi v^2}}\right)^N \exp\left(\frac{-\sum_{i,k} \delta^2_{i,k,j}}{2v^2}\right) = \frac{1}{Z} \exp\left(\frac{-\sum_{i,k} \delta^2_{i,k,j}}{2v^2}\right) \tag{4.7}$$

Here, we denoted the first factor as $Z$, as it acts as normalization constant. The exponential term is the one which describes the probability of encountering $I_e$ as a function of $\sigma$. Note that $P(I_e|\sigma_j)$ is maximized when the sum in the nominator in exponent is lowest, independent of the free parameter $v$. That is, our analysis arrived to the least squares method, which states that the model which represents data the best is the one, which has the lowest *standard deviation*. That is, we arrive at the final equation:

$$\sigma_{best} = \text{argmin}\left(\sum_{i,k} \delta^2_{i,k,j}\right) \tag{4.8}$$

For the case of a log-normal distribution the distribution $\ln(I_e)$ is a normal distribution and the same argumentation leads to the fact that we can use the results obtained in eq. 4.7, but on logarithmic scale. For that purpose, we denote as $\lambda_{i,k,j} = \left(\ln(I_m^{\sigma_j}(V_i, T_k)) - \ln(I_e(V_i, T_k))\right)$. The corresponding result is then:

$$\sigma_{best} = \text{argmin}\left(\sum_{i,k} \lambda^2_{i,k,j}\right) \tag{4.9}$$

#### Determination of the disorder parameter

Applying eq. 4.8 to the modeling and experimental data results in fig. 4.10-a. Standard deviations are calculated for different values of the disorder parameter for every data point (i.e. for every temperature and every applied bias). One can see that the resulting plot shows a marked minimum for a disorder parameter between 55 and 60$meV$. Higher values correspond to a rapid increase in the deviation between model and experiment. Second plot, fig. 4.10-b, correspond to the same data and the log-normal distribution eq. 4.9. One can see that the disorder parameter, deduced from this plot is also located between 55 - 60 $meV$. Both distributions show consistent results for every other plot in this section. Hence we will limit ourselves to only one plot with normal distribution for every scenario.

The methodology outlined above is known to be susceptible to outlier data points. Normal distributions very rapidly decrease away from the mean value. Captured outlier value may therefore result in a huge shift in the fit. To test if the methodology yields reliable predictions, one must also identify and remove outliers. The first type of outliers are currents obtained at low voltage points ( $<$ 8 $V$), which are either noisy or contain leakage current contributions. The second type of outlier is the lowest temperature curve, which does not possess turn on regime. Just to be safe, we also

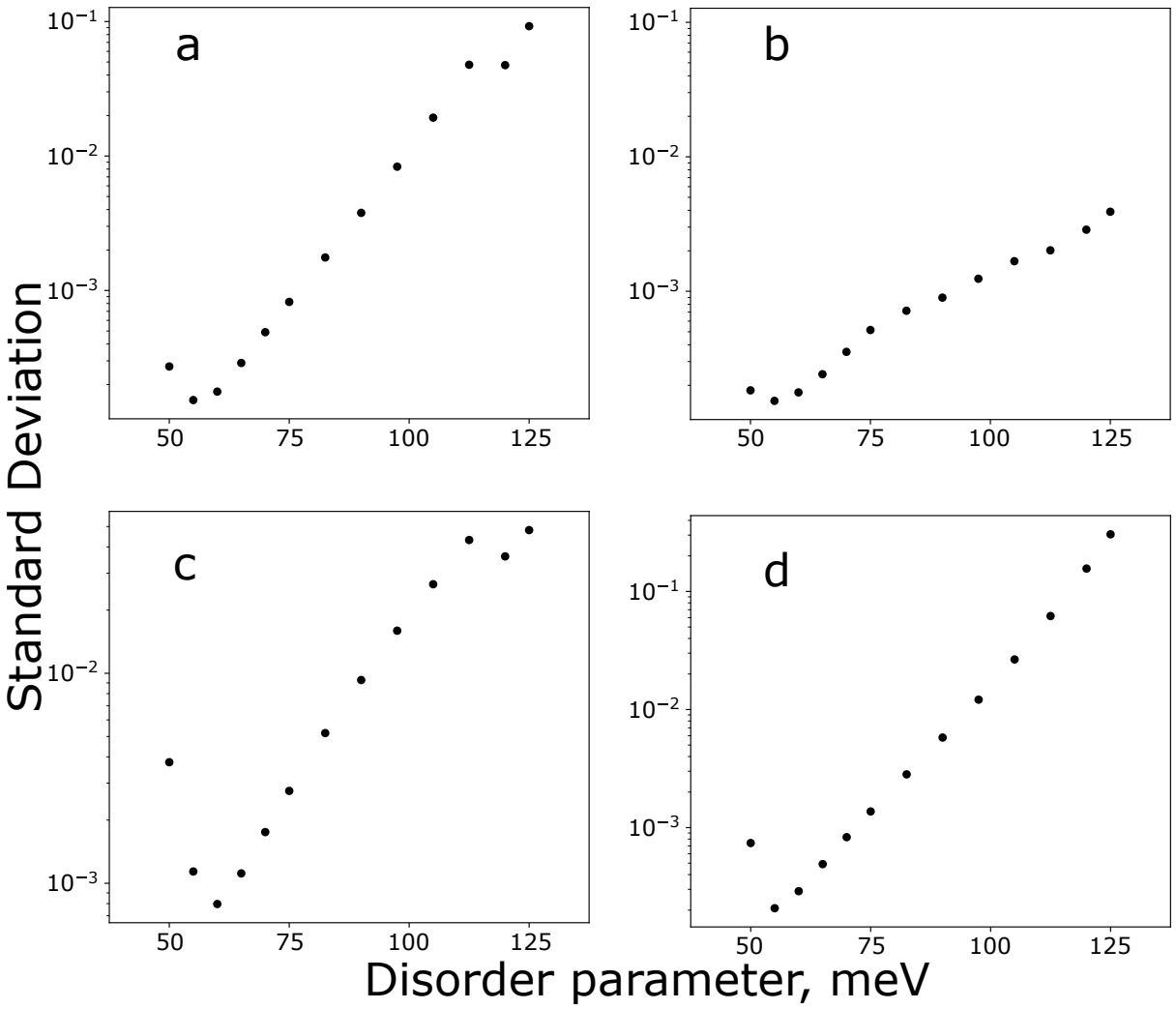


Figure 4.10: Standard deviation of the current predicted by the model compared to experiment for different disorder parameters. (a) and (b) are averaged squared distances between all data points for all different voltages and temperatures, where (a) correspond to a straightforward substraction between experimental and model values and (b) corresponds to the difference of logarithms between the values, exponentiated afterwards to bring plot (b) to the same scaleas plot (a). The plot (c) is the same as (a) except that data points related to lowest and highest temperatures are removed from the calculation, together with low voltage region. (d) On this plot, the analysis determines the standart deviation of the residuals of the slope between model and experiment.

removed the highest-temperature curve, as the simulation results might not be reliable in that region due to long convergence. Upon excluding all these data points from the comparison we obtained results in fig. 4.10-c. After that procedure, the minimum at $55meV$ became even more pronounced, because both lower and higher values of $\sigma$ lead to a sharper increase in standart deviation. Therefore, we can draw the conclusion that (i) $\sigma = 55meV$ is the disorder parameter which describes the experiment the best and (ii) the less pronounced difference for separate disorder parameters was coming from the noise in the experimental data.

#### Temperature contribution to the device bahavior

As discussed in sec. 4.1.1, we are also additionally interested in how current depends on temperature when the voltage is fixed. This is valuable for our investigation, where temperature plays a crucial role, but specifically to cross-check the previously determined value of the disorder parameter, whose value has the largest influence on the temperature dependence[6]. Results, reformatted to depict current-temperature characteristics, are presented at fig. 4.11, which was obtained for the same value of the disorder parameter as in fig. 4.5, $\sigma = 50meV$.

As the data, used to prepare these plots, is the same as used for current-voltage plots, we can observe the same behavior. Namely, low voltage modeling results are much larger than the experimental one and this behavior changes towards high voltage. However, from these curves one can see that, contrary to IV curves, the temperature dependence of the modeling curves is quite close to the experimental ones. To see this even better, we propose to the reader results, where curves are shifted in such a way, that mean current on a logarithmic scale is the same for both experimental and modeling curve. One can see the results on fig. 4.12.

From the look on the second plot one can clearly see that our model is capable of capturing the correct current-temperature dependence. We want to emphasize, that:

- The ability to capture the temperature dependence is quite remarkable, as it is influenced by several different phenomena, like mobility, diffusion, inorganic/organic and organic/organic injection.
- The complicated thermoelectric coupling, observed in the previous section, did only occur at large voltages. We correctly capture both (i) current value and (ii) current-temperature dependence for relevant, larger voltages. Together, it gives us more confidence, that the results presented in ch. 3 are correct.

Despite that the current-temperature result is clearly beneficial for our confidence in the presented model, it also raises some questions. First of all, why does the temperature dependence remains valid, despite an order of magnitude difference in the current value? To explain that, it makes sense first describe the low-voltage regime, in which the electric field and the carriers density will be low. Then, the mobility value should be uniquely determined by the temperature, which is fixed in this modeling, and the change in the total current due to the temperature change must come purely from an explicit and implicit (due to the mobility factor) dependence of the injection current on temperature. Then, it should not come as a surprise that these

[6]Temperature dependence, which is not parameterized by the disorder parameter, comes as exponential prefactor from eq. 2.45

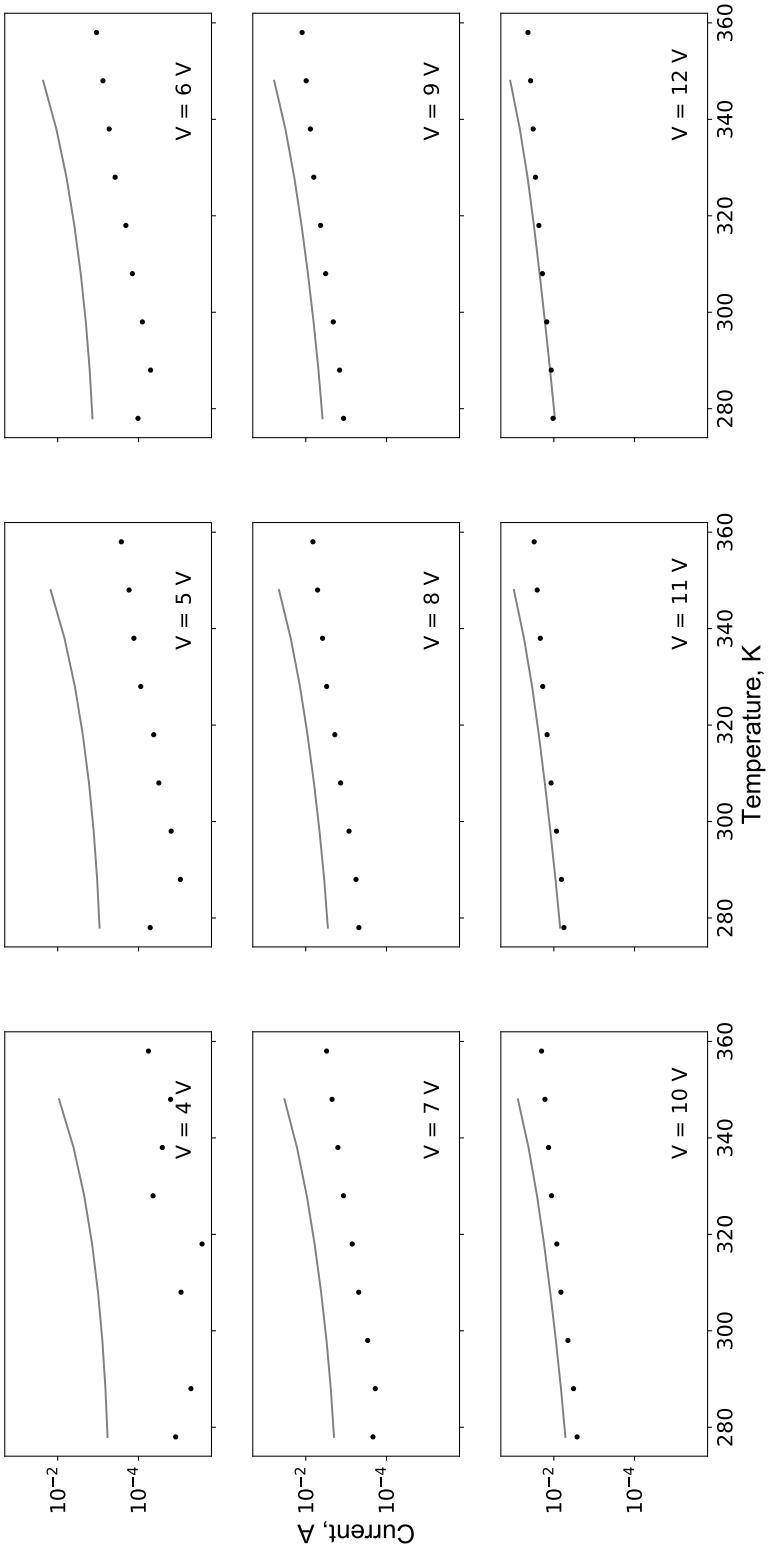


Figure 4.11: Current -temperature characteristics of the device for different applied voltages for the disorder parameter $\sigma = 50meV$. Note that the model behavior resembles the experimental data. The offset between experimental and predicted current strongly decreases with increasing voltage.

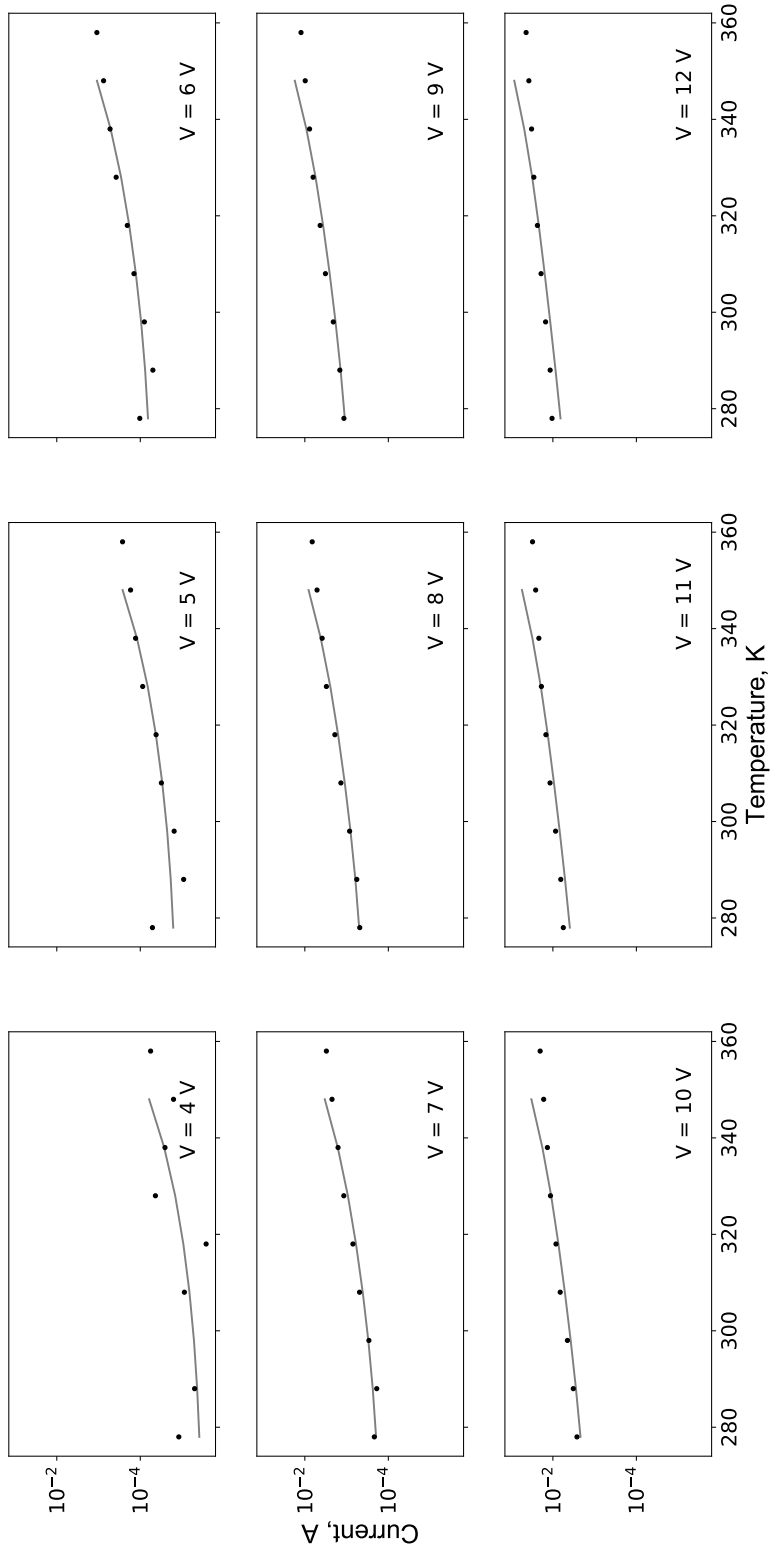


Figure 4.12: Current -temperature characteristics of the device for different applied biases for the disorder parameter $\sigma = 50meV$. Curves on this plot are shifted compared to fig. 4.11 in such a way that mean is equal for both curves and, therefore, we are getting rid of the current-voltage discrepancies at low voltages.

two parametrizations, which are in a good agreement with the experiment, result in a good agreement in our investigation, despite the incorrect current value in that region. We cannot make the same argument about the high voltage region, where the electric field and the carrier densities are large enough to substantially change mobility as in fig. 3.4. However, at that voltage, the experimental current catches up with the modeling and the initial question does not make sence anymore. This means that when the interplay between all quantities in the modeling is active, the results are still correct.

However, there are also some problems with the presented plot. We see that every modeling curve in the fig. 4.11 appears to have higher slope towards the larger temperature values, however, experimental ones do not possess this behavior. This can mean that for the temperatures higher than 348 $K$ the model may be inadequate, but unfortunately we do not have any experimental data to prove or disprove it.

To be able to see how the current temperature characteristics will change due to the different value of the disorder parameter, we present here the same plot for the value of the disorder parameter $\sigma = 125meV$, fig. 4.13. In this figure, we present simultaneously both shifted and not shifted by the mean value of an electric current modeling results. We see that while the difference is not that noticeable as it were in case of current-voltage characteristics, it is still definitely present. The slope of every curve is larger, underestimating current values in the low voltage region and overestimating it towards the high voltage region. This was expected, as we already know that the best fit for the disorder parameter value lies around $55meV$.

Now we may alternatively determine the disorder parameter from the *slope* of the current-temperature characteristics, i.e., from focusing on the change of the current with temperature. That is, we are using a normal distribution and the quantity of interest is now the derivative of the current with respect to temperature $\frac{\partial}{\partial T} I_{m/e}$. The derivative was estimated as the difference between current at the point $T_k$ and $T_{k+1}$:

$$\left(\frac{\partial}{\partial T} I_{m/e}\right)_{i,k} = \frac{I_{m/e}^{i,k+1} - I_{m/e}^{i,k}}{T_{k+1} - T_k} \tag{4.10}$$

Standard deviations, calculated this way, are shown on fig. 4.10-d. These standard deviations assume their minimum at a disorder parameter of $60meV$, i.e. quite close to the previously obtained value equal to $55meV$. This means that (i) the model is consistent as different methods of its evaluation yield consistent results and (ii) we can trust the disorder parameter value, because the value of $55 - 60meV$ captures both thermal and electric behavior best.

Other current-temperature plots for different disorder parameters can be found in Appendix sec. 6.

Last but not least, we want to discuss how the discrepancy between the current-temperature and the current-voltage plot will influence the results of ch. 3. The fig. 3.6 will be the only one which is directly influenced by new knowledge, as it presents current-voltage characteristics under presence of self-heating. On the one hand, $h$-coefficient values ranging from $10^3$ to $10^5$ $W/m^2K$ should still be valid, as the vicious cycle of self-heating starts in the high voltage region, in which our model can be applied. However, it is not the case for the low value $10^2$ $W/m^2K$ of $h$-coefficient. This means that actual abrupt current increase in fig. 3.6 should be shifted towards higher voltage values, because we always overestimate the current. Nevertheless, the

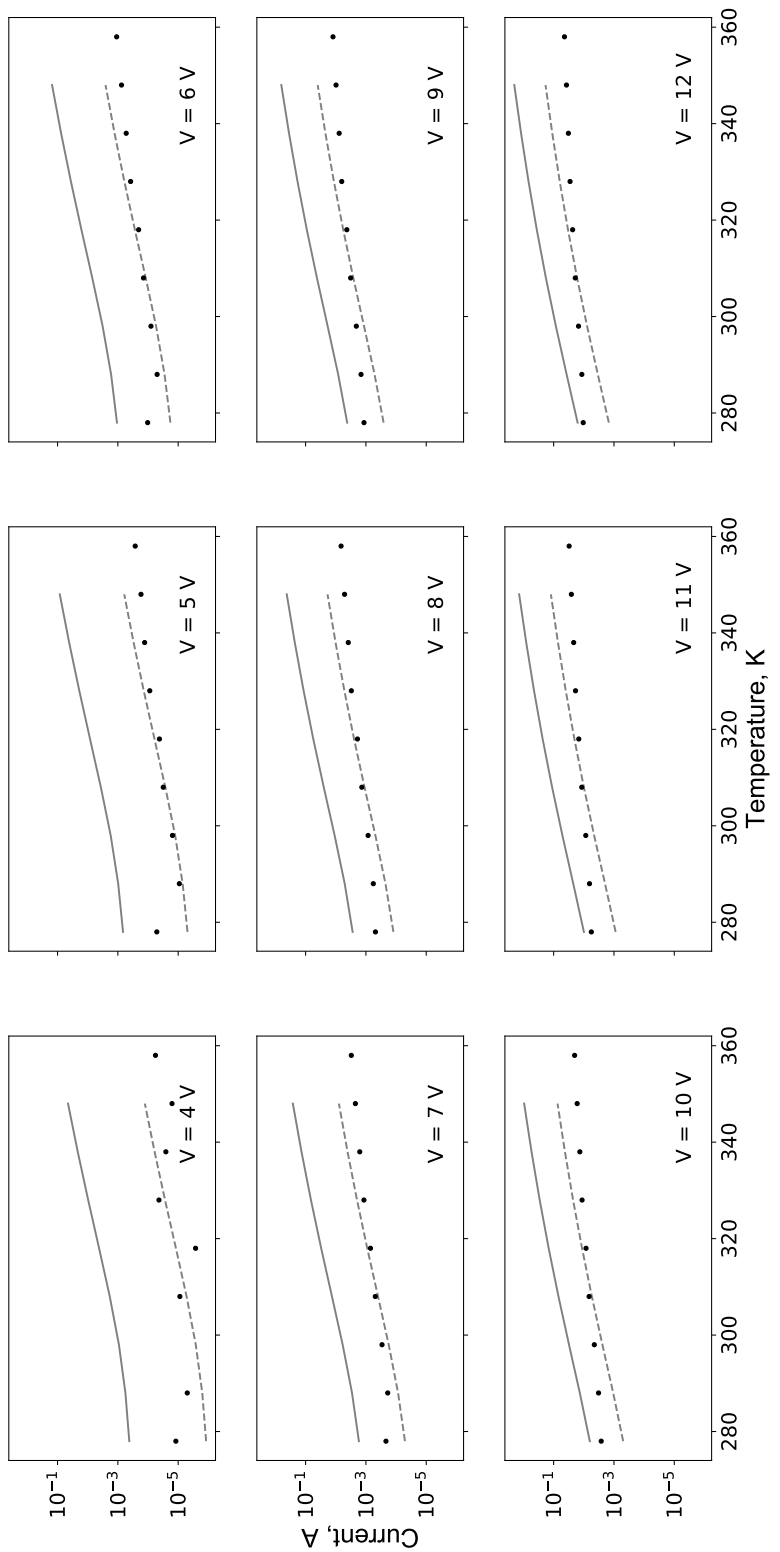


Figure 4.13: Current-temperature characteristics for different applied biases for the value of disorder parameter equal $125meV$. Solid lines correspond to the modeling results, dots correspond to experimental results, dashed lines are the modeling results, shifted to the average difference between modeling and experimental curves, emphasizing the temperature behavior.

correct temperature dependence of the current in the model means that the shape of the current elevation due to self heating must stay the same. Figures like the fig. 3.2 should remain the same, as we capture correctly high-voltage behavior, however, the onset of temperature elevations should in fact happen at higher voltages.

## 4.3 Influence of mobility, interface carrier density and injection barriers on current-voltage characteristics

Here, we investigate how parameters such as the mobility prefactor $\mu_0$, the injection barrier $\phi_B$ and the density of charge carriers $N_0$ in the contacts affect the current-voltage behavior. While they will influence the entire current-voltage characteristics, we are mostly interested in their influence in the low-voltage region. We have already shown that with a proper choice of the disorder parameter, the simulations at high-voltage may come very close to the experimental data. We see no reason to carefully fit the high voltage region to the experimental values, at the same time a large part of the experimental data is orders of magnitude away from the modeling results. Hence, the low-voltage and turn on regions must be addressed first.

Another reason not to go use the mobility, interface carrier density, and injection barriers to fit the experimenal curves best is that the influence of the mobility [208–210] and the injection barriers [211–214] on the OLEDs performance has been extensively investigated topic in literature, both from a theoretical and experimental point of view. It is not surprising, because these parameters are mostly responsible for efficiency also in inorganic LEDs and are normally viewed as go-to parameters to improve OLED performance. This means, that we will probably not discover anything new varying these parameters. What we are, however, extremely interested in is, whether by changing the parameters of our model we could achieve a turn on behavior. Very few theoretical works even bother to fit this region, most notably [140, 198, 199]. It is often either neglected [215, 216] or attributed to the leakage currents [217]. Of course, we have a leakage in the experimental data, which, however, does not explain the turn on voltage. Hence, in this section we will only have a quick glance on how current-voltage characteristics will behave under the changes of model parameters, to see whether they can trigger anything similar to the low-voltage behavior.

First, we will take a look at the mobility prefactor $\mu_0$. We discretized this parameter from values one order of magnitude lower to one order of magnitude higher than the reported value ca. $10^{-9}\mathrm{m}^2/(\mathrm{Vs})$, that is from $10^{-10}\mathrm{m}^2/(\mathrm{Vs})$ to $10^{-8}\mathrm{m}^2/(\mathrm{Vs})$. The related I-V curves are depicted in fig. 4.14. Note that results are obtained for a temperature of 300 K, and do not contain any electrothermal coupling, i.e. there are no time evolution in the heat transport equation 2.42.

The mobility increases the total current in the device without introducing a turn-on behavior. One could argue, that the turn on happens exactly at the point $V = 0V$, the behavior we already described at 4.1.1. Rather than displaying a turn-on, the current in the voltage region between 4 $V$ and 8 $V$ appears to rise less steeply with increasing voltage. The change in current due to the mobility prefactor $\mu_0$ is different at low and in high voltages, indicating a change in the transport regime[7]. The higher the mobility is, the larger is the exponential growth of the current. This effect basically comes

[7]Under change of the transport regime we mean the change of the exponential dependence of the current. When the mobility changes, the injection currents must change almost linearly. The drift

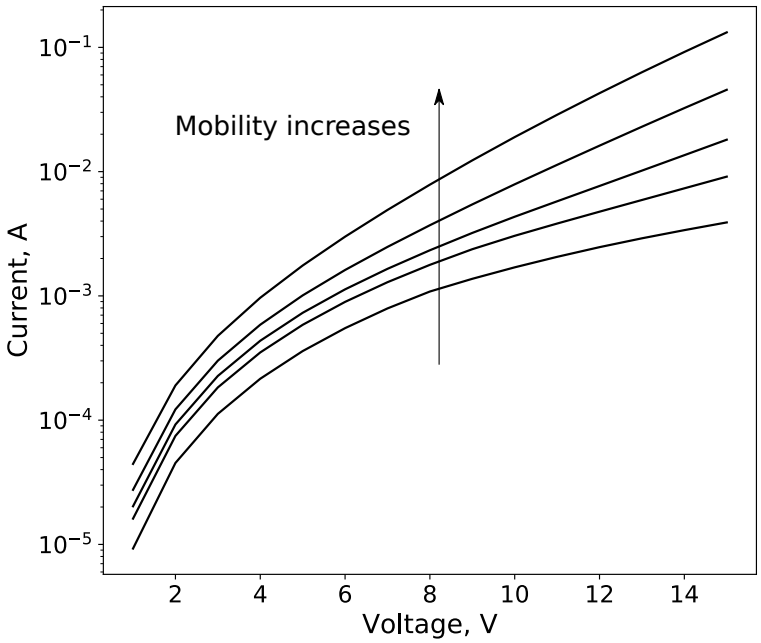


Figure 4.14: Influence of the mobility prefactor $\mu_0$ on the current-voltage characteristics. Different curves correspond to values:$\mu_0$ = $10^{-10}$, $10^{-9.5}$, $10^{-9}$, $10^{-8.5}$ and $10^{-8}$ $m^2/(Vs)$.

from less charge carrier accumulation due to (i) easier recombination, as Langevin recombination rate eq. 2.58 is higher in case the mobilitiy of the charge carriers is higher and (ii) the more efficient charge carrier transport to the organic/organic interface [140].

The next parameter we are going to look at is the density of charge carriers $N_0$ at the contacts, which was discretized between $10^{27}$ and $10^{29}$ $m^{-3}$. As described previously, its value is known precisely [169] for the silver contact, however, from both anode an cathode sides there are additional layers between silver and trasport layers. Hence, it looks plausible that it can differ from the exact value of charge carrier density in silver, equal to $10^28m^{-3}$. It also makes sense to vary $N_0$ from purely theoretical perspective. $N_0$ influences only the thermal injection current in eq. 2.45 and as such changes the balance between tunneling eq. 2.49 and injection [8]. On top of that, it increases thermal injection in a linear manner $J_{tot} \propto N_0 J_{th} + J_{tun}$ making the analysis of its impact simpler. Results are presented in fig. 4.15.

The influence of $N_0$ on the current-voltage characteristics appears to be less than that of mobility fig. 4.14. On top of that, the characteristics, corresponding to the lower values of $N_0$ are becoming noticeably closer to each other. This is probably caused by low values of the thermal injection current, i.e. the tunneling current $J_{tun}$ becomes the leading contribution to the total injection current $J_{tot}$. We do not see substantial

and diffusion bulk currents similarly will linearly change, as mobility is proportionality coefficient between the electric field and the current. Hence, the change in the exponential dependence of the electric current on IV plot should be caused by the interplay between both. We will call it, for a lack of better word, as a transport regime

[8]This of course only happens due to the chosen parametrization, where $N_0$ is a parameter for the thermal injection but not for the tunneling. Intuitively it is clear that the high charge carrier concentration at the contact should cause a large tunneling current and vice versa.

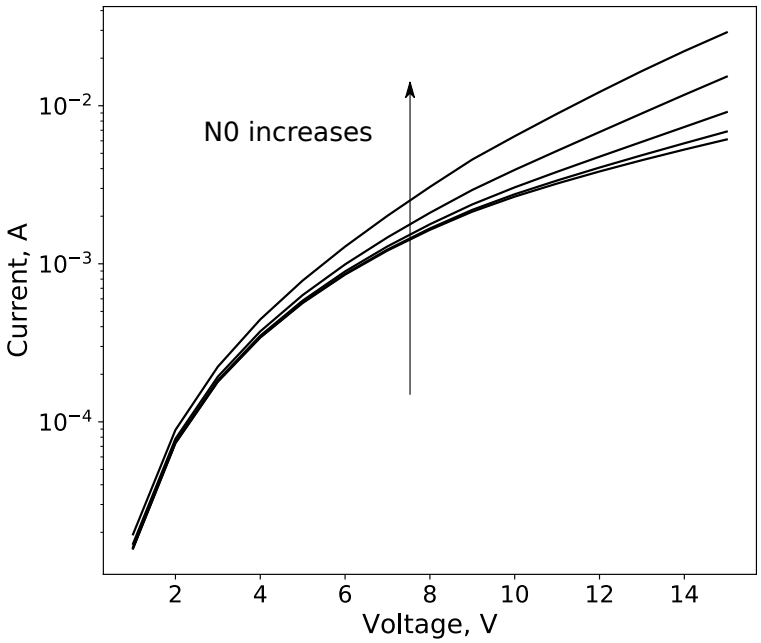


Figure 4.15: Influence of $N_0$ on the current-voltage characteristics. Different curves correspond to values: $10^{27}$, $10^{27.5}$, $10^{28}$, $10^{28.5}$ and $10^{29}$ $m^{-3}$.

changes in the transport regime for a high voltages and, most importantly, turn on voltage does not appear in the case of changing $N_0$ either.

The last parameter is the injection barrier that was varied from 0.4 eV to 0.8 eV with a step of 0.1 eV, fig. 4.16. We see that injection barriers below the value of $0.6eV$ drastically lower the current when the barrier increases. For larger barriers, the change is less pronounced and the curves "converge" to the $0.8eV$ one. Note, that an injection barrier of 0.8 $eV$ is so large that it should prevent any current flow in actual experiment. This observation indicates, that the considered injection mechanism fail to provide a plausible trend in terms of injection. In sec. 4.4 we will explore this in more detail. Injection barrier also does not change carrier transport regime. Most importantly, there are also no turn on behavior in this case either. As we already mentioned, a lot of works suggest that turn on appears when the flat band condition is fullfilled [199]. The injection barrier is in essence the only parameter in our simulations which is somehow related to the energy level diagram and its changes could trigger the flat band condition. Clearly, this is not the case, moreover, the model dependence on the injection barrier value is overall suspicious.

To summarize our findings, all three parameters have a pronounced influence on current-voltage characteristics, but none of them can induce a turn-on behavior. It is not clear why the injection barrier has such a tiny influence on current voltage characteristics after certain barrier value. Intuitively, it is clear that higher barriers should substantially decrease both tunneling and thermal injection currents. The tunneling of charge carriers into the material should decline as a barrier width grows and the thermal injection should be weaken by the barrier height. This indicates the existence of problems with the chosen injection model.

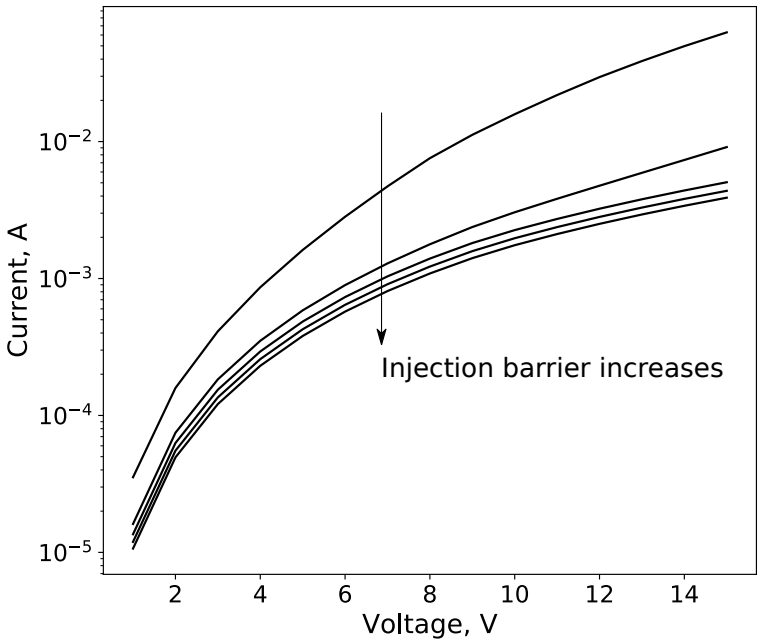


Figure 4.16: Injection barrier influence on the current-voltage characteristics. Different curves correspond to values: $\phi = 0.4$, 0.5, 0.6, 0.7 and $0.8eV$.

## 4.4 Origin of the model behavior at low voltages

In the previous section we found that our device model cannot capture scenarios in which either currents or voltages are small. To possibly provide leads to further improve our model approach, we inspect more closely which part of the modeling approach is responsible for the problematic behavior.

#### Possible reasons for the model to fail in low-voltage region

We were able to come up with four possible reasons why our model cannot reproduce a turn on voltage.

1. The drift-diffusion equations to describe transport in the organic semiconductor are not applicable for such thin layers.
2. The mobility model is incorrect.
3. The turn on voltage is related to the barrier at the organic/organic interface, the properties of which we are not able to capture properly [9].
4. Injection currents from the metal to the OSC are captured incorrectly.

The drift-diffusion model is a macroscopic approximation to the microscopic transport and may, thus, fail. A thorough analysis of reference models including all assumptions made therein would be necessary. The same can be said about the mobility model. Moreover, mobility model we use is widely accepted and passed a lot of benchmarks. Both aspects are beyond the scope of this thesis.

[9]Remember, that we use very simple thermal injection model in case of organic/organic interface.

The last two reasons, however, are directly accessible within our model setup, i.e. we can test directly the impact of assumptions by changing the corresponding values of parameters contained in the model. Assessing the impact of the ill-defined organic/organic injection turned out to be difficult within our model. In an attempt to do so, we performed first a simple benchmark test, where we assumed that the extremely low experimental current values ($< 10^{-5} A$) at low voltages ($V < 4\ V$) are limited by the organic/organic interface. This scenario is easy to test - one just has to explicitly set the current across the interface in the simulation to be equal to the experimental one, while maintaining the corresponding bias. Unfortunately, such simulations are difficult to converge. Low currents in the device require a large charge carrier accumulation near the contact to limit the metal/organic injection. Therefore, low currents correspond to enormous periods of time to accumulate enough charge carriers and thus the model never converges. What we observe is a slow but steady growth of charge carrier density, which persists after several weeks of CPU-hours. We estimated that the density of charge carriers, which is required to limit the contact/organic injection to the low current values imposed at organic/organic interface, should be in the order of $10^{26-27} m^{-3}$ [10]. For such large charge carrier densities, the mobility model used here and the Einstein relation (eq. 2.14) will not be valid any more.

Therefore, we will exclusively focus on the injection from the metal to the OSC, as it is (i) straightforward to investigate, due to the lower amount of free parameters and (ii) it already displayed a strange behavior for large biases in sec. 4.3.

#### Inspection of the injection current in the model

To take a deeper look at injection, we need both the simulation results together with corresponding injection current values. In this way, we can compare the "bare" injection current values with the real ones in the simulation and see better, which injection current may be the root of the problem. The following set of parameters is required to calculate the total injection current according to eq. 2.45 and eq. 2.49:

- Charge carrier density in the contact $N_0$ *
- Injection barrier $\phi$ *
- Mobility prefactor $\mu_0$ *
- Temperature at the interface $T$
- Disorder parameter $\sigma$*.
- Charge carrier densities in the $p$ and $n$. They influence the injection current by (i) lowering electric field at the interface and (ii) by increasing the mobility [11].
- Electric field at the interface $E$. In the reference calculation we will assume it to be equal to the applied bias divided by the device thickness.

To perform the comparison, we took one particular simulation from sec. 4.1.1 with a disorder parameter $\sigma = 55meV$ and with $T = 297\ K$. Parameters marked with * are the ones, which are readily available from the simulation so while doing the following

[10] This estimation can be easily made by (i) calculating the electric field, which is introduced by a sheet of charge carriers near interface and (ii) plugging it into the equations for the injection to find the carrier density value, which would result in the required current value

[11] We will assume that there are no charge carriers, because due to their complex influence on the model, it is nearly impossible to make quantitative analysis.

comparison their values will be set exactly from the simulated values. Strictly speaking, other parameters as $E$, $p$, and $n$ should be available from the simulation too, but they were not saved. $n$ and $p$ at the interface were then set to 0. We can then calculate separately both injection currents for a given bias as well as extract the total current, fig. 4.17.

We see that the injection in the low voltage region is dominated by the tunneling current, while the thermal injection current becomes more prominent at large voltages. At the large voltages, the thermal current is solely responsible for the current injected into the device, as it exceeds by an order of magnitude the tunneling current. This result might not be intuitive, as normally opposite happens and the tunneling current dominates large voltages, see for example [218]. However, there are two reasons for that to happen. The first reason comes from the fact that the used model for the thermal injection 2.45 combines both the interface recombination (which lowers injection) with the actual thermionic injection current. The the recombination at the interface is specifically made to counterbalance thermionic injection under zero bias and naturally lowers the injection values there, which explains the low voltage region.

Domination of the thermal injection in the high voltage region is more tricky. The tunneling injection values depend heavily on the bending of the injection barrier and its resulting thickness [151] and should eventually become worse under high applied fields. Intuitively, one can understand that under certain applied biases the injection barrier will be almost gone. When this happens, we expect the tunneling injection model to fail. On top of that, the mobility dependence on the electric field starts to grow much faster [159] when the applied field comes to the region of $10^{8-9}V/m$. For the highest applied bias of 15 $V$ the average value of the electric field in 100 $nm$ device the electric field will be equal to $E = 15/10^{-7} = 1.510^8 V/m$. In other words, we strongly suspect that we may get to a regime, where the applicability of the chosen injection models is dubious. Unfortunately, authors of the model [151] have not provided when the model could fail and we cannot test our suspicions. We will further see other problems related to the tunneling current, which suggest that future use of this injection model for such OLED devices might be not an optimal choice.

Note the difference between experimental currents at low voltage fig. 4.1 and the thermal current at the same bias. As we have a problem for large currents in the low voltage region, the obvious candidate introducing the error is the tunneling current. However thermal injection still appears to be too large compared to experimental results, fig. 4.1. Experimental results show the current value of $10^{-5}$ $A$ at $V = 4$ $V$, however, the thermal injection current there is already higher than $10^{-4}$ $A$.

#### Current-voltage characteristics without tunneling current

Previously, we saw that tunneling injection current is the one, which could possibly hide the low voltage features. If we remove it, the high-voltage results will not be invalidated, as the thermal current has the highest contribution to injection in that region. On the other hand, the low voltage region will not be affected by tunneling anymore and we may notice something there.

To demonstrate how much tunneling current dominates the injection under low injection barriers, we prepared several simulations which are made with the same set of parameters as in fig. 4.16, but the tunneling injection was manually set to zero, fig. 4.18.

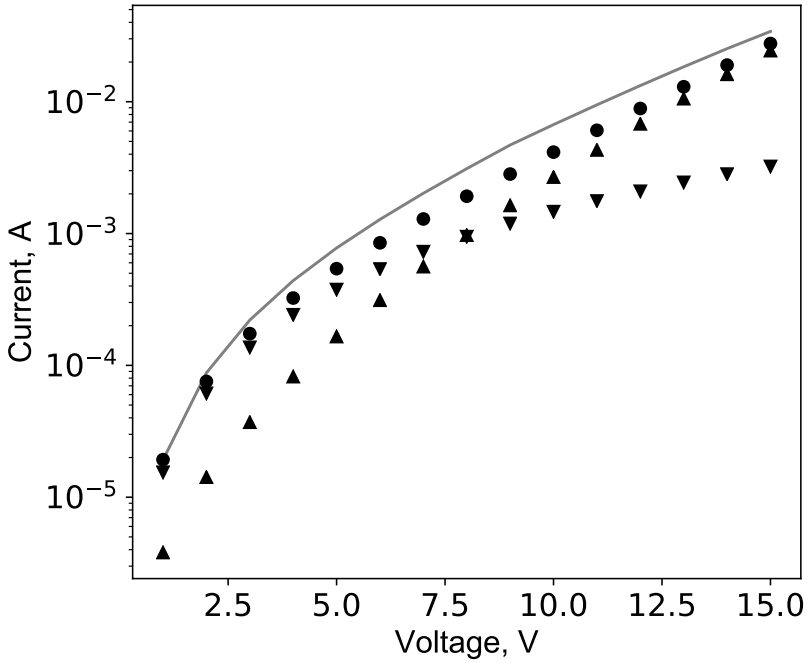


Figure 4.17: Current voltage characteristics of the model (solid gray line), thermal injection current (upward triangles), tunneling injection current (downward triangles) and their sum, depicted with the circles.

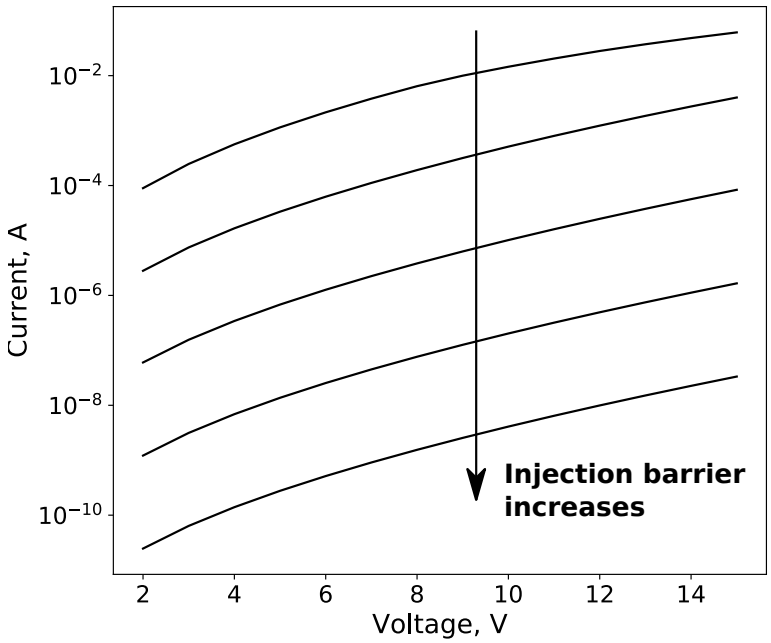


Figure 4.18: Injection barrier influence on the current-voltage characteristics in case of the absence of tunneling injection for the same barriers values as on fig. 4.16

As one sees from this plot, there are now drastic changes compared to fig. 4.16. First of all, there is now a clear distinction between different injection barrier values. The electrical current experiences now a drastic drop with every increase of the injection barrier by $0.1eV$. This was expected due to the exponential dependence of thermal injection current eq. 2.45 on the injection barrier. It seems that the chosen tunneling current model heavily homogenizes the results for different values of the injection, which made the simulation less dependent on the barriers.

Due to the large scale of current axis in 4.18, which is caused by orders of magnitude changes in the current, it might be hard to distinguish the individual features of each characteristics. However, overall these characteristics appear to be very similar. To enable a better visual comparison between low- and high-voltage region, we show a representative current-voltage curve for the barrier of 0.5 $eV$ in fig. 4.19.

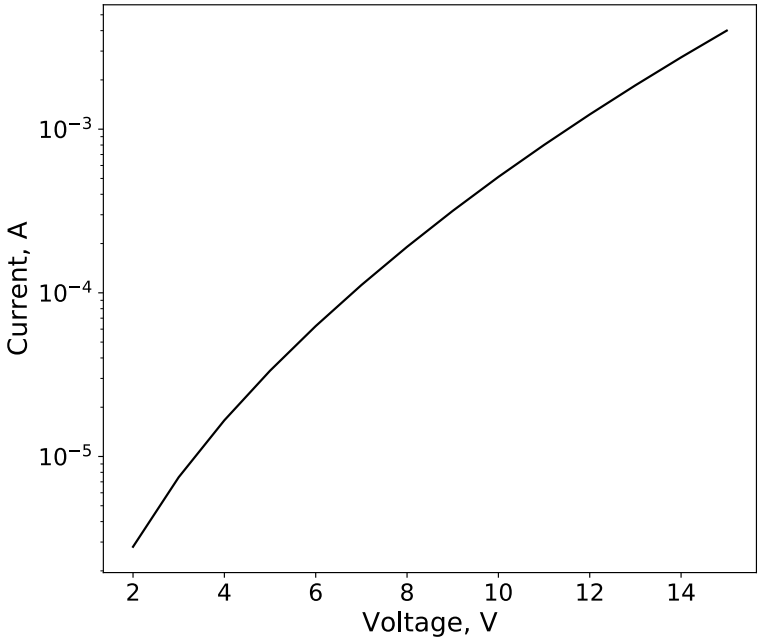


Figure 4.19: Injection barrier influence on the current-voltage characteristics in case of absent tunneling injection. injection barrier is 0.5 $eV$

From this figure we see, that the I-V curve still does not possess desirable low-voltage features. The plot resembles now a smooth exponential dependence. Apparently, tunneling current did not mask the turn on behavior, in fact, it was responsible for higher curvature of the plot. At this point, we decided to stop the investigation of the low voltage results as it became apparent that there is no parameter, which could cause the simulation to display desired low voltage properties. We would also like to emphasize the convergence issue we briefly covered in the sec. 4.4. The problem that the simulation requires large charge carrier accumulation to be converged, but at the same time one only has very low charge carrier fluxes (due to low overall current) poses immediate problems to even start solving this issue. On the one hand, one requires large time steps to account for low charge carrier fluxes, otherwise it will take too much time to get such simulations converged. On the other hand, large charge carrier densities may easily result in large diffusion currents, which then have to be

accounted for with small time steps. Otherwise simulated values start to oscillate, which is normala common behavior for forward Euler methods [184].

From our point of view, there are several possible solutions to these problems. The first solution is to avoid the use of drift-diffusion methods in the low voltage region. There are other investigations, which successfully describe low voltage region and are not based on drift-diffusion [198, 199]. The second solution would be to employ better injection current model which shows correct low voltage behavior. Last but not least, one may try to find approximate analytical solutions to the particular problem and use them as a starting point of the simulation. This may allow avoiding the necessary requirement of small time steps for large charge carrier densities, because precoverged simulation will not possess large charge carrier fluxes. We could not recommend however any literature for the last two options.

### Summary

In this chapter we performed the analysis of our model against experimental results. We have demonstrated that the large currents, which appear for large applied biases, can be captured well within the model. Moreover, the behavior of current when the device temperature gets higher follows the experimental trend very closely. This is important, as large temperature elevations due to self-heating happen only when the electric current through the device is high. However, at low voltages the results were not consistent with experiments, with deviations by orders of magnitude.

Afterwards, the influence of the model parametrization on the simulation results was briefly investigated. Our model has a large amount of free parameters and a full investigation for every possible set of parameters was impossible. Therefore, the investigation focused on the parameters which can actually be changed in real OLEDs, such as the mobility of the organic semiconductor, injection barriers from contacts to the OSC and the amount of free charge carriers in the contact. All of them have a pronounced influence on the modeling results, however, none of them helps to explain the low voltage behavior. Under these circumstances, we focused on the parameter, whose influence on the OLED is rarely addressed - the disorder parameter $\sigma$. This parameter has substantial influence both on the electric and thermal behavior and, as such, was the most interesting candidate to focus on. We found that a value of disorder parameter $\sigma = 55meV$ best describes both the thermal and the electric behavior of the device studied by our collaborators; furthermore, we robustly extract the same value for different methods of evaluation.

Last but not least, we tried to identify the source of the incorrect behavior of the model at low voltages. It was possible to narrow down the culprits to the injection from the metal into the OSC. We found that large tunneling injection at low voltage will always be present within the model and this will never allow simulation currents to approach experimental ones. However, the problem persists even if one removes the tunneling injection from the model. That indicates that it will be very hard to account for the low voltage region in drift-diffusion simulation in the absence of more comprehensive models for the injection currents.

# 5 Summary and conclusions

In this thesis, we utilized theoretical modeling of organic light emitting diodes to explore the thermal behavior of OLEDs, in particular its operating temperature.

For that purpose, a three-dimensional device simulation was developed, which was capable to capture thermal transport, electric transport within the organic layers of the device, as well as their interplay. In particular, it is capable to capture in action a vicious cycle, which is responsible for infamous bright spots on the surface of OLED devices. It can also include the more conventional thermoelectric effects, however, their effect is negligible compared to the vicious cycle, as constants responsible for thermoelectric effects are low in the materials of interest.

The implemented simulation incorporates a novel formulation of drift-diffusion equations, which were derived directly from hopping transport equations. Despite that, the resulting drift-diffusion equations kept their shape and we could see that, indeed, the drift-diffusion equations can be used to describe organic semiconductors. This approach was already described theoretically but has never to the best of our knowledge been employed in numerical simulations. For the conditions prevalent in our simulations, this approach becomes very close to conventional drift-diffusion equations. Nevertheless, it might be useful to deduce under which conditions drift-diffusion equations will fail to describe charge transport in amorphous organics, as one can test every made assumption explicitly. To estimate its full power, one would require different OLED setup with a significantly varying width of the density of states.

We investigated the impact of thermal transport parameters of the electrically active organic layers, such as the thermal conductivity and the heat transfer coefficient, and their influence on the device temperature. Specifically, we investigated the operating temperature for varying voltages, thermal conductivities of the electrically active organic layers and heat transport coefficient between them and the ambient environment. These simulations demonstrate that the voltage and the heat transport coefficient are the major players responsible for the temperature increase. The thermal conductivity, however, has no impact, due to the small thickness of the organic layers ($< 100nm$). This implies, that the temperature is distributed almost equally along the perpendicular, stacking axis. This conclusion is crucial, as it is often used as an underlying assumption in different modeling techniques, e.g, Kinetic Monte Carlo simulations. It also demonstrates that the real bottleneck for thermal transport in OLEDs is the heat outflow.

To unlock the capabilities of the 3D device simulation tool, we simulated the impact of an inhomogeneous voltage applied to a contact. Such an inhomogeneous voltage may readily lead to a local hot spot. The temperature-activated behavior of amorphous organic semiconductors makes the effect much more pronounced than in conventional LEDs. Hot spots are preferentially concentrated near the device contact, which leads to (and, simultaneously, is caused by) the total injection being dominated by the current, located near the hot spot. If one would want to continue this investigation, one would

require to (i) dive deeper into the injection current and its temperature dependence, as this seems to be the most important constituent of the hot spot and (ii) investigate how the thermal parameters are influencing the device temperature.

In the last part, we utilized the simulations to predict the impact of a given temperature on the device performance. These simulations allow us to assess to which extent the methodology proposed in this thesis captures observations from the experiment. While our drift-diffusion simulations are capable of correctly describing the behavior at higher voltages, they are incapable of describing the extremely low currents at the low voltage regime and to cover the transition between low and high voltages. We think. that the root cause for the inconsistencies between measured and predicted currents is the used description of the tunneling injection current, whose field dependence is inappropriate.

In the high voltage regime, we successfully determined the parameter, which most decisively controls the thermal behavior, the disorder parameter. The disorder parameter corresponds to the width of the density of states in an organic semiconductor. It was determined by several different evaluation methods from the comparison of predicted and measured current-voltage curves, based on Bayesian inference, each of which consistently leads to the same value. We think that due to its pronounced influence on the device behavior, any theoretical model should include it alongside with quiantities which are traditionally considered, such as mobility, injection barriers or activation energies.

# Bibliography


[1] Wikipedia article on luminous efficacy. Accessed: 2018-07-23. 1.2.1, 1.3.2

[2] H. J. Round. A note on carborundum. *Electrical World*, 19:309, 1907. 1.2.1

[3] O.V. Lossev. Cii. luminous carborundum detector and detection effect and oscillations with crystals. *The London, Edinburgh, and Dublin Philosophical Magazine and Journal of Science*, 6(39):1024–1044, 1928. 1.2.1

[4] Nick Holonyak and S. F. Bevacqua. Coherent (visible) light emission from ga/as junctions. *Applied Physics Letters*, 1(4):82–83, 1962. 1.2.1

[5] T. S. Perry. M. george craford [biography]. *IEEE Spectrum*, 32(2):52–55, Feb 1995. 1.2.1

[6] Shuji Nakamura, Takashi Mukai, and Masayuki Senoh. Candela-class high-brightness ingan/algan double-heterostructure blue-light-emitting diodes. *Applied Physics Letters*, 64(13):1687–1689, 1994. 1.2.1

[7] A. Bernanose; M. Comte ; P. Vouaux. A new method of light emission by certain organic compounds. *J. Chim. Phys.*, 50:64, 1953. 1.2.1

[8] P. Bernanose, A.; Vouaux. Organic electroluminescence type of emission. *J. Chim. Phys.*, 50:261, 1953. 1.2.1

[9] A. Bernanose. The mechanism of organic electroluminescence. *J. Chim. Phys.*, 52:396, 1955. 1.2.1

[10] P. Bernanose, A. Vouaux. Relation between organic electroluminescence and concentration of active product. *J. Chim. Phys.*, 52:509, 1955. 1.2.1

[11] M. Kallmann, H.; Pope. Positive hole injection into organic crystals. *The Journal of Chemical Physics.*, 32:300, 1960. 1.2.1, 1.3.5

[12] M. Kallmann, H.; Pope. Bulk conductivity in organic crystals. *Nature*, 186(4718):31–33, 1960. 1.2.1

[13] Wolfgang Mark, Peter; Helfrich. Space-charge-limited currents in organic crystals. *Journal of Applied Physics*, 33:205, 1962. 1.2.1, 1.3.5

[14] C. W. Tang and S. A. VanSlyke. Organic electroluminescent diodes. *Applied Physics Letters*, 51(12):913–915, 1987. 1.2.1

[15] Hyunkoo Lee, Insun Park, Jeonghun Kwak, Do Y. Yoon, and Changhee Lee. Improvement of electron injection in inverted bottom-emission blue phosphorescent organic light emitting diodes using zinc oxide nanoparticles. *Applied Physics Letters*, 96(15):153306, 2010. 1.2.1

[16] Yang Wan Kim, Won Kyu Kwak, Jae Yong Lee, Wong Sik Choi, Ki Yong Lee, Sung Chul Kim, and Eui Jin Yoo. 9.1: 40 inch fhd am-oled display with ir drop compensation pixel circuit. *SID Symposium Digest of Technical Papers*, 40(1):85–87, 2009. 1.2.1

[17] Andras I. Lakatos. Introduction. *Journal of the Society for Information Display*, 8(1):1–1, 2000. 1.2.1

[18] Myung Ho Lee, Song Myoung Seop, Jong Soo Kim, Jung Ho Hwang, Hye Jin Shin, Sang Kyun Cho, Kyoung Wook Min, Won Kyu Kwak, Sun I Jung, Chang Soo Kim, Woong Sik Choi, Sung Cheol Kim, and Eu Jin Yoo. 53.4: Development of 31-inch full-hd amoled tv using ltps-tft and rgb fmm. *SID Symposium Digest of Technical Papers*, 40(1):802–804, 2009. 1.2.1

[19] Joo Yee Low, Zulkifli Merican Aljunid Merican, and Mohammed Falalu Hamza. Polymer light emitting diodes (pleds): An update review on current innovation and performance of material properties. *Materials Today: Proceedings*, 16:1909 – 1918, 2019. Conference on Biomedical and Advanced Materials, 28-29 November 2017. 1.3

[20] Bernard Geffroy, Philippe le Roy, and Christophe Prat. Organic light-emitting diode (oled) technology: materials, devices and display technologies. *Polymer International*, 55(6):572–582, 2006. 1.3.1, 1.1, 1.3.2, 1.4.2

[21] V. Bulović, P. Tian, P. E. Burrows, M. R. Gokhale, S. R. Forrest, and M. E. Thompson. A surface-emitting vacuum-deposited organic light emitting device. *Applied Physics Letters*, 70(22):2954–2954, 1997. 1.3.1

[22] G. Gu, G. Parthasarathy, and S. R. Forrest. A metal-free, full-color stacked organic light-emitting device. *Applied Physics Letters*, 74(2):305–307, 1999. 1.3.1

[23] V. Bender, T. Marchesan, and J. Alonso. Solid-state lighting: A concise review of the state of the art on led and oled modeling. *IEEE Industrial Electronics Magazine*, 9:6–16, 2015. 1.3.1, 1.2

[24] Mohammed Azzouzi, Jun Yan, Thomas Kirchartz, Kaikai Liu, Jinliang Wang, Hongbin Wu, and Jenny Nelson. Nonradiative energy losses in bulk-heterojunction organic photovoltaics. *Phys. Rev. X*, 8:031055, Sep 2018. 1.3.1

[25] Yutaka Ohmori, Akihiko Fujii, Masao Uchida, Chikayoshi Morishima, and Katsumi Yoshino. Observation of spectral narrowing and emission energy shift in organic electroluminescent diode utilizing 8-hydroxyquinoline aluminum/aromatic diamine multilayer structure. *Applied Physics Letters*, 63(14):1871–1873, 1993. 1.3.1

[26] Liu Zugang and Helena Nazarè. White organic light-emitting diodes emitting from both hole and electron transport layers. *Synthetic Metals*, 111-112:47 – 51, 2000. 1.3.1

[27] K. Walzer, B. Maennig, M. Pfeiffer, and K. Leo. Highly efficient organic devices based on electrically doped transport layers. *Chemical Reviews*, 107(4):1233–1271, 2007. PMID: 17385929. 1.3.1, 1.3.3, 1.3.3

[28] Xuezhong Jiang, Yunqi Liu, Xinqi Song, and Daoben Zhu. Multilayer organic light-emitting diodes. *Solid State Communications*, 99(3):183 – 187, 1996. 1.3.1

[29] R. Meerheim, B. Lussem, and K. Leo. Efficiency and stability of p-i-n type organic light emitting diodes for display and lighting applications. *Proceedings of the IEEE*, 97(9):1606–1626, 2009. 1.3.1

[30] N. et al. Aizawa. Solution-processed multilayer small-molecule light-emitting devices with high-efficiency white-light emission. *Nat. Commun.*, 5:5776, 2014. 1.3.1

[31] H. Baek, H. Cho, and C. Lee. Multilayer white organic light emitting diode with optimum emitting layer sequence. In *2007 Conference on Lasers and Electro-Optics - Pacific Rim*, pages 1–2, 2007. 1.3.1

[32] A. Moliton. *Molecular and polymer optoelectronics: from Concepts to Devices.* 2005. 1.3.2

[33] Elison Matioli and C. Weisbuch. *Internal Quantum Efficiency in LEDs*, volume 126, pages 121–152. 01 2013. 1.3.2

[34] M. R. Krames, M. Ochiai-Holcomb, G. E. Höfler, C. Carter-Coman, E. I. Chen, I.-H. Tan, P. Grillot, N. F. Gardner, H. C. Chui, J.-W. Huang, S. A. Stockman, F. A. Kish, M. G. Craford, T. S. Tan, C. P. Kocot, M. Hueschen, J. Posselt, B. Loh, G. Sasser, and D. Collins. High-power truncated-inverted-pyramid (alxga1-x)0.5ino.5p/gap light-emitting diodes exhibiting ¿50% external quantum efficiency. *Applied Physics Letters*, 75(16):2365–2367, 1999. 1.3.2

[35] Motokazu Yamada, Tomotsugu Mitani, Yukio Narukawa, Shuji Shioji, Isamu Niki, Shinya Sonobe, Kouichiro Deguchi, Masahiko Sano, and Takashi Mukai. InGaN-based near-ultraviolet and blue-light-emitting diodes with high external quantum efficiency using a patterned sapphire substrate and a mesh electrode. *Japanese Journal of Applied Physics*, 41(Part 2, No. 12B):L1431–L1433, dec 2002. 1.3.2

[36] J. J. Wierer, M. R. Krames, J. E. Epler, N. F. Gardner, M. G. Craford, J. R. Wendt, J. A. Simmons, and M. M. Sigalas. Ingan/gan quantum-well heterostructure light-emitting diodes employing photonic crystal structures. *Applied Physics Letters*, 84(19):3885–3887, 2004. 1.3.2

[37] I. Schnitzer, E. Yablonovitch, C. Caneau, T. J. Gmitter, and A. Scherer. 30% external quantum efficiency from surface textured, thin-film light-emitting diodes. *Applied Physics Letters*, 63(16):2174–2176, 1993. 1.3.2

[38] J.C. Goldschmidt. *1.27 - Luminescent Solar Concentrator*. Elsevier, Oxford, 2012. 1.3.2

[39] A. Anselm. *Introduction to Semiconductor Theory*. 1978. 1.3.3, 1.3.3, 1.3.4, 1.5, 2

[40] Saumen Mandal and Yong-Young Noh. Printed organic thin-film transistor-based integrated circuits. *Semiconductor Science and Technology*, 30(6):064003, may 2015. 1.3.3

[41] Yifan Yao, Huanli Dong, and Wenping Hu. Charge transport in organic and polymeric semiconductors for flexible and stretchable devices. *Advanced Materials*, 28(22):4513–4523, 2016. 1.3.3

[42] Henning Sirringhaus. 25th anniversary article: Organic field-effect transistors: The path beyond amorphous silicon. *Advanced Materials*, 26(9):1319–1335, 2014. 1.3.3

[43] Gerwin Gelinck, Paul Heremans, Kazumasa Nomoto, and Thomas D. Anthopoulos. Organic transistors in optical displays and microelectronic applications. *Advanced Materials*, 22(34):3778–3798, 2010. 1.3.3

[44] James M. Campbell, Fiona C. Meldrum, and Hugo K. Christenson. Observing the formation of ice and organic crystals in active sites. *Proceedings of the National Academy of Sciences*, 114(5):810–815, 2017. 1.3.3

[45] Chengliang Wang, Huanli Dong, Lang Jiang, and Wenping Hu. Organic semiconductor crystals. *Chem. Soc. Rev.*, 47:422–500, 2018. 1.3.3

[46] M. Samoc, J.O. Williams, and D.F. Williams. Molecular organic crystals: A survey of their purification, growth and characterization. *Progress in Crystal Growth and Characterization*, 4(1):149 – 172, 1981. 1.3.3

[47] H. Staudinger. Über polymerisation. *Berichte der deutschen chemischen Gesellschaft (A and B Series)*, 53(6):1073–1085, 1920. 1.3.3

[48] Michael Cölle, Stefan Forero-Lenger, Jürgen Gmeiner, and Wolfgang Brütting. Vibrational analysis of different crystalline phases of the organic electroluminescent material aluminium tris(quinoline-8-olate) (alq3). *Phys. Chem. Chem. Phys.*, 5:2958–2963, 2003. 1.3.3

[49] F. Bloch. Uber die quantenmechanik der elektronen in kristallgittern. *Z. Physik*, 52:555–600, 1929. 1.3.3

[50] J H de Boer and E J W Verwey. Semi-conductors with partially and with completely filled3d-lattice bands. *Proceedings of the Physical Society*, 49(4S):59–71, aug 1937. 1.3.3

[51] Yao Yao, Wei Si, WenChao Yang, and Chang-Qin Wu. Charge transport in organic semiconductors: From incoherent to coherent. *Chinese Science Bulletin*, 58(22):2669–2676, Aug 2013. 1.3.3

[52] Nir Tessler, Yevgeni Preezant, Noam Rappaport, and Yohai Roichman. Charge transport in disordered organic materials and its relevance to thin-film devices: A tutorial review. *Advanced Materials*, 21(27):2741–2761, 2009. 1.3.3

[53] Ilhan Yavuz. Dichotomy between the band and hopping transport in organic crystals: insights from the experiments. *Phys. Chem. Chem. Phys.*, 19, 09 2017. 1.3.3

[54] Harald et al. Oberhofer. Charge transport in molecular materials: An assessment of computational methods. *Chemical Reviews*, 117(15):10319–10357, 2017. 1.3.3, 1.3.3

[55] G Paasch, Thomas Lindner, and S Scheinert. Variable range hopping as possible origin of a universal relation between conductivity and mobility in disordered organic semiconductors. *Synthetic Metals*, 132:97–104, 12 2002. 1.3.3

[56] Sung-Min Lee, Jeong Hyun Kwon, Seonil Kwon, and Kyung Choi. A review of flexible oleds toward highly durable unusual displays. *IEEE Transactions on Electron Devices*, PP:1–10, 01 2017. 1.3.3

[57] Sung-Min Lee, Yunil Cho, Dong-Young Kim, Joon-Sik Chae, and Kyung Cheol Choi. Enhanced light extraction from mechanically flexible, nanostructured organic light-emitting diodes with plasmonic nanomesh electrodes. *Advanced Optical Materials*, 3(9):1240–1247, 2015. 1.3.3

[58] Rocco P. Fornari and Alessandro Troisi. Theory of charge hopping along a disordered polymer chain. *Phys. Chem. Chem. Phys.*, 16:9997–10007, 2014. 1.3.3

[59] Veaceslav Coropceanu et al. Charge transport in organic semiconductors. *Chemical Reviews*, 107(5):926–952, 2007. 1.3.3

[60] I. I. Fishchuk, V. I. Arkhipov, A. Kadashchuk, P. Heremans, and H. Bässler. Analytic model of hopping mobility at large charge carrier concentrations in disordered organic semiconductors: Polarons versus bare charge carriers. *Phys. Rev. B*, 76:045210, Jul 2007. 1.3.3

[61] H. Bässler. Charge transport in disordered organic photoconductors a monte carlo simulation study. *Physica Status Solidi (b)*, 175(1):15–56, 1993. 1.3.3, 1.5

[62] Vadim Rodin, Franz Symalla, Velimir Meded, Pascal Friederich, Denis Danilov, Angela Poschlad, Gabriele Nelles, Florian von Wrochem, and Wolfgang Wenzel. Generalized effective-medium model for the carrier mobility in amorphous organic semiconductors. *Phys. Rev. B*, 91:155203, Apr 2015. 1.3.3

[63] Nianduan Lu, Ling Li, and Ming Liu. Universal carrier thermoelectric-transport model based on percolation theory in organic semiconductors. *Phys. Rev. B*, 91:195205, May 2015. 1.3.3, 2.2.2, 4.1

[64] B. Maennig, M. Pfeiffer, A. Nollau, X. Zhou, K. Leo, and P. Simon. Controlled p-type doping of polycrystalline and amorphous organic layers: Self-consistent description of conductivity and field-effect mobility by a microscopic percolation model. *Phys. Rev. B*, 64:195208, Oct 2001. 1.3.3

[65] K. Feron, X. Zhou, W. J. Belcher, and P. C. Dastoor. Exciton transport in organic semiconductors: Förster resonance energy transfer compared with a simple random walk. *Journal of Applied Physics*, 111(4):044510, 2012. 1.3.4

[66] M. Scheidler, U. Lemmer, R. Kersting, S. Karg, W. Riess, B. Cleve, R. F. Mahrt, H. Kurz, H. Bässler, E. O. Göbel, and P. Thomas. Monte carlo study of picosecond exciton relaxation and dissociation in poly(phenylenevinylene). *Phys. Rev. B*, 54:5536–5544, Aug 1996. 1.3.4

[67] Alice Ruini, Marilia J. Caldas, Giovanni Bussi, and Elisa Molinari. Solid state effects on exciton states and optical properties of ppv. *Phys. Rev. Lett.*, 88:206403, May 2002. 1.3.4

[68] V. Coropceanu J.-L. Bredas, D. Beljonne and J. Cornil. *Chem. Rev.*, 104,:4971–5004, 2004,. 1.3.4

[69] Oleksandr V. Mikhnenko, Paul W. M. Blom, and Thuc-Quyen Nguyen. Exciton diffusion in organic semiconductors. *Energy Environ. Sci.*, 8:1867–1888, 2015. 1.3.4

[70] Gregory H. Wannier. The structure of electronic excitation levels in insulating crystals. *Phys. Rev.*, 52:191–197, Aug 1937. 1.3.4

[71] Hai-Wei Chen, Jiun-Haw Lee, Bo-Yen Lin, Stanley Chen, and Shin-Tson Wu. Liquid crystal display and organic light-emitting diode display: present status and future perspectives. *Light: Science and Applications*, 7:17168, 2018. 1.3.4

[72] Yoga Divayana, Shuwei Liu, Aung Ko Ko Kyaw, and Xiao Wei Sun. Efficient extraction of singlet–triplet excitons for high-efficient white organic light-emitting diode with a multilayer emission region. *Organic Electronics*, 12(1):1 – 7, 2011. 1.3.4

[73] Xiantong Tang, Yeqian Hu, Weiyao Jia, Ruiheng Pan, Junquan Deng, Jinqiu Deng, Zhenghong He, and Zuhong Xiong. Intersystem crossing and triplet fusion in singlet-fission-dominated rubrene-based oleds under high bias current. *ACS Applied Materials and Interfaces*, 10((2)):1948–1956, 2018. 1.3.4

[74] Masanobu Wakasa, Tomoaki Yago, Yoriko Sonoda, and Ryuzi Katoh. Structure and dynamics of triplet-exciton pairs generated from singlet fission studied via magnetic field effects. *Communications Chemistry*, 1:2399–3699, 2018. 1.3.4

[75] Dandan Song, Suling Zhao, Yichun Luo, and Hany Aziz. Causes of efficiency roll-off in phosphorescent organic light emitting devices: Triplet-triplet annihilation versus triplet-polaron quenching. *Applied Physics Letters*, 97(24):243304, 2010. 1.3.4

[76] N. C. Giebink, B. W. D'Andrade, M. S. Weaver, J. J. Brown, and S. R. Forrest. Direct evidence for degradation of polaron excited states in organic light emitting diodes. *Journal of Applied Physics*, 105(12):124514, 2009. 1.3.4

[77] Yuki Seino, Hisahiro Sasabe, Yong-Jin Pu, and Junji Kido. High-performance blue phosphorescent oleds using energy transfer from exciplex. *Advanced Materials*, 26(10):1612–1616, 2014. 1.3.4

[78] Egbert Zojer, Thomas C. Taucher, and Oliver T. Hofmann. The impact of dipolar layers on the electronic properties of organic/inorganic hybrid interfaces. *Advanced Materials Interfaces*, 6(14):1900581, 2019. 1.3.5

[79] Norbert Koch. Organic electronic devices and their functional interfaces. *ChemPhysChem*, 8(10):1438–1455, 2007. 1.3.5

[80] K. Walzer, B. Maennig, M. Pfeiffer, and K. Leo. Highly efficient organic devices based on electrically doped transport layers. *Chemical Reviews*, 107(4):1233–1271, 2007. PMID: 17385929. 1.3.5

[81] D. F. O'Brien, M. A. Baldo, M. E. Thompson, and S. R. Forrest. Improved energy transfer in electrophosphorescent devices. *Applied Physics Letters*, 74(3):442–444, 1999. 1.3.5

[82] Vadim I. Adamovich, Steven R. Cordero, Peter I. Djurovich, Arnold Tamayo, Mark E. Thompson, Brian W. D'Andrade, and Stephen R. Forrest. New charge-carrier blocking materials for high efficiency oleds. *Organic Electronics*, 4(2):77 – 87, 2003. High Efficiency Light Emitters. 1.3.5

[83] Hisao Ishii, Kiyoshi Sugiyama, Eisuke Ito, and Kazuhiko Seki. Energy level alignment and interfacial electronic structures at organic/metal and organic/organic interfaces. *Advanced Materials*, 11(8):605–625, 1999. 1.3.5, 1.3.5

[84] Antoine Kahn, Norbert Koch, and Weiying Gao. Electronic structure and electrical properties of interfaces between metals and pi-conjugated molecular films. *Journal of Polymer Science Part B: Polymer Physics*, 41(21):2529–2548, 2003. 1.3.5

[85] J. Campbell Scott. Metal–organic interface and charge injection in organic electronic devices. *Journal of Vacuum Science & Technology A*, 21(3):521–531, 2003. 1.3.5

[86] Slawomir Braun, William R. Salaneck, and Mats Fahlman. Energy-level alignment at organic/metal and organic/organic interfaces. *Advanced Materials*, 21(14-15):1450–1472, 2009. 1.3.5

[87] Jaehyung Hwang, Alan Wan, and Antoine Kahn. Energetics of metal–organic interfaces: New experiments and assessment of the field. *Materials Science and Engineering: R: Reports*, 64(1):1 – 31, 2009. 1.3.5

[88] Yongli Gao. Surface analytical studies of interfaces in organic semiconductor devices. *Materials Science and Engineering: R: Reports*, 68(3):39 – 87, 2010. 1.3.5

[89] R. Otero, A.L. Vázquez de Parga, and J.M. Gallego. Electronic, structural and chemical effects of charge-transfer at organic/inorganic interfaces. *Surface Science Reports*, 72(3):105 – 145, 2017. 1.3.5

[90] Gilles Horowitz. Organic thin film transistors: From theory to real devices. *Journal of Materials Research*, 19(7):1946–1962, 2004. 1.3.5

[91] H. Sirringhaus. Device physics of solution-processed organic field-effect transistors. *Advanced Materials*, 17(20):2411–2425, 2005. 1.3.5

[92] Dario Natali and Mario Caironi. Charge injection in solution-processed organic field-effect transistors: Physics, models and characterization methods. *Advanced Materials*, 24(11):1357–1387, 2012. 1.3.5

[93] Egbert Zojer, Thomas C. Taucher, and Oliver T. Hofmann. The impact of dipolar layers on the electronic properties of organic/inorganic hybrid interfaces. *Advanced Materials Interfaces*, 6(14):1900581, 2019. 1.3.5, 1.3.5

[94] Hee Cheul Choi Chibeom Park, Ji Eun Park. Crystallization-induced properties from morphology-controlled organic crystals. *Acc. Chem. Res*, 8(47):2353–2364, 2014. 1.3.5

[95] Andrew O. F. Jones, Basab Chattopadhyay, Yves H. Geerts, and Roland Resel. Substrate-induced and thin-film phases: Polymorphism of organic materials on surfaces. *Advanced Functional Materials*, 26(14):2233–2255, 2016. 1.3.5

[96] P. Lenard. Ueber die lichtelektrische wirkung. *Annalen der Physik*, 313(5):149–198, 1902. 1.3.5

[97] W. Kohn N.D. Lang. *Phys. Rev. B*, 7:3541, 1973. 1.3.5

[98] A. Natan, L. Kronik, H. Haick, and R. T. Tung. Electrostatic properties of ideal and non-ideal polar organic monolayers: Implications for electronic devices. *Advanced Materials*, 19(23):4103–4117, 2007. 1.3.5

[99] Christof Woll. The chemistry and physics of zinc oxide surfaces. *Progress in Surface Science*, 82(2):55 – 120, 2007. 1.3.5

[100] Bjoern Bieniek, Oliver T. Hofmann, and Patrick Rinke. Influence of hydrogen on the structure and stability of ultra-thin zno on metal substrates. *Applied Physics Letters*, 106(13):131602, 2015. 1.3.5

[101] Raymond T. Tung. The physics and chemistry of the schottky barrier height. *Applied Physics Reviews*, 1(1):011304, 2014. 1.3.5

[102] Heimel G. Salzmann I. et al. Duhm, S. Orientation-dependent ionization energies and interface dipoles in ordered molecular assemblies. *Nature Mater*, 7:326–332, 2008. 1.3.5

[103] Seungjun Chung, Jae-Hyun Lee, Jaewook Jeong, Jang-Joo Kim, and Yongtaek Hong. Substrate thermal conductivity effect on heat dissipation and lifetime improvement of organic light-emitting diodes. *Applied Physics Letters*, 94(25):253302, 2009. 1.4.1

[104] Hui Lin, Jun-sheng Yu, and Wei Zhang. Investigation of top-emitting oleds using molybdenum oxide as anode buffer layer. *Optoelectronics Letters*, 8(3):197–200, May 2012. 1.4.1, 1.4.2

[105] K. Tong, Sai-Wing Tsang, K. Tsung, S. Tse, and S. So. Hole transport in molecularly doped naphthyl diamine. *Journal of Applied Physics - J APPL PHYS*, 102, 11 2007. 1.4.2

[106] C. H. B. Mee A. W. Dweydari. Work function measurements on (100) and (110) surfaces of silver. *Physica status solidi*, 27, 01 1975. 1.4.2

[107] I.G. Hill, D. Milliron, J. Schwartz, and A. Kahn. Organic semiconductor interfaces: electronic structure and transport properties. *Applied Surface Science*, 166(1):354 – 362, 2000. 7TH INTERNATIONAL CONF. ON FORMATION OF SEMICONDUCTOR INTERFACES. 1.4.2

[108] Han You, Yanfeng Dai, Zhiqiang Zhang, and ma Dongge. Improved performances of organic light-emitting diodes with metal oxide as anode buffer. *Journal of Applied Physics*, 101:026105 – 026105, 02 2007. 1.4.2

[109] Han You, Yanfeng Dai, Zhiqiang Zhang, and Dongge Ma. Improved performances of organic light-emitting diodes with metal oxide as anode buffer. *Journal of Applied Physics*, 101(2):026105, 2007. 1.4.2

[110] Dhrubajyoti Saikia and Ranjit Sarma. Fabrication of organic light-emitting diode using molybdenum trioxide interlayer between electrode and organic interface. *Bulletin of Materials Science*, 41(4):95, Jul 2018. 1.4.2

[111] Mario Petrosino and Alfredo Rubino. Analysis of pinning effect at the alq3/metal interface in organic light emitting diodes. *Journal of Applied Physics*, 112(1):014504, 2012. 1.4.2

[112] Chongfei Shen and Antoine Kahn. The role of interface states in controlling the electronic structure of alq3/reactive metal contacts. *Organic Electronics*, 2:89–95, 09 2001. 1.4.2

[113] V.-E. Choong, M. G. Mason, C. W. Tang, and Yongli Gao. Investigation of the interface formation between calcium and tris-(8-hydroxy quinoline) aluminum. *Applied Physics Letters*, 72(21):2689–2691, 1998. 1.4.2

[114] Po-Ching Kao, Jie-Han Lin, Jing-Yuan Wang, Cheng-Hsien Yang, and Sy-Hann Chen. Improved electron injection into alq3 based oleds using a thin lithium carbonate buffer layer. *Synthetic Metals*, 160(15):1749 – 1753, 2010. 1.4.2

[115] G. E. Jabbour, B. Kippelen, N. R. Armstrong, and N. Peyghambarian. Aluminum based cathode structure for enhanced electron injection in electroluminescent organic devices. *Applied Physics Letters*, 73(9):1185–1187, 1998. 1.4.2

[116] S. Kim, Joo Hyun Kim, and J. Lee. Formation of a ca/lif/alq3 cathode for an organic light-emitting diode: Evolution of the electronic structure as studied by photoemission spectroscopy. *Journal of The Korean Physical Society - J KOREAN PHYS SOC*, 53, 08 2008. 1.4.2

[117] K.L Wang, B Lai, Ming Lu, Xunxiu Zhou, L. S. Liao, X. Ding, X.Y. Hou, and S. Lee. Electronic structure and energy level alignment of alq3/al203/al and alq3/al interfaces studied by ultraviolet photoemission spectroscopy. *Thin Solid Films*, 363:178–181, 03 2000. 1.4.2

[118] T.P Nguyen, P Jolinat, P Destruel, R Clergereaux, and J Farenc. Degradation in organic light-emitting diodes. *Thin Solid Films*, 325(1):175 – 180, 1998. 1.5

[119] D. Klotzkin H. Mu, H. Shen. Dependence of film morphology on deposition rate in ito/tpd/alq3/al organic luminescent diodes. *Solid-State Electronics*, 48:2085–2088, 2004. 1.5

[120] J. Steiger, S. Karg, R. Schmechel, and H. von Seggern. Aging induced traps in organic semiconductors. *Synthetic Metals*, 122(1):49 – 52, 2001. Proceedings of the E-MRS 2000 Spring Meeting, Symposium I. 1.5

[121] Nenna G., Flaminio G., Fasolino T., Minarini C., Miscioscia R., Palumbo D., and Pellegrino M. A study on thermal degradation of organic leds using ir imaging. *Macromolecular Symposia*, 247(1):326–332, 2007. 1.5

[122] Dong Hoe Chung, Sung Woo Hur, Sang Keol Kim, Joon Ung Lee, Chung Hyeok Kim, Jin Woong Hong, and Tae Wan Kim. Temperature-dependent electrical properties of organic light-emitting diodes depending on cathodes. *Current Applied Physics*, 4(6):667 – 670, 2004. 1.5

[123] O'Brien Diarmuid F., Burrows Paul E., Forrest Stephen R., Koene Bryan E., Loy Douglas E., and Thompson Mark E. Hole transporting materials with high glass transition temperatures for use in organic light-emitting devices. *Advanced Materials*, 10(14):1108–1112, 1999. 1.5

[124] George Vamvounis, Hany Aziz, Nan-Xing Hu, and Zoran D. Popovic. Temperature dependence of operational stability of organic light emitting diodes based on mixed emitter layers. *Synthetic Metals*, 143(1):69 – 73, 2004. 1.5

[125] M S Xu and J B Xu. Real-time visualization of thermally activated degradation of the ito/cupc/npb/alq 3 stack used in one of the organic light-emitting diodes. *Journal of Physics D: Applied Physics*, 37(12):1603, 2004. 1.5

[126] Xiang Zhou, Jun He, Liang S. Liao, Ming Lu, Xun M. Ding, Xiao Y. Hou, Xiao M. Zhang, Xiao Q. He, and Shuit T. Lee. Real-time observation of temperature rise and thermal breakdown processes in organic LEDs using an IR imaging and analysis system. *Advanced Materials*, 12:265–269, 2000. 1.5

[127] Paulo N.M dos Anjos, Hany Aziz, Nan-Xing Hu, and Zoran D Popovic. Temperature dependence of electroluminescence degradation in organic light emitting devices without and with a copper phthalocyanine buffer layer. *Organic Electronics*, 3(1):9 – 13, 2002. 1.5

[128] Xue Li, Xinfang Yuan, Wenjuan Shang, Yuqiao Guan, Lingling Deng, and Shufen Chen. Lifetime improvement of organic light-emitting diodes with a butterfly wing's scale-like nanostructure as a flexible encapsulation layer. *Organic Electronics*, 37:453 – 457, 2016. 1.5

[129] Seungjun Chung, Jae-Hyun Lee, Jaewook Jeong, Jang-Joo Kim, and Yongtaek Hong. Substrate thermal conductivity effect on heat dissipation and lifetime improvement of organic light-emitting diodes. *Applied Physics Letters*, 94(25):253302, 2009. 1.5

[130] A. Fischer, P. Pahner, B. Lüssem, K. Leo, R. Scholz, T. Koprucki, K. Gärtner, and A. Glitzky. Self-heating, bistability, and thermal switching in organic semiconductors. *Phys. Rev. Lett.*, 110:126601, Mar 2013. 1.5, 4.1

[131] Axel Fischer, Thomas Koprucki, Klaus Gärtner, Max L. Tietze, Jacqueline Brückner, Björn Lüssem, Karl Leo, Annegret Glitzky, and Reinhard Scholz. Feel the heat: Nonlinear electrothermal feedback in organic leds. *Advanced Functional Materials*, 24(22):3367–3374, 2014. 1.5, 3.1.2

[132] C. Gärditz, A. Winnacker, F. Schindler, and R. Paetzold. Impact of Joule heating on the brightness homogeneity of organic light emitting devices. *Applied Physics Letters*, 90(10):103506, mar 2007. 1.5

[133] Yansha Jin, Chen Shao, John Kieffer, Michael L. Falk, and Max Shtein. Spatial nonuniformity in heat transport across hybrid material interfaces. *Phys. Rev. B*, 90:054306, Aug 2014. 1.5

[134] J W Park, D C Shin, and S H Park. Large-area OLED lightings and their applications. *Semiconductor Science and Technology*, 26(3):034002, mar 2011. 1.5

[135] Jongwoon Park, Hyokyun Ham, and Cheolyoung Park. Heat transfer property of thin-film encapsulation for OLEDs. *Organic Electronics*, 12(2):227–233, feb 2011. 1.5

[136] Jongwoon Park, Jongho Lee, and Yong-Young Noh. Optical and thermal properties of large-area oled lightings with metallic grids. *Organic Electronics*, 13(1):184 – 194, 2012. 1.5

[137] J W Park and J H Lee. Heat dissipation property of cover glasses with heat sink films for transparent organic light-emitting diodes. *Semiconductor Science and Technology*, 29(9):095023, sep 2014. 1.5

[138] Xiangfei Qi and Stephen R. Forrest. Thermal analysis of high intensity organic light-emitting diodes based on a transmission matrix approach. *Journal of Applied Physics*, 110(12):124516, 2011. 1.5

[139] Ross E. Triambulo and Jin-Woo Park. Heat evolution and dissipation in organic light-emitting diodes on flexible polymer substrates. *Organic Electronics*, 28:123 – 134, 2016. 1.5

[140] Axel Fischer, Manuel Pfalz, Koen Vandewal, Simone Lenk, Matthias Liero, Annegret Glitzky, and Sebastian Reineke. Full electrothermal oled model including nonlinear self-heating effects. *Phys. Rev. Applied*, 10:014023, Jul 2018. 1.5, 4.1, 4.3, 4.3

[141] Kristiaan Neyts, Matthias Marescaux, AU NIETO, A ELSCHNER, W LOVENICH, K FEHSE, Q HUANG, K WALZER, and K LEO. Inhomogeneous luminance in organic light emitting diodes related to electrode resistivity. *JOURNAL OF APPLIED PHYSICS*, 100(11), 2006. 1.5

[142] Xiangfei Qi and Stephen R. Forrest. Thermal analysis of high intensity organic light-emitting diodes based on a transmission matrix approach. *Journal of Applied Physics*, 110(12):124516, 2011. 1.5

[143] Hyeong Woo Bae, Young Hoon Son, Byoung Yeop Kang, Jung Min Lee, Hyoungsik Nam, and Jang Hyuk Kwon. Luminance uniformity study of oled lighting panels depending on oled device structures. *Opt. Express*, 23(24):30701–30708, Nov 2015. 1.5

[144] LáSzló Pohl, Ern KolláR, AndráS Poppe, and Zsolt KoháRi. Nonlinear electrothermal modeling and field-simulation of oleds for lighting applications i: Algorithmic fundamentals. *Microelectron. J.*, 43(9):624–632, September 2012. 1.5

[145] V. C. Bender, N. D. Barth, F. B. Mendes, R. A. Pinto, J. M. Alonso, and T. B. Marchesan. Modeling and characterization of organic light-emitting diodes including capacitance effect. *IEEE Transactions on Electron Devices*, 62(10):3314–3321, 2015. 1.5

[146] G. Krikun and K. Zojer. Impact of thermal transport parameters on the operating temperature of organic light emitting diodes. *Journal of Applied Physics*, 125(8):085501, 2019. 2, 2.8, 3, 3.1.3, 3.1.3, 3.1.3

[147] G. Krikun and K. Zojer. Impact of thermal transport parameters on the operating temperature of organic light emitting diodes. *Journal of Applied Physics*, 125(8):085501, Feb 2019. 2, 2.8, 3, 3.1.3, 3.1.3, 3.1.3, 3.1.3

[148] L.D. Landau and E.M. Lifshitz. *The classical theory of fields, 3rd ed.* 1971. 2

[149] Murat Mesta, Marco Carvelli, Rein J de Vries, Harm van Eersel, Jeroen J M van der Holst, Matthias Schober, Mauro Furno, Björn Lüssem, Karl Leo, Peter Loebl, Reinder Coehoorn, and P Bobbert. Molecular-scale simulation of electroluminescence in a multilayer white organic light-emitting diode. *Nature materials*, 12, 04 2013. 2.2.1, 4.1

[150] Alfred Liemant. A drift-diffusion equation for charge transport in inhomogeneous materials. *WIAS Preprint*, (384):384, 1997. 2.2.2

[151] P. S. Davids, Sh. M. Kogan, I. D. Parker, and D. L. Smith. Charge injection in organic light-emitting diodes: Tunneling into low mobility materials. *Applied Physics Letters*, 69(15):2270–2272, 1996. 2.2.2, 4.1, 4.4

[152] E. Knapp, R. Häusermann, H. U. Schwarzenbach, and B. Ruhstaller. Numerical simulation of charge transport in disordered organic semiconductor devices. *Journal of Applied Physics*, 108(5):054504, sep 2010. 2.2.2, 4.1

[153] Evelyne Knapp and Beat Ruhstaller. Numerical analysis of steady-state and transient charge transport in organic semiconductor devices. *Optical and Quantum Electronics*, 42(11-13):667–677, oct 2011. 2.2.2, 4.1

[154] Dan Mendels and Nir Tessler. Drift and diffusion in disordered organic semiconductors: The role of charge density and charge energy transport. *The Journal of Physical Chemistry C*, 117(7):3287–3293, 2013. 2.2.2

[155] I. I. Fishchuk, D. Hertel, H. Bässler, and A. K. Kadashchuk. Effective-medium theory of hopping charge-carrier transport in weakly disordered organic solids. *Phys. Rev. B*, 65:125201, Mar 2002. 2.2.2

[156] I. I. Fishchuk, A. K. Kadashchuk, J. Genoe, Mujeeb Ullah, H. Sitter, Th. B. Singh, N. S. Sariciftci, and H. Bässler. Temperature dependence of the charge carrier mobility in disordered organic semiconductors at large carrier concentrations. *Phys. Rev. B*, 81:045202, Jan 2010. 2.2.2

[157] I. I. Fishchuk, A. Kadashchuk, S. T. Hoffmann, S. Athanasopoulos, J. Genoe, H. Bässler, and A. Köhler. Unified description for hopping transport in organic semiconductors including both energetic disorder and polaronic contributions. *Physical Review B*, 88(12):125202, sep 2013. 2.2.2

[158] I. I. Fishchuk, V. I. Arkhipov, A. Kadashchuk, P. Heremans, and H. Bässler. Analytic model of hopping mobility at large charge carrier concentrations in disordered organic semiconductors: Polarons versus bare charge carriers. *Phys. Rev. B*, 76:045210, Jul 2007. 2.2.2

[159] W. F. Pasveer, J. Cottaar, C. Tanase, R. Coehoorn, P. A. Bobbert, P. W. M. Blom, D. M. de Leeuw, and M. A. J. Michels. Unified description of charge-carrier mobilities in disordered semiconducting polymers. *Phys. Rev. Lett.*, 94:206601, May 2005. 2.2.2, 2.7, 4.1, 4.2, 4.2, 4.4

[160] H. P. Huinink, P. A. Bobbert, W. F. Pasveer, and M. A. J. Michels. Structure and conductivity of clusters generated by variable-range hopping percolation. *Phys. Rev. B*, 73:224204, Jun 2006. 2.2.2

[161] Yohai Roichman and Nir Tessler. Generalized einstein relation for disordered semiconductors—implications for device performance. *Applied Physics Letters*, 80(11):1948–1950, 2002. 2.2.2

[162] J. E. Sutherland and J. R. Hauser. A computer analysis of heterojunction and graded composition solar cells. *IEEE Transactions on Electron Devices*, 24:363–372, 1977. 2.4.2

[163] P. S. Davids, I. H. Campbell, and D. L. Smith. Device model for single carrier organic diodes. *Journal of Applied Physics*, 82(12):6319–6325, 1997. 2.4.2, 2.4.2, 2.4.3, 4.1

[164] J. C. Scott and G. G. Malliaras. Charge injection and recombination at the metal organic interface. *Chemical Physics Letters*, 299:115–119, January 1999. 2.4.2

[165] Mohammad Javad Sharifi and Farzad Ahmadi Gooraji. A quantitative index for injection/transport mechanism in organic light-emitting diodes. *Journal of Organic Semiconductors*, 1(1):1–6, 2013. 2.4.2

[166] M. Gruber, F. Schürrer, and K. Zojer. Relation between injection barrier and contact resistance in top-contact organic thin-film transistors. *Organic Electronics*, 13(10):1887 – 1899, 2012. 2.4.2

[167] D. Mahaveer Sathaiya and Shreepad Karmalkar. Thermionic trap-assisted tunneling model and its application to leakage current in nitrided oxides and algan/gan high electron mobility transistors. *Journal of Applied Physics*, 99(9):093701, 2006. 2.4.2, 4.1

[168] Semjon Adlaj. An eloquent formula for the perimeter of an ellipse. *Notices of the American Mathematical Society*, 59, 09 2012. 2.4.2, 6

[169] Christopher C. Lindn. *Density of Charge Carriers in Silver*. 2008. 2.4.2, 4.1.1, 4.3

[170] Wikipedia article on gaussian units. Accessed: 2020-11-21. 2.4.3, 2.4.3

[171] Wikipedia article on si units. Accessed: 2020-11-21. 2.4.3

[172] Kevin J. Bergemann, Robert Krasny, and Stephen R. Forrest. Thermal properties of organic light-emitting diodes. *Organic Electronics*, 13(9):1565 – 1568, 2012. 2.4.4

[173] Philipp Schwamb, Thilo C.G. Reusch, and Christoph J. Brabec. Passive cooling of large-area organic light-emitting diodes. *Organic Electronics*, 14(8):1939 – 1945, 2013. 2.4.4

[174] László Pohl, Ernő Kollár, András Poppe, and Zsolt Kohári. Nonlinear electro-thermal modeling and field-simulation of oleds for lighting applications i: Algorithmic fundamentals. *Microelectronics Journal*, 43(9):624 – 632, 2012. THERMINIC 2010. 2.4.4

[175] Joon Sang Kang, Man Li, Huan Wu, Huuduy Nguyen, and Yongjie Hu. Experimental observation of high thermal conductivity in boron arsenide. *Science*, 361(6402):575–578, 2018. 2.4.4

[176] L. Lindsay, D. A. Broido, and T. L. Reinecke. First-principles determination of ultrahigh thermal conductivity of boron arsenide: A competitor for diamond? *Phys. Rev. Lett.*, 111:025901, Jul 2013. 2.4.4

[177] Tianli Feng, Lucas Lindsay, and Xiulin Ruan. Four-phonon scattering significantly reduces intrinsic thermal conductivity of solids. *Phys. Rev. B*, 96:161201, Oct 2017. 2.4.4

[178] C. Uher. Keeping it cool. *Physics (College Park Md.)*, 6, 2013. 2.4.4

[179] D. A. Broido, L. Lindsay, and T. L. Reinecke. Ab initio study of the unusual thermal transport properties of boron arsenide and related materials. *Phys. Rev. B*, 88:214303, Dec 2013. 2.4.4

[180] S. K. Estreicher, T. M. Gibbons, and M. B. Bebek. Thermal phonons and defects in semiconductors: The physical reason why defects reduce heat flow, and how to control it. *Journal of Applied Physics*, 117(11):112801, 2015. 2.4.4

[181] M. P. Langevin. *Ann. Chim. Phys.*, 28:433, 1903. 2.5

[182] Yiming Liu, Karin Zojer, Benny Lassen, Jakob Kjelstrup-Hansen, Horst-Günter Rubahn, and Morten Madsen. The role of charge transfer state on the reduced langevin recombination in organic solar cells: A theoretical study. *The Journal of Physical Chemistry C*, 119, 10 2015. 2.5

[183] Matthew J. Carnieb Derya Baranc Lewis M. Cowena, Jonathan Atoyob and Bob C. Schroeder. Review—organic materials for thermoelectric energy generation. *ECS J. Solid State Sci. Technology*, 6:N3080–N3088, 2017. 2.5.1

[184] J. C. BUTCHER. *Numerical Methods for Ordinary Differential Equations*. 2003. 2.6.1, 4.4

[185] James Nagel. Numerical solutions to poisson equations using the finite-difference method [education column]. *IEEE Antennas and Propagation Magazine*, 56:209, 08 2014. 2.6.2

[186] D. L. Scharfetter and H. K. Gummel. *IEEE Trans. Electron Devices*, ED-16:64, 1969. 2.6.3

[187] Thomas Koprucki and Klaus Gärtner. Discretization scheme for drift-diffusion equations with strong diffusion enhancement. *Optical and Quantum Electronics*, 45, 08 2012. 2.6.3

[188] Thomas Koprucki, Nella Rotundo, Patricio Farrell, Duy Hai Doan, and Jürgen Fuhrmann. On thermodynamic consistency of a scharfetter–gummel scheme based on a modified thermal voltage for drift-diffusion equations with diffusion enhancement. *Optical and Quantum Electronics*, 47(6):1327–1332, Jun 2015. 2.6.3

[189] Marianne Bessemoulin-Chatard. A finite volume scheme for convection–diffusion equations with nonlinear diffusion derived from the scharfetter–gummel scheme. *Numerische Mathematik*, 121(4):637–670, Aug 2012. 2.6.3

[190] Iris Hehn. Investigation of the impact of interface dipole layers on the performance of organic solar cells by drift-diffusion simulations, 2012. 2.6.3

[191] James C. Blakesley, Fernando A. Castro, William Kylberg, George F.A. Dibb, Caroline Arantes, Rogério Valaski, Marco Cremona, Jong Soo Kim, and Ji-Seon Kim. Towards reliable charge-mobility benchmark measurements for organic semiconductors. *Organic Electronics*, 15(6):1263 – 1272, 2014. 2.7

[192] T. Beilstein Kirchartz. Influence of diffusion on space-charge-limited current measurements in organic semiconductors. *Beilstein J. Nanotechnol.*, 4:180–188, 2013. 2.7

[193] Reisdorffer, Frederic, Garnier, Bertrand, Horny, Nicolas, Renaud, Cedric, Chirtoc, Mihai, and Nguyen, Thien-Phap. Thermal conductivity of organic semiconducting materials using 3omega and photothermal radiometry techniques. *EPJ Web of Conferences*, 79:02001, 2014. 2.9, 3.1.2

[194] Nicolas Horny Cedric Renaud Mihai Chirtoc Frederic Reisdorffer, Bertrand Garnier and Thien-Phap Nguyen. Thermal conductivity of organic semi-conducting materials using 3omega and photothermal radiometry techniques. *EPJ Web of Conferences*, 79:02001, 2014. 3.1.2

[195] Namsu Kim, Benoit Domercq, Seunghyup Yoo, Adam Christensen, Bernard Kippelen, and Samuel Graham. Thermal transport properties of thin films of small molecule organic semiconductors. *Applied Physics Letters*, 87(24):241908, 2005. 3.1.2

[196] An-Chi Wei, Yih-Jong Huang, Bo-Lin Huang, and Jyh-Rou Sze. Integration of Optical and Thermal Models for Organic Light-Emitting Diodes. *Electronics*, 8(1):17, January 2019. Number: 1 Publisher: Multidisciplinary Digital Publishing Institute. 3.1.3

[197] Yansha Jin, Chen Shao, John Kieffer, Kevin P. Pipe, and Max Shtein. Origins of thermal boundary conductance of interfaces involving organic semiconductors. *Journal of Applied Physics*, 112(9):093503, 2012. 3.1.4

[198] Chang Hyun Kim, Omid Yaghmazadeh, Yvan Bonnassieux, and Gilles Horowitz. Modeling the low-voltage regime of organic diodes: Origin of the ideality factor. *Journal of Applied Physics*, 110(9):093722, November 2011. Publisher: American Institute of Physics. 4.1, 4.2, 4.3, 4.4

[199] L. Zhang, L. Wang, W. Wu, and M. Chan. Modeling Current–Voltage Characteristics of Bilayer Organic Light-Emitting Diodes. *IEEE Transactions on Electron Devices*, 66(1):139–145, January 2019. Conference Name: IEEE Transactions on Electron Devices. 4.1, 4.1.1, 4.3, 4.3, 4.4

[200] Axel Fischer, Manuel Pfalz, Koen Vandewal, Simone Lenk, Matthias Liero, Annegret Glitzky, and Sebastian Reineke. Full electrothermal oled model including nonlinear self-heating effects. *Phys. Rev. Applied*, 10:014023, Jul 2018. 4.1.1

[201] Peter Mark and Wolfgang Helfrich. Space-charge-limited currents in organic crystals. *Journal of Applied Physics*, 33(1):205–215, 1962. 4.1.1

[202] P N Murgatroyd. Theory of space-charge-limited current enhanced by frenkel effect. *Journal of Physics D: Applied Physics*, 3(2):151–156, feb 1970. 4.1.1

[203] Blom Paul W M Wetzelaer, Gert-Jan A H. Diffusion-driven currents in organic-semiconductor diodes. *NPG Asia Materials*, 6(7), 2014. 4.1.1

[204] Jason A Röhr, Thomas Kirchartz, and Jenny Nelson. On the correct interpretation of the low voltage regime in intrinsic single-carrier devices. *Journal of Physics: Condensed Matter*, 29(20):205901, apr 2017. 4.1.1

[205] J. Campbell Scott. Metal–organic interface and charge injection in organic electronic devices. *Journal of Vacuum Science & Technology A*, 21(3):521–531, 2003. 4.1.1

[206] N. I. Craciun, J. Wildeman, and P. W. M. Blom. Universal arrhenius temperature activated charge transport in diodes from disordered organic semiconductors. *Phys. Rev. Lett.*, 100:056601, Feb 2008. 4.1.1

[207] M. Schober, M. Anderson, M. Thomschke, J. Widmer, M. Furno, R. Scholz, B. Lüssem, and K. Leo. Quantitative description of charge-carrier transport in a white organic light-emitting diode. *Phys. Rev. B*, 84:165326, Oct 2011. 4.1.1

[208] S. Rhee, K. Nam, C.s Kim, Myungkwan Song, W. Cho, S.-H Jin, and Seungyoon Ryu. Effect of electron mobility of the electron transport layer on fluorescent organic light-emitting diodes. *ECS Solid State Letters*, 3:R19–R22, 02 2014. 4.3

[209] R. A. K. Yadav, D. K. Dubey, M. Dembla, S. Z. Chen, T. Liang, and J. Jou. Carrier mobility effect of electron transporting layer on oled performance. In *2018 25th International Workshop on Active-Matrix Flatpanel Displays and Devices (AM-FPD)*, pages 1–3, 2018. 4.3

[210] Hossein Movla. Influence of the charge carrier mobility on the dynamic behavior and performance of the single-layer oled. *Optik*, 126(24):5237 – 5240, 2015. 4.3

[211] Yuvraj Singh Negi, Poornima Mittal, and Dr. Brijesh Kumar. Impact of different layers on performance of oled. *Microsystem Technologies*, 24, 05 2018. 4.3

[212] Zhenlin Yang, Cheng Cheng, Xudong Pan, Fei Pan, Fei Wang, Mengying Tian, and Hongmei Zhang. Effects of hole injection layer on performance of green oleds based on flexible ito. *Materials Chemistry and Physics*, 239:121828, 2020. 4.3

[213] S. Mehdi and A. Aissat. Effect of the charges injection contact on the performance of organic light emitting diode (oled). In *2018 6th International Renewable and Sustainable Energy Conference (IRSEC)*, pages 1–4, 2018. 4.3

[214] Lan-Sheng Yang, Hsin-Fei Meng, Yu-Chiang Chao, Hu-Chi Huang, Chih-Wei Luo, Hsiao-Wen Zan, Sheng-Fu Horng, Heh-Lung Huang, Cheng-Chang Lai, and Yiing-Mei Liou. The influence of the interfacial layer on the stability of all-solution-processed organic light-emitting diodes. *RSC Adv.*, 10:28766–28777, 2020. 4.3

[215] Kiyeol Kwak, Kyoungah Cho, and Sangsig Kim. Analysis of thermal degradation of organic light-emitting diodes with infrared imaging and impedance spectroscopy. *Opt. Express*, 21(24):29558, December 2013. 4.3

[216] J. Park and Y. Kawakami. Temperature-Dependent Dynamic Behaviors of Organic Light-Emitting Diode. *Journal of Display Technology*, 2(4):333–340, December 2006. Conference Name: Journal of Display Technology. 4.3

[217] D. Buso, S. Bhosle, Y. Liu, M. Ternisien, C. Renaud, and Y. Chen. OLED Electrical Equivalent Device for Driver Topology Design. *IEEE Transactions on Industry Applications*, 50(2):1459–1468, March 2014. Conference Name: IEEE Transactions on Industry Applications. 4.3

[218] Manfred Gruber, Egbert Zojer, Ferdinand Schürrer, and Karin Zojer. Impact of materials versus geometric parameters on the contact resistance in organic thin-film transistors. *Advanced Functional Materials*, 23(23):2941–2952, 2013. 4.4

# 6 Supplementary material

## Derivation of Poisson equation and current conservation law

Important to notice our materials of interest are amorphous. Therefore they are invariant to any coordinate rotation and therefore, cannot have any "special" direction with spontaneous polarization, i.e. spontaneous polarization is always zero and we may have only polarization induced by external field. In general then one speaks about polarization being some function of electric field. In practice it is often sufficient to truncate this function at linear term and that is what will assume here. Now we are left with polarization being linear function of applied field. In principle, linear connection between two vectors should be a tensor, but here we can again invoke symmetry argument and finally arrive to conclusion that field inside our material is some scalar times the applied field. Following common conventions we write $\mathbf{D} = \epsilon\mathbf{E}$ and $\mu\mathbf{H} = \mathbf{B}$. Permeability $\mu$ is very close to 1 in organic amorphous compounds. Permittivity on the other hand can be quite high, because organic molecules naturally can be easily polarized.

To proceed we need to use potentials $\phi$ and $\mathbf{A}$, which make everything easier when working with Maxwell equations. Electric and magnetic field can be extacted from two potentials in the way presented in eq. 6.1 and eq. 6.2. Because only derivatives of these potentials have physical meaning (in classics) they are not strictly defined we can also impose additional conditions, which is often referred to as *choosing gauge*. We will work in Coulomb gauge, which imposes conditions on vector potential in form $\nabla \cdot \mathbf{A} = 0$.

$$\mathbf{E} = -\nabla\phi - \frac{\partial \mathbf{A}}{\partial t} \tag{6.1}$$

$$\mathbf{B} = \nabla \times \mathbf{A} \tag{6.2}$$

Putting this definitions into Maxwell equations and using the Coulomb gauge one can arrive to set of eqs. 6.3 - 6.6.

$$\Delta\phi = -\frac{\rho}{\epsilon} \tag{6.3}$$

$$\nabla \cdot (\nabla \times \mathbf{A}) = 0 \tag{6.4}$$

$$-\nabla \times (\nabla\phi) = 0 \tag{6.5}$$

$$\frac{1}{\mu}\nabla \times \nabla \times \mathbf{A} = \mathbf{J} - \epsilon\nabla\frac{\partial\phi}{\partial t} - \epsilon\frac{\partial^2 \mathbf{A}}{\partial t^2} \tag{6.6}$$

These equations can be straightforwardly simplified if we assume that there are no magnetic field in the system. This assumption is reasonable because there are no

known magnetic phenomena happening in organic amorphous materials. Then left sides of eqs. 6.4 - 6.6 immediately turn to zero. Then eq. 6.4 is removed from the system. Moreover, curl of gradient is always zero, therefore eq. 6.5 can be also removed. We are left with two equations.

Eq. 6.3 is called Poisson equation and it is the equation we were searching for. If one provides charge density to that equation one can theoretically get electrostatic potential out of it. Nevertheless, this is yet not the end of the story because electric field depends on time derivative of vector potential and we still have eq. 6.6. Although it seems that in this equation it is impossible to decouple different quantities it is actually not important. To realize that it is actually more beneficial to look at it in more natural for electrodynamics Gaussian units, eq. 6.7. From here one immediately can see that time dependence comes from the fact that speed of light is limited. Because we are looking at small system and we are not really interested in transition process from one picture to another, in other words, electron and hole velocities in out system will be much less that the speed of light. This term would be more important if one would look on plasma oscillations of electron gas under oscillating electromagnetic field. We are interested in different phenomena, and put speed of light to infinity, therefore neglecting this term.

$$\nabla \times \mathbf{H} = \frac{1}{c}\left(4\pi\mathbf{J} + \frac{\partial \mathbf{D}}{\partial t}\right) \tag{6.7}$$

Before we completely forget about this equation it still can serve us purpose of deriving continuity equation for current density. To do so, one can take divergence of it. Vector potential will disappear according to Coulomb gauge condition and with use of Poisson equation one can obtain eq. 6.8 which is in essence the conservation law of electric charge.

$$\mathrm{div}\mathbf{J} + \frac{\partial \rho}{\partial t} = 0 \tag{6.8}$$

Charge carrier conservation law written in this differential law and Poisson equation will be extremely useful for us afterwards and, as I shown here, they are just consequences of Maxwell equations in certain approximations.

## Calculation of elliptic integrals

Here we present fast and efficient FORTRAN 90 functions which were used to calculate elliptic integrals according to [168].

```
double precision function ellipticK(x)
    double precision, intent(in) :: x
    double precision :: a, g, anew, gnew, e
    if (x < 0.0d0 .or. x .ge. 1.0d0) then
        print*, "x < 0.0d0 or x >= 1.0d0, PRESS ANY KEY TO EXIT,x :", x
        read*,
        return
    end if
    a = (1+dsqrt(1-x**2))/2
    g = dsqrt(dsqrt(1-x**2))
```

```
    e = 1.0d-15
    do
        anew = (a+g)/2
        gnew = dsqrt(a*g)
        if (anew-gnew < e) then
            exit
        end if
        a = anew
        g = gnew
    end do
    ellipticK = 3.1415926/(2*anew)
end function ellipticK

double precision function ellipticE(x)
    double precision, intent(in) :: x
    double precision :: a, g,o, anew, gnew,onew, e
    a = (1+dsqrt(1-x**2))/2
    g = dsqrt(dsqrt(1-x**2))
    e = 1.0d-15
    if (x == 1.0d0) then
        EllipticE = 1.0d0
        return
    end if
    if (x < 0.0d0 .or. x > 1.0d0) then
        print*, "x < 0.0d0 or x > 1.0d0, PRESS ANY KEY TO EXIT, x:", x
        read*,
        return
    end if
    do
        anew = (a+g)/2
        gnew = dsqrt(a*g)
        if (anew-gnew < e) then
            exit
        end if
        a = anew
        g = gnew
    end do
    ellipticE = 3.1415926/(2*anew)
    a = 1-x**2
    g = 1
    o = 0
    do
        anew = (a + g)/2
        gnew = o + dsqrt(((a-o)*(g-o)))
        onew = o - dsqrt(((a-o)*(g-o)))
        if (anew-gnew < e) then
            exit
        end if
```

```
        a = anew
        g = gnew
        o = onew
    end do
    ellipticE = ellipticE*anew
end function ellipticE
```

## Full equations for discretized heat equations

Full equation instead of collapsed eq. 2.65.

$$\begin{aligned} T_{i,j,k}^{t+\Delta t} = T_{i,j,k}^{t} + \frac{\Delta t}{\rho_{i,j,k} c_{p_{i,j,k}}} \Bigg[ Q_{i,j,k} + \frac{\kappa_{i+1,j,k} - \kappa_{i-1,j,k}}{x_{i+1} - x_{i-1}} \frac{T_{i+1,j,k} - T_{i-1,j,k}}{x_{i+1} - x_{i-1}} + \\ + 2\kappa_{i,j,k} \frac{\frac{T_{i+1,j,k} - T_{i,j,k}}{x_{i+1} - x_i} - \frac{T_{i,j,k} - T_{i-1,j,k}}{x_i - x_{i-1}}}{x_{i+1} - x_{i-1}} + \frac{\kappa_{i,j+1,k} - \kappa_{i,j-1,k}}{y_{j+1} - y_{j-1}} \frac{T_{i,j+1,k} - T_{i,j-1,k}}{y_{j+1} - y_{j-1}} + \\ + 2\kappa_{i,j,k} \frac{\frac{T_{i,j+1,k} - T_{i,j,k}}{y_{j+1} - y_j} - \frac{T_{i,j,k} - T_{i,j-1,k}}{y_j - y_{j-1}}}{y_{j+1} - y_{j-1}} + \frac{\kappa_{i,j,k+1} - \kappa_{i,j,k-1}}{z_{k+1} - z_{k-1}} \frac{T_{i,j,k+1} - T_{i,j,k-1}}{z_{k+1} - z_{k-1}} + \\ + 2\kappa_{i,j,k} \frac{\frac{T_{i,j,k+1} - T_{i,j,k}}{z_{k+1} - z_k} - \frac{T_{i,j,k} - T_{i,j,k-1}}{z_k - z_{k-1}}}{z_{k+1} - z_{k-1}} \Bigg] \end{aligned} \tag{6.9}$$

Poisson equation discretization results

$$\begin{aligned} \phi_{i,j,k}^{t+\Delta t} = \phi_{i,j,k}^{t} + \Delta t \Bigg[ \frac{e(p_{i,j,k} - n_{i,j,k})}{\epsilon_0} + \frac{\epsilon_{Ri+1,j,k} - \epsilon_{Ri-1,j,k}}{x_{i+1} - x_{i-1}} \frac{\phi_{i+1,j,k} - \phi_{i-1,j,k}}{x_{i+1} - x_{i-1}} + \\ + 2\epsilon_{Ri,j,k} \frac{\frac{\phi_{i+1,j,k} - \phi_{i,j,k}}{x_{i+1} - x_i} - \frac{\phi_{i,j,k} - \phi_{i-1,j,k}}{x_i - x_{i-1}}}{x_{i+1} - x_{i-1}} + \frac{\epsilon_{Ri,j+1,k} - \epsilon_{Ri,j-1,k}}{y_{j+1} - y_{j-1}} \frac{\phi_{i,j+1,k} - \phi_{i,j-1,k}}{y_{j+1} - y_{j-1}} + \\ + 2\epsilon_{Ri,j,k} \frac{\frac{\phi_{i,j+1,k} - \phi_{i,j,k}}{y_{j+1} - y_j} - \frac{\phi_{i,j,k} - \phi_{i,j-1,k}}{y_j - y_{j-1}}}{y_{j+1} - y_{j-1}} + \frac{\epsilon_{Ri,j,k+1} - \epsilon_{Ri,j,k-1}}{z_{k+1} - z_{k-1}} \frac{\phi_{i,j,k+1} - \phi_{i,j,k-1}}{z_{k+1} - z_{k-1}} + \\ + 2\epsilon_{Ri,j,k} \frac{\frac{\phi_{i,j,k+1} - \phi_{i,j,k}}{z_{k+1} - z_k} - \frac{\phi_{i,j,k} - \phi_{i,j,k-1}}{z_k - z_{k-1}}}{z_{k+1} - z_{k-1}} \Bigg] \end{aligned} \tag{6.10}$$

Drift-diffusion equation discretization results for electrons

$$\begin{aligned} J_{x}{}_{i+0.5,j,k}^{t} = \frac{e D_{i+0.5,j,k}^{t}}{x_{i+1} - x_i} \Bigg[ n_{i+1,j,k}^{t} B \left( \frac{e(\phi_{i+1,j,k}^{t} - \phi_{i,j,k}^{t})}{k_B T_{i,j,k}^{t}} \right) - \\ - n_{i,j,k}^{t} B \left( - \frac{e(\phi_{i+1,j,k}^{t} - \phi_{i,j,k}^{t})}{k_B T_{i,j,k}^{t}} \right) \Bigg] \end{aligned} \tag{6.11}$$

$$J_{y}{}^{t}_{i,j+0.5,k} = \frac{eD^t_{i,j+0.5,k}}{y_{j+1}-y_j}\left[n^t_{i,j+1,k}B\left(\frac{e(\phi^t_{i,j+1,k}-\phi^t_{i,j,k})}{k_BT^t_{i,j,k}}\right)- -n^t_{i,j,k}B\left(-\frac{e(\phi^t_{i,j+1,k}-\phi^t_{i,j,k})}{k_BT^t_{i,j,k}}\right)\right] \tag{6.12}$$

$$J_{z}{}^{t}_{i,j,k+0.5} = \frac{eD^t_{i,j,k+0.5}}{z_{k+1}-z_k}\left[n^t_{i,j,k+1}B\left(\frac{e(\phi^t_{i,j,k+1}-\phi^t_{i,j,k})}{k_BT^t_{i,j,k}}\right)- -n^t_{i,j,k}B\left(-\frac{e(\phi^t_{i,j,k+1}-\phi^t_{i,j,k})}{k_BT^t_{i,j,k}}\right)\right] \tag{6.13}$$

Drift-diffusion equation discretization results for holes.

$$J_{x}{}^{t}_{i+0.5,j,k} = -\frac{eD^t_{i+0.5,j,k}}{x_{i+1}-x_i}\left[p^t_{i+1,j,k}B\left(-\frac{e(\phi^t_{i+1,j,k}-\phi^t_{i,j,k})}{k_BT^t_{i,j,k}}\right)- -p^t_{i,j,k}B\left(\frac{e(\phi^t_{i+1,j,k}-\phi^t_{i,j,k})}{k_BT^t_{i,j,k}}\right)\right] \tag{6.14}$$

$$J_{y}{}^{t}_{i,j+0.5,k} = -\frac{eD^t_{i,j+0.5,k}}{y_{j+1}-y_j}\left[p^t_{i,j+1,k}B\left(-\frac{e(\phi^t_{i,j+1,k}-\phi^t_{i,j,k})}{k_BT^t_{i,j,k}}\right)- -p^t_{i,j,k}B\left(\frac{e(\phi^t_{i,j+1,k}-\phi^t_{i,j,k})}{k_BT^t_{i,j,k}}\right)\right] \tag{6.15}$$

$$J_{z}{}^{t}_{i,j,k+0.5} = -\frac{eD^t_{i,j,k+0.5}}{z_{k+1}-z_k}\left[p^t_{i,j,k+1}B\left(-\frac{e(\phi^t_{i,j,k+1}-\phi^t_{i,j,k})}{k_BT^t_{i,j,k}}\right)- -p^t_{i,j,k}B\left(\frac{e(\phi^t_{i,j,k+1}-\phi^t_{i,j,k})}{k_BT^t_{i,j,k}}\right)\right] \tag{6.16}$$

Continuity equations for electrons

$$n^{t+\Delta t}_{i,j,k} = n^t_{i,j,k} + \Delta t\left[G^t_{i,j,k} - R^t_{i,j,k} + \frac{J^t_{i+0.5,j,k}-J^t_{i-0.5,j,k}}{0.5e(x_{i+1}-x_{i-1})} + + \frac{J^t_{i,j+0.5,k}-J^t_{i,j-0.5,k}}{0.5e(y_{j+1}-y_{j-1})} + \frac{J^t_{i,j,k+0.5}-J^t_{i,j,k-0.5}}{0.5e(z_{k+1}-z_{k-1})}\right] \tag{6.17}$$

Continuity equations for holes

$$p_{i,j,k}^{t+\Delta t} = p_{i,j,k}^{t} + \Delta t \left[ G_{i,j,k}^{t} - R_{i,j,k}^{t} - \frac{J_{i+0.5,j,k}^{t} - J_{i-0.5,j,k}^{t}}{0.5e(x_{i+1} - x_{i-1})} - \right. \\ \left. - \frac{J_{i,j+0.5,k}^{t} - J_{i,j-0.5,k}^{t}}{0.5e(y_{j+1} - y_{j-1})} - \frac{J_{i,j,k+0.5}^{t} - J_{i,j,k-0.5}^{t}}{0.5e(z_{k+1} - z_{k-1})} \right] \tag{6.18}$$

## Heat transfer parameters against the maximum obtained temperature in the device

All plots in this section depict the behavior of maximum temperature in the device against both thermal conductivity and the heat transfer coefficient for different voltages.

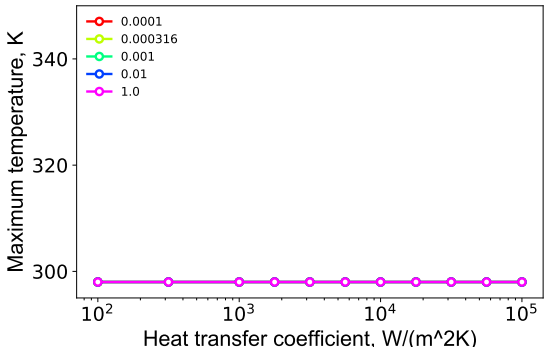


Figure 6.1: Maximal device temperatures as a function of heat transfer coefficient for an applied bias of 1 $V$. Different colors correspond to the varied thermal conductivities, value is given on the legend in $W/mK$.

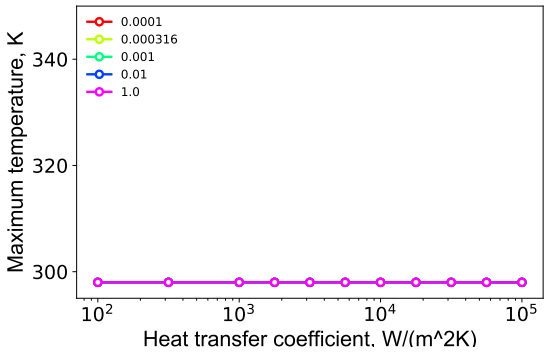


Figure 6.2: Maximal device temperatures as a function of heat transfer coefficient for an applied bias of 2 $V$. Different colors correspond to the varied thermal conductivities, value is given on the legend in $W/mK$.

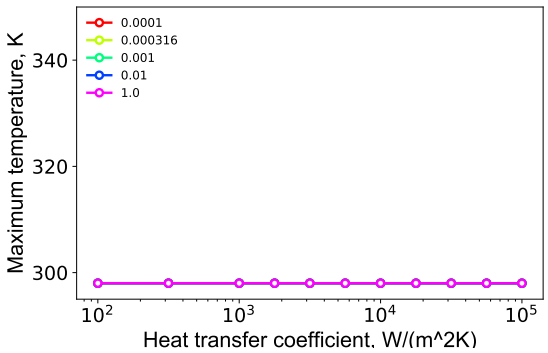


Figure 6.3: Maximal device temperatures as a function of heat transfer coefficient for an applied bias of 3 $V$. Different colors correspond to the varied thermal conductivities, value is given on the legend in $W/mK$.

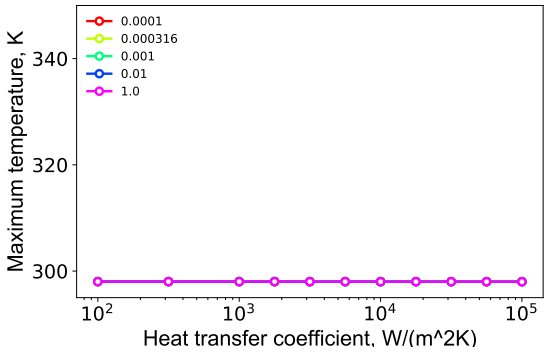


Figure 6.4: Maximal device temperatures as a function of heat transfer coefficient for an applied bias of 4 $V$. Different colors correspond to the varied thermal conductivities, value is given on the legend in $W/mK$.

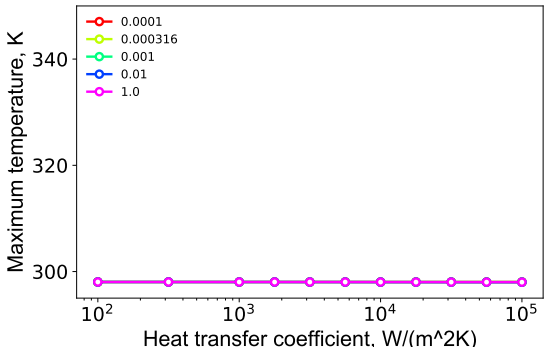


Figure 6.5: Maximal device temperatures as a function of heat transfer coefficient for an applied bias of 5 $V$. Different colors correspond to the varied thermal conductivities, value is given on the legend in $W/mK$.

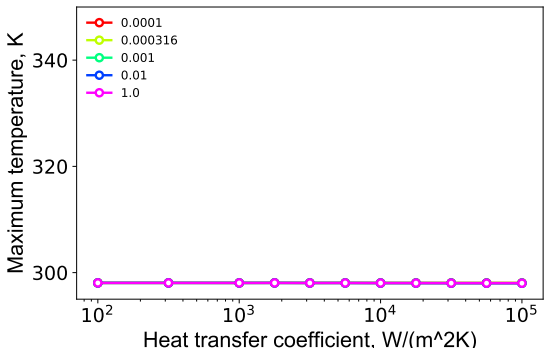


Figure 6.6: Maximal device temperatures as a function of heat transfer coefficient for an applied bias of 6 $V$. Different colors correspond to the varied thermal conductivities, value is given on the legend in $W/mK$.

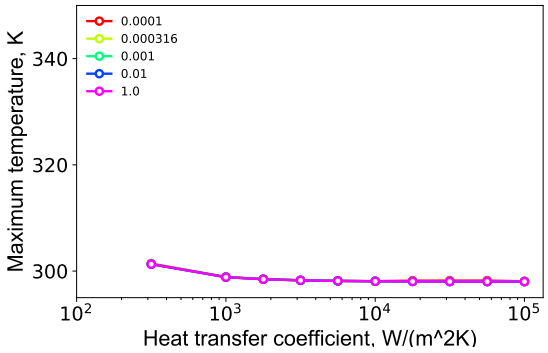


Figure 6.7: Maximal device temperatures as a function of heat transfer coefficient for an applied bias of 7 $V$. Different colors correspond to the varied thermal conductivities, value is given on the legend in $W/mK$.

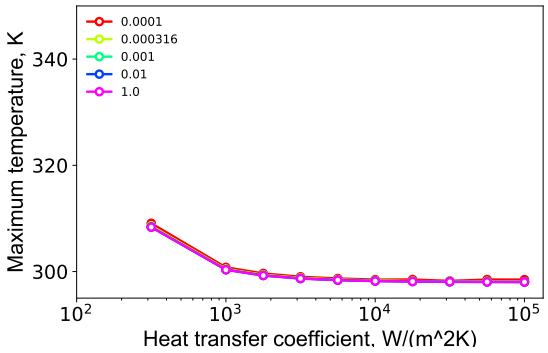


Figure 6.8: Maximal device temperatures as a function of heat transfer coefficient for an applied bias of 8 $V$. Different colors correspond to the varied thermal conductivities, value is given on the legend in $W/mK$.

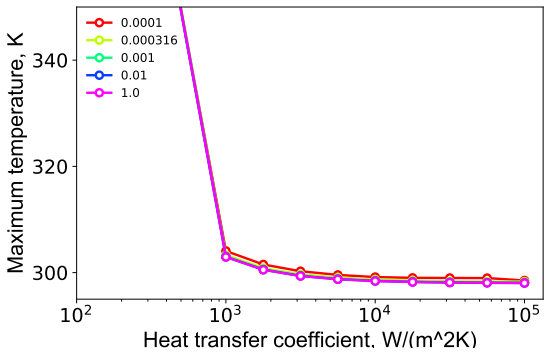


Figure 6.9: Maximal device temperatures as a function of heat transfer coefficient for an applied bias of 9 $V$. Different colors correspond to the varied thermal conductivities, value is given on the legend in $W/mK$.

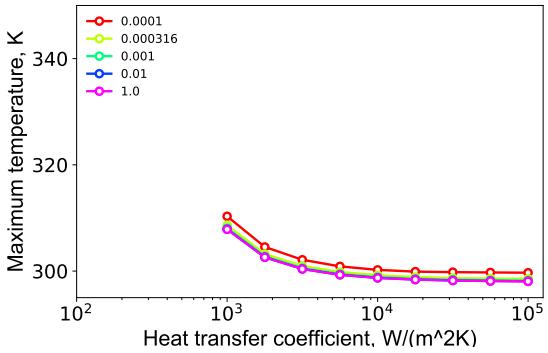


Figure 6.10: Maximal device temperatures as a function of heat transfer coefficient for an applied bias of 10 $V$. Different colors correspond to the varied thermal conductivities, value is given on the legend in $W/mK$.

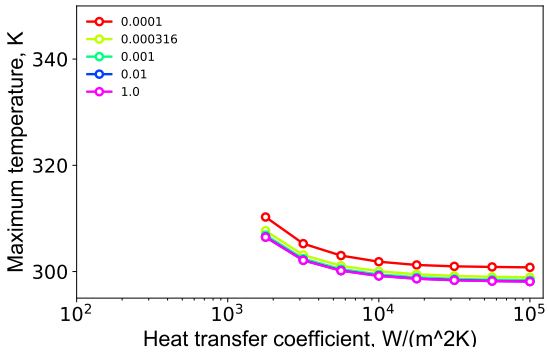


Figure 6.11: Maximal device temperatures as a function of heat transfer coefficient for an applied bias of 11 $V$. Different colors correspond to the varied thermal conductivities, value is given on the legend in $W/mK$.

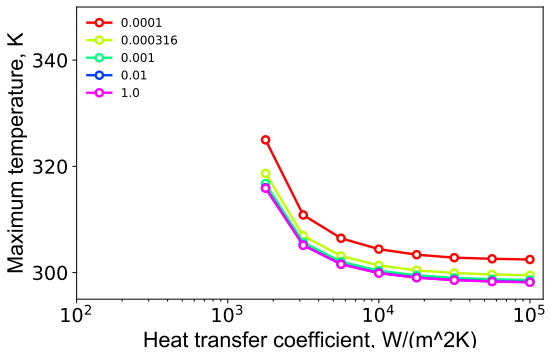


Figure 6.12: Maximal device temperatures as a function of heat transfer coefficient for an applied bias of 12 $V$. Different colors correspond to the varied thermal conductivities, value is given on the legend in $W/mK$.

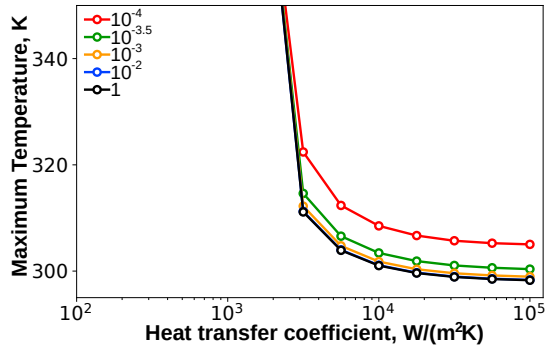


Figure 6.13: Maximal device temperatures as a function of heat transfer coefficient for an applied bias of 13 $V$. Different colors correspond to the varied thermal conductivities, value is given on the legend in $W/mK$.

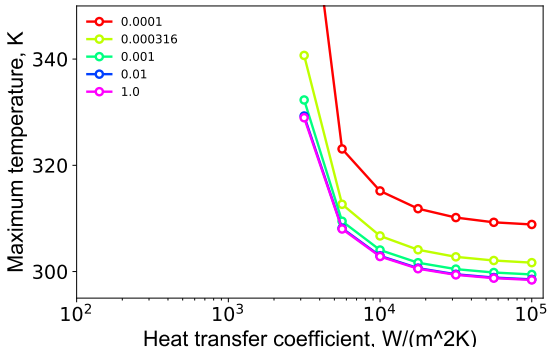


Figure 6.14: Maximal device temperatures as a function of heat transfer coefficient for an applied bias of 14 $V$. Different colors correspond to the varied thermal conductivities, value is given on the legend in $W/mK$.

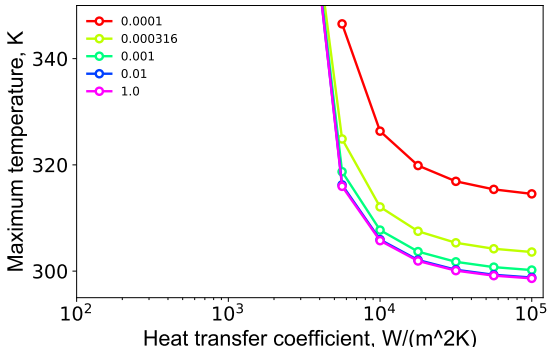


Figure 6.15: Maximal device temperatures as a function of heat transfer coefficient for an applied bias of 15 $V$. Different colors correspond to the varied thermal conductivities, value is given on the legend in $W/mK$.

## Experimental and modeling current voltage characteristics for different temperatures.

In this section we will put the rest I-V curves for different disorder parameters.

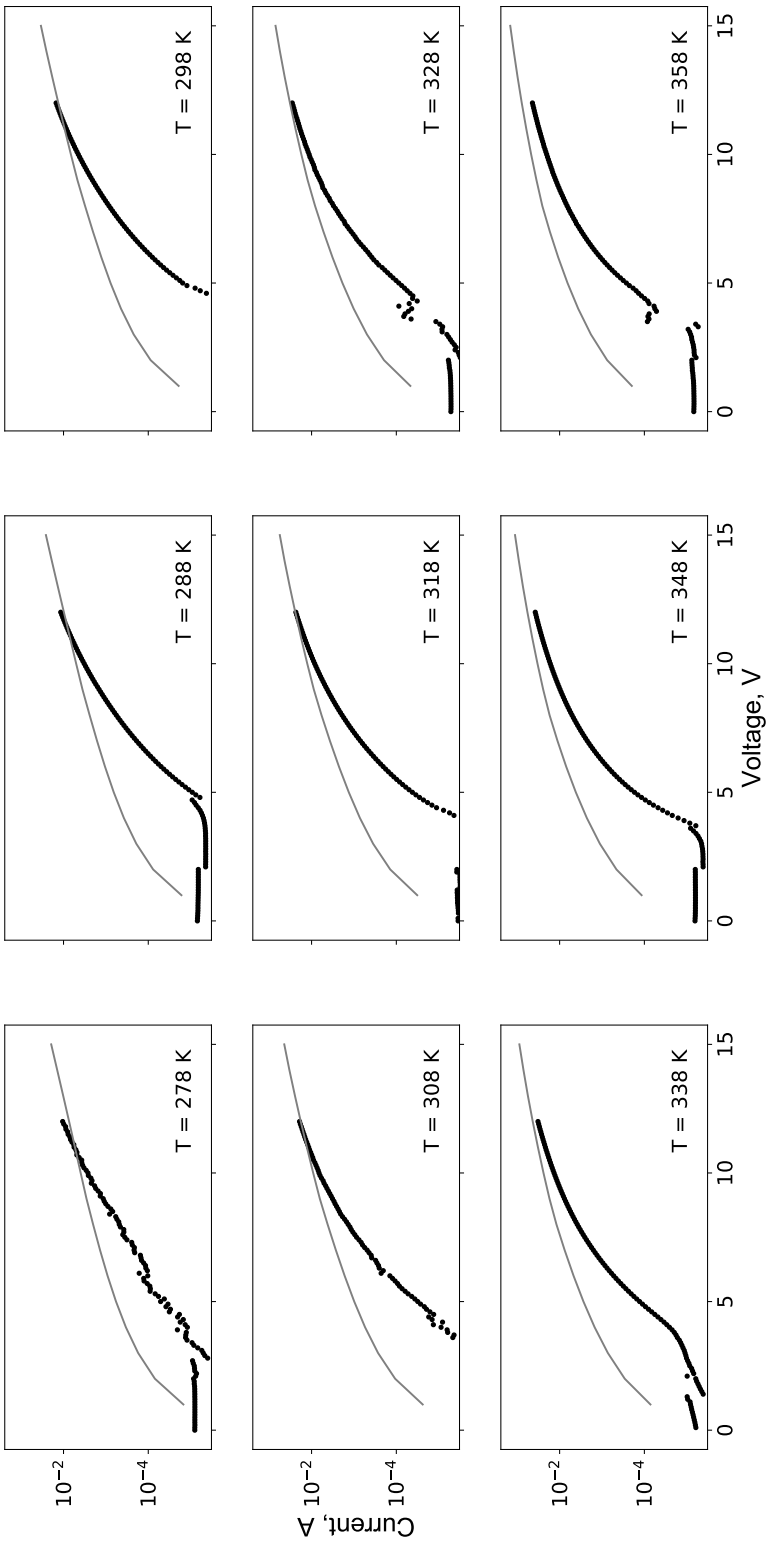


Figure 6.16: Current-voltage characteristics for different temperatures for the value of the disorder parameter equal $55meV$. Solid lines correspond to the modeling results and dots correspond to experimental results.

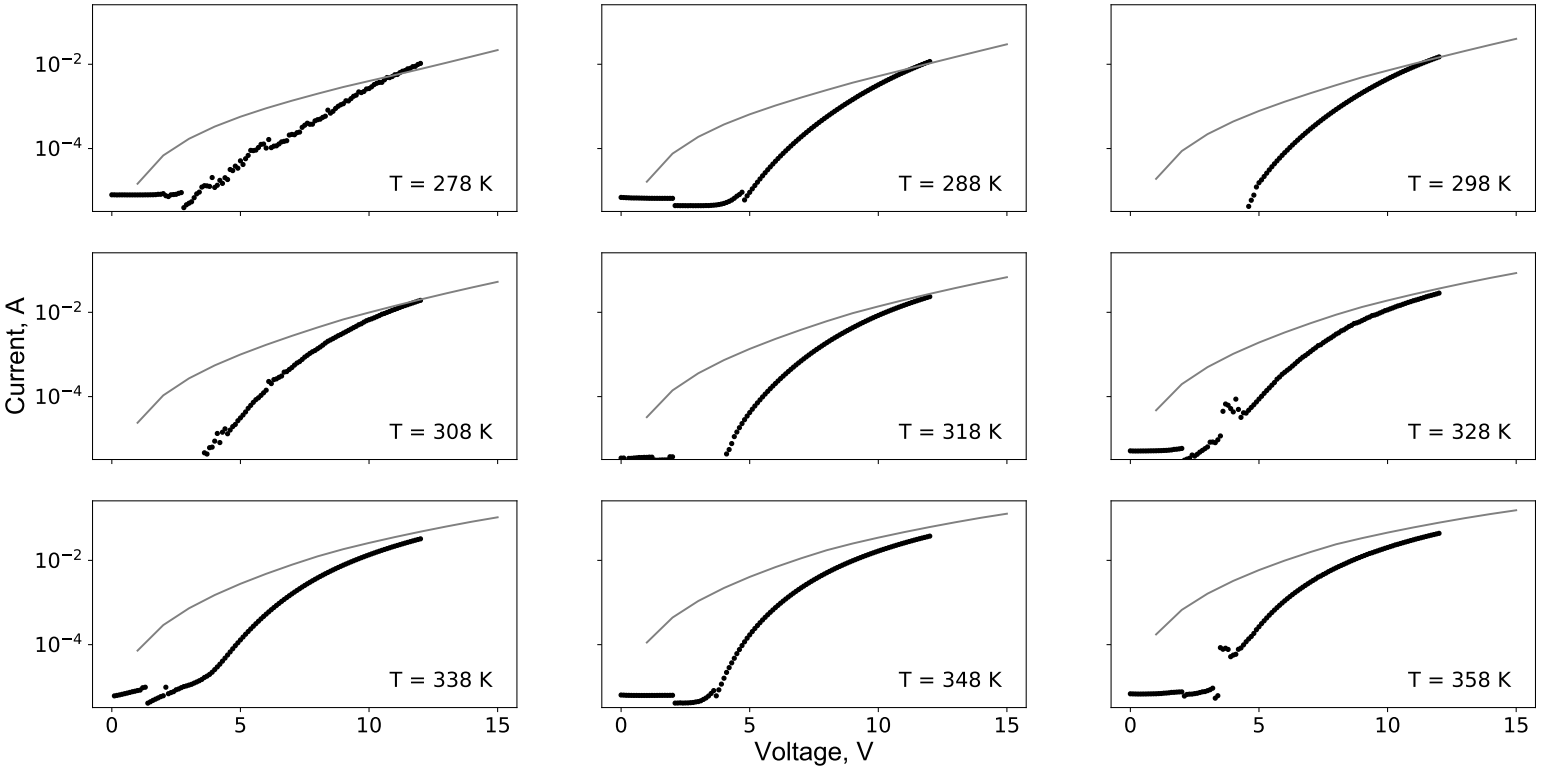


Figure 6.17: Current-voltage characteristics for different temperatures for the value of the disorder parameter equal $60meV$. Solid lines correspond to the modeling results and dots correspond to experimental results.

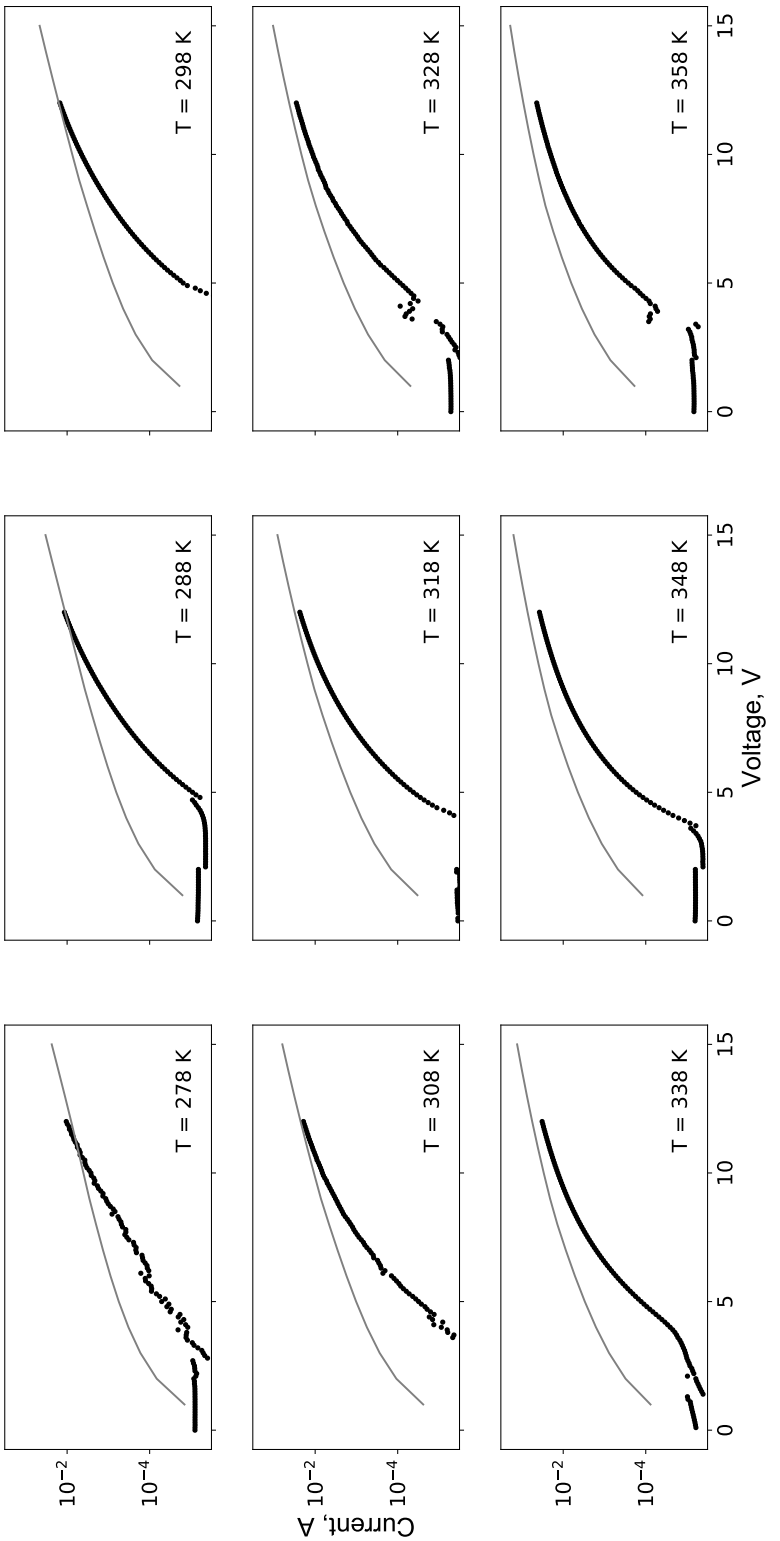


Figure 6.18: Current-voltage characteristics for different temperatures for the value of the disorder parameter equal $65meV$. Solid lines correspond to the modeling results and dots correspond to experimental results.

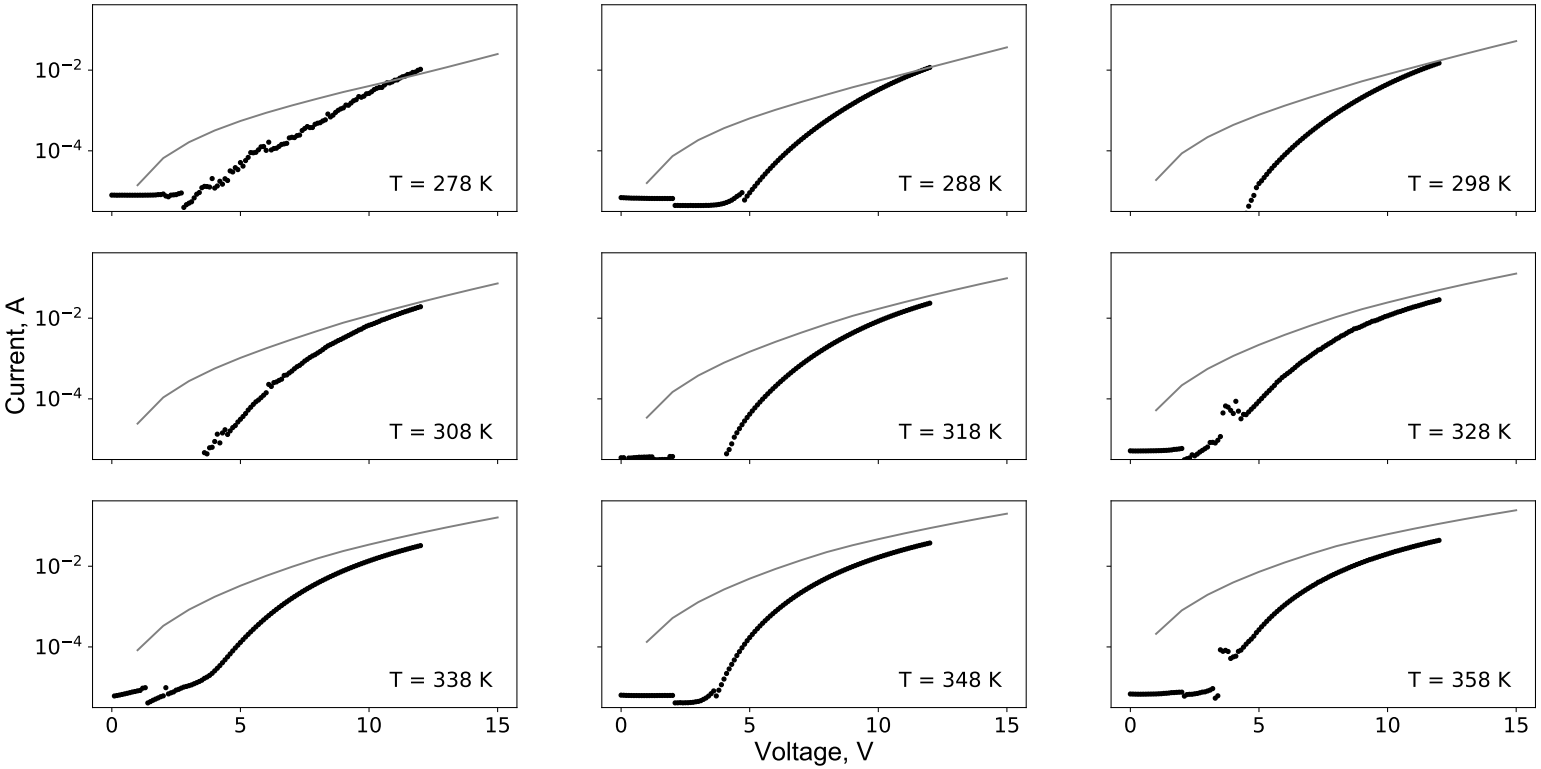


Figure 6.19: Current-voltage characteristics for different temperatures for the value of the disorder parameter equal $70meV$. Solid lines correspond to the modeling results and dots correspond to experimental results.

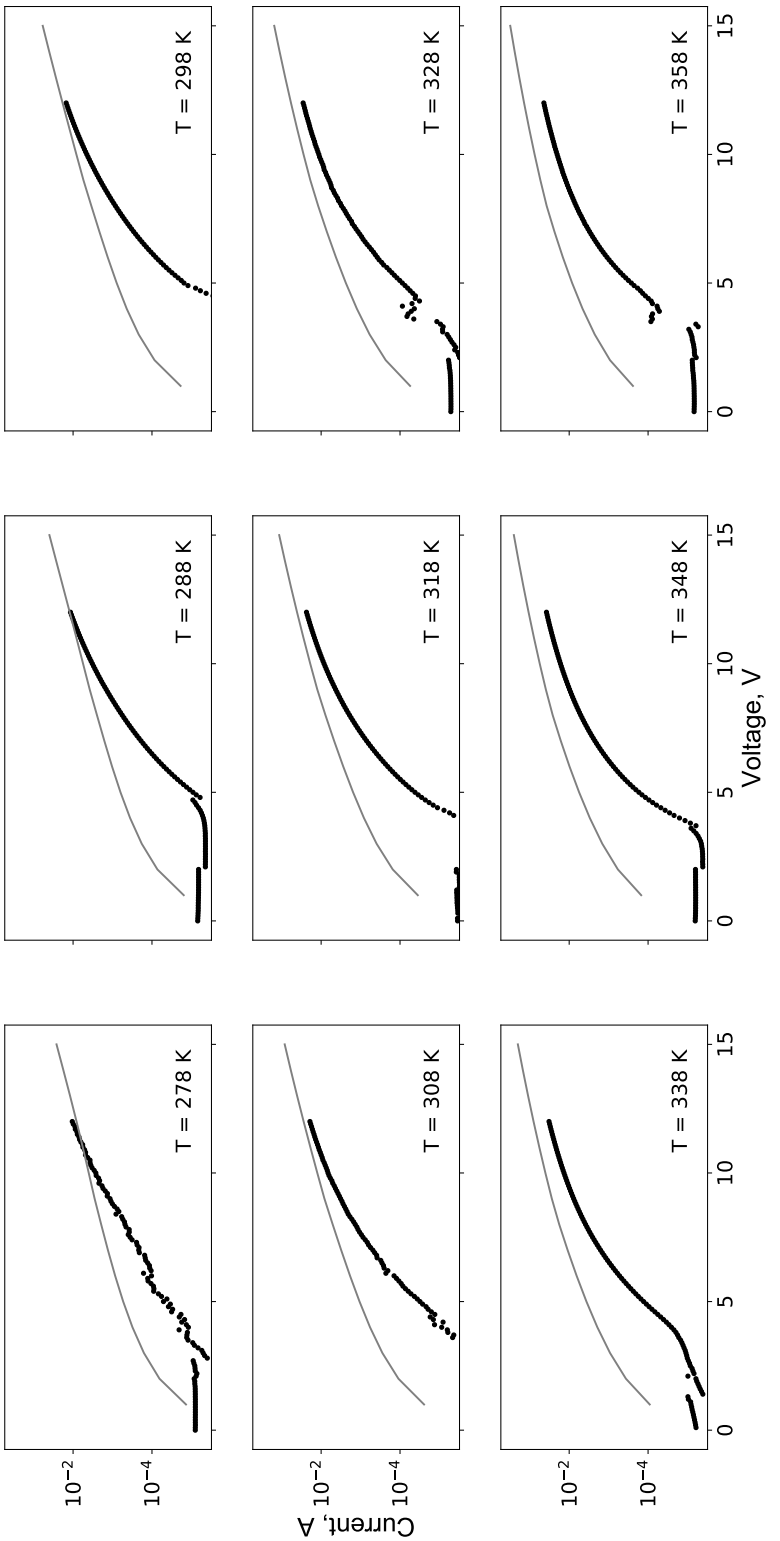


Figure 6.20: Current-voltage characteristics for different temperatures for the value of the disorder parameter equal $75meV$. Solid lines correspond to the modeling results and dots correspond to experimental results.

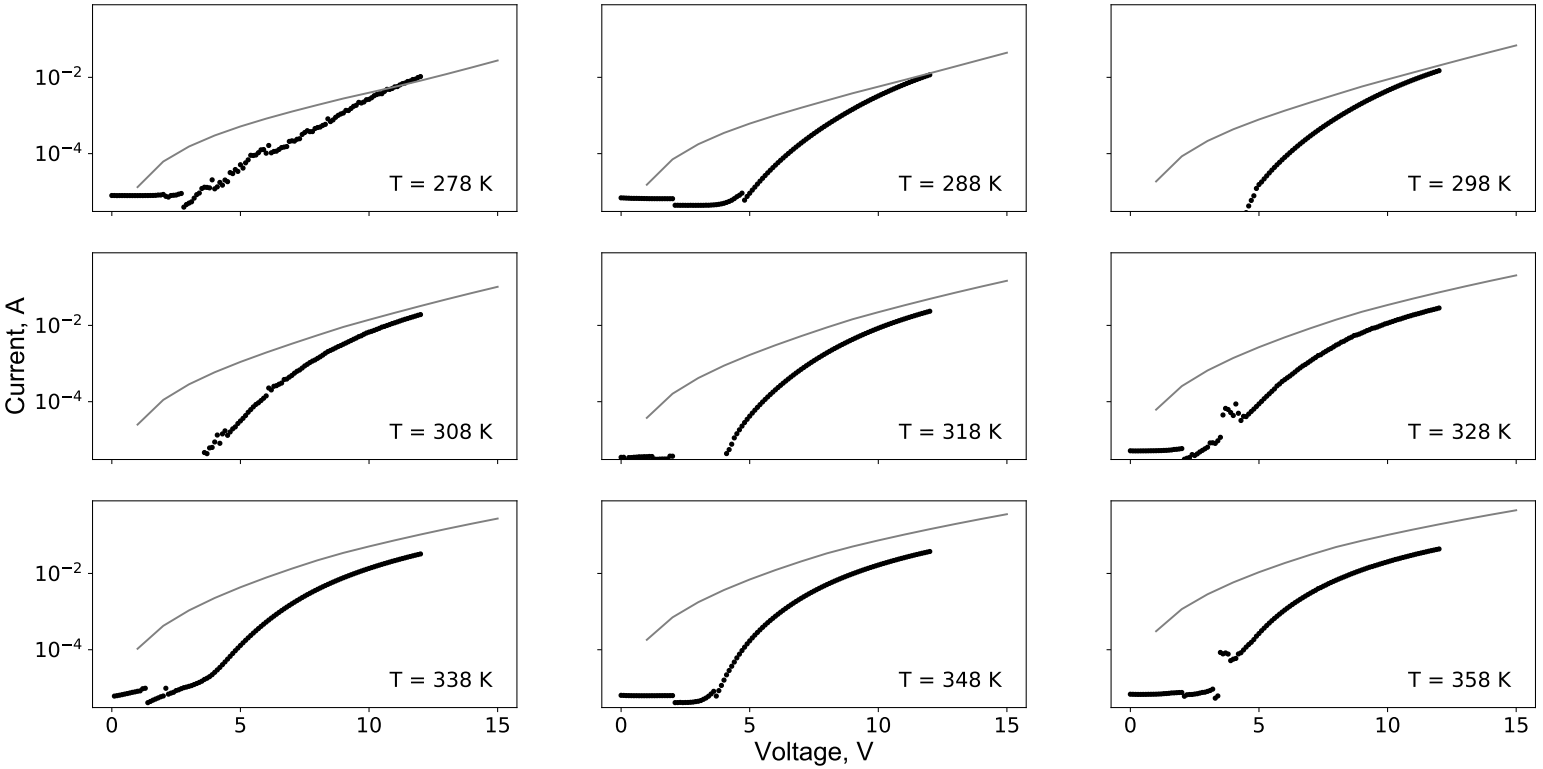


Figure 6.21: Current-voltage characteristics for different temperatures for the value of the disorder parameter equal $82.5meV$. Solid lines correspond to the modeling results and dots correspond to experimental results.

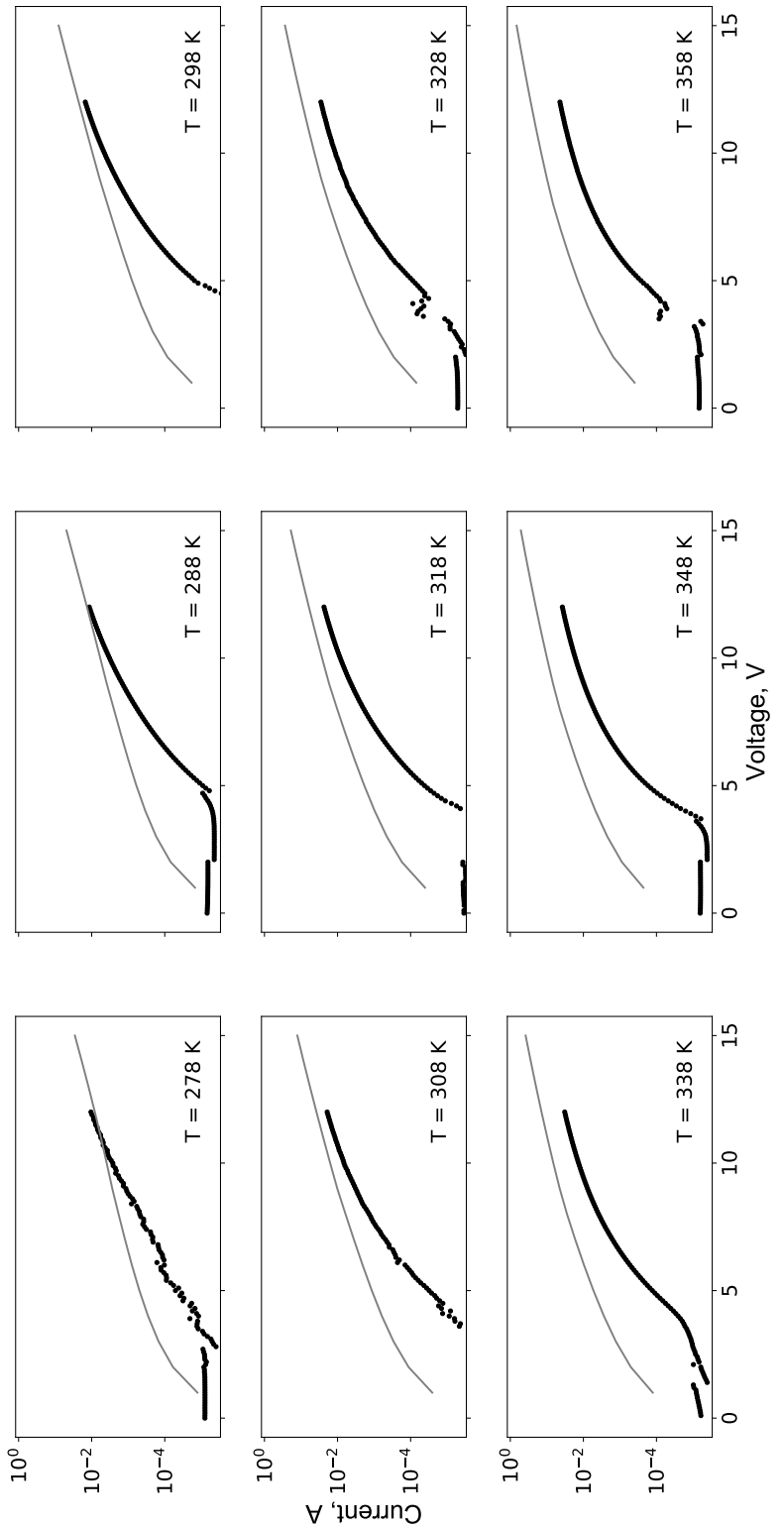


Figure 6.22: Current-voltage characteristics for different temperatures for the value of the disorder parameter equal $90meV$. Solid lines correspond to the modeling results and dots correspond to experimental results.

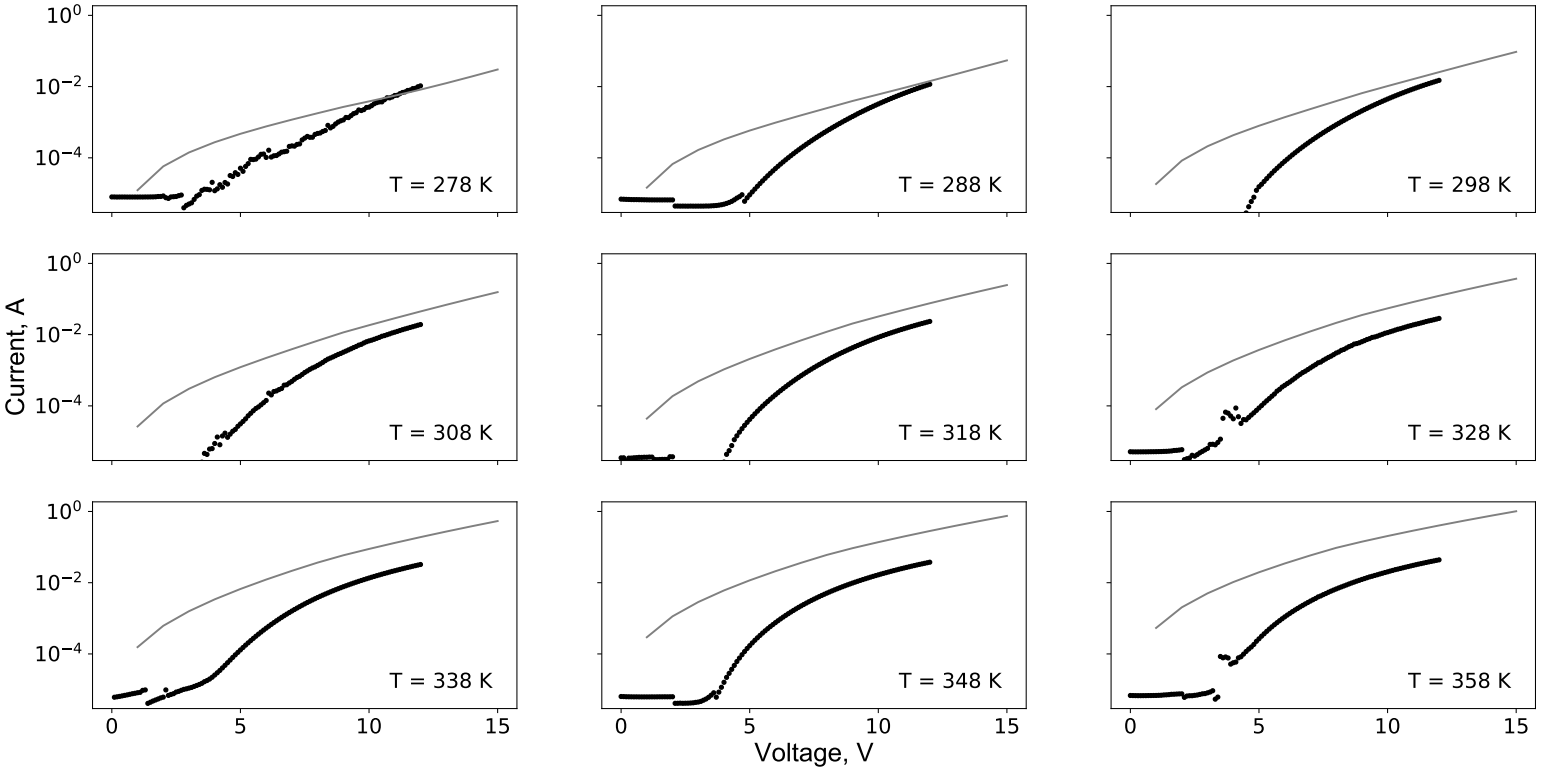


Figure 6.23: Current-voltage characteristics for different temperatures for the value of the disorder parameter equal $97.5meV$. Solid lines correspond to the modeling results and dots correspond to experimental results.

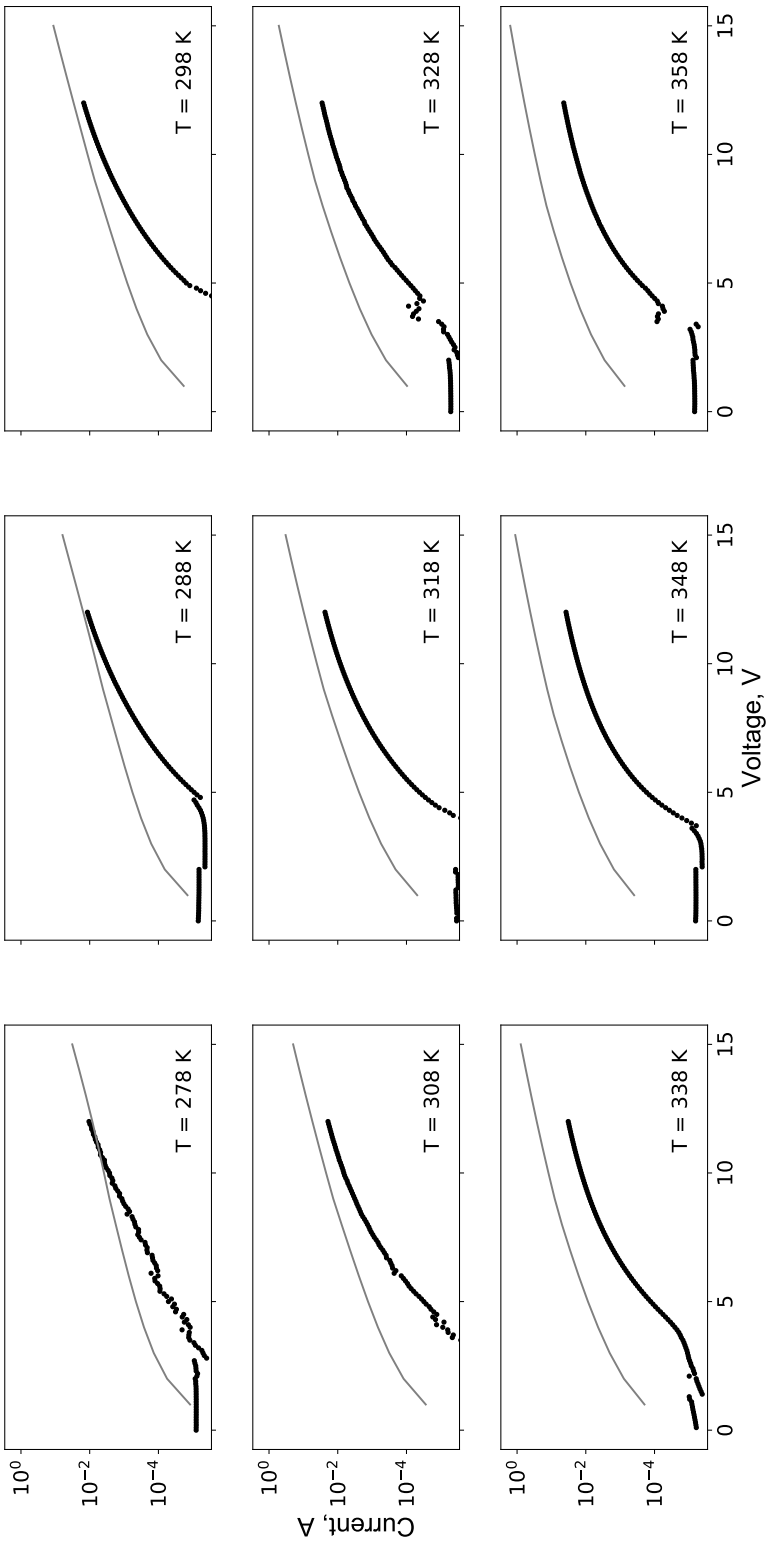


Figure 6.24: Current-voltage characteristics for different temperatures for the value of the disorder parameter equal $105meV$. Solid lines correspond to the modeling results and dots correspond to experimental results.

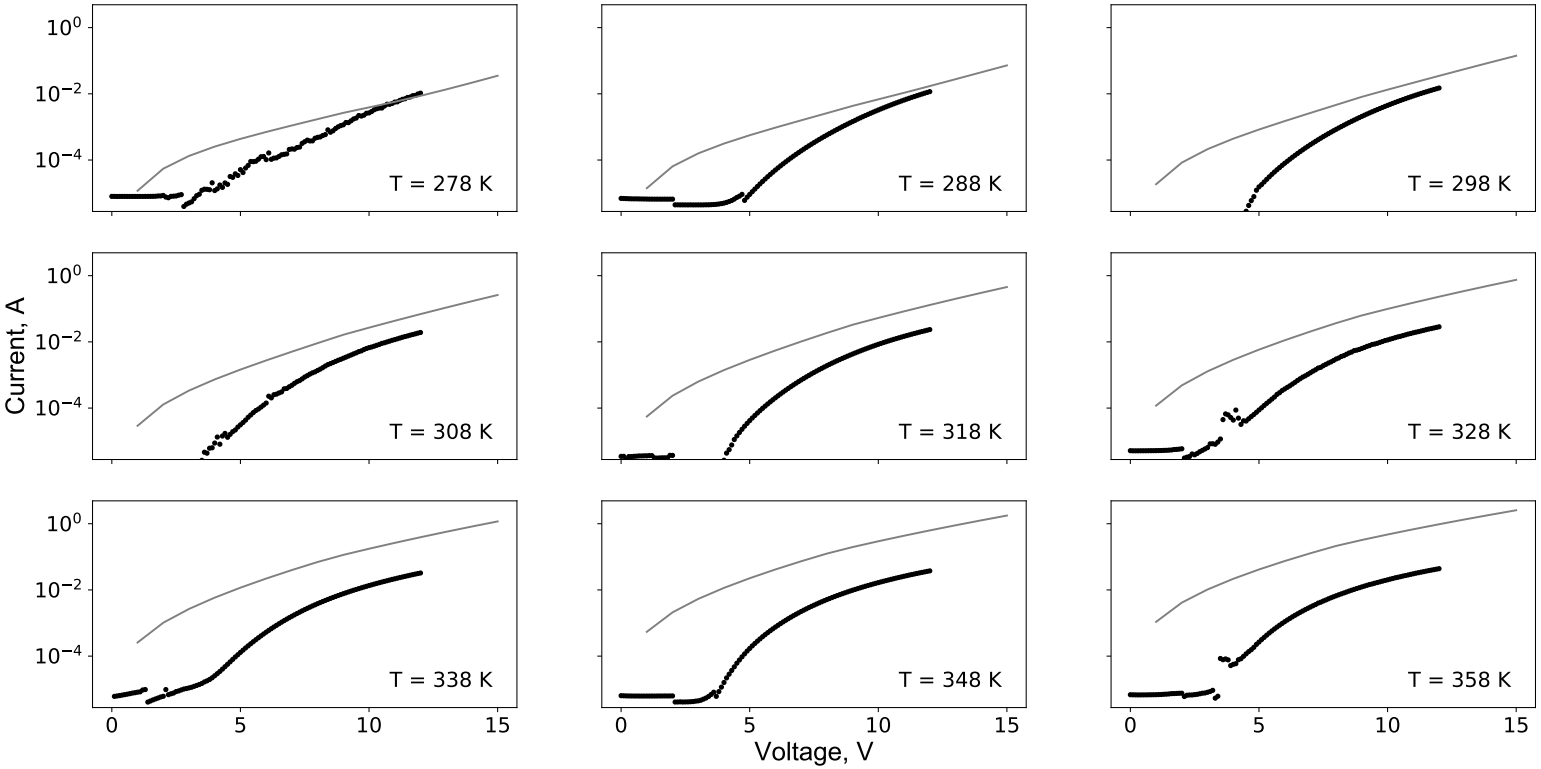


Figure 6.25: Current-voltage characteristics for different temperatures for the value of the disorder parameter equal 112.5$meV$. Solid lines correspond to the modeling results and dots correspond to experimental results.

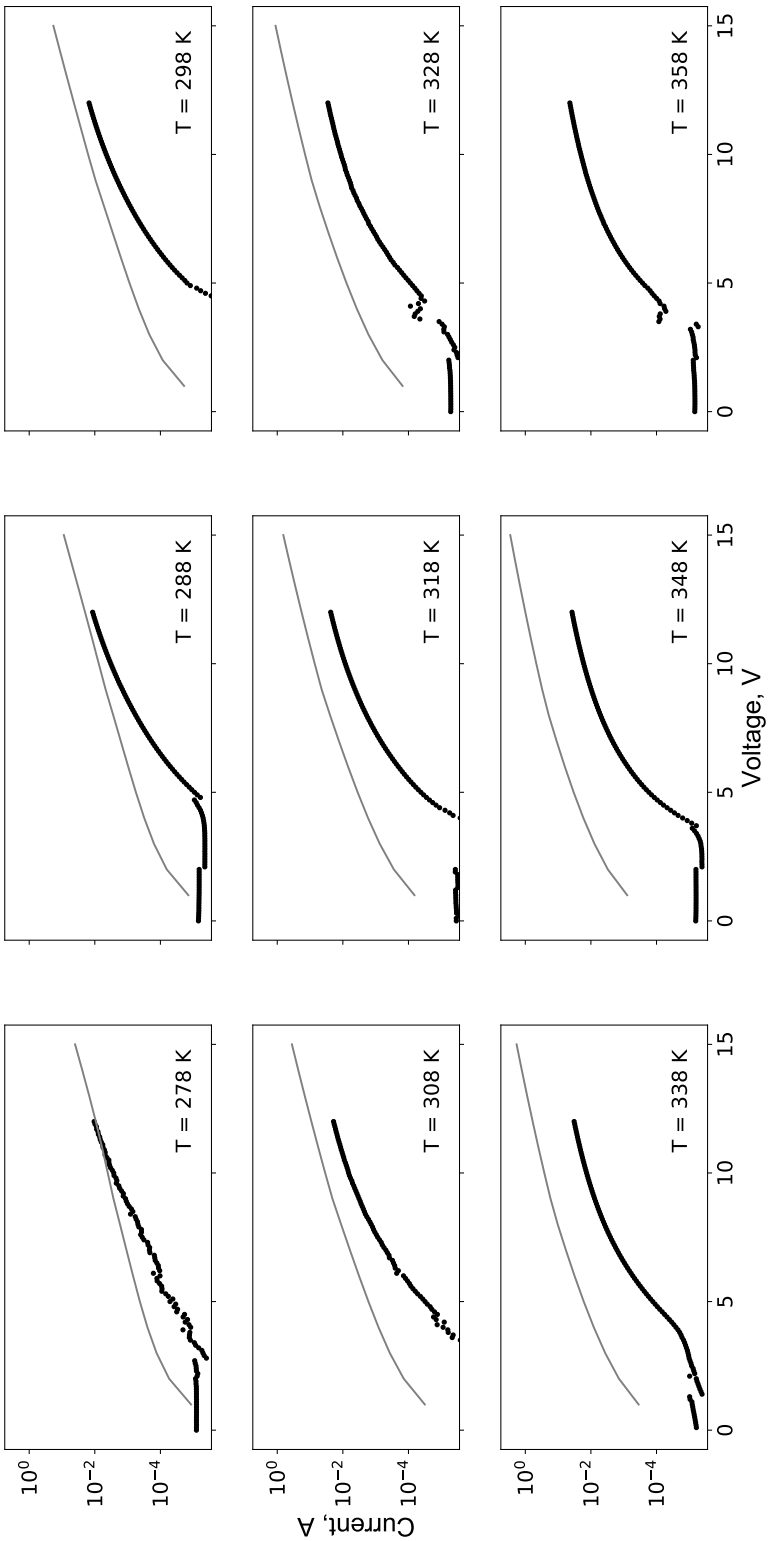


Figure 6.26: Current-voltage characteristics for different temperatures for the value of the disorder parameter equal $120meV$. Solid lines correspond to the modeling results and dots correspond to experimental results.

# Experimental and modeling current voltage characteristics for different temperatures.

In this section we will put the rest T-V curves for different disorder parameters.

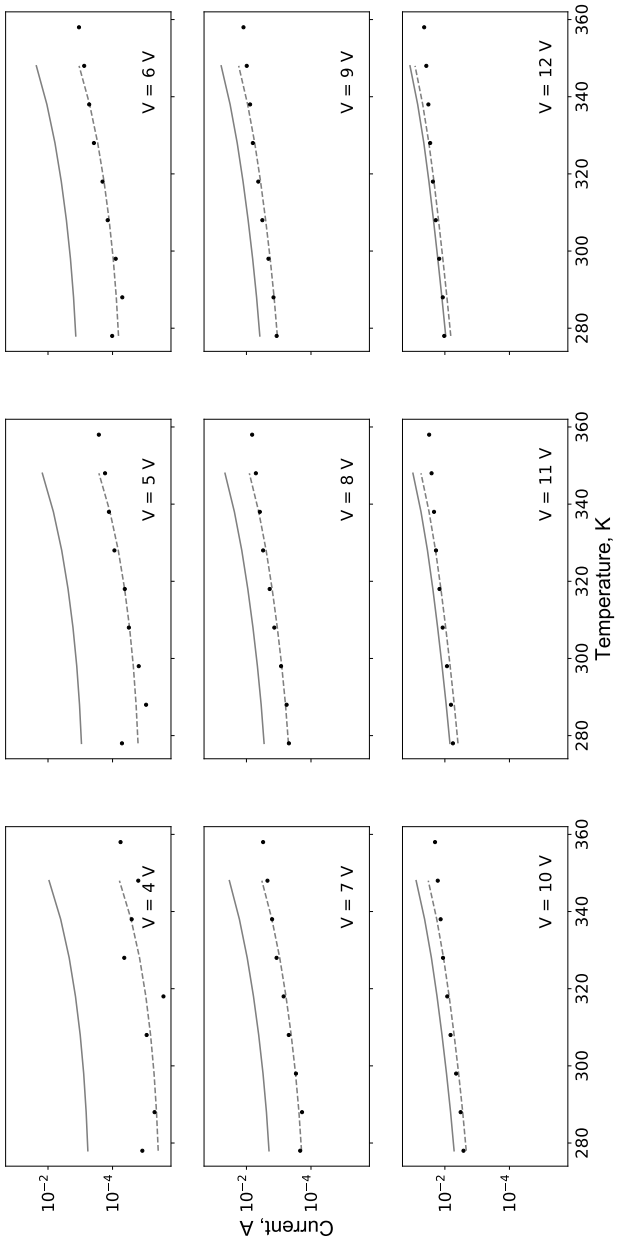


Figure 6.27: Current-temperature characteristics for different applied biases for the value of disorder parameter equal $50meV$. Solid lines correspond to the modeling results, dots correspond to experimental results, dashed lines are the modeling results, shifted to the average difference between modeling and experimental curves, emphasizing the temperature behavior.

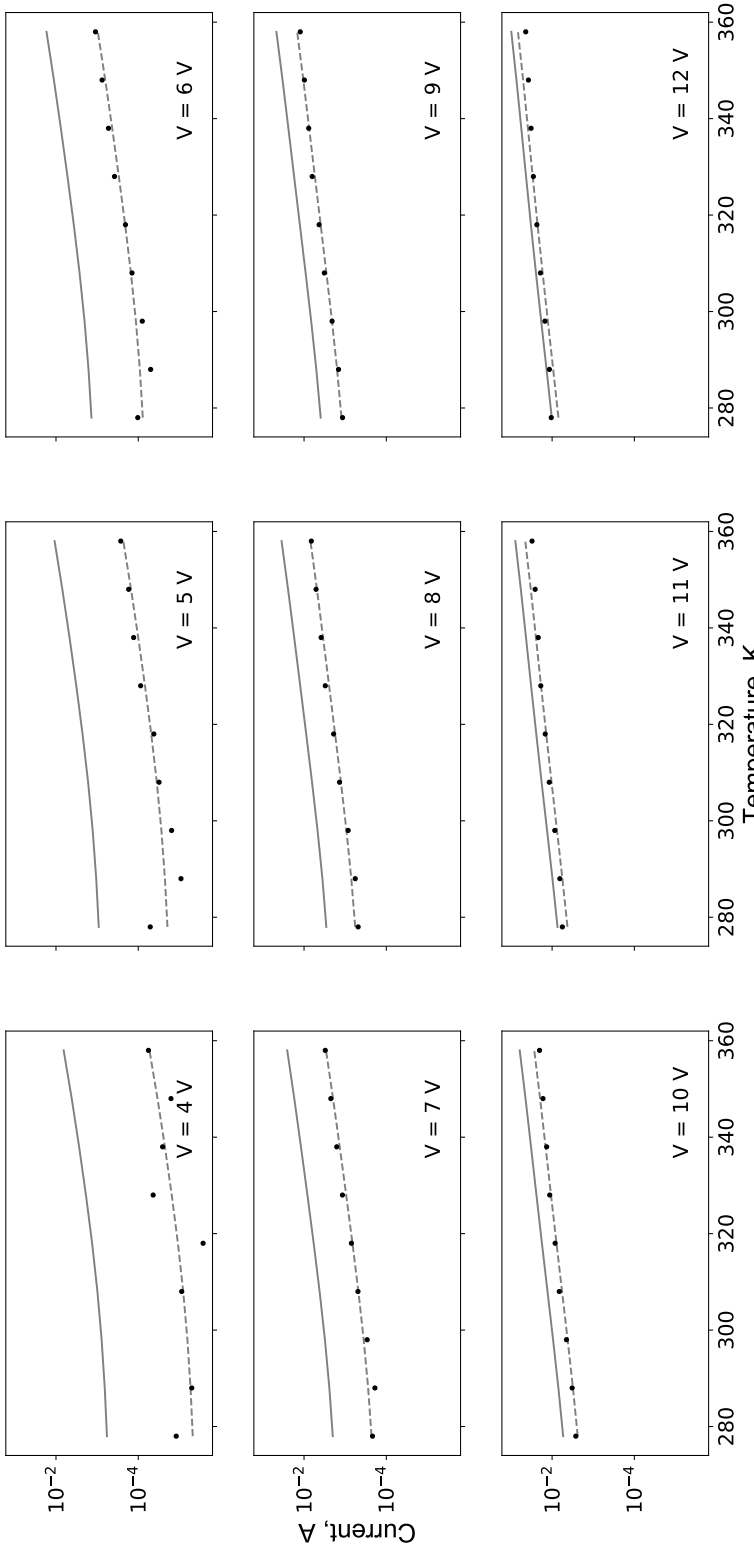


Figure 6.28: Current-temperature characteristics for different applied biases for the value of disorder parameter equal $55meV$. Solid lines correspond to the modeling results, dots correspond to experimental results, dashed lines are the modeling results, shifted to the average difference between modeling and experimental curves, emphasizing the temperature behavior.

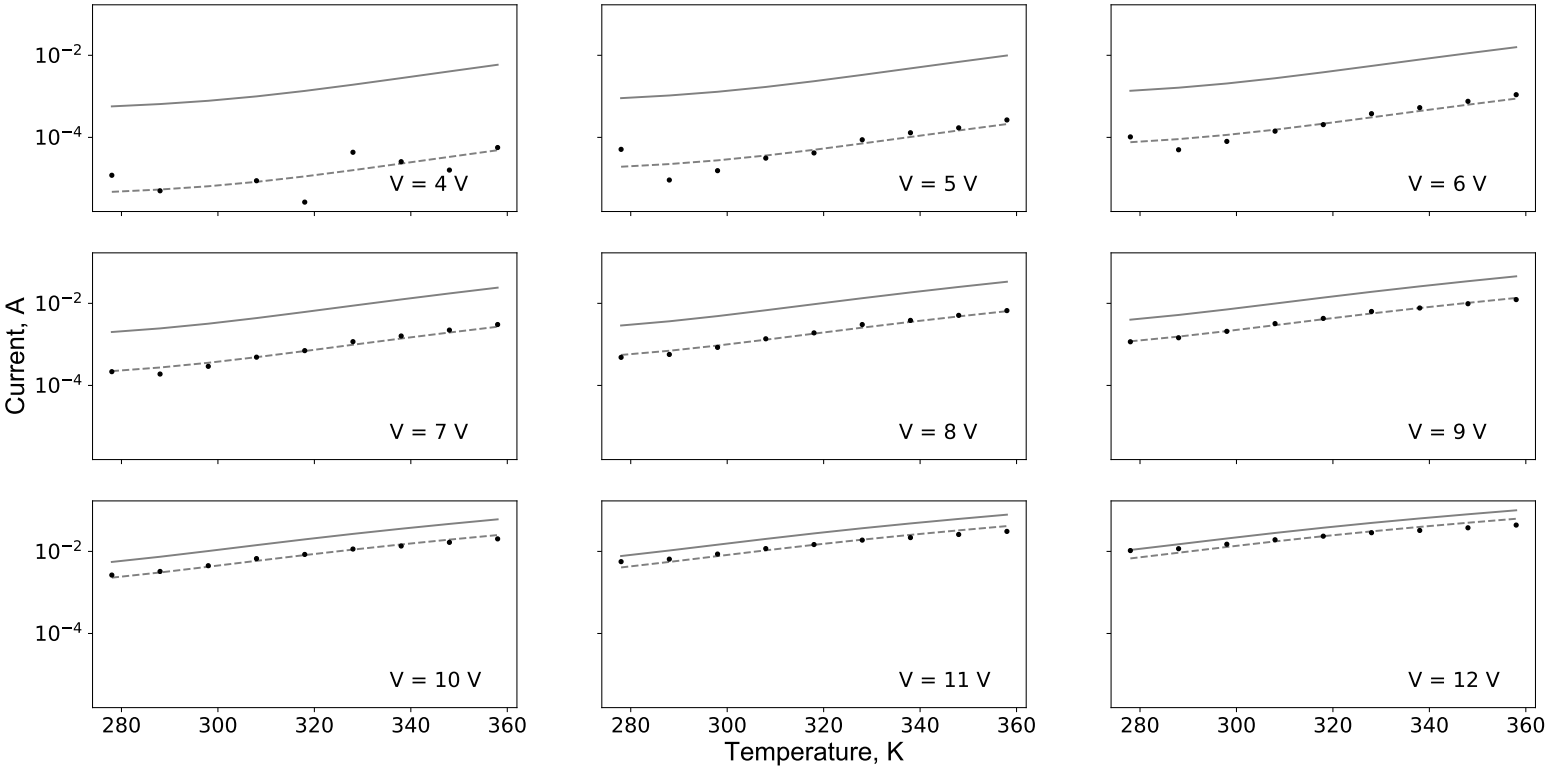


Figure 6.29: Current-temperature characteristics for different applied biases for the value of disorder parameter equal $60meV$. Solid lines correspond to the modeling results, dots correspond to experimental results, dashed lines are the modeling results, shifted to the average difference between modeling and experimental curves, emphasizing the temperature behavior.

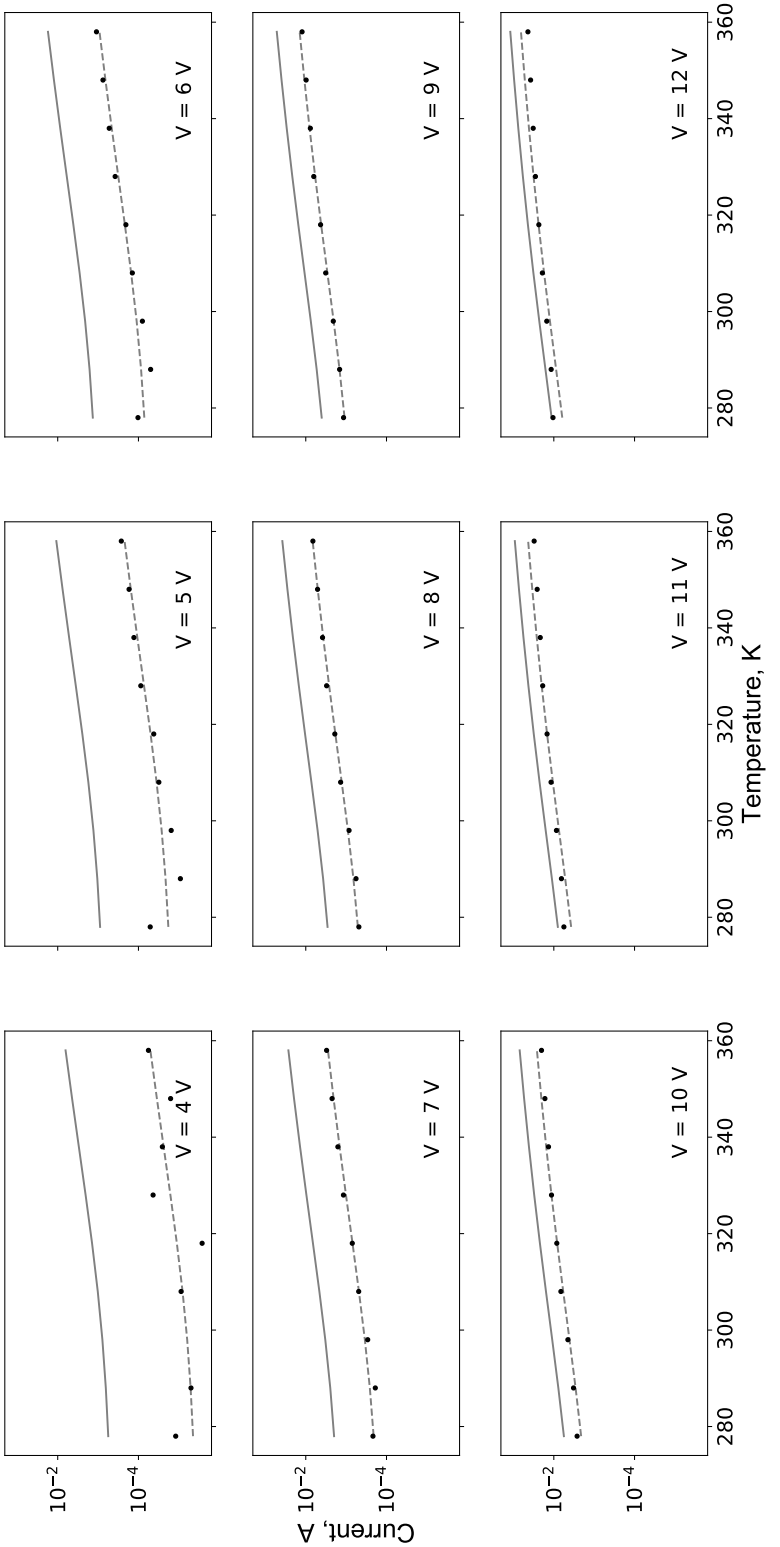


Figure 6.30: Current-temperature characteristics for different applied biases for the value of disorder parameter equal $65meV$. Solid lines correspond to the modeling results, dots correspond to experimental results, dashed lines are the modeling results, shifted to the average difference between modeling and experimental curves, emphasizing the temperature behavior.

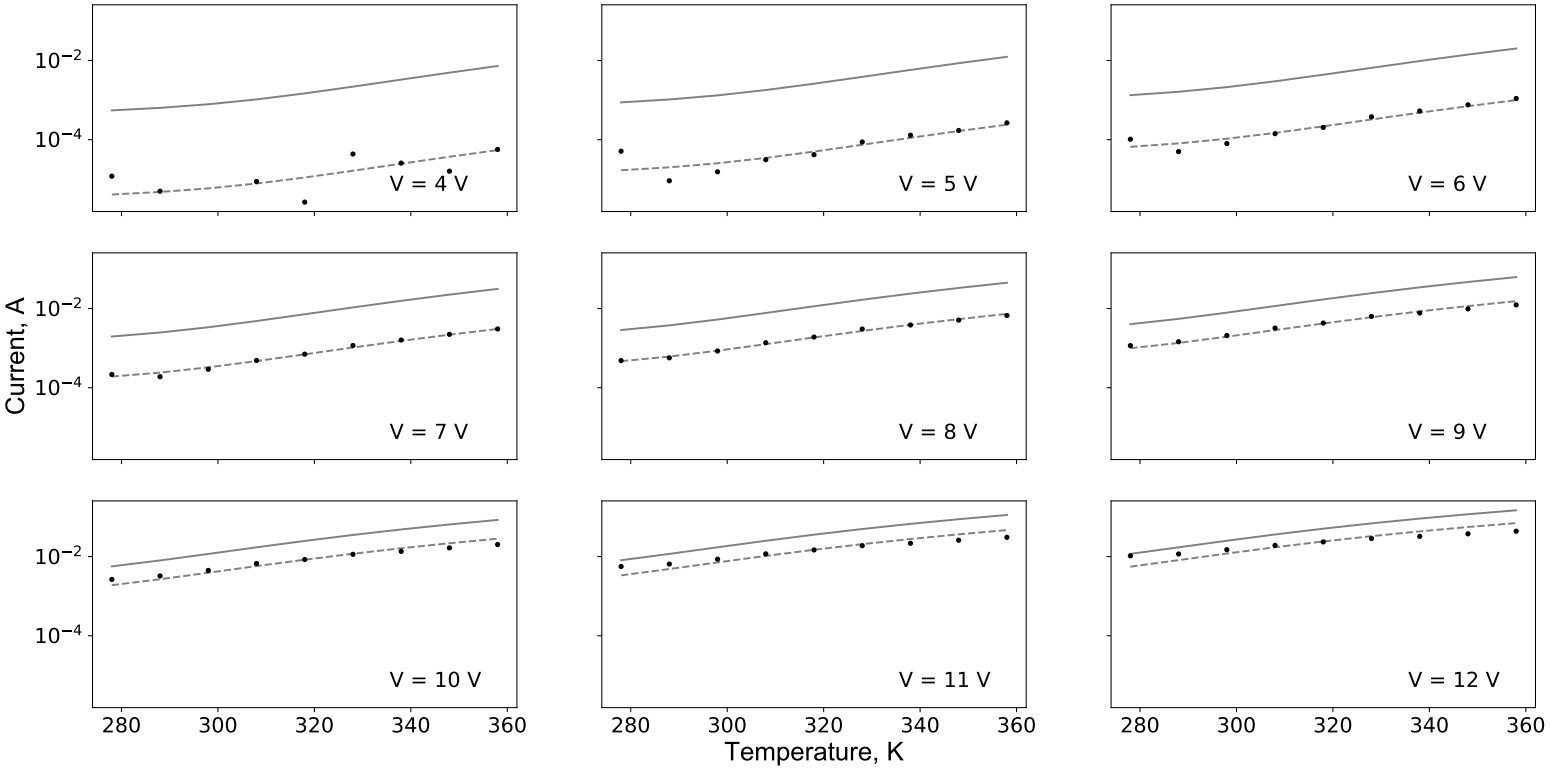


Figure 6.31: Current-temperature characteristics for different applied biases for the value of disorder parameter equal $70meV$. Solid lines correspond to the modeling results, dots correspond to experimental results, dashed lines are the modeling results, shifted to the average difference between modeling and experimental curves, emphasizing the temperature behavior.

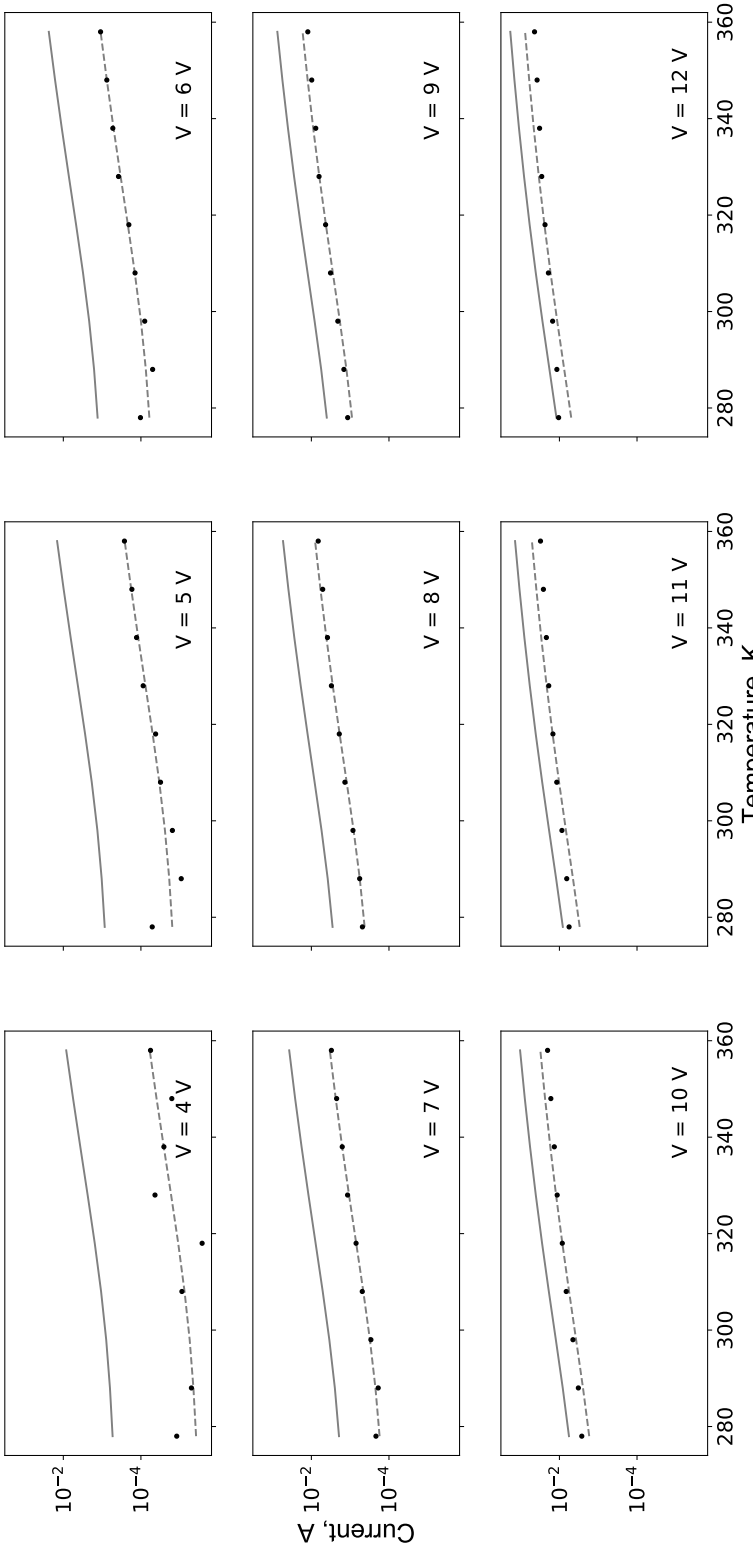


Figure 6.32: Current-temperature characteristics for different applied biases for the value of disorder parameter equal $75meV$. Solid lines correspond to the modeling results, dots correspond to experimental results, dashed lines are the modeling results, shifted to the average difference between modeling and experimental curves, emphasizing the temperature behavior.

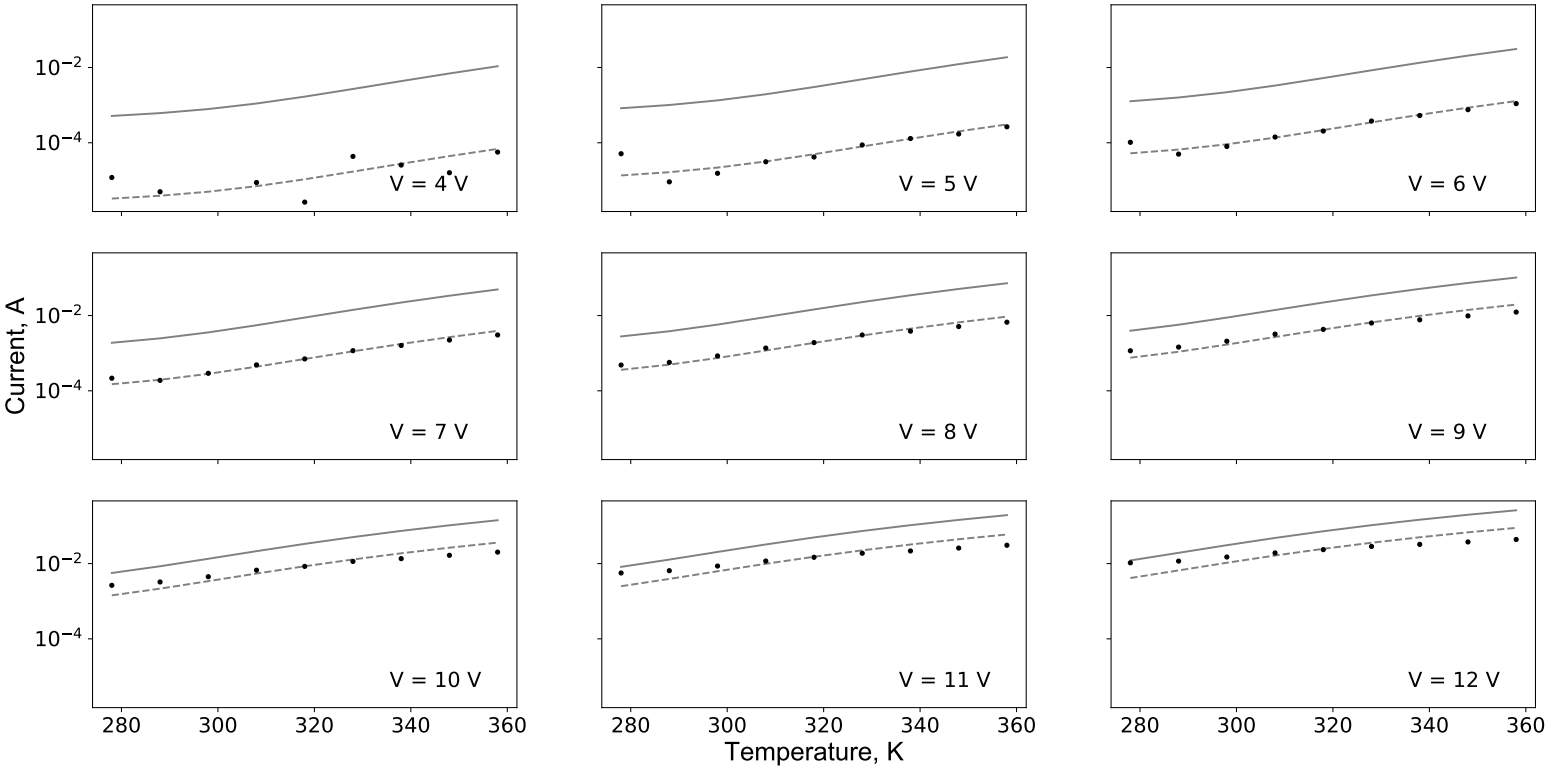


Figure 6.33: Current-temperature characteristics for different applied biases for the value of disorder parameter equal 82.5$meV$. Solid lines correspond to the modeling results, dots correspond to experimental results, dashed lines are the modeling results, shifted to the average difference between modeling and experimental curves, emphasizing the temperature behavior.

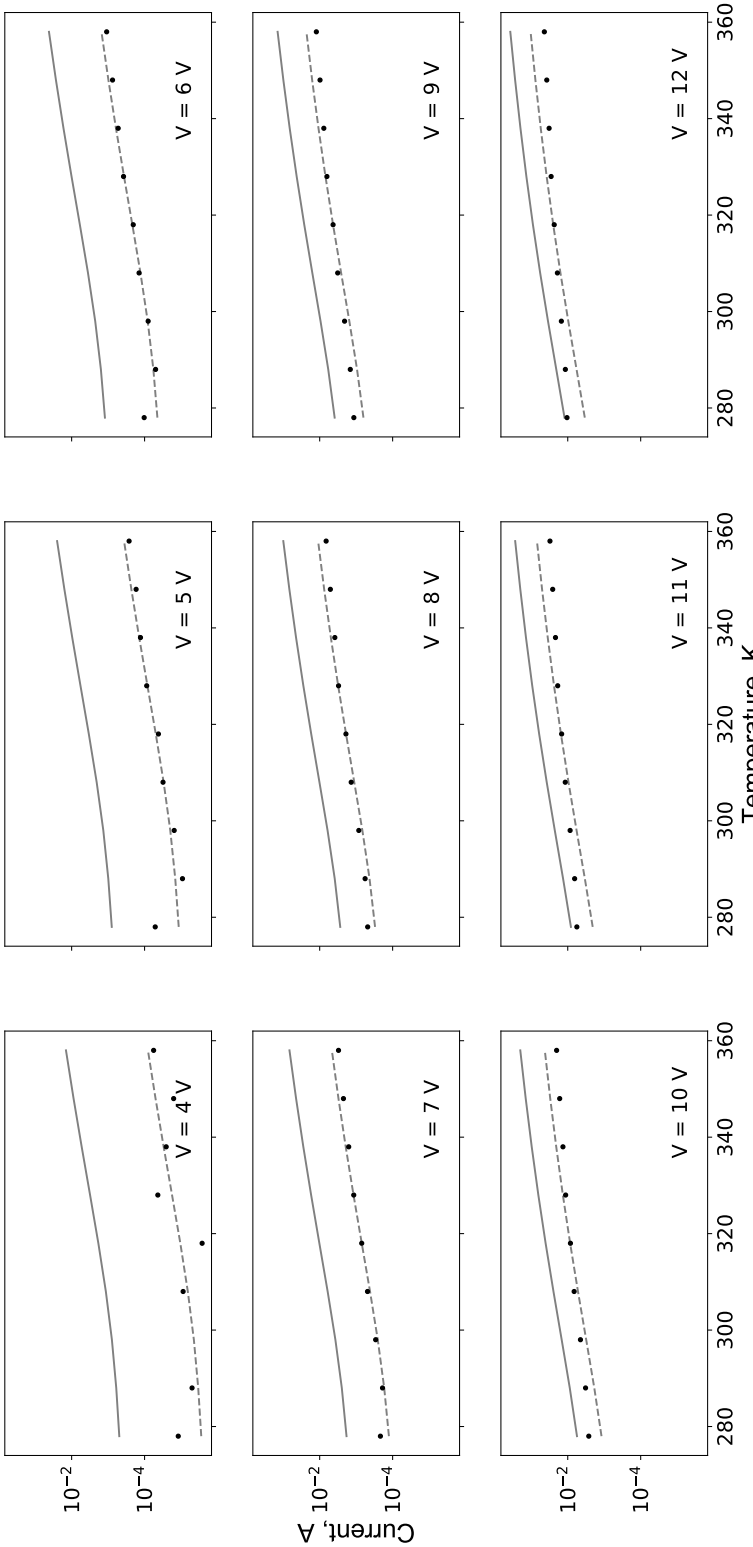


Figure 6.34: Current-temperature characteristics for different applied biases for the value of disorder parameter equal $90meV$. Solid lines correspond to the modeling results, dots correspond to experimental results, dashed lines are the modeling results, shifted to the average difference between modeling and experimental curves, emphasizing the temperature behavior.

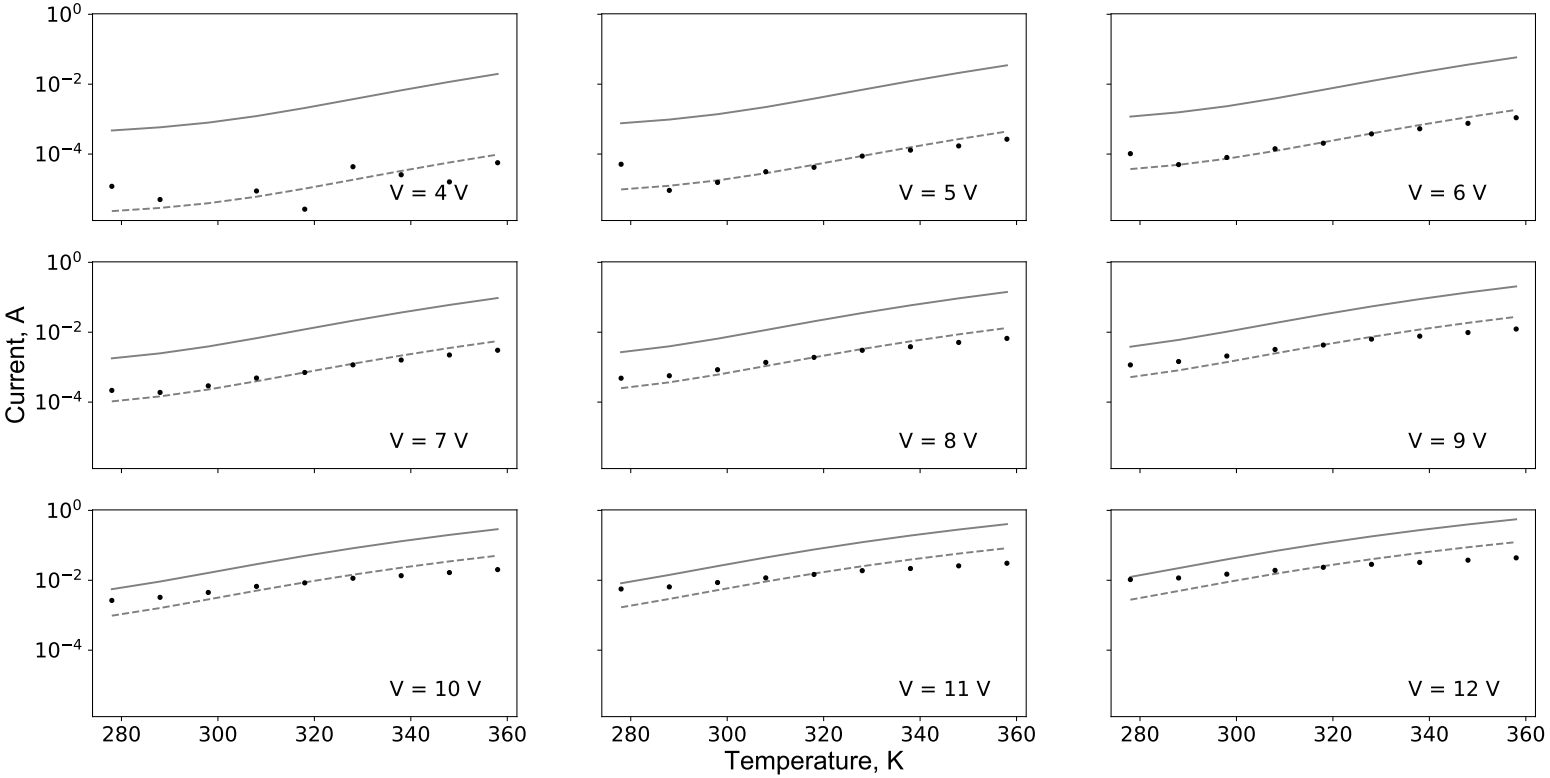


Figure 6.35: Current-temperature characteristics for different applied biases for the value of disorder parameter equal 97.5$meV$. Solid lines correspond to the modeling results, dots correspond to experimental results, dashed lines are the modeling results, shifted to the average difference between modeling and experimental curves, emphasizing the temperature behavior.

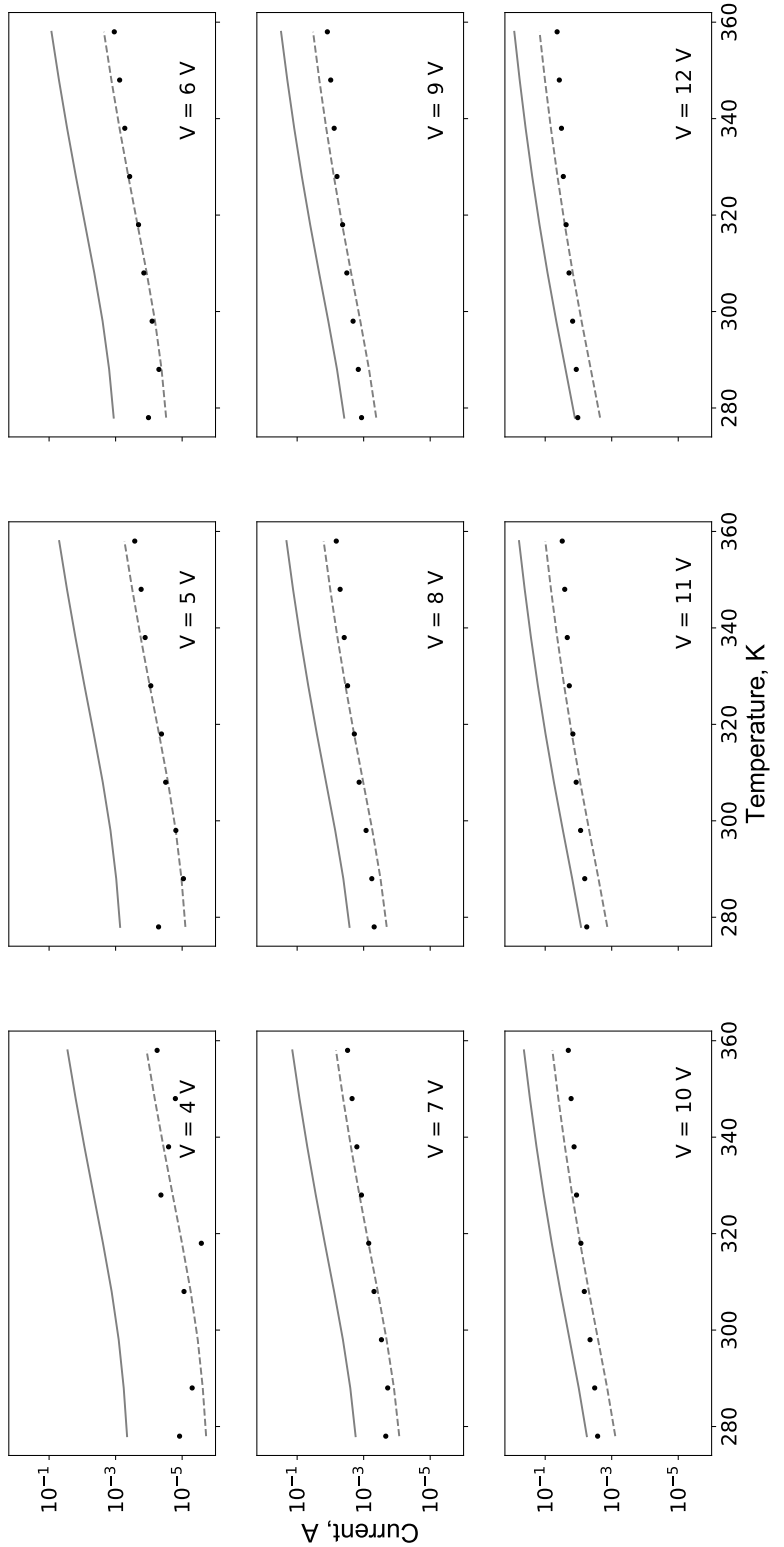


Figure 6.36: Current-temperature characteristics for different applied biases for the value of disorder parameter equal $105meV$. Solid lines correspond to the modeling results, dots correspond to experimental results, dashed lines are the modeling results, shifted to the average difference between modeling and experimental curves, emphasizing the temperature behavior.

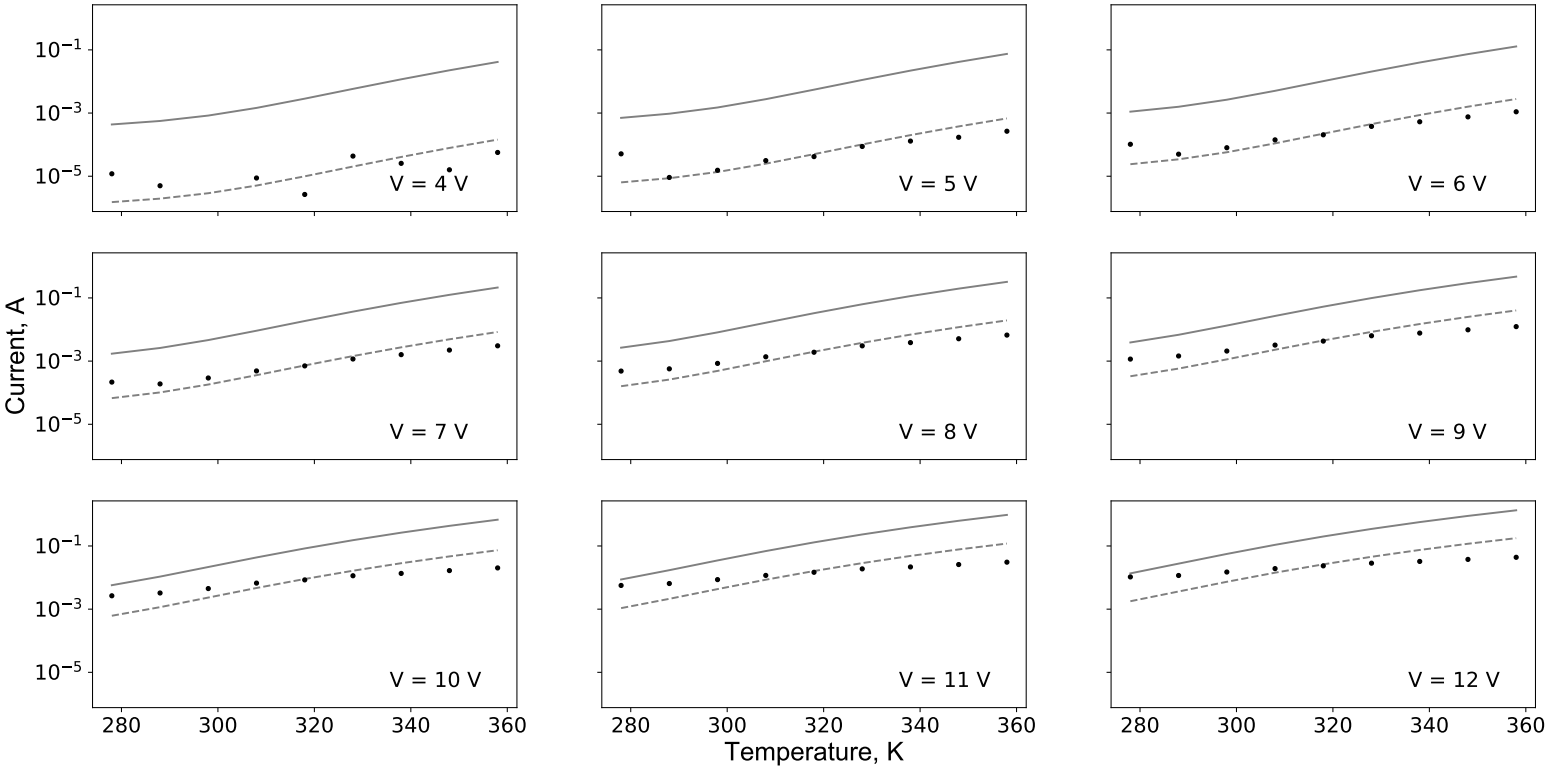


Figure 6.37: Current-temperature characteristics for different applied biases for the value of disorder parameter equal 112.5$meV$. Solid lines correspond to the modeling results, dots correspond to experimental results, dashed lines are the modeling results, shifted to the average difference between modeling and experimental curves, emphasizing the temperature behavior.

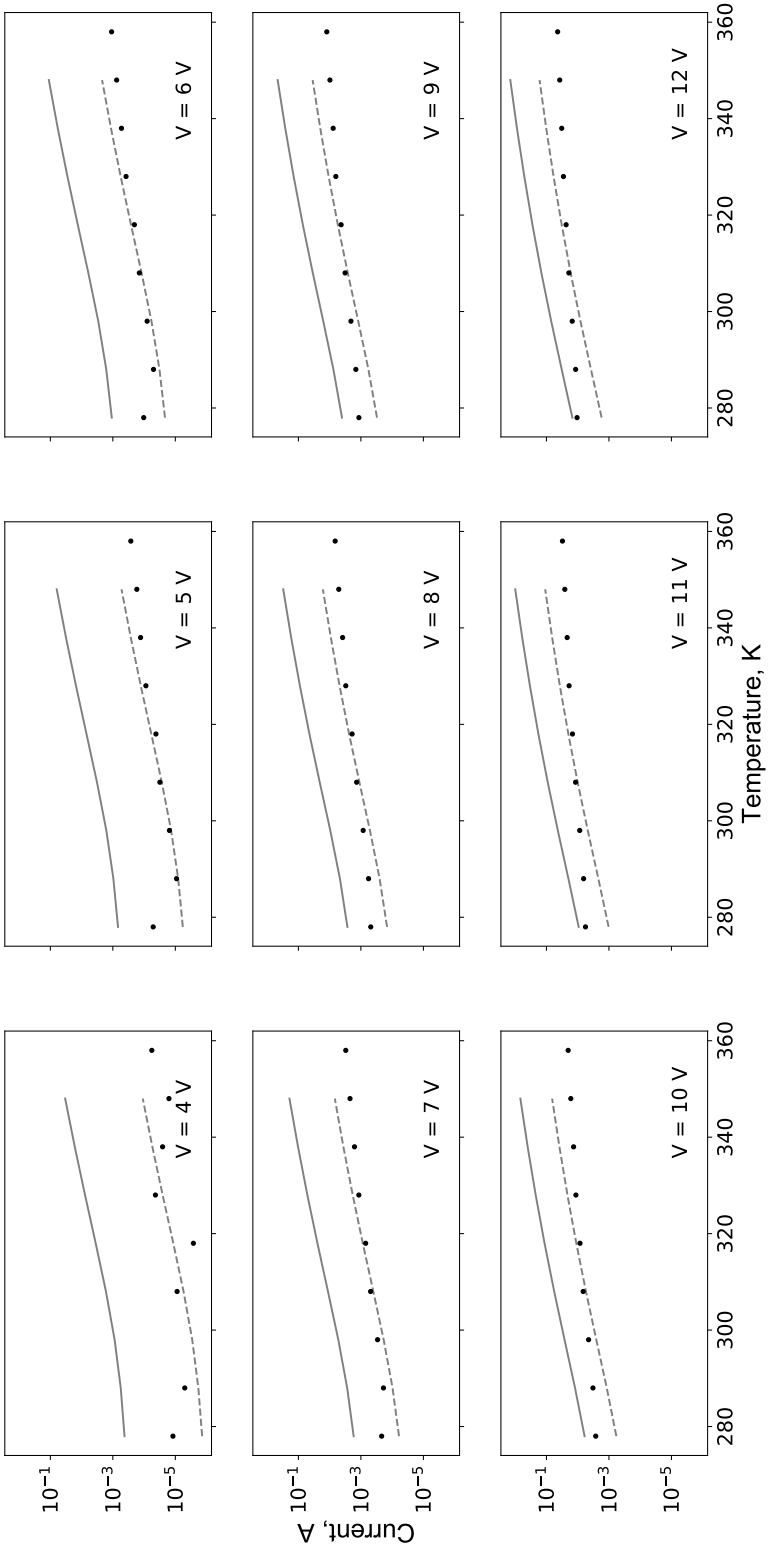


Figure 6.38: Current-temperature characteristics for different applied biases for the value of disorder parameter equal $120meV$. Solid lines correspond to the modeling results, dots correspond to experimental results, dashed lines are the modeling results, shifted to the average difference between modeling and experimental curves, emphasizing the temperature behavior